DEFENCE S&T TECHNICAL BULLETIN

VOL. 12 NUM. 2 YEAR 2019 ISSN 1985-6571

CONTENTS

Ministry of Defence
Malaysia

SCIENCE & TECHNOLOGY RESEARCH INSTITUTE FOR DEFENCE (STRIDE)

AIMS AND SCOPE

The Defence S&T Technical Bulletin is the official technical bulletin of the Science & Technology Research Institute for Defence (STRIDE). The bulletin, which is indexed in, among others, Scopus, Index Corpenicus, ProQuest and EBSCO, contains manuscripts on research findings in various fields of defence science & technology. The primary purpose of this bulletin is to act as a channel for the publication of defence-based research work undertaken by researchers both within and outside the country.

WRITING FOR THE DEFENCE S&T TECHNICAL BULLETIN

Contributions to the bulletin should be based on original research in areas related to defence science & technology. All contributions should be in English.

PUBLICATION

The editors' decision with regard to publication of any item is final. A manuscript is accepted on the understanding that it is an original piece of work that has not been accepted for publication elsewhere.

PRESENTATION OF MANUSCRIPTS

The format of the manuscript is as follows:

a) Page size A4
b) MS Word format
c) Single space
d) Justified
e) In Times New Roman, 11-point font
f) Should not exceed 20 pages, including references
g) Texts in charts and tables should be in 10-point font.

Please e-mail the manuscript to:

1) Gs. Dr. Dinesh Sathyamoorthy (dinesh.sathyamoorthy@stride.gov.my)
2) Dr. Mahdi bin Che Isa (mahdi.cheisa@stride.gov.my)

The next edition of the bulletin (Vol. 13, Num. 1) is expected to be published in April 2020. The due date for submissions is 15 January 2020. **It is strongly iterated that authors are solely responsible for taking the necessary steps to ensure that the submitted manuscripts do not contain confidential or sensitive material.**

The template of the manuscript is as follows:

TITLE OF MANUSCRIPT

Name(s) of author(s)

Affiliation(s)

Email:

ABSTRACT

Contents of abstract.

Keywords: *Keyword 1; keyword 2; keyword 3; keyword 4; keyword 5.*

1. TOPIC 1

Paragraph 1.

Paragraph 2.

1.1 Sub Topic 1

Paragraph 1.

Paragraph 2.

2. TOPIC 2

Paragraph 1.

Paragraph 2.

Figure 1: Title of figure.

Table 1: Title of table.

Content	**Content**	**Content**
Content	Content	Content
Content	Content	Content
Content	Content	Content

Equation 1 (1)
Equation 2 (2)

REFERENCES

Long lists of notes of bibliographical references are generally not required. The method of citing references in the text is 'name date' style, e.g. 'Hanis (1993) claimed that...', or '…including the lack of interoperability (Bohara *et al.*, 2003)'. End references should be in alphabetical order. The following reference style is to be adhered to:

Books

Serra, J. (1982). *Image Analysis and Mathematical Morphology*. Academic Press, London.

Book Chapters

Goodchild, M.F. & Quattrochi, D.A. (1997). Scale, multiscaling, remote sensing and GIS. *In* Quattrochi, D.A. & Goodchild, M.F. (Eds.), *Scale in Remote Sensing and GIS*. Lewis Publishers, Boca Raton, Florida, pp. 1-11.

Journals / Serials

Jang, B.K. & Chin, R.T. (1990). Analysis of thinning algorithms using mathematical morphology. *IEEE T. Pattern Anal.*, **12**: 541-550.

Online Sources

GTOPO30 (1996). *GTOPO30: Global 30 Arc Second Elevation Data Set*. Available online at: http://edcwww.cr.usgs.gov/landdaac/gtopo30/gtopo30.html (Last access date: 1 June 2009).

Unpublished Materials (e.g. theses, reports and documents)

Wood, J. (1996). *The Geomorphological Characterization of Digital Elevation Models*. PhD Thesis, Department of Geography, University of Leicester, Leicester.

AN OVERVIEW OF SHIP MAGNETIC SIGNATURE AND SILENCING TECHNOLOGIES

Mahdi Che Isa*, Hasril Nain, Nik Hassanudin Nik Yusoff, Abdul Rauf Abdul Manap, Roslan Slamatt & Mohd Hambali Anuar

Magnetic Research & Treatment Centre, Science & Technology Research Institute for Defence (STRIDE), Malaysia

*Email: mahdi.cheisa@stride.gov.my

ABSTRACT

There are multiple sources for the signatures that emanate from ships, such as magnetic, acoustic, radar, pressure, electric, seismic and optical. Over the past few years, the international community's efforts have mainly centred on reducing magnetic signature with the aim of decreasing a ship's detectability by reducing the generated levels of the Earth's magnetic distortion in the sea. Nowadays, the need to act on the magnetic risk is becoming increasingly clear, both in the military and civilian fields, based on requirements for ship stealthiness, security of harbour, critical infrastructures and environmental protection. In order to determine the ship's vulnerability to magnetic detection, all sources generating permanent and induced magnetic fields must be considered. Understanding and controlling magnetic signatures on naval ships is one of the most important aspects for naval forces around the world. A great deal of consideration has been put in this field in many countries such as the USA, European nations including Germany, Netherlands, Sweden and Norway, as well as in our country, Malaysia. The aim of this paper is to provide a basis for understanding underwater ship magnetic signature. This paper deals with an overview of natural magnetism, ship magnetic signature sources, their magnetism characteristics, signature detection and current technology for reducing the resulting magnetic signature.

Keywords: *Ship signature; magnetism; magnetic measurement; degaussing (DG); deperming.*

1. INTRODUCTION

The Earth has a substantial magnetic field, which generates complex forces that have immeasurable effects on animal and human everyday lives. The Earth's magnetic field exists because of its composition, especially because of its core. The core is made up of superheated molten metals or alloys disorder with fluctuating magnetic moments under great pressure. Since the molten metals are in electrical contact with each other, current flows between them, generating a magnetic field and creates magnetosphere. The electronic and thermal transport properties of the Earth's core are crucial for the Earth's magnetic field (Drchal *et al*., 2019). This field has both a North and South pole, which can be used for navigational purposes, and they are not static (Chulliat *et al*., 2015). Variations in the electric current have caused the poles to migrate as much as 16 km per year (US DoE, 2019). The Earth's magnetic field is generated by an interaction between rotation in the planet's core and electrical currents. The intensity of the Earth's magnetic field is in reality quite irregular in spite of the general symmetry indicated in Figure 1. Indeed the field intensity slowly varies at different rates according to the position at the Earth's surface. The field then creates the magnetosphere, which in turn, protects the planet from solar radiation, making it important for life on Earth. Without it, the planet's surface would be bombarded by charged particles streaming from the sun that would ultimately rip away Earth's atmosphere (Filipski & Abdullah, 2006).

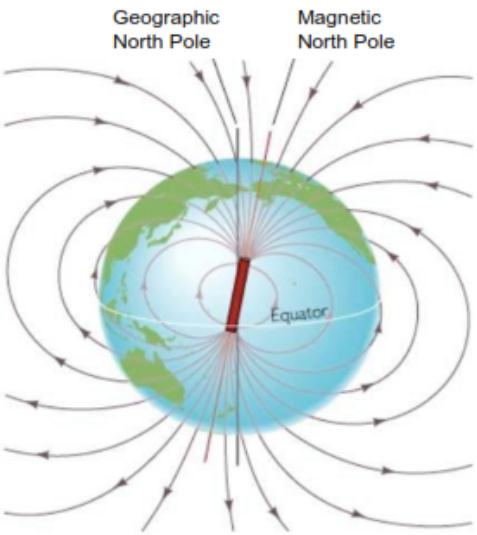

Figure 1: The Earth's magnetic field lines (Filipski & Abdullah, 2006).

Over the past 400 years or so that humans have been measuring the Earth's magnetic field, it has drifted inexorably to the west. Figures 2 show the map of predicted annual rate of change of the total intensity of the Earth's magnetic field for the period of 2015 to 2020, derived from the 12th Generation International Geomagnetic Reference Field (IGRF) model (BGS, 2019). Now, a new hypothesis suggests that weird waves in the Earth's outer core may cause this drift. Throughout those four centuries, the anomalies revealed by these declination measurements have shown a tendency to move westward (Bardsley, 2018).

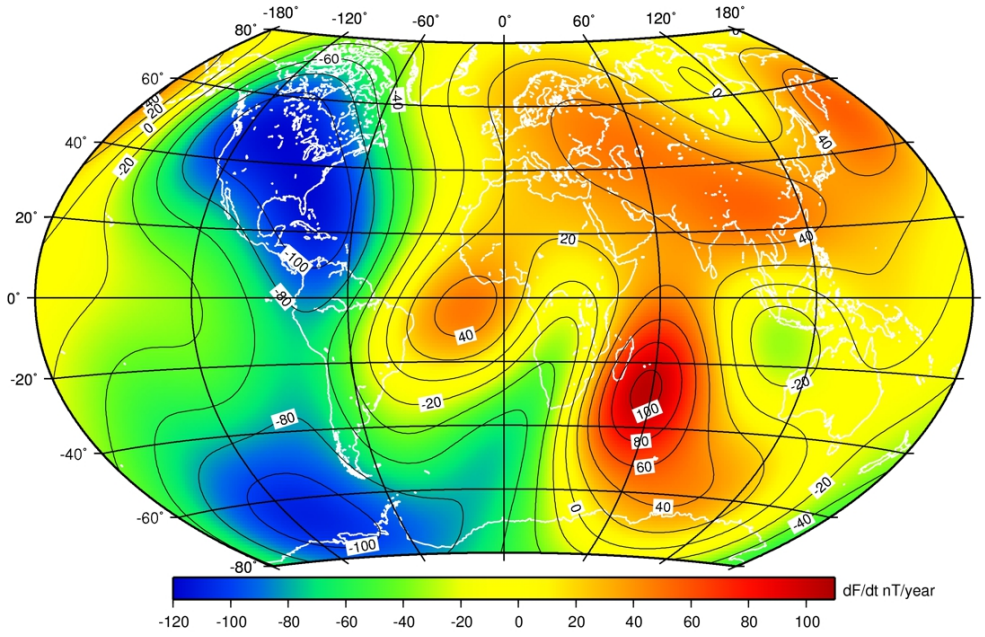

Figure 2: Map of predicted annual rate of change of the total intensity of the Earth's magnetic field for the period of 2015 to 2020 (BGS, 2019).

Magnetic signatures occur because of the interaction of ferromagnetic components and conducting materials with the Earth's magnetic field (Froidurota *et al.*, 2002; Holmes, 2006; 2008). It is important to understand that there are two different types of magnetism, which are. permanent or remnant magnetism, and induced magnetism. Permanent magnetism is when an object creates its own

magnetic field (de Boer, 2001; Skomki & Coey, 2016), whereas induced magnetism is the act of a force changing a material's ambient field into a magnet (Gatteschi *et al*., 2003). More specifically, induced magnetism is the combined effect of a magnetic property of the material (permeability), the Earth's magnetic field, and the shape and orientation of the object in the Earth's magnetic field. When an object's permeability is high, it is considered ferromagnetic and in the presence of the Earth's magnetic field, the two fields create a stronger magnet, which will produce a higher magnetic signature (Bright *et al*., 2014; Gearhart, 2014).

Most of metallic structures, independent of their shape and size, are mainly built from ferromagnetic materials, causing them to disturb the Earth's magnetic field and make up the so called magnetic signature (Aird, 2000). Figure 3 is an example of magnetic signature that can be characterised and identified univocally as a ship, the same way fingerprints identifies human beings. The importance of this signature is well-known since early in the past century, mainly in the defence field and especially centred on the so-called ship's magnetic signatures. For example, the detection of ships by naval mines based on their magnetic signatures was quite important in the naval field during World War II. In parallel with advanced sensors and technological improvements during the 21st century, and especially in the defence field, specific techniques have been developed to reduce the level of magnetic signature emitted into the sea (Holmes, 2006, 2007).

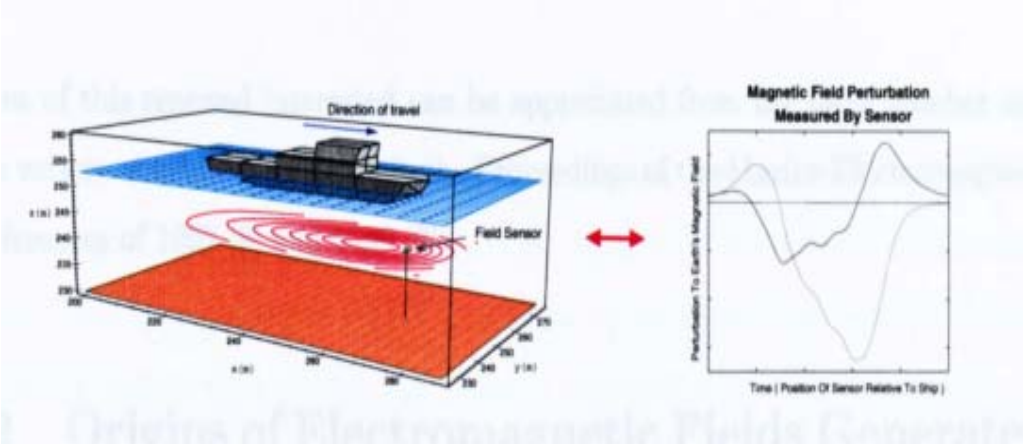

Figure 3: Schematic showing the change in the Earth's magnetic field recorded by a sensor as a ship passes above (Aird, 2000).

This paper comprises of four sections in addition to this introduction section. The second section briefly describes the magnetic signature of naval ships. In the next two sections, the importance of understanding the magnetic signature emitted from ships is discussed. In the following section, a ranging and treatment procedure used to reduce or control the magnetic signatures is described. Finally, the paper is completed with the way forward and conclusions.

2. THE MAGNETIC SIGNATURE OF A SHIP

2.1 The Phenomena of Ship's Magnetic Signature

Naval ships are mainly constructed of steel, causing them to disturb the Earth's magnetic field. Due to its distortion effects on the Earth's magnetic field, a naval ship can be easily detected magnetically using a trigger magnetic sensitive ordnance or devices that are designed to detect these distortions. During World War II, the Germans introduced magnetic mines, an inexpensive and highly effective weapon tethered to anchoring devices. Most naval mines are actually designed to be triggered when the magnetic field around them is disrupted which occurs when large amounts of ferromagnetic structures in the form of ships or submarines passed overhead (Richardson, 1981; LaGrone, 2014).

Therefore, countermeasure systems should be installed aboard a ship to reduce the ship's effect on the Earth's magnetic field disruption and makes the ship virtually undetectable by magnetic mines or

other device, with the intention of increasing its survivability (Poteete, 2010). As sensor technologies advanced and becoming more sensitive, the process of reducing the magnetic signatures of any naval ships or submarines is very critical and important today as compared as it was 80 years ago. This is due to the fact that magnetic signatures can easily be detected in the presence of any objects or structures made from ferromagnetic materials. In the case of a naval ship's magnetic signature, it is mainly caused by the following four contributions (Holmes, 2006, 2007).

i. The interaction between the steel ship's structure and the static Earth's magnetic field.
ii. The use of cathodic protection to control the corrosion of the metal surface of the ship.
iii. Eddy currents in the ship's hull by the motion of the ship in the Earth's magnetic field.
iv. Stray fields generated by electrical equipment and cabling inside the ship.

A smaller signature, called the Eddy current signature, also occurs due to the motion of the ship, especially its side-to-side rocking motion (Zivi *et al*., 2001). The motion of the ferromagnetic and other conducting materials in the Earth's magnetic field induces Eddy currents and these, in turn, cause a reaction field. In addition, all ships also include equipment for cathodic protection, which creates a direct current (DC) electric field surrounding the platform and, in the sea, causes currents to flow and return through the hull and produce so-called corrosion-related magnetic signature field (Polyamp, 2011).In this paper, we limit ourselves to the first contribution, the interaction between the ferromagnetic steel ship and the Earth's magnetic field. The knowledge of electric and magnetic fields can be described in detail using the Maxwell equations (Kaufman *et al*., 2014).

The ship structure is made out of welded steel plates. Due to the ferromagnetic behaviour of steel, the ship structure is magnetised in the presence of the Earth's magnetic field. This is due to the fact that steel has the following complex magnetic behaviour or characteristics (Wagner *et al*., 1996; Sehitoglu *et al*. 2005; Berti *et al*., 2015; Aydin *et al*., 2017; Kachniarz *et al*., 2018):

(i) Hysteresis: The magnetic memory of steel constantly changes its properties. The changes are due to a present background field. The way how the steel is magnetised thus changes over time. This complex behaviour can be expressed by a so-called hysteresis curve that shows the magnetisation of the steel is in relation to the background field.

(ii) Magneto-mechanical effects: The behaviour and properties of steel change due to mechanical stress. Examples of mechanical stress are bending or welding of steel plates, and damage to the ship's hull because of any incidents. For submarines, the different effects play an important role. As the pressure on the submarine's pressure hull rises when it is deep below sea level, the hysteresis curve of the steel hull changes significantly. These effects are called the Villari effects (Bieńkowski & Kulikowski, 1980).

(iii) Inhomogeneous magnetisation: Zooming in onto a steel plate leads to the visibility of so-called magnetic domains. In each domain, the magnetisation is uniform, but these magnetic domains vary in shape and cover the steel plate quite randomly. Therefore, the magnetisation of a steel plate is inhomogeneous. When a background field changes, the shape of these magnetic domains changes as well and therefore changing the magnetisation of steel.

2.2 Magnetic Signatures Design and Simulation

As magnetic sensors become more sophisticated and are incorporated into naval weapon systems, the need to update the magnetic signature management of naval ships becomes increasingly important. However magnetic signature management is not always well understood within the naval community and there is a tendency to rely on information that may be outdated. For example, when magnetic mines were first developed, they could only sense variation in the vertical magnetic field. Therefore the initial naval ship demagnetising systems were configured to deal with that threat using horizontal main degaussing (DG) coils. Nowadays, the majority of naval mines inventoried around the world use multi-axis sensors and trigger on horizontal fields. Thus, it is important to recognise the advancement

of magnetic signature technology for the effectiveness in reducing the risk of being detected. To this end, identifying, understanding, simulating and modelling the underlying physical processes of magnetic signatures have been pursued by previous researchers (Lucas & Richards, 2015; Riley, 2016).

In general, there are two methods for determining magnetic signature; by measurement and simulation. Although measurement has more precision and is more reliable than the simulation, its practical restrictions and expenses make it almost impossible to perform this procedure for all types of ships and submarines. Besides, in a ship's designing phase, when the ship is not built yet, the only method for signature determination is simulation. Simulation is fast, cheap and convenient for all types of ships. However, there are some difficulties in simulation, such as to produce a uniform magnetic field just like the Earth's magnetic field, as well as to have a real model of a ship that includes most of its properties and at the same time is simple enough to avoid long simulation time (Mahmoudnezhad & Ghorbani, 2014).

For example, in Rosu *et al*. (2014), in order to assess ship magnetism induced by the Earth's magnetic field, a virtual ship was built, which was further analysed in a special simulation software environment (e.g., Ansoft Maxwell). The virtual ship model's main dimensions and material characteristics were similar to the ones of the actual ship. An example of the simulation results in the magnetic field representation is shown in Figure 4 (Rosu *et al*., 2014). The analysis showed the impact on ship magnetisation of an external magnetic field oriented vertically. The external magnetic field values were chosen from the main IGRF reference model and the simulation results were compared to a set of measurements performed on the ship itself, and differences between simulated and measured values were further analysed and discussed.

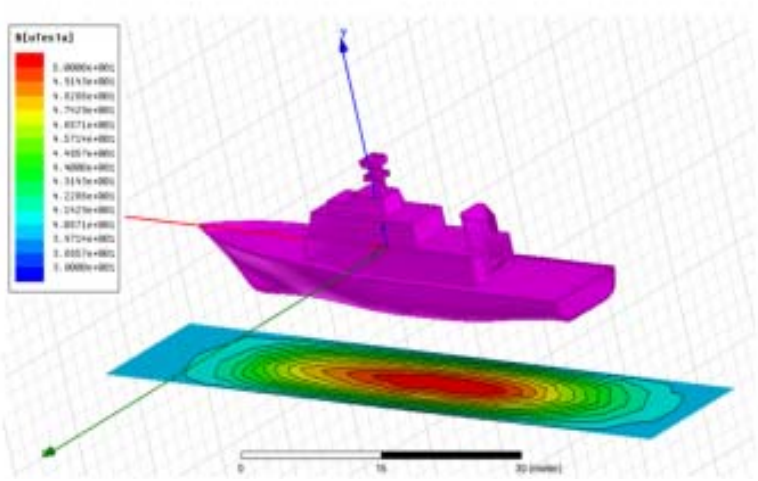

Figure 4: Simulation of ship magnetic signature conducted in Rosu *et al*. (2014).

The study of a ship's magnetic signature, based on modelling and simulation, consists of finding theoretical models that can approximate the ship's behaviour in a real magnetic field. Based on related mathematical formulas or algorithm, among the parameters to be considered in this step include theoretical computation of the field at different depths, comparing the results with computer simulations, and determining the demagnetisation coils and the variation of the currents passing through them (Hubbard, 1996; Aird & Watt, 1999; Wu *et al*., 2015). In the case of a DG coil undergoing a breakdown, simulation can be used as an efficient and practical method to carry out the re-degaussing process for a naval ship based on a mock up scale model studied by Kim *et al.* (2016). This is helpful in assessing the risk of a ship, either in an operational situation or at a design stage, and in determining the right moment for a deperming treatment (Holmes, 2007; Tian *et al*., 2017).

The Magnetic Research Group in STRIDE is currently conducting a preliminary study in obtaining and describing the signatures of naval ships, focusing mainly on the underwater magnetic signature. The magnetic signature characteristics collected will then be used to reduce the magnetic induction field around naval ships. The outcome from this study will be used as an early warning system, to enhance ship readiness and to give further advice if the magnetic signature level becomes critical.

3. MAGNETIC SIGNATURE DETECTION

3.1 Magnetic Ranging

The first step in reducing ship magnetic signature is to identify the areas of the ship that are contributing to the signature, which calls for an accurate measurement. Determining the coil effects and initial optimisation of the magnetic signature require the use of a magnetic range. Due to the various steps and physical processes involved, each signature is measured in a different manner, using highly sensitive sensors under controlled conditions. Static magnetic ranges are typically equipped with a linear array of magnetometers located along east-west and north-south polygon navigation routes, which measure the ship's magnetic field strength as it passes over. Accurate position measurement of the ship during this pass allows the field strength to be plotted against the ship's keel position, allowing the effects of the various coils to be evaluated (Choi *et al.*, 2012). For example, a typical result of magnetic ranging is given in the Figure 5. The DG system installed on board calculates the value of the current of the coil in the downwards (*Z*) axis direction with the aim of reducing the induced magnetisation of the ship with respect to the direction of the Earth's magnetic field (Abdul Rauf *et al.*, 2018).

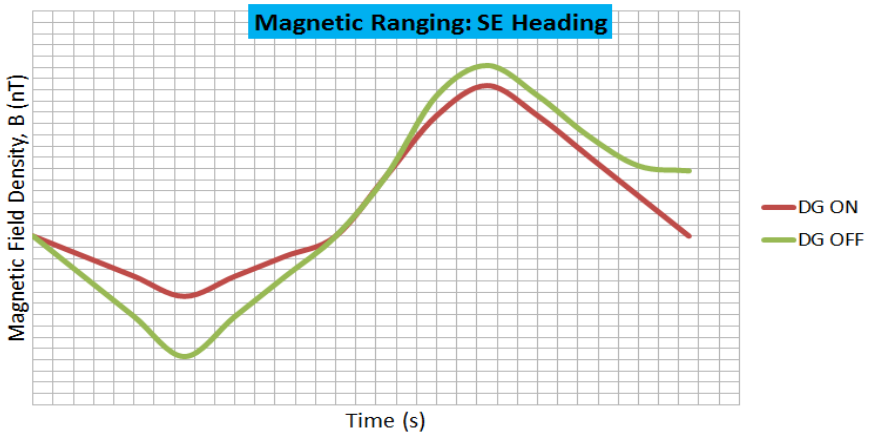

Figure 5: Example of the magnetic signature of a ship with the DG system switched ON and OFF (Abdul Rauf *et al.*, 2018).

In order to fix the ranging system, these sensitive magnetometers or sensors, are placed inside the support structures fixed on the seabed and are connected to an onshore instrumentation building by cables that provide power and a medium for data transmission. It is compulsory to install the support structure made of non-magnetic material in order to prevent unwanted magnetic influence. Typically, these support structures consist of concrete, fiber glass or polyvinyl chloride (PVC) tubes embedded in the bottom. In some cases, more elaborate support structures are employed, depending upon local bottom conditions and facility requirements. A complete ranging is an iterative process, combining range data with knowledge of the ship's magnetic characteristics (Polyamp AB, 2011; SAM Electronics, 2019a).

In the case of using a portable ranging system, the magnetometer and its digitiser can be embedded in an unmanned airborne vehicle (UAV) or drone (ECA Group, 2016), autonomous underwater vehicle (AUV) (Amstrong *et al.*, 2009; 2010; Folk *et al.*, 2010; Christopher *et al.*, 2013; Funaki *et al.*, 2014) or underwater multi-influence sensor system (Polyamp AB, 2011). The data is transmitted onboard, the detection risk is automatically estimated, and the degaussing parameters are computed. For

example, the ECA Group announced a first successful mission using a drone based magnetic ranging at sea for the Indonesian Navy in July 2018. STERNA is the first UAV based portable aerial magnetic range used by a navy in the South East Asian region for operational conditions (Rees, 2018). The main advantages of a portable system are the quickness of deployment of the solution (within 15 min) and the speed of the measurement (within 45 min). The total operation is performed within 1 h when conventional systems require up to a day. Both types of ranging systems require a specific or suitable sea area for deployment. The area must be free from regular shipping traffic, depth of the sea range area, low current and sea state of less than 2.

3.2 Magnetic Components

As mentioned previously, there are two types of magnetic signatures that can occur, namely permanent and induced signatures. The permanent signature, caused by realignment of domain walls beyond their reversible energy, occurs when the ship maintains a constant heading in the Earth's magnetic field over a considerable period of time, is subjected to a violent shock or undergoes very large changes in mechanical stress (Holmes, 2007). The induced signature results from the instantaneous response of the magnetisation due to the heading at a particular time. Permanent and induced signatures are often of similar magnitude, although most ships undergo a deperming process to try to reduce the former (Santana-Diaz & Tim, 2019).

The components of a ship's permanent magnetisation are vertical, longitudinal and athwartship (transverse) magnetisation. These three components are constant (except for slow changes with time) and are unaffected by changes in heading or magnetic latitude. Magnetisation is induced in a body of magnetic material when it is brought into a magnetic field. The induced magnetisation depends on the strength of the magnetic field and the orientation of the body of magnetic material with respect to the inducing field (Bekers & Lepelaars, 2013). For example, consider a ship heading to the magnetic north: the horizontal component of the Earth's magnetic field induces a north pole in the bow and a south pole in the stern, or induces a longitudinal (fore and aft) component of magnetisation. The stronger the horizontal component of the magnetic field, the greater the longitudinal component of magnetisation (NES 617, 2001).

If the ship starts at the Earth's south magnetic pole and heads north, the longitudinal component of the induced magnetisation starts at zero at the Earth's south magnetic pole, increases to a maximum at the magnetic equator, and decreases to zero at the Earth's north magnetic pole. Thus, for a constant heading, the longitudinal component changes when the ship moves to a position where the horizontal component of the magnetic field is different, or as it is commonly expressed, when the ship changes its magnetic latitude. If at a given magnetic latitude, the ship changes its heading from north to east, the longitudinal component of the induced magnetisation changes from a maximum on the north heading to zero on the east heading. When the ship changes its heading from east to south, the longitudinal component increases from zero on the east heading to a maximum on the south heading. On southerly headings, a north pole is induced at the stern and a south pole at the bow, just the reverse of the conditions on northerly headings (Naval Ships' Technical Manual, 1992; Bekers & Lepelaars, 2013).

The longitudinal component of induced magnetisation also changes, to some extent, as the ship pitches. The Earth's field induces an arthwartship component of a north pole on the port side and a south pole on the starboard side when a ship is on an east heading. This is the athwartship component of induced magnetisation. Its magnitude depends on the strength of the longitudinal component of the magnetic field of the Earth where the magnetic field is at a maximum at the magnetic equator and zero at the magnetic poles. The athwartship component also changes when the heading changes. Its strongest magnitude is when the ship is headed magnetic east or west, and zero magnitude is present when the ship is headed to the magnetic north or south. The athwartship component of induced magnetisation also changes, to some extent, as the ship rolls (Naval Ships' Technical Manual, 1992).

The magnitude of the vertical induced magnetisation depends on the magnetic latitude. The magnitude is maximum at the magnetic poles and zero at the magnetic equator. The vertical induced magnetisation is directed down when the ship is north of the magnetic equator and up when the ship is south of the magnetic equator. The vertical induced magnetisation thus changes with magnetic latitude. Unlike longitudinal and athwartship induced magnetisation, vertical induced magnetisation does not change with heading, since a change of heading does not change the orientation of the ship with respect to the vertical component of the magnetic field of Earth. The vertical induced magnetisation changes, to some extent, when the ship rolls or pitches. In summary, the three components of induced magnetisation change as follows (Naval Ships' Technical Manual, 1992; Holmes, 2006, 2007):

i. Longitudinal induced magnetisation changes when either the magnetic latitude or the heading changes, and when the ship pitches.

ii. Athwartship induced magnetisation changes when either the magnetic latitude or the heading changes, and when the ship rolls.

iii. Vertical induced magnetisation changes when the magnetic latitude changes or when the ship rolls or pitches, but not when the heading changes.

4. MAGNETIC TREATMENT

4.1 Magnetic Signature Management

Magnetic signature management is a term used by defence scientists to describe the appearance of objects on magnetic sensors. Once a ship is delivered and approved at the first magnetic ranging, it needs to come back regularly to the range to fine tune its magnetic signature. If not, the signature will deteriorate and be a hazard for the ship and its crew, in case it enters lethal waters (Thompson *et al*., 2000). Magnetic treatment or silencing is the science of reducing the magnetic signature of a ship or submarine. Generally, reduction of the permanent magnetic signature is accomplished by deperming process, constructing ships of non-magnetic materials, controlling Eddy current fields and controlling stray fields caused by various items of the ship's equipment. Due to magnetic fields that are constantly being encountered during operations, naval ships and submarines build up a magnetic signature. The Earth's natural magnetic fields between the North and South poles are being crossed routinely while the ships are underway. The traversing of these natural fields and ships lying dormant for extended periods of time during scheduled maintenance result in changes to a ship's magnetic signature. Correcting these changes requires a thorough treatment process to minimise the level of permanent magnetism. Removing or neutralising a magnetic field is a process known as degaussing, and the local range is often called a degaussing range. Specifically, magnetic silencing can be achieved using the degaussing and deperming processes (Daya *et al.,* 2005; Zolotarevskii *et al*., 2005).

The magnetic management procedure is responsible for measuring, analysing and maintaining records of magnetic signature database. All naval ships shall conduct magnetic ranging procedure for calibration and checking signature. Every new ship will run the degaussing range for calibration. This will determine the initial ship's signature and degaussing coil current settings. This process determines the systems' reliability, accuracy and the effectiveness of the ship's degaussing system (Hasril *et al*., 2013; Daya *et al*., 2005). Magnetic signature usually recorded when a ship's entry or leaving naval base. After passing over measuring equipment located at or near the bottom of the sea in which the ship travel, a report of its magnetic characteristics will be produced. If the strength of its magnetic field exceeds a safe operational level, the ship is scheduled to report for calibration ranging. Calibration ranging requires the ship to make a number of passes over the range while its shipboard degaussing coils are being adjusted and calibrated from information supplied from the control station. When the new settings for the degaussing coils have been determined, new degaussing control settings are placed in the degaussing folder. The data of degaussing coil or current setting will be used

as reference for conducting magnetic ranging and treatment to other ship of the same class. If the ship is unable to compensate adequately for its magnetic field because of excessive permanent longitudinal or permanent athwartship magnetisation or an irregular permanent vertical magnetisation, the ship is scheduled to report for deperming (Sarwito *et al.*, 2017).

4.2 Degaussing Systems

The current protocol for reducing a ship's prevailing magnetic signature is twofold. Firstly, the ship is depermed, i.e., it is treated so as to temporarily eliminate the magnetisation. Secondly, the induced magnetisation is countered by passing electrical currents through strategically placed on-board coils so as to set up an opposing field and thus null out the net field. This procedure is referred to as the degaussing process. It is important to remember that magnetic signatures be considered together with the available countermeasures and with the defined threats (Naval Ships' Technical Manual, 1992).

There is a common misconception that magnetic treatment technology can make ships invisible to magnetic sensors. The aim of magnetic treatment is to reduce the signatures in specific ships below the sensor acuity in a given set of environmental conditions. In certain cases, the signature need only be reduced below the certain level at which naval mines are effective. Therefore, the treatment process must be able to reduce the magnetic signatures of a ship in order to maintain minimal susceptibility of the ship to naval mines. To achieve this, a degaussing system (DG system) will seek to compensate for the ship's own magnetic signature as well as for the induced magnetism associated with the ship's navigation through the Earth's magnetic field (Gonjari *et al*, 2017).

Figure 6 showed an illustration of DG coils system (Varma, 2014). The types of compensating coils are the main coils (M) that compensate the induced and permanent vertical components of the ship's magnetic field; the forecastle induced - quarterdeck induced coils (L) that compensate for the longitudinal induced component of the ship's magnetic field; the athwartship coils (A) that compensate the athwartship induced and athwartship's permanent components of the ship's magnetic field (Holmes, 2008). These coils have an optimum effect on the ship's magnetic field when they are used together. The demagnetising coils are very useful to erase the ship's magnetic background, and the compensating coils reduce the inductive effect when the ship is moving through Earth's magnetic field (Choi *et al*, 2012).

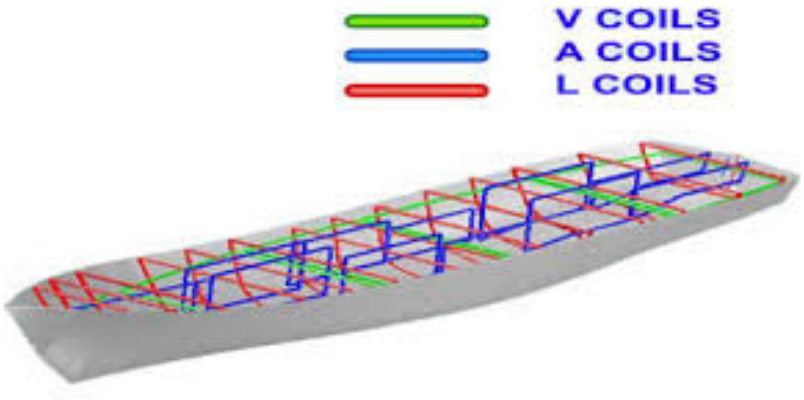

Figure 6: Typical DG coil system installed on a ship (Varma, 2014).

A closed loop degaussing (CLDG) system is an onboard electromechanical system that measures onboard local magnetic fields and, using the onboard measurements, estimates the off board magnetic fields (Henocq *et al*, 2003). CLDG basically involves coil design, modern electronics and computer technology (including algorithmic control) (MOD, 2008). Figure 7 showed the operational aspect of a

CLDG system, where the apparatuses needed to perform CLDG include onboard magnetometers, degaussing coils, analog-to-digital conversion/control equipment and a processing computer to execute the CLDG algorithm (Demilier *et al*., 2011).

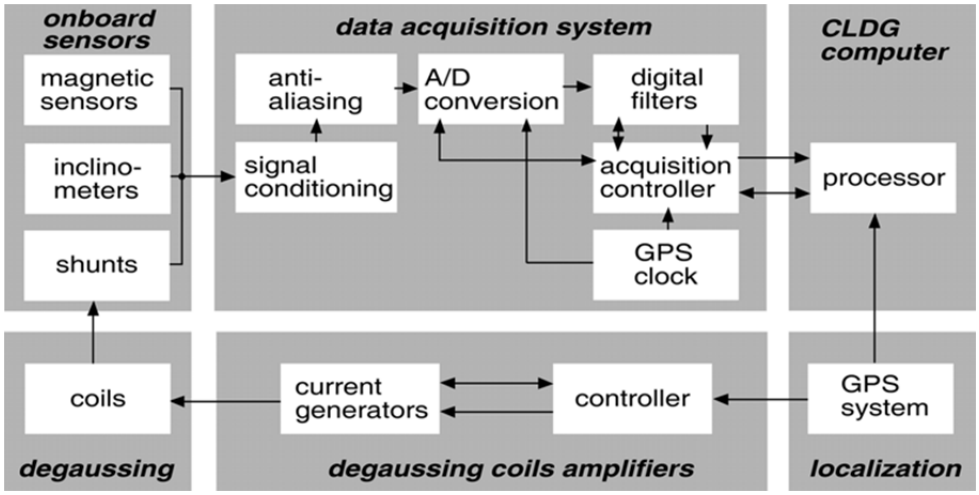

Figure 7: Schematic diagram showing the operational aspects of a CLDG system (Daya *et al.*, 2005)

Not unlike a conventional degaussing (non-CLDG) system, CLDG system employs degaussing coils to conduct electrical current. However, in contrast to conventional degaussing, closed loop degaussing involves a computerised feedback control system that, in real time on a continuous basis, compensates for the changes in the ship's magnetisation on the basis of onboard magnetic measurements. CLDG implements an array of magnetic field sensors situated throughout the ship. During navigation, these onboard sensors constantly monitor the magnetic environment of the ship so as to detect variations in the ship's magnetic signature. In principle, as compared with conventional degaussing systems currently installed on many naval ships, CLDG can afford more accurate control of degaussing currents for purposes of minimising the ship's magnetic signature and permitting longer ship deployment periods between calibrations (Liu *et al*., 2012; Sarwito *et al*., 2017).

4.3 Deperming

In conjunction with magnetic treatment technique, ships are routinely bulk demagnetised in a process called deperming. The demagnetising process can be made in two ways: component or general demagnetisation. Component demagnetisation is conducted using three coils: a longitudinal coil for the vertical component of the longitudinal magnetisation; a transversal coil for the vertical component of the transversal magnetisation; and a vertical coil for the vertical component of the vertical magnetisation. Each of the three coils is powered from separate power supplies where each power supply is capable of precise control over the magnitude and current of the power applied (Kim *et al.,* 2017).

The conventional deperming procedure is called Flash-D (Baynes *et al*,, 2002). The concept is to demagnetise the ship's longitudinal magnetisation, and to bias the permanent vertical magnetisation so as to almost exactly cancel the locally induced vertical component. Flash-D is implemented by subjecting the ship to a sequence of "shots" of an external magnetic field. Each shot consists of a stepwise incremental ramping of the externally applied magnetic field components to a predetermined maximum amplitude and then a stepwise decremental ramping to zero (Mayo, 2010). With each subsequent shot, the polarity of the applied magnetic field is reversed and the amplitude reduced linearly. The maximum amplitude is chosen to be large enough so that all magnetic domains are aligned. In this way the magnetic history is erased. However, for the larger, highly permed ships, facilities are not in place to deliver the required external fields (Holmes, 2008).

Newer deperming technologies have been designed to modify the magnetic signature of ships to within acceptable levels. Deperming is a process of putting the ship inside a collection of coils or placing an arrangement of coils around the ship, and then passing powerful electric impulses throughout the coils to generate a magnetic field in opposition to the magnetic field of the ship. In the same magnetic treatment facility, cables are connected to the power supply house. Pulses of current (up to 6,000 A) are sent through the cable wrapped around the ship or installed on an offshore structure. The purpose is to reduce permanent magnetisation and bring all ships of the same class into a standard condition. It is normally accomplished only once in a ship's life or when major structural changes occur during overhaul. Before deperming begins, all magnetically sensitive equipment is removed from the ship. The deperming process is conducted at a specially designed facility. The process requires the cables to be energised by a high DC current for a specific duration and magnitude. Then, a reverse polarity DC current of the same duration and magnitude is passed through the cables. This process is repeated by reducing the duration and magnitude until the ship is depermed (Arantes do Amaral, 1996; Holmes, 2006, 2007, 2008).

High DC currents are applied to the magnetic treatment coils to create large magnetic fields within the ship under test that reduce the permanent magnetic field of the ship being treated. The onshore control station contains a console to allow operator configuration of the power system and applied current. It also permits the reporting of status information on the power supplies. Magnetometers stationed along the seabed monitor the treatment process, thereby providing magnetic signatures to the treatment officer. The sensor array is positioned at the seabed at a depth of between typically 9 to15m. These sensors measure and monitor the signature of the ship being treated. The data from the sensors is collected by a data acquisition system and is processed by a control computer situated in a control office. A DG officer at the onshore station provides a graphical interface to allow analysis of the measured signature data. Recommendations of the current pulse magnitudes to be applied are provided by the software to assist the operator (Ultra Electronics, 2019; SAM Electronic, 2019a, b).

The deperming range system requires the location of the ship in relationship to the sensors' relevant points during magnetic treatment process. Therefore, the ship's position is tracked using a high accuracy differential Global Positioning System (DGPS) receiver to enable accurate signature measurement (Hasril *et al*., 2013). The DGPS position measurement system consists of two rovers mounted at the bow and stern of the ship, and a base station in the control office is used to determine the precise position of the ship with respect to the measurement range sensors. Ship position data together with the outputs from the magnetic sensor array are used to produce a magnetic model that predicts a keel line magnetic signature (Birsan, 2010). Signature measurements are taken at various points in the treatment process and are used to determine the required treatment setting and to confirm the success of the procedure. Most of the navies around the world practice the use of the deperming process on their newly built ships before commissioning. During the sea acceptance test (SAT) procedure, the newly installed onboard DG system will be tested and verified in terms of its functionality. After the SAT, the onboard DG system will be used to minimise excess permanent and induced magnetic field to achieve magnetic conditions with the acceptable safety limit (ECA Group, 2016; SAM Electronic, 2019a, b).

Drive-In, Over-Run and Close-Wrap are among the deperming systems used in magnetic treatment. Facilities with the Drive-In system (Figure 8) comprise of a fixed construction with the treatment coils permanently installed. The ship to be treated enters the facility from one end and is moored in-situ. The ship is magnetically treated using high magnetic fields, then is unmoored and exits on completion. This type of facility provides for a very fast set up time and treatment of ships. However, construction and power supply costs are the highest of all the available types of magnetic treatment facilities (Ultra Electronics, 2019; SAM Electronic, 2019a). In 2022, the German and Royal Dutch Navy ships are expected to utilise new magnetic treatment facilities in Kiel, Germany. The facility will be able to treat naval ships of up to 180 m long and 25 m wide, and is claimed as the most modern facility of its kind in Northern Europe, jointly funded by Germany and Netherlands at a cost of €54 million (Naval Today, 2017).

The second option is the Over-Run system (Figure 9), which comprises of treatment coils permanently installed on the seabed. These coils produce a large magnetic field that deperm the ship as it transits over the treatment facility in a succession of runs. The greater the depth of water, the greater the current required to achieve the magnetic field levels at the ship's hull necessary to modify the magnetisation and provide the required level of signature reduction. The Over-Run system is the simplest method of treating a ship as there is no requirement for mooring or berthing the ship although treatment can still take many runs over the coils for some ships. Whilst less expensive than the Drive-In treatment system, it is still an expensive system, and the sea-bed installed coils and sensors can be susceptible to damage from dredging, trawling or anchorage (Ultra Electronics, 2019; SAM Electronics, 2019b).

Figure 8: A Drive-In magnetic silencing facility at Kings Bay, Georgia, USA (SSFM International, 2019).

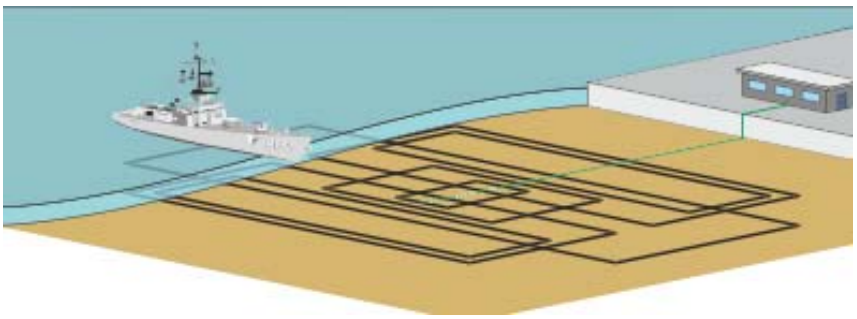

Figure 9: Schematic drawing for a static Over-Run deperming process (UltraElectronics, 2019).

Third option is the Close-Wrap system (Figure 10) with configurable coils sets to treat both ships and submarines, and can be supplied in various formats from fixed, permanent systems to fully portable systems with floating coils with independent power supplies. The treatment has a long lasting effect for all ship types. The system requires a set of coils turn to be wrapped directly around the ship to be treated. The cables are specially designed for each ship to prevent unwanted contribution factors to the treatment process (Ross *et al*., 2012). A floating *Z*-coil is also provided. A portable version of the treatment system is available, which allows the system to be used in several different locations or put into storage when not in use, thereby freeing up the dockyard and jetty space. The main difference between a fixed and portable close wrap treatment facility is that with the fixed arrangement, the *Z* coils and sensors are permanently installed, whereas with the portable systems the *Z* coils are free-floating and hence removable **(**SAM Electronics GmBH, 2019a, b**).**

After the deperming process, ideally the ship is nearly demagnetised. In reality, it actually has a vertical permanent magnetisation that is counter to the assumed induced vertical component so that the total magnetisation vanishes to within a few percent. This situation does not persist for long since the ship is constantly subjected to the Earth’s magnetic field and to mechanical stresses. Thus a

recently depermed ship relaxes to a state in which the locally induced magnetisation is the dominant magnetic signature. On a longer time scale of months, components of the permanent magnetisation recover to values comparable to those before the deperming treatment. Therefore, it is necessary to range the magnetic signature of in service ships regularly to determine when deperming is necessary. It is unfortunate that temporal changes in the permanent magnetisation after deperming have not been adequately monitored. The disadvantage of deperming is that it is not stable, and the ship must be checked periodically once every three or six months (Navy Daily, 2013; Goldberg, 2015).

Figure 10: HMCS Toronto, which is being depermed (close wrap) at Lambert's Point Deperming Station in Norfolk, Virginia (Rago, 2018).

5. CONCLUSION AND WAY FORWARD

Ships are made from a great number of metallic components with distinct magnetisation properties, which is sailed through the sea, produce a magnetic signature. This signature is unique and will be different for each class of ships and depends on the latitude of the navigation area, operational nature and also of the ship's geometry. Understanding the effect of magnetic signatures and treatment selection in dealing with this issue will provide naval operators with advanced information on the readiness and capability to operate safely in high risk waters.

Advances in magnetic sensing technologies have increased the threat from underwater mines, a trend that is expected to continue. Reducing mine risk requires significant signature advancements. Thus, magnetic ranging and DG systems must be capable to measure and reduced the ship magnetic signature. Measurement of the magnetic signature of naval ships allows one to determine a ship's vulnerability to magnetic mines. In addition to improved magnetic signature measurement, analysing and treatment capabilities as well as magnetic ranging and treatment facilities are required and must respond to current and emerging threat capabilities to achieve adequate magnetic reduction properties. The temporal, spectral, and spatial characteristics of ship magnetic signatures that can be exploited by threat sensors must be quantified, and their sources identified and understood in order to find effective approaches to mitigate the risk. Significant investment has to be made in technical expertise and facilities to ensure evolutionary technology in ship signature reduction is achieved and permitted to the operational mission successes.

In the military context, we are interested in ways to avoid detection. Thus, magnetic modelling for signature prediction of in-service ships and ship at design phases is very important. The threat must be countered through continued research and development in the nature of the ambient magnetic environment, magnetic signature management and magnetic countermeasures. Simulation and mock up model measurement are used to study or predict the magnetic signature properties of various ships and other objects of interest, especially in the design phase. Clearly, specific measures are needed to

ensure that adequate ship magnetic signature technology is available and applied in the future to achieve the required standards of ship magnetic signature safety levels. The emphasis should be given in maintaining a ship signature database, develop improved and modern measurement capabilities and treatment facilities, develop physical and computational tools necessary to effectively predict, and support ship signature analysis.

ACKNOWLEDGMENT

The authors gratefully acknowledge the Magnetic Research Group, STRIDE for their help and commitment to support, assist and review throughout all aspects as well as to provide comments that greatly improved the manuscript.

REFERENCES

Abdul Rauf, A.M., Mohd Hambali, A., Mahdi. C.I., Mohd Hazri, R., Roslan, S., Mohd Yusri, O., Hasril, N., Zuraini, A.M. & Muhammad Syauqat, A.K. (2018). Magnetic Assessment of Newly Installed Onboard Degaussing System. *Defence S&T Tech. Bull*., **11**: 265-276

Aird, G. & Watt, A. (1999). Numerical models to study the induced magnetic field generated by the internal structure of ships. *MARELEC Conf. 1999*, ENSIETA, Brest, France.

Aird, G.J.C. (2000). *Modelling the Induced Magnetic Signature of Naval Ship*. PhD Thesis, University of Glasgow, Scotland, U.K.

Arantes do Amaral, J.A.A., Botelho, P.L., Ebecken, N.F.F. & Caloba, L.P. (2002). Ship's Classification Bby Its Magnetic Signature, 4-9 May 1998, Anchorage, Arkansas, USA

Arantes do Amaral. J.A. (1996). *Classification of Ships Through Their Magnetic Signatures*. Master Thesis, COPPE-UFRJ, Brazil

Armstrong, A., Pentzer, J., Odell, D.L., Bean, T.W., John R. Canning, J.R., Pugsley, D., Frenzel, J. F., Anderson, M.J. & Edwards, D.B. (2009). Field Measurement of Surface Ship Magnetic Signature Using Multiple Auvs. *OCEANS 2009*, *26-29 October 2009*, Biloxi, Mississippi, USA.

Armstrong, B., Wolbrecht, E. & Edwards, D.B. (2010). AUV Navigation in the Presence of a Magnetic Disturbance with an Extended Kalman Filter. *OCEANS '10*, 24-27 May 2010, Sydney, Australia.

Aydin, U., Rasilo, P., Martin, F., Singh, D. & Arkkio, A. (2017). Magneto-Mechanical Modeling of Electrical Steel Sheets. *J. Mag. Mag. Mat*., **439**: 82-90.

Bardsley, O.P. (2018). Could Hydrodynamic Rossby Waves Explain The Westward Drift? *Proc. Royal Soc A: Math, Physical Eng. Sci*., **474**: 2213

Baynes, T.M., Russell, G.J. & Bailey, A. (2002). Comparison of Stepwise Demagnetization Techniques. *IEEE Trans. Mag.*, **38**: 1753-1758.

Bekers, D. & Lepelaars, E. (2013). Degaussing System Design Optimization. *8th Int. Marine Electromag. Conf.* (MARELEC 2013), Hamburg, 16-19 July 2013, pp. 16-19.

Berti, A., Giorgi, C. & Vuk, E. (2015). Hysteresis and Temperature-Induced Transitions in Ferromagnetic Materials. *Appl. Math. Model.*, **39**: 820-837.

BGS (British Geological Survey) (2019). *The Earth's Magnetic Field: An Overview.* http://www.geomag.bgs.ac.uk/education/Earthmag.html (Last access date: 28 February 2019).

Bieńkowski A. & Kulikowski, J. (1980). The magneto-elastic Villari effect in ferrites. *J. Mag. Mag. Mat*., **19**: 120-122.

Birsan, M. (2010). *Measurement and Model Predicted Corrosion Related Magnetic Signature Applied on CFAV Quest*. Defence R&D Canada - Atlantic, Technical Memorandum DRDC, TM 2009-253.

Birsan, M. & Tan, R. (2016). The Effect of Roll and Pitch Motion on Ship Magnetic Signature. *J. Magn*., **21**: 503-508.

Bright, J., Conlin, D. & Wall, S. (2014). *Marine Magnetic Survey Modeling: Custom Geospatial Processing Tools for Visualizing and Assessing Marine Magnetic Surveys for Archaeological Resources*. Bureau of Ocean Management, USA.

Choi, N. K., Jeung, G., Yang, C. S., Chung, H. J. & Kim,D. H. (2012). Optimization of degaussing coil currents for magnetic silencing of a ship taking the ferromagnetic hull effect into account. *IEEE Tran. App. Sup*. **22:** 4904504.

Christopher, R., Walkera Jordan, Q., Stringfielda Eric, T., Wolbrechta Michael J., Andersona John R., Canninga Thomas, A., Beana Douglas, L., Odellb James F., & Frenzela Dean B. Edwardsa. (2013). Measurement of the magnetic signature of a moving surface ship with multiple magnetometer-equipped AUVs. *Ocean Eng*., **64**: 80-87.

Chulliat, A., Macmillan, S., Alken, P., Beggan, C., Nair, M., Hamilton, B., Woods, A., Ridley, V., Maus. S. and Thomson, A. (2015). *The US/UK World Magnetic Model for 2015-2020*. Technical Report, National Geophysical Data Center, National Oceanic and Atmospheric Administration (NOAA), USA.

Daya, Z. A., Hutt, D. L. & Richards, T. C. (2005). *Maritime Electromagnetism and DRDC Signature Management Research*. Defence R&D Canada - Atlantic, Technical Report DRDC, TR 2005-278.

de Boer, F.R. (2001). *Encyclopedia of Materials: Science and Technology*, Elsevier, Amsterdam, pp. 5013-5018.

Demilier, L., Cauffet, G., Chadebec, O., Coulomb, J. L., &Rouve, L.L. (2011). *Validation of Closed Loop Degaussing System for Double Hull Submarines*. Available online at: https://hal.archives-ouvertes.fr/hal-00567150 (Last access date: Accessed 20 April 2019).

Drchal, V., Kudrnovský, J., Wagenknecht, D. & Turek, I. (2019). Alloy Disorder and Fluctuating Magnetic Moments in The Earth's Core. *J. Mag. Mag. Mat*., **475**: 767-771.

ECA Group (2016). *ECA Group Unveils STERNA: A Portable Magnetic Ranging System for Protection of Ships*. Available online at: https://www.ecagroup.com/en/event/eca-group-unveils-sterna-portable-magnetic-ranging-system-protection-ships (Last access date: 28 February 2019).

Filipski, M. N. & Abdullah, E.J. (2006). Nanosatellite navigation with the WMM2005 geomagnetic field model. *Turkish J. Eng. Env. Sci*., **30**: 43-55.

Folk, A., Armstrong, B., Wolbrecht, E., HåvardFjær Grip, Anderson, M. & Edwards, D.B. (2010). Autonomous underwater vehicle navigation using moving baseline on a target ship. Proc. IEEE OCEANS 2010, Seattle, Washington.

Froidurota, B., Rouvea, L.-L., Foggiab, A. Bongirauda, J.-P. &Meunierb, G. (2002). Magnetic discretion of naval propulsion machines. *J. Mag. Mag. Mat*. **242–245**: 1190-1194.

Funaki, M., Higashino, S. I., Sakanaka, S., Iwata, N., Nakamura, N., Hirasawa, N., Obara, N. & Kuwabara, M. (2014). Small unmanned aerial vehicles for aeromagnetic surveys and their flights in the South Shetland Islands, Antarctica. *Pol. Sci.,* **8**: 342-356.

Gatteschi, D., Sessoli, R. & Cornia, A. (2003). Magnetism: General introduction. *In* McCleverty, J.A. & Meyer, T.J. (Eds.), *Comprehensive Coordination Chemistry II, Vol. 2*, Elsevier, Amsterdam, pp. 393-419.

Gearhart, R. (2014). Archaeological interpretation of marine magnetic data. *In* Catsambis, A., Ford, B. & Hamilton, D.L. (Eds.), *The Oxford Handbook of Maritime Archaeology*, Oxford University Press US, New York.

Goldberg, K. (2015). USS America Completes Deperming Evolution. Available online at https://www.navy.mil/submit/display.asp?story_id=87348 (Last access date: 22 April 2019).

Gonjari, V., Rakshe, T. & Khadse, S. (2017). Magnetic silencing of naval ships using ridge regression. *Int. J. Res.App. Sci.Eng. Tech.* **5**:756-760.

Gonjari, V., Rakshe, T. & Khadse, S. (2017). magnetic silencing of naval vessels using ridge regression. *Int. J. Res. App. Sci. Eng. Tech*., **5:** 756-760.

Hasril, N, Mahdi, C.I., Mohd Moesli, M., Nik Hassanuddin, N.Y., Mohd Subhi, D.Y. & Irwan Mohd, N. (2013). Management of naval ships' electromagnetic signatures: a review of sources and countermeasures. *Defence S&T Tech. Bull*., **6(2)**: 93-110.

Henocq, H. Toniazzi, J.L, Coulomb, C., Chadebec, O. & Bongiraud, J.P. (2003). Advanced studies in closed loop degaussing. *Electromag. Silencing Symp. (EMSS)*.

Holmes, J.J. (2006). Exploitation of a ship's magnetic field signatures. *Syn. Lect. Comp. Electromag.* **1**:1-78.

Holmes, J. J. (2007). Modeling a ship's ferromagnetic signatures. *Syn. Lect. Comp. Electromag* **2**1-75.

Holmes, J. J. (2008). *Reduction of a Ship's Magnetic Field Signatures*, Morgan & Claypool Publishers, San Rafael, California.

Hubbard, J. (1996). Practical measures for reduction management of the electromagnetic signature of in service surface ships and submarines. *Proc. Conf. Undersea Tech. Def.*, pp. 480-485.

Kachniarz, M., Kołakowska, K., Salach, J. & Nowak, P. T. (2018). Magnetoelastic Villari effect in structural steel magnetized in the Rayleigh region. *Acta Phy. Pol. Ser. A* **133:**660-662.

Kaufman, A.A., Alekseev, D. & Oristaglio, M. (2014). The system of equations of the constant electric and magnetic fields. *Meth.in Geochem. Geophy*., **45**: 3-50.

Kim, D.W., Lee, S.K., Kang, B., Cho, J., Lee, W.S.,Yang, C.S., Chung, H.J. & Kim, D.H. (2016). Efficient re-degaussing technique for a naval ship undergoing a breakdown in degaussing coils. *J. Mag.*, **21** 197-203.

Kim, J.W., Kim, S.H., Kim, J.H., Lee, H.B. & Chung, H.J. (2017). Efficient search method of deperming protocol for magnetic silence of vessel. *J. Mag.* **22**: 85-92

LaGrone, S. (2014). A *Terrible Thing That Waits (Under the Ocean)*. Available online at: https://www.popsci.com/blog-network/shipshape/terrible-thing-waits-under-ocean (Last access date: Accessed 20 April 2019)

Liu, S., Zhou, G., Xiao, C. & Liu, D. (2012). The study on the deployment regions of magnetic sensors in the closed loop degaussing system for double hull submarines. *Proc. IEEE, 6th Int. Conf. Electromag. Field Probl. Appl.*, 19-21 June 2012, Dalian, Liaoning, China

Lucas C.E. & Richards, T.C. (2015). A novel technique for modelling ship magnetic signatures. *MARELEC Conf. 2015*, Philadelphia, USA.

Mahmoudnezhad, S.& Ghorbani, A. (2014). Ship's magnetic signatures simulation using Halbach magnet array as uniform static magnetic field source. 3rd Iranian Conf. Eng. Electromag. (ICEEM 2014), 3-4 December 2014.

Mayo, B. (2010). *Magnetic Silencing Facility Provides Unique Service*. Available online at: https://www.navy.mil/submit/display.asp?story_id=51513 (Last access date: Accessed 22 April 2019).

MOD (Ministry of Defence) (2008). *DEF STAN 02-612 Issue 2: Guide to the Design of Ferromagnetic Signature Control System and Degaussing*. Ministry of Defence, UK.

Naval Ships' Technical Manual. (1992). *S9086-QN-STM-010 Chapter 475 Magnetic Silencing*. Direction of Commander, Naval Sea Systems Command, USA

Naval Today. (2017). *German Navy to Receive New Degaussing Facility by 2022*. Available online at: https://navaltoday.com/2017/10/06/german-navy-to-receive-new-degaussing-facility-by-2022 (Last access date: Accessed 28 February 2019).

Navy Daily. (2013). *HMAS Melbourne Makes Amend of Her Magnetic Ways*. Available online at: http://news.navy.gov.au/en/Sep2013/Fleet/413/HMAS-Melbourne-makes-amend-of-her-magnetic-ways.htm https://hal.archives-ouvertes.fr/hal-00567150 (Last access date: Accessed 28 April 2019).

NES 617, Ministry of Defence Interim Defence Standard 02-617. (2001). *Design Guide and Requirements for Equipment to Achieve a Low Magnetic Signature*. Defence Procurement Agency, UK Ministry of Defence.

Polyamp AB. (2011). *Magnetic and Electric Signature Control*. Polyamp AB, Box 925, 191 29 Sollentuna, Sweden.

Poteete, S. (2010).*Navy's N-Layer Magnetic Model with Application to Naval Magnetic Demining*. Master Thesis, Department of Oceanography, University of Washington, US.

Rago, G. (2018). *There's a House in The Middle of The Elizabeth River With a Critical Job for The U.S. Navy*. Available online at: https://pilotonline.com/news/military/local/article_acd7117c-8529-11e8-848c-db1203677306. (Last access date: Accessed 29 January 2019).

Rees, M. (2018). *Indonesian Navy Deploys Drone-Based Magnetic Measurement Solution*. Available online at: https://www.unmannedsystemstechnology.com/2018/09/indonesian-navy-deploys-drone-based-magnetic-measurement-solution (Last access date: Accessed 26 Mac 2019).

Richardson. F.D. (1981). *The German WWII Magnetic Mine*. Biographical Memoirs of Fellows of the Royal Society Vol. 27

Riley, C. (2016). *Recent Advances in Simulation of Naval Vessel Signatures*. Available online at: https://operafea.com/magnets/naval-vessel-signatures-2 (Last access date: Accessed 28 February 2019).

Ross, R., Meijer, C.G. & van de Mheen, R.J. (2012). Degaussing by normal and superconductive windings. *Proc. 11th Int. Nav. Eng. Conf. & Exh.*, Edinburgh. Paper 20.

Rosu, G., Samoilescu, G. & Baltag, O. (2018). Statistical approach of underwater magnetic field measurements of the naval magnetic signature. *Rev. Roum. Sci. Techn.,* **63:** 132–137.

Rosu, G., Samoilescu, G., Baltag, O. & Iorgulescu, D. (2014). *Evaluation of a Numerical Model for Ship Magnetic Signature Induced by an External Field*.: Fundamentals of Electrical Engineering (ISFEE).

SAM electronics GmBH (2019a). *Magnetic Ranging and Treatment Facilities for Naval Application*. Available online at: https://www.l-3mps.com/products/datasheet/SAM/1.029.pdf (Last access date: Accessed 29 January 2019).

SAM electronics GmBH (2019b). *Mobile Magnetic and Multi Influence Range*. Available online at: https://www.l-3mps.com/products/datasheet/SAM/1.024.pdf (Last access date: Accessed 29 January 2019).

Santana-Diaz, E. & Tims, R. (2019). *A Complete Underwater Electric and Magnetic Signature Scenario Using Computational Modeling*. Available online at: https://www.beasy.com/images/dmc/signature-management/publications/a-complete-underwater-electric-and-magnetic-signature.pdf (Last access date: Accessed 20 April 2019).

Sarwito, S., Prananda, J., Koenhardono, E.S. & Kurniawan, A.W. (2017). Study of calculation of degaussing system for reducing magnetic field from submersible vehicle. *Int. J. Mar. Eng. Inno. & Res.*, **1**: 68-75.

Sehitoglu, H., Efstathiou, C., Maier, H.J. & Chumlyakov, Y. (2005). Magnetisation, shape memory and hysteresis behavior of single and polycrystalline FeNiCoTi. *J. Mag. Mag. Mat*. **292**: 89-99.

Skomski, R. & Coey, J.M.D. (2016). Magnetic Anisotropy - How much is enough for a permanent magnet. *Scripta Mat*., **112**: 3-8.

Somsen, O.J.G. & Wagemakers, G.P.M. (2015). Separating permanent and induced magnetic signature: A simple approach. *Int. J. Elec. Comm. Eng*. **9:** 1236-1239.

SSFM International Inc. (2019). *Submarine Drive-In Magnetic Silencing Facility.* Available online at https://ssfm.com/project/submarine-drive-in-magnetic-silencing-facility/ (Last access date: 22 April 2019).

Tian, D., Liu, S & Li, Z.X. (2017). A Ship's magnetic field camouflage method based on multi-objective genetic algorithm. *Vibroeng. Proc* .**11**: 135-139.

Ultra Electronics. (2019). *Magnetic Treatment & Deperming. Signature Reduction for Surface Ships & Submarines*. Available online at: https://www.ultra-pmes.com/images/Magnetic_Treatment_and_Deperming.pdf (Last access date: Accessed 23 April 2019).

US DOE, US Dept of Energy. (2019). *New Analysis Suggests Earth's Magnetic Field is Destabilizing*; Available online at: https://www.iflscience.com/environment/Earth-s-magnetic-field-about-flip/ (Last access date: Accessed 29 January 2019)

Varma. R.A.R. (2014). Design of degaussing system and demonstration of signature reduction on ship model through laboratory experiments. *Phy. Proc*., **54**: 174 – 179.

Wagner, D., Yu Romanov, A & Silin, V.P. (1996). Magnetic properties of inhomogeneous ferromagnets. *Am. Inst. Phy. JETP* **82**: 945-950.

Wu, Z. Zhu, X. & Li, B. (2015). Modeling and measurements of alternating magnetic signatures of ships. *Sen. Trans.,* **186:** 161-167.

Zivi, P.Y., LeDoux, A. & Pillsbury, Jr. R.D. (2001). *Electromagnetic Signature of a Ship Rolling in Earth's Magnetic Field*. Compumag, Evian, France.

Zolotarevskii, Y.M., Bulygin, F.V., Ponomarev, A.N., Narchev, V.A. & Berezina, L.V. (2005). Methods of measuring the low-frequency electric and magnetic fields of ships. *Meas. Tech.,* **48:** 1140-1141.

ELECTRICAL PERFORMANCES OF GRAPHENE MATERIALS WITH DIFFERENT FILLER LOADING FOR FUTURE SUPER CONDUCTOR

Maizura Mokhlis[1], Mohd Azli Salim[1,2,*], Nor Azmmi Masripan[1], Adzni Md. Saad[1] & Ghazali Omar[1,2]

[1]Fakulti Kejuruteraan Mekanikal
[2]Advanced Manufacturing Centre
Universiti Teknikal Malaysia Melaka, Malaysia

[*]Email: azli@utem.edu.my

ABSTRACT

In recent years, there has been an increasing interest in the field of engineering materials all over the world. Many researchers are now competing to fabricate an electronic device to meet the technological demand by using new conductive materials. This study is focusing on the development of the new material, grapheme, and the procedure that was carried out by using a simple method involving mixing, printing and curing processes in order to produce conductive ink according to the formulation. Four samples with different percentage of filler loading are successfully done starting from 10 to 40 wt. %. Fabricated samples were characterised by using four-point probe and image analyser in order to determine the best formulation of conductive ink. From the obtained result, it was found that 40% of graphene filler had the best formulation with low resistivity which resulting high conductivity ink.

Keywords: *Conductive ink; graphene nanoparticle; electrical properties; microstructure.*

1. INTRODUCTION

Many countries all over the world including Malaysia are now focusing more on conductive ink in order to enhance its characteristics to be useful and applicable in variety of fields such as radio frequency identification (RFID), automotive sensor, touch screen, flexile batteries as well as printed circuit board (PCB) (Chang *et al*., 2012). In the last few years, the development of technologies for conductive ink grew significantly. Nowadays, countless devices are relying on printed electronic technologies that possess remarkable characteristics such as flexibility, stretch ability and lightweight, and enormously used in many applications and designs. Conductive ink can be described as an ink that is printed on an object and is capable of conducting electricity as shown in Figure 1 (Woo *et al*., 2008; Hu *et al*., 2010).

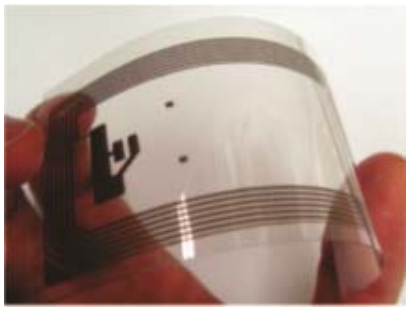

Figure 1: Ink jet printing on Polyethylene terephthalate (PET) substrate (Source: Woo *et al*., 2008).

Generally, there are three main components involved in producing an effective conductive ink; a conductive material, a polymer binder and a solvent. There is a wide range of conductive materials that are being used for conductive inks namely metal based materials (silver and copper), carbon

based materials (graphene and carbon nanotubes) as well as nanoparticles metals (Merilampi *et al*., 2009; Jeong *et al*., 2011; Chatterjee *et al*., 2012). Furthermore, each of these materials offers their own excellent properties that produce distinguished characteristics of conductive ink. However, the high cost, low content and electro migration behaviour especially for silver, limit their widespread industrial application. In addition, copper has become an attractive alternative material to silver due to its comparable bulk conductivity. However, copper can be easily oxidised. This study is focusing on graphene because it is one of the major components in conductive ink that acts as a conductive material called filler. Filler is used to strengthen the composite and minimise polymerisation shrinkage, which leads to the forming of conductive coating. Graphene is also known as one of the best electrical conductor (Zhang *et al*., 2016).

Currently, variety of techniques have been developed to prepare good quality graphenes including mechanical cleavage, epitaxial growth, chemical vapour deposition (CVD), total organic synthesis as well as chemical method (Singh *et al*., 2011). Clearly, graphene is extensively explored due to its promising carbon nano filler that contains high surface area (2,630 m^2/g), excellent thermal conductivity (5,000 W/ms), high Young's modulus (1 TPA) (ability of the material to withstand the changes under tension and compression), high value of white light transmittance (97.7%), electron mobility (2.5x105cm^2/vs) (how quickly an electron moves through a metal), electromagnetic interference (EMI) shielding ability, flexibility and transparency (Novoselov *et al*., 2012). Figure 2 shows the SEM of fracture surface of Graphene Nanoparticle (GNP) / epoxy composite.

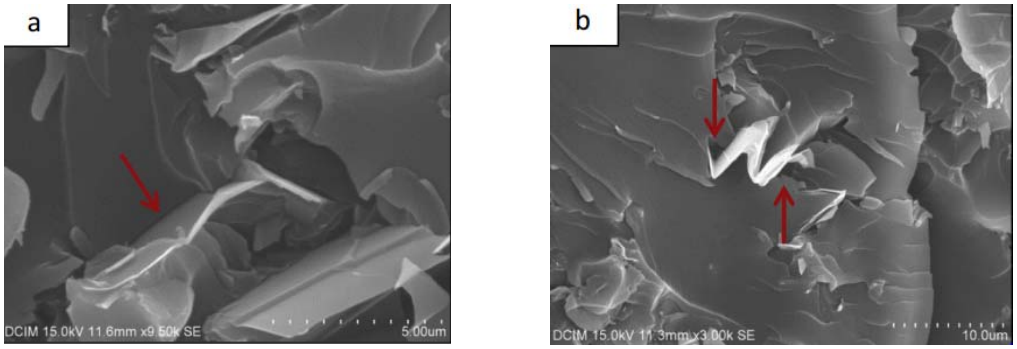

Figure 2: SEM of fracture surfaces of GNP/epoxy composite (Source: Prolongo *et al*., 2014).

On the other hand, polymer binder (epoxy resin), which is one of the most important thermosetting plastic with a wide range of applications in various industries is used as a binder in this study. Epoxy is typically consisted of two parts: the resin and hardener, which are mixed to cause it to cure. In order to form conductive inks, epoxy resin is the most compatible polymer binder mostly to its viscosity behaviours. It is frequently used in demanding applications due to excellent chemical and corrosion resistances, outstanding adhesion properties, low shrinkage and low price (Chatterjee *et al*., 2012).

As for hardener, it is a solvent that is added in the ink mixture to harden and produce strong and more durable ink as well as curing agent for epoxy. Hardener plays an important role in water absorption of epoxy (Wu *et al*., 2005). Furthermore, other than major components of conductive ink (filler, binder and hardener), substrate is also important. It functions as the medium for surface printing and must has the ability to withstand the curing temperature. In addition, the properties of the substrate must be kept constant during the experiment, so that it will not affect the ink during curing process. Therefore, glass slides are used due to its great resistance to moisture and oxygen, chemical barrier, good quality of surface and high stability of thermo-mechanical combination (Hrehorova *et al*., 2011).

Basically, the procedure of producing effective conductive ink that contains high conductivity involves the formulation of ink loading, printing procedure, ink-substrate interaction and the curing process. For the formulation of conductive ink, the relationship between filler, binder and hardener is important. It determines which ink loading contains high conductivity. The ink loading is printed on the glass substrate and it will go through curing process in the oven at certain time and temperature (Yang *et al*., 2016).

In this study, three main objectives were investigated specifically in the formulation of the composite, the characterisation with the determination of electrical and morphological properties and material as well as the potential applications of the composites. The experiment was first given to the formulation of the composite formed by an epoxy matrix in which graphene particles are dispersed, providing conductivity to the material. Besides, the main concerned part is the characterisation of these materials, which helps to understand their behaviour. The investigation regarding the characterisation of conductive ink is able to give proper understanding through various methods including 4-point probe and image analyser. All the above steps are repeated for the ink loading with the highest conductivity and printed out in various patterns. The purpose is to identify which type of pattern has the lowest resistivity or highest conductivity. In this experiment, the formulation of the conductive ink is studied to find the optimum ratio of graphene reinforced epoxy. The obtained results from this study will open up opportunities to produce new generation of high conductive inks.

2. METHODOLOGY

Graphene Nano platelets with the surface area of 500 m^2/g were used as the main filler in this study. Epoxy resin used as binder to bind the particles together and hardener is used for hardening the mixture, respectively. The composition of the filler loading was tabulated in Table 1.

Table 1: The composition of filler loading.

Sample	Filler		Binder		Hardener (g)	Total (g)
	(%)	(g)	(%)	(g)		
1	10	0.2	90	1.8	0.54	2.54
2	20	0.4	80	1.6	0.48	2.48
3	30	0.6	70	1.4	0.42	2.42
4	40	0.8	60	1.2	0.36	2.36
5	50	1.0	50	1.0	0.30	2.30
6	60	1.2	40	0.8	0.24	2.24
7	70	1.4	30	0.6	0.18	2.18
8	80	1.6	20	0.4	0.12	2.12
9	90	1.8	10	0.2	0.06	2.06

The filler loading of the samples were set at 10 wt.%, 20 wt.%, 30 wt.%, 40 wt.%, 50 wt.%, 60 wt.%, 70 wt.%, 80 wt.% and 90 wt.%. The amount of hardener loading was 30 wt. % of the amount of the binder loading. This total value had been decided before the formulation process started.

The dispersion of graphene, reinforced epoxy resin and hardener were achieved by a simple method involving mixing, printing and curing processes as shown in Figure 3. Firstly, the materials were weighed by using digital analytical balance. As the loss of weight of the materials was taken into consideration, the weight of the mixture should be slightly higher than the desired value within the tolerance of ±0.05. The same process was repeated for each case with different weight ratio depending on mixture composition. After the weighing process, all the materials were mixed together in a beaker. Then, it proceeded with the stirring process, which took about 10 minutes at room temperature by using glass rod. In order to obtain well-dissolved mixture, the stirring process was done in one direction either clockwise or anticlockwise and the stirring speed must be consistent throughout the stirring process. Before the printing process started, the gap was constructed on the glass slide by using scotch tape with the space of 0.3 cm.

(a)

(b)

(c)

(d)

Figure 3: The procedure of the experiment: (a) Weighing the materials (b) Mixing and stirring process (c) Printing process (d) Curing process.

After the construction of the gap on the glass slide was completed, printing process was carried out. The selected method to print the mixture of ink on the substrate in this experiment was doctor-blading techniques. This technique allows the thickness of the ink exposure to be controlled manually. A sharp blade was used to move the ink across the substrate at a constant speed to ensure the ink was fully exposed at the constructed gap. The exact same steps were repeated in adjusting the exposure of ink over the gap until the desired thickness was obtained.

In the final step, curing process took place in order to improve the bonding between the particles of filler, binder and hardener. Curing was also applied to melt and harden the mixture with the help of the hardener. Therefore, adhesion between ink and the substrate could be improved. The gaps constructed on samples are shown in Figure 4.

Figure 4: Gap constructed on samples.

After the printed sample was fully dried, the scotch tape was removed manually from the glass slide in order to view a well-defined track of ink before proceeding with analysis process. Then, three marks were constructed on the glass slide next to the ink layer in order to indicate the position of spot to be analysed.

The characterisation of the samples consists of the analysis of particle shape and size, morphology and the dispositions of nanoparticles. The surface microstructure of the printed samples was analysed using image analyser to determine the homogenous of the ink. Determination of sheet resistivity values of the samples in ohms-per-square was carried out by using four-point probe. It is very importance to know the conductivity of the samples. Four-point probe works by forcing a constant current along two outer probes and the voltage is read out from the two inner probes (Gao *et al*., 2014). The apparatus of the four-point is probe shown in Figure 5.

Figure 5: Four-point probe and image analyser that been used in characterisation process.

3. RESULTS & DISCUSSION

The resistivity, stability and microstructure of ink were discussed to find out the best ink formulation based on the recorded data through four-point probe and the images from the microscope. Figure 6 shows the obtained samples after curing process. Three lines of rectangular shape of ink were produced on the sample. The lines were marked as Line 1, Line 2 and Line 3. On each line, three points were marked as Point 1, Point 2 and Point 3 to determine the electrical properties and microstructure behaviour of the samples.

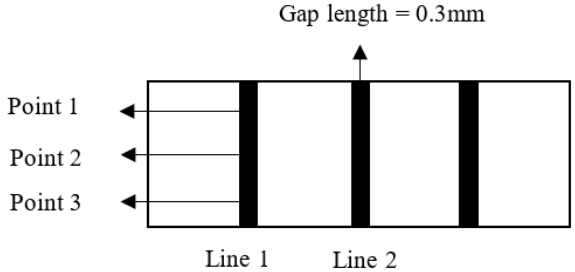

Figure 6: The schematic of printed sample ink on the glass slide substrate.

Table 2 shows the obtained values of resistivity for each marked point on the sample by using four-point probe. Notably, the average thickness of each ink is 0.0625 mm, measured by image analyser at the cross section of the printed sample.

From all the prepared samples, the results reveal that only two samples have the existence of resistivity (30 wt. % and 40 wt. %). When the samples have the existence of resistivity, it means the samples have the own conductivity level, respectively. At 10 wt. % and 20 wt. %, there is no existence of resistivity due to the small amount of filler loading. Small amount of filler loading leads to agglomeration effect. No electrical conductivity is produced due to agglomeration effect. Therefore, there is no resistivity values obtained. Whereas, 50 wt. %, 60 wt.%, 70 wt.%, 80 wt.% and 90 wt.% unable to form an ink mixture since the combination of the three materials still producing powder during mixing and stirring processes (Merilampi *et al*., 2009).

Table 2: Result of electrical performances of the differences filler loading.

Filler (%)	Point	10	20	30	40	50
Line 1 (Ω/sq)	1	-	-	6408.86	5109.51	-
	2	-	-	6189.85	5396.41	-
	3	-	-	6325.46	5364.05	-
Average (Ω/sq)		-		-	5289.99	
Line 2 (Ω/sq)	1	-	-	6207.71	5035.27	-
	2	-	-	5711.82	4887.01	-
	3	-	-	5852.33	4917.43	-
Average (Ω/sq)		-		-	4946.57	
Line 3 (Ω/sq)	1	-	-	6473.63	4058.13	-
	2	-	-	6459.89	4286.02	-
	3	-	-	6096.76	4293.72	-
Average (Ω/sq)		-	-	-	4212.623	
Average resistivity (Ω/sq)		-	-	-	4816.394	-

The change of resistivity at different determination points on the samples are shown in Figure 7. From the graph, 30 wt. % of ink mixture shows higher resistivity as compared to 40 wt. %. This is due to more conductive graphene exists in the sample and causes the resistivity to become low. Low content of graphene produces higher resistivity for the sample. It is proven that the higher the percentage of filler loading, the lower is the resistivity (Merilampi *et al*., 2009).

During the printing process, there is a possibility that the ink is not well-distributed all over the gap between the scotch tape on the glass slide when the blade is moved across the gap due to the speed or the viscosity of the ink. When the speed of blade increases, the ink may lose and as a result, may not cover all the gap area. As for the viscosity of the ink, it increases with higher filler content. Ink with high viscosity is hard to print in compliance with the texture of ink. Some regions may have different thickness, which leads to the different spreads of conducting material.

During the measurement of electrical properties by using four-point probe which is to measure the resistivity, basically the values are not stable due to the time gap produced by four-point probe before taking the data. Longer time is needed to obtain the resistivity value for high resistive samples due to RC (resistance-capacitance) delay (Prolongo *et al*., 2014). It is because, current requires some time to climb up to the saturation value. Once the data is stable, only certain measurement points can be taken and the average value can be obtained. Thus, when an inconsistent of time is spent, it produces unstable resistivity values (Merilampi *et al*., 2009).

Image analyser was used to determine an image analysis on the ink to investigate its microscopic condition. In this section, all of the microstructure images were divided into two categories, which were microstructure with no conductivity as in Figure 8 (a) and (b) and microstructure with conductivity as in Figure 8 (c) and (d).

The microstructure images were organised in accordance to their filler loading with tales of magnification of 5x. Figure 8 (a) to (d) show the microstructure of the samples. The samples are from 10% to 40% of the graphene nanoparticles. The figure shows different image of microstructure particularly the shape of particle and size for different filler loadings. In Figure 8 (a) and (b), the dark spots show the occurrence of agglomeration effect in the microstructure due to less presence of graphene as compared to (c) and (d). From Figure 8 (b) to (c), the ink is well-dispersed because of higher filler loading. Higher filler loading enables the percolation network to transform the insulator to conductor.

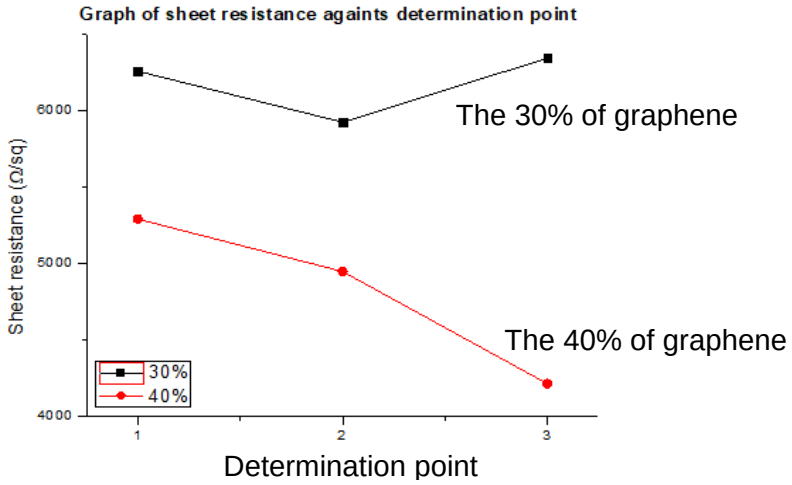

Figure 7: The sheet resistance of graphene ink against determination point (level of conductivity vice versa of level of sheet resistance).

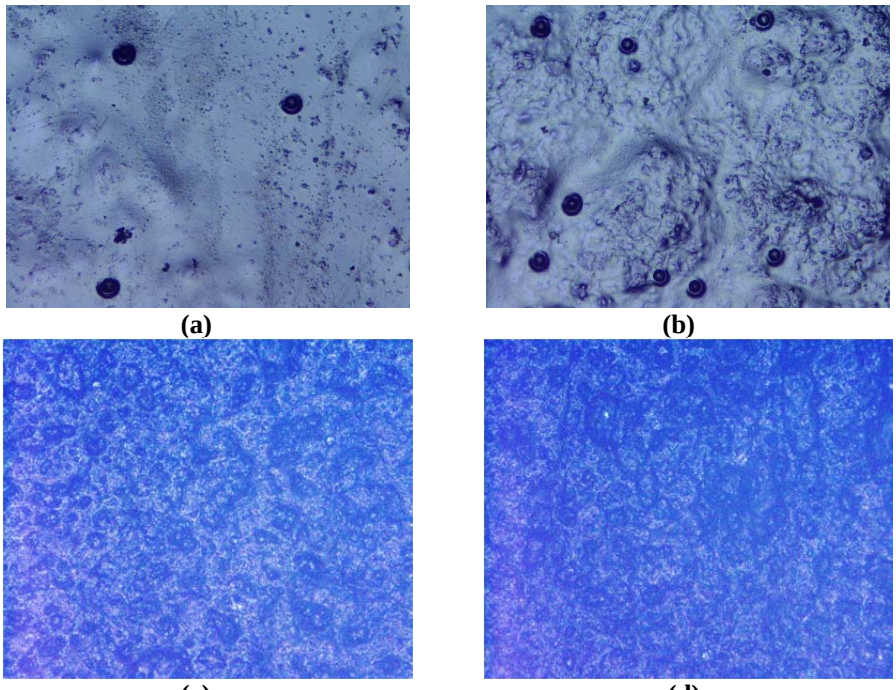

Figure 4. Microstructure image of graphene as filler loading: (a) 10 wt. %, (b) 20 wt.%, (c) 30 wt.% (d) 40 wt.%.

4. CONCLUSION

The aim of this work was to study systems formed by carbon-based filler dispersed in a polymer matrix. This work was done to characterise them, allowing a better understanding of the complex system and to propose adequate formulations of the final material in order to control and optimise the electrical properties for the target applications. To complete the study, optical microscopy ensures that the fabrication process led to composite that appeared homogeneous. Based on the results, it can be pointed out that the filler loadings of 10 wt. %, and 20 wt. % did not have any existence of conductivity, while 30 wt. % and 40 wt. % showed the existence of conductivity. Hence, the decision to choose the optimum filler loading was merely based on the filler loading of 30 wt. % and 40 wt. %. Various compositions between filler, binder and hardener were able to produce different results based on resistivity and the microstructure behaviour. The composition and amount of polymer matrix, the particles amount and distribution have an effect on electrical properties as well as mechanical properties of graphene ink conductor. Percolation was also an important theory or property that was required to be properly understood. As for now, filler at 40% was chosen as the base formulation to produce high conductive ink. Moreover, the process to formulate the 40 wt. % ink was easier as compared to ink that contains higher percentage of filler loading. Although much remains to be done, the extensive formulation and characterisation work has been accomplished, and given the fundamental tools and knowledge that has been researched, this will hopefully lead to many commercial applications of these material in the future.

5. ACKNOWLEDGEMENTS

Special thanks to Fakulti Kejuruteraan Mekanikal, Universiti Teknikal Malaysia Melaka (UTeM) for providing the laboratory facilities and financial supports under PJP/2016/FKM-CARE/S01506, PJP/2017/FKM/S01551, PJP/2018/FKM (2B)/S01592 and also FRGS/1/2015/TK01/FKM/02/F00275.

REFERENCES

Gao, Y., Shi, W., Wang, W., Leng, Y. 7 Zhao, Y. (2014). Inkjet printing patterns of highly conductive pristine graphene on flexible substrates. *Ind. Eng. Chem. Res.*, **53**: 16777–16784

Hrehorova, E., Rebros, M., Pekarovicova, A., Bazuin, B., Ranganathan, A., Garner, S., Merz, G., Tosch, J. & Boudreau, R. (2011). Gravure printing of conductive inks on glass substrates for applications in printed electronics. *J. Display Technol.*, 7: 318–324.

Wu, L., Hoa, S. V., (2006). Effects of composition of hardener on the curing and aging for an epoxy resin system. *J. Appl. Polym. Sci.*, **99**: 580-588.

Yang, W. & Wang, C. (2016). Graphene and the related conductive inks for flexible electronics. *J. Mater. Chem. C*, **4**: 7193–7207.

Chang, Y., Wang, D.-Y., Tai, Y.L & Yang, Z.G. (2012). Preparation, characterization and reaction mechanism of a novel silver-organic conductive ink. *J. Mater. Chem.*, **22**: 25296.

Chatterjee, S., Nafezarefi, F., Tai, N.H., Schlagenhauf, L., Nüesch, F.A. & Chu, B.T.T. (2012). Size and synergy effects of nanofiller hybrids including graphene nanoplatelets and carbon nanotubes in mechanical properties of epoxy composites. *Carbon*, 50: 5380-5386.

Chatterjee, S., Wang, J.W., Kuo, W.S., Tai, N.H., Salzmann, C., Li, W.L., Rebecca Hollertz, R., Nuesch, F.A. & Chu, B.T.T. (2012). Mechanical reinforcement and thermal conductivity in expanded graphene nanoplatelets reinforced epoxy composites. *Chem. Phys. Lett.*, 531: 6-10.

Hu, L., Pasta, M., La Mantia, F., Cui, L., Jeong, S., Deshazer, H.D., Choi, J.W., Han, S.M. & Cui, Y. (2010). Stretchable, porous, and conductive energy textiles. *Nano Lett., 10*: 708-714.

Jeong, S., Song, H.C., Lee, W.W., Lee, S.S., Choi, Y., Son, W., Kim, E.D., Paik, C.H., Oh, S.H. & Ryu, B.H. (2011). Stable aqueous based Cu nanoparticle ink for printing well-defined highly conductive features on a plastic substrate. *Langmuir, 27:* 3144-3149.

Merilampi, S., Laine-Ma, T. & Ruuskanen, P. (2009). The characterization of electrically conductive silver ink patterns on flexible substrates. *Microelectron. Reliab.*, 49: 782-790.

Novoselov, K.S., Fal, V.I., Colombo, L., Gellert, P.R., Schwab, M.G. & Kim, K. (2012). A roadmap for graphene. *Nature*, 490: 192.

Prolongo, S.G., Moriche, R., Jiménez-Suárez, A., Sánchez, M. & Ureña, A. (2014). Advantages and disadvantages of the addition of graphene nanoplatelets to epoxy resins. *Eur. Polym. J.*, 61: 206-214.

Singh, V., Joung, D., Zhai, L., Das, S., Khondaker, S.I. & Seal, S. (2011). Graphene based materials: past, present and future. *Prog. Mater. Sci.*, 56: 1178-1271.

Woo, K., Kim, D., Kim, J.S., Lim, S. & Moon, J. (2008). Ink-Jet printing of Cu− Ag-based highly conductive tracks on a transparent substrate. *Langmuir*, 25: 429-433.

Zhang, W., Bi, E., Li, M. & Gao, L. (2016). Synthesis of Ag/RGO composite as effective conductive ink filler for flexible inkjet printing electronics. *Colloids Surf. A: Physicochem. Eng. Aspects*, 490: 232-240.

PERFORMANCE INVESTIGATION OF DEEP CRYOGENICALLY TREATED AND TEMPERED CARBIDE INSERTS IN TURNING OF INCONEL 718

Venkat Pradeep Allu[1,2*], Linga Raju Dumpala[1] & Ramakrishna Shinagam[3]

[1]Department of Mechanical Engineering, Jawaharlal Nehru Technological University, Kakinada (JNTUK), India.
[2]Department of Mechanical Engineering, Vignan's Institute of Engineering for Women, India
[3]Department of Mechanical Engineering, Gayatri Vidhya Parishad College of Engineering, India

[*]Email: venkatpradeepallu@gmail.com

ABSTRACT

While nickel based alloys possess great chemical attraction and very low thermal conductivity, their machining is very complex. Shorter tool life with high wear is quite obvious during turning of these alloys, due to excessive friction and temperature. With the intention of increasing tool life, cryogenic treatment followed by tempering was carried out on multilayer coated inserts. The treated and tempered inserts were compared with the untreated ones for dry turning of Inconel 718 alloy. The outcome revealed that the tempered inserts outperformed the untreated and treated ones while investigating tool wear and cutting forces. In addition, the tempered inserts exhibited higher scratch resistance and lower chip tool contact distance.

Keywords: *Inconel 718; chemical vapour deposition; cryogenic treatment; dry turning; nickel based alloy.*

1. INTRODUCTION

Nickel-chromium super alloys (Inconel 718) have great functioning capability at extreme temperatures (around 800 to 900 °C). Due to its high creep and corrosion resistance, Inconel 718 is the most widely used alloy in aerospace engineering applications (Thakur *et al*., 2009; Zhang *et al*., 2018). As nickel (Ni) based alloys offer great resistance to wear and high thermal stability, they are capable of withstanding elevated stress and thermal conditions, particularly for prolonged periods (Thakur & Gangopadhyay, 2016; Oliveira *et al.*, 2017; Kuppuswamy *et al.*, 2017). Conversely, due to its low thermal conductivity and great chemical attraction, Ni based alloys possess very poor machinability characteristics (Arunachalam & Mannan, 2000; Zhu *et al.*, 2013). This makes machining difficult by enormously augmenting the friction and temperature at work zone.

Machining Inconel 718 under dry environment has become a major challenge to all the researchers in the field of manufacturing. The severe heat generation during machining of these alloys results in intense adhesion and abrasion of the cutting tools. This in return shortens the life of the cutting tool, affecting the overall performance (Cantero *et al.*, 2013; Adem Çiçek *et al.,* 2013). Therefore, the prime challenge in the machining of Ni-based alloys is to exploit a cutting insert that asserts great stiffness, elevated wear resistance and hot hardness, along with great chemical and thermal stability (Sharman *et al.*, 2004).

Cryogenic treatment (CT) is a flourishing method to improve strength and toughness, thermal conductivity, microstructure and microhardness, and resistance to wear and fatigue of the substrate (Nirmal *et al*., 2010; Firouzdor *et al.*, 2011). In this technique, the substance is cooled to sub-zero temperature to facilitate enhanced mechanical properties. Basing on the temperature of soaking, the cryogenic process is classified as deep cryogenic treatment (DCT) (-145 to -196 °C) and shallow cryogenic treatment (SCT) (-80 to -145 °C) (Molinari *et al.*, 2001; Deshpande *et al.*, 2018).

So far, extensive research work has been conducted in enhancing the wear properties and life of cutting tools using cryogenic treatment. It has been successful and efficiently implemented in many machining methods, such as drilling, milling and turning (Vadivel & Rudramoorthy, 2009). Yet, cryogenic processing in the field of metal cutting is mostly restricted to ferrous materials. In a study by Firouzdor *et al.* (2011), carbide inserts were subjected to DCT (-196 °C) and SCT (-110 °C), and tool surface roughness (*Ra*) and flank wear (*VB*) being examined. It was observed that the cryogenically treated inserts outperformed untreated inserts. In addition, it was concluded that there was subsequent improvement in tool life of DCT inserts as compared to SCT inserts.

Dhananchezian *et al*. (2011) conducted a turning experiment on Ti-6Al-4V (Titanium alloy) using a TiAlN coated carbide insert. The insert was cryogenically processed and operated at two different cutting speeds. The results exhibited that at the higher cutting speed, there was substantial improvement in tool life of the DCT inserts, which also presented reduced tool wear. This can be ascribed to the enhanced hardness of the DCT inserts, which prevented edge chipping. In a previous work by Çiçek *et al*. (2013), uncoated carbide inserts were subjected to DCT at -145 °C and were used in AISI H13 steel turning. The outcome suggested that the enhancement of wear resistance improved flank, crater and notch wear by 29, 69 and 81% respectively. Furthermore, the severity of the plastic deformation was reduced because of the increased thermal conductivity of the DCT inserts. Özbek *et al.* (2014) performed a turning experiment on AISI 316 steel using DCT inserts. The inserts were cryogenically processed at -145 °C for 12, 24, 36, 48 and 60 h. The results suggested that the DCT insert with 24 h soaking time yielded better life of tool and wear resistance. This was ascribed to the improved grain refinement and hardness in the insert.

A study was conducted by Podgornik *et al.* (2016) to determine the influence of cryogenic treatment over the wear resistance and toughness of tools. It was found that depending on the chemical composition, the tool steels responded to the treatment. It was concluded that there was an enhancement of 70% in mechanical properties of low carbon and high tungsten-cobalt tool steel, but limited improvement in high-speed steel. Chetan *et al.* (2017) performed a study comparing the performance of coated and uncoated inserts that were processed with DCT. The experiment was carried out under dry turning of Nimonic 90. It was found that the scratch resistance substantially improved when coated inserts are subjected to the cryogenic process. Apart from this, the work disclosed that the DCT for coated tools reduced tool forces and wear. Kursuncu *et al*. (2018) performed an experiment on turning Inconel 718 using carbide inserts of different coatings subjected to CT. The outcome revealed that the hard eta-phase improved by 18%, which resulted in good adhering between coating and substrate. In addition, the improvement in hot hardness and thermal conductivity in DCT inserts resulted in enhanced tool life.

According to the literature study, the evolution of cryogenically treated carbide inserts has been very successful in the field of manufacturing. However, the use of DCT carbide inserts has been very limited in turning of nickel based alloys. Being the first of its kind, Thakur *et al*. (2015) performed a turning experiment on Inconel 718 using uncoated DCT inserts. Besides that, Chetan *et al*. (2017) studied the performance of coated and uncoated DCT inserts in machining Nimonic 90. However, the literature presented no apparent conclusion on the wear behaviour of DCT inserts while turning nickel alloys. Moreover, as there has been very limited investigations regarding tool forces, surface roughness and wear mechanism, the accurate machining performance is not comprehensible. However, the above literature works stated that the performance of DCT inserts depend on soaking period, but no work was performed for turning of nickel based alloys. Therefore, this study concentrates on investigating the machining performance of DCT inserts followed by tempering of various soaking periods during dry turning of Inconel 718.

2. METHODS AND MATERIALS

2.1 Inserts

Multilayer coated carbide inserts produced by Sandvik Coromant, with ISO designation of DNMG 11 04 08 PM 4325) were used in the experiment. The tool geometry is shown in Figure 1, where it can be seen that the insert has 11 mm cutting edge effective length (LE), 9.525 mm diameter of inscribed circle (IC), 4.763 mm thickness (S) and 0.8 mm tool nose radius (RE), with four cutting edges.

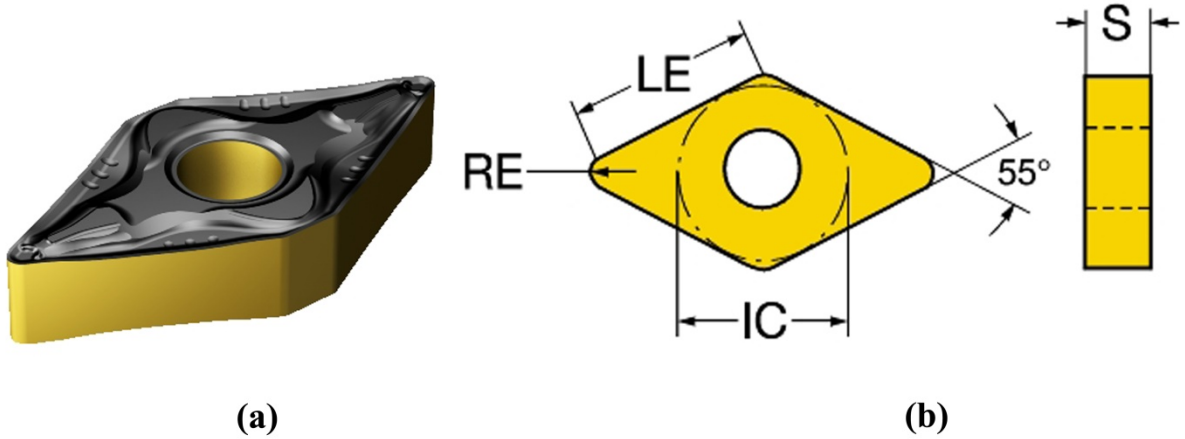

Figure 1: Pictorial presentation of tool geometry (Photo courtesy of Sandvik Coromant, India).

A multilayer coating (TiCN/Al_2O_3/TiN) of 2 µm average thicknesses each (Figure 2) was applied on the cemented carbide using the chemical vapour deposition (CVD) technique. A tool holder from Sandvik Coromant, with ISO designation of PDJNR 25 25 M 11, was used to mount the insert. The combined tool designation offers 93° principle cutting edge angle, -6° back rake angle, 5° clearance angle, 80° including angle and 95° approach angle.

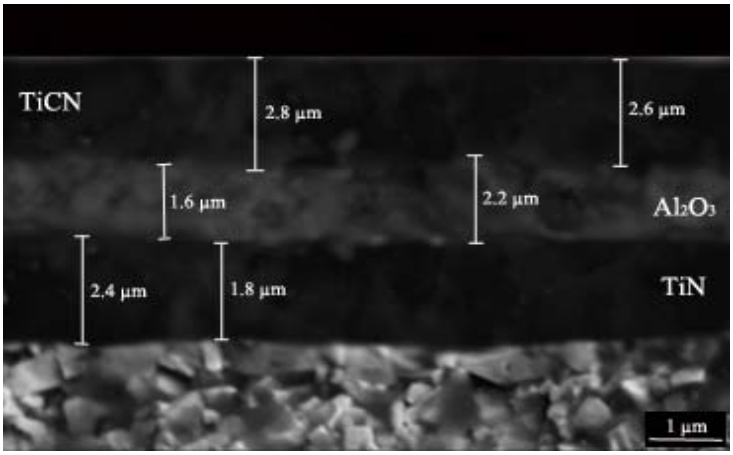

Figure 2: Microscope image of the coating thickness.

2.2 Workpiece Material

The commercial grade nickel super alloy Inconel 718 was used in this experiment. As the alloy possesses excellent tensile and impact strength as well as high oxidation and corrosion resistance, they are particularly used in gas turbines and jet applications. The round rods of 40 mm diameter were turned to a length of 250 mm. In order to avoid vibrations during turning operation, a central drill was holed and the support was taken from the tail stock. The elemental analysis of the workpiece was given in Table 1.

Table 1: Elemental analysis of material.

Element	C	Mn	P	S	Si	Cr	Ni	Mo	Ti	Al	Co	Cu	Fe
W %	0.07	0.3	0.009	0.012	0.27	18.3	52.67	2.92	0.78	0.64	0.9	0.27	Balance

2.3 Cryogenic Treatment (CT)

DCT was performed on multilayer coated carbide inserts in three groups, as DCT, DCT followed by tempering (DCT+1T) and DCT followed by double tempering (DCT+2T). These three classified inserts were compared to an untreated carbide insert (UT). The CT was performed using a microcontrolled PT-100 sensor with cryogenic processor, which has an accuracy of 1 °C. The processor is connected to a Worthington dewar with containment of 240 L to ensure the supply of liquid nitrogen. The cryogenic equipment is displayed in Figure 3(a), while the cryogenic cycle is shown in Figure 3(b). Initially the inserts were cooled down to a temperature of -196 °C, with 2 °C per min cooling rate. As per the previous literature study (Özbek *et al*., 2014; Chetan *et al*., 2017) and their recommendations, soaking period of 12 h was chosen. Then, the inserts were brought to ambient temperature at heating rate of 2 °C per min. As the final step in the treatment, the inserts were tempered at 200 °C for 2 h. This step was taken to relieve the internal residual stresses that are formed during the processing (Nirmal *et al*., 2015). This procedure is common for all DCT processes. Furthermore, tempering at 200 °C for 2 h was performed for the DCT+1T insert, while an additional tempering at the same temperature for another 2 h was performed for the DCT+2T insert. Lastly, the inserts were air cooled to room temperature.

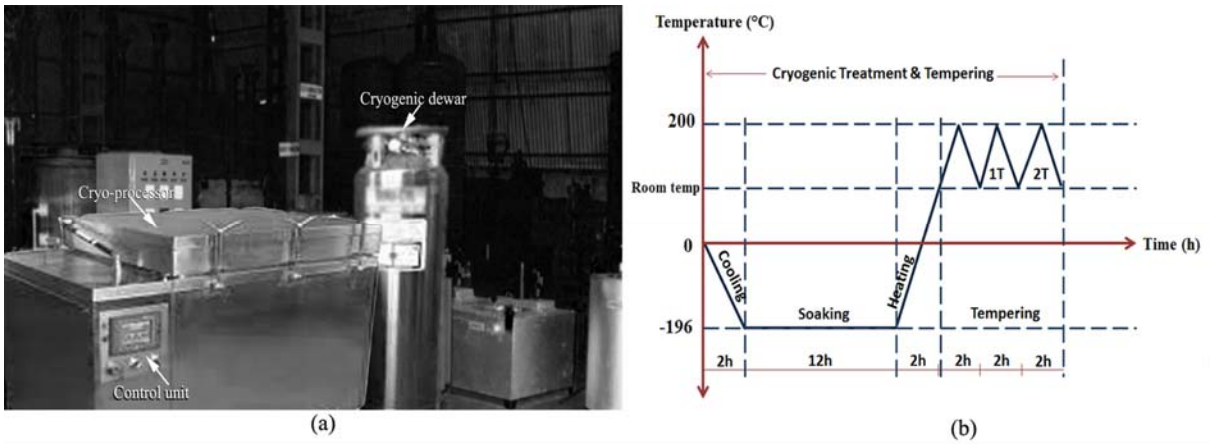

Figure 3: Cryogenic treatment of the inserts: (a) Cryogenic plant (b) Cryogenic treatment cycle.

2.4 Machining and Inspection

A computerised (automated) Vickers hardness tester was employed for measurement of microhardness of the inserts. Indentation was imposed on the specimen using a diamond intender. The intender has a tip angle of 136°, which applied a load of 5 N for dwell time of 10 s. Microhardness was measured at three different areas and the average was considered the final value.

Scratch test using a Tribo tester was performed on all the inserts to identify the impact of cryogenic processing on CVD coating. A diamond intender with 200 µm nose radius and 120° tip angle was used to inflict a scratch of 6 mm length at 30 mm/min sliding velocity. The experiment was performed for all the inserts at constant loads of 30, 40 , 50, 100 and 150 N, and variable loads of 10 to 150 N.

A semi-automated machine was used to perform the turning operations. The specifications and machining parameters are presented in Table 2. The operating conditions were selected based on the literature study (Aouici *et al.,* 2016; D'addona & Raykar, 2016) and the previous work of the authors (Pradeep *et al.,* 2019a, b, c). During machining, a piezoelectric tool force dynamometer assisted in measuring the tool forces. An ESAW binocular type optical microscope with maximum magnification of 1,500 X was used for quantifying the tool flank wear. In addition, an energy-dispersive X-ray (EDX), chemical characterisation and scanning electron microscopy (SEM) analyses were used to evaluate the wear mechanism and microstructural changes occurring on the inserts. The evaluation was performed using a ZEISS field emission SEM (GeminiSEM 500), with 50 to 2,000,000 magnification and 32k X 24k pixels resolution, as well as equipped with energy dispersive spectroscopy (EDS).

Table 2: Equipment details and machining parameters.

	Constituent	Specifics
Equipment details	Machine tool	Semi automated lathe (75 kW)
	Bed length	1830 mm
	Bed swing	370 mm
	Centre height	185 mm
	Spindle speed range	45-2000 rpm
Machining parameters	Cutting speed (m/min)	70, 110, 150
	feed (mm/rev)	0.05, 0.10, 0.15
	depth of cut (mm)	0.3

3. RESULTS AND DISCUSSION

3.1 Scratch Test

The improvement in scratch resistance of the inserts after cryogenic treatment was examined using the scratch test at constant and variable loads. The scratches formed by the diamond nib during the test for the DCT insert is shown in Figure 4(a). The SEM images of scratches formed on the DCT+2T and UT inserts at 50 N steady loads are shown in Figures 4 (b) and 4(c) respectively. From the figure, it is apparent that the resistance offered to the penetration of the diamond nib is quite high for the DCT+2T insert as compared to the UT insert. This may be because of the improved scratch resistance of the inserts due to the cryogenic treatment followed by tempering. The main mechanism of the coating grate is localised peeling, which was evident on the UT insert, leaving the substrate perceptible. Better binding properties can be developed between the coating and substrate by enhancement of fine eta (η) carbide particles during the cryogenic process (Huang *et al.*, 2003).

Figure 4(d) shows the DCT+2T insert after being subjected to the variable load (10-150 N) scratch test. Figure 4(e) shows the UT insert after the test. The severe coating breach of the UT insert during scratch test left the substrate exposed, indicating the underperformance of the insert. On the contrary, from Figure 4(d), the retainment of the coating might be the reason for the better performance of the DCT+2T insert during the test.

Figure 5 shows the graph plotted for the scratch time and penetration depth, for all the inserts at 10-100 N (Figure 5(a)) and 10-150 N loads (Figure 5(b)). From the figure, CT with tempering substantially decreased the penetration depth of the indenter at both the loads. This is due to the refinement of grain size in CT, which improved the hardness of the inserts. In addition, CT followed by tempering increased the binding properties, which resulted in higher scratch resistance of the tempered inserts (DCT+1T and DCT+2T) as compared to the untempered inserts (DCT and UT).

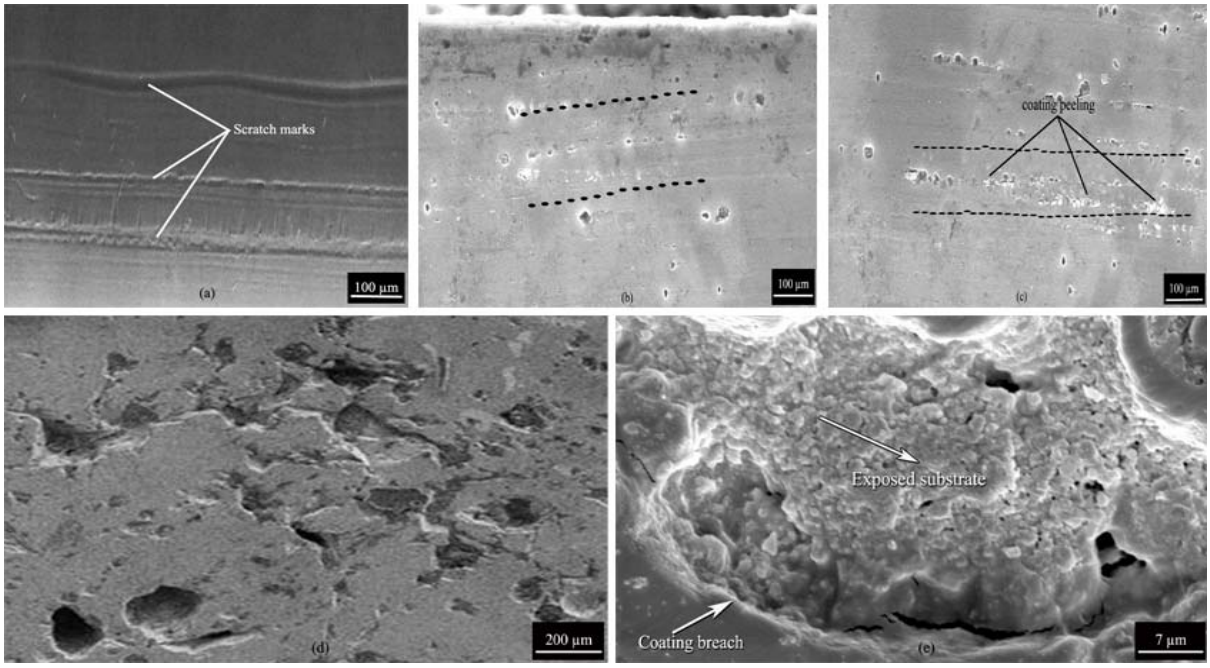

Figure 4: Inserts after the scratch test: (a) Micrograph of the DCT insert with scratches. (b) Scratch on the DCT+2T insert at 50 N constant load. (c) Scratch on the UT insert at 50 N constant load. (d) DCT+2T insert at 10-150 N variable load. (e) UT insert at 10-150 N variable load.

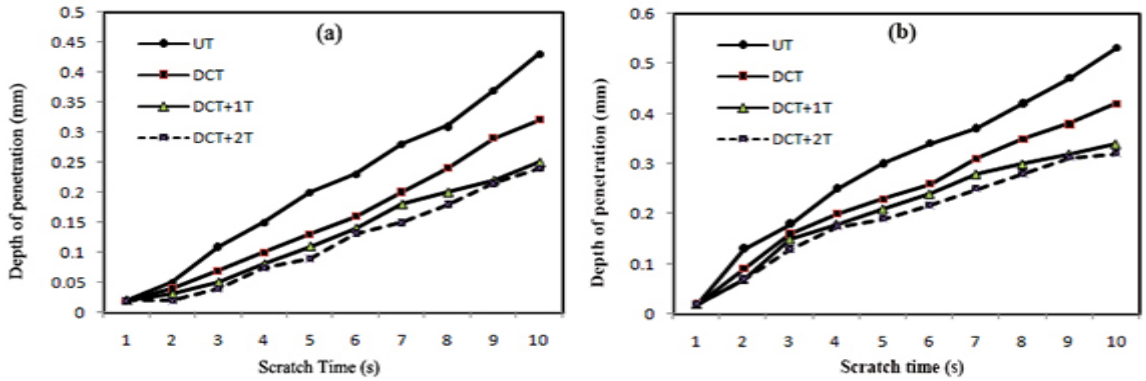

Figure 5: Scratch test graph at variable loads: (a) 10-100 N (b) 10-150 N.

3.2 Cutting Force

Figure 6 displays the tool force comparison graph for all the inserts at varying speeds (70, 110 and 150 m/min) and constant feed (0.10 mm/rev). From the figure, at all the conditions, the UT insert has maximum value of cutting force when compared to the other inserts. At lower speed of 70 m/min, the DCT+2T insert outperformed all the inserts with a reduction of cutting force by 20.7 % as compared to the UT insert. There were reductions of 12.3 and 19.0% for the DCT and DCT+1T inserts respectively as compared to the UT insert. At medium speed of 110 m/min, the decrements of cutting force were 17.8, 30.0 and 41.8% for the DCT, DCT+1T and DCT+2T inserts respectively as compared to the UT insert. The high speed (150 m/min) ensued in reduction of cutting force of 22.7, 25.8 and 30.1% for the DCT, DCT+1T, and DCT+2T inserts as compared to the UT insert. On the whole, the tempered inserts performed better than the untempered inserts, particularly at medium and high cutting speeds. This trend may be ascribed to the reduced coefficient of friction, tool wear and work zone temperature for the tempered inserts, which leads to better performance.

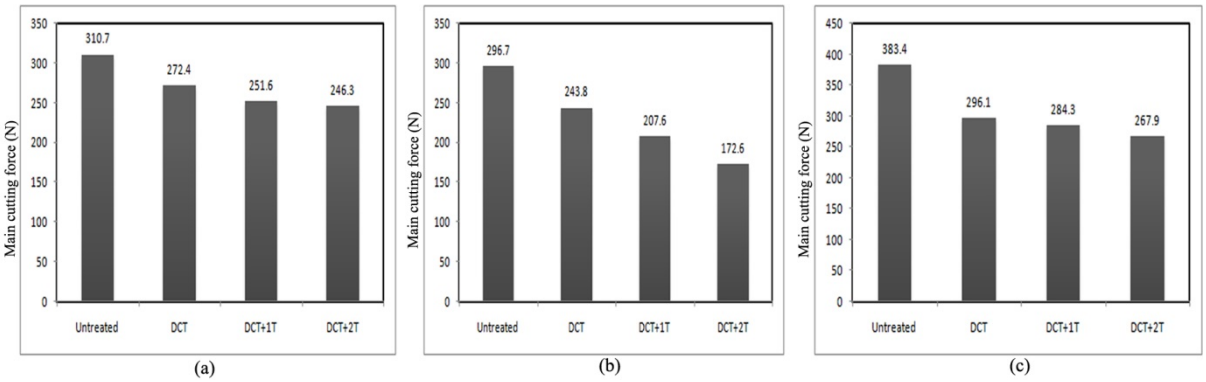

Figure 6: Comparison of tool forces at 0.1 mm/rev feed and cutting speed of (a) 70, (b) 110 and (c) 150m/min.

The cutting forces were considerably reduced for the tempered inserts as compared to the untempered inserts. This can be attributed to the evolution of fine η-carbide particles in the carbide substrate during the tempering process. As the η-carbides are very hard in nature, and when combined with the merit of enhanced scratch resistance, improved the hardness of the tempered inserts. This in return aided the tempered inserts to sustain high cutting forces, outperforming all the untempered inserts (Zhang *et al.,* 2015; Chetan *et al.*, 2017).

3.3 Tool-Chip Contact Length

The rake side of the inserts experienced continuous abrasion from the chip flow during the turning operation. This left a worn out surface at the rake surface, with this wear track known as tool-chip contact length (TCCL). It is considered as the prime factor influencing working temperature, friction, and tool forces and wear. This wear length was evaluated three times using an optical microscope and the average value was considered. Figure 7 shows the performance comparisons of the cutting inserts at varying cutting speeds and feed, in terms of TCCL.

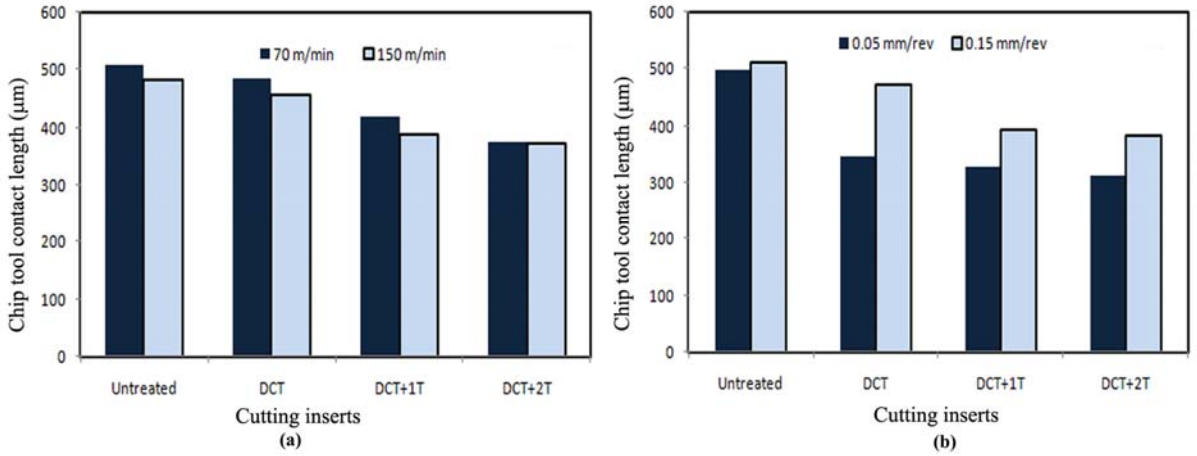

Figure 7: TCCL comparison of the inserts at (a) 70 and 150 m/min speed (b) 0.05 and 0.15 mm/rev feed rate.

In all the cases, the tempered inserts performed better than the untampered inserts. From Figure 7(a), it can be observed that the performance variation at low and high cutting speeds was minimum for the DCT+2 insert. Moreover, at 70 m/min, the DCT+2T insert exhibited 36.0% better performance as compared to the UT inserts, whereas the DCT+1T and DCT inserts provided 21.4 and 4.9% betterment respectively. Similarly, at 150 m/min, the performance enhancements for the DCT+2T,

DCT+1T and DCT inserts in comparison to the UT insert were 28.8, 21.4 and 4.9%, respectively. From Figure 7(b), it is quite obvious that even though the higher feed resulted in lower performance, the tempered inserts yielded minimum TCCL. Moreover, at 0.05 mm/rev, the DCT+2T insert exhibited 59.2% improved performance as compared to the UT insert, whereas the DCT+1T and DCT inserts presented 51.5% and 43.2% betterment respectively. Similarly, at 0.15 mm/rev, the performance enhancements for the DCT+2T, DCT+1T and DCT inserts as compared to UT insert were 33.3, 30.2 and 8.4%, respectively. This can be attributed to the reduced thermal conductivity and coefficient of friction in the tempered inserts. In addition, due to the enhanced binding between the coating and substrate, the welding tendency between the chip and rake may be reduced, resulting in better performance of the tempered inserts. Furthermore, the increase in binding strength of the coating during the tempering offered resistance towards extreme coating breach and premature delamination (Zhang *et al.,* 2015; Chetan *et al.*, 2017). As compared to the UT insert, the treated insert (DCT) exhibited less wear track, even though the tempered inserts outperformed the DCT insert. This can be attributed to the improved scratch resistance due to the cryogenic process. As tempering in addition to CT was provided to the coated inserts, it altogether formed a heat barricade during the machining, resulting in decreased tool-chip contact surface.

3.4 XRD Analysis and Microhardness

Figure 8 shows the comparison of microhardness values for all the inserts (UT, DCT, DCT+1T and DCT+2T). It is quite evident that the cryogenic process followed tempering on the inserts increased the value of microhardness. This trend was in acceptance with previous experimental studies (Yong & Ding, 2011; Chetan *et al.*, 2017). Many authors noticed substantial improvement in the microhardness values of the carbide tools with cryogenic treatment (Zhang *et al.*, 2015). The restructuring of the tungsten-carbide (WC) matrix into fine η-carbide phase is observed to be the reason for the enhancement of hardness of the insert. When WC is subjected to sub-zero atmospheric conditions, a phase with inadequate carbon is formed, known as the η-carbide phase. The fine and homogeneous dispersion of η-carbides (Co_3W_3C and Co_6W_6C) in the carbide inserts during the cryogenic and tempering processes enhanced their strength, hardness and toughness. Senthilkumar *et al.* (2011) suggested that the carbide insert's hardness and wear resistance augment because of cryogenic and tempering treatment.

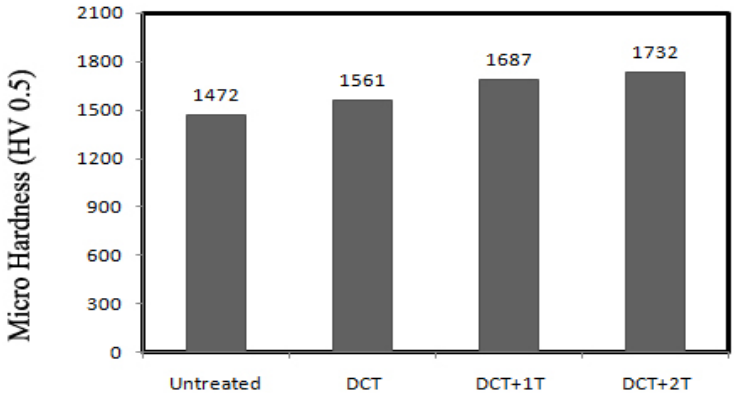

Figure 8: Comparison of microhardness for the inserts.

A microstructural examination was performed on the inserts in order to validate the evolution of the η-carbide phase. Figure 9 shows the microstructural images, comparing the best (DCT+2T) and worst (UT) performed inserts. It can be observed that the α-particle in WC matrix was very fine and structured in the DCT+2T insert as compared to the UT insert. This is observed to be the prime reason for the improvement in the binding properties of the tempered inserts (Nirmal *et al.*, 2015). Furthermore, the η-carbides were found to be quite dense and finely dispersed in the tempered inserts. Conversely, the η- phase in the UT insert was very coarse and distributed very meagrely.

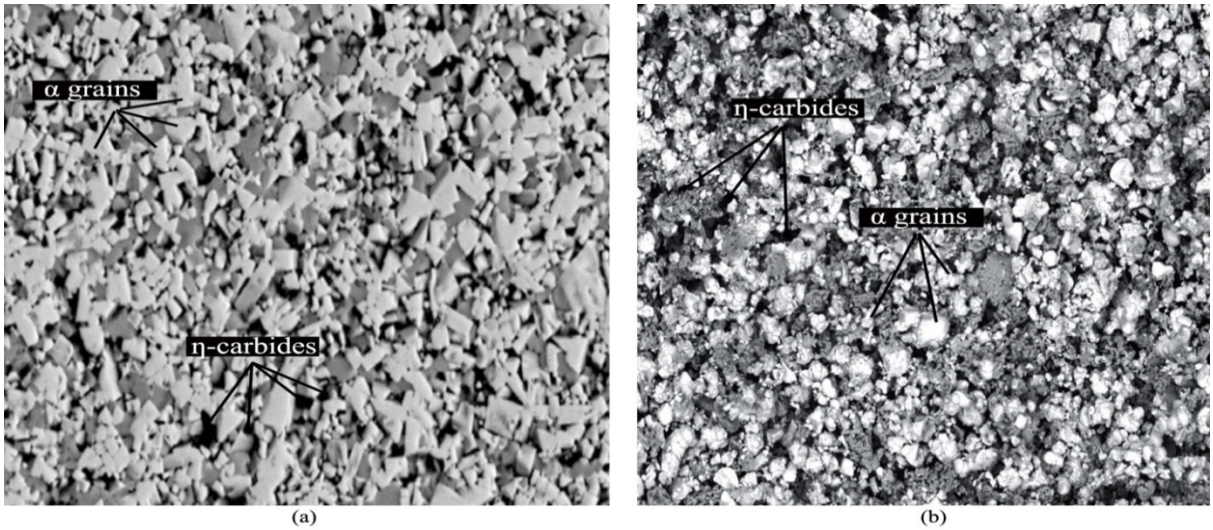

Figure 9: Microstructural image of the (a) DCT+2T and (b) UT inserts.

Figure 10 shows the XRD analysis performed on the best (DCT+2T) and worst (UT) performed insert in order to validate the evolution of the η-carbide phase. From the figure, it is obvious that the count of WC in the tempered inserts (Figure 10(a)) decreased, partially transforming the WC matrix to complex η-carbides, increasing the count of Co_3W_3C and Co_6W_6C atoms. A recent study demonstrated the evolution of η-carbides in cryogenically treated carbide inserts at 2θ angle (angle between reflected and incident X-ray) during XRD analysis (Huang *et al.*, 2003; He *et al.*, 2014). As the η-particles dispersed finely after the tempering, the thermal conductivity of the inserts improved by reducing the quantity of binder (β) phase in the carbide matrix. Besides that, the intense sub-zero temperature in the cryogenic process instigated grain refinement, yielding improved hardness of the inserts.

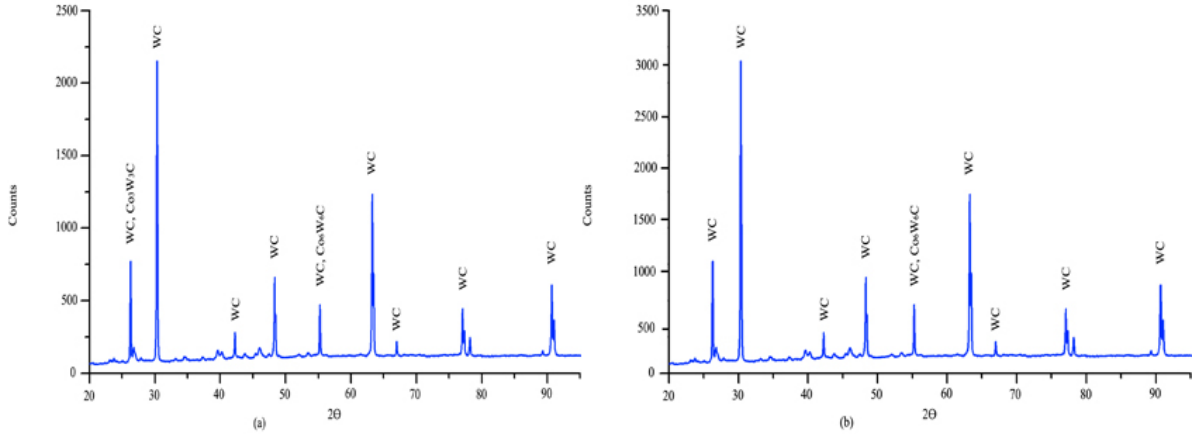

Figure 10: XRD profiles of the (a) DCT+2T and (b) UT inserts.

3.5 Tool Wear

The tool wear of the inserts were evaluated during the turning of Inconel 718 to a length of 150 mm. The tool wear evolution was examined under an optical microscope for three times and the average value was considered. The comparison of tool wear for all the inserts (UT, DCT, DCT+1T and DCT+2T) throughout the experimentation at all the speeds (70, 110 and 150 m/min) is presented in Figure 11.

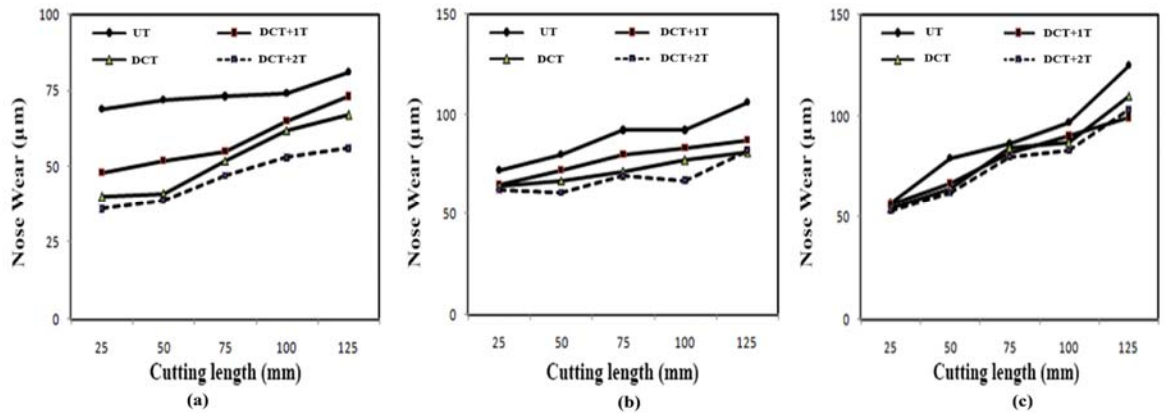

Figure 11: Tool wear comparison for all the inserts at feed rate of 0.1 mm/rev and different speeds: (a) 70 (b) 110 and (c) 150 m/min.

The tool wear at each of the cutting speed was observed being minimum for the tempered inserts (DCT+1 and DCT+2) as compared to the other inserts (UT and DCT). It was also found that the DCT insert has shown lower tool wear in comparison to the UT insert. At speed of 70 m/min, the wear was reduced by 28.2, 19.2 and 11.5% for the DCT+2, DCT+1T and DCT inserts as compared to the UT insert. At medium cutting speed (110 m/min), the reduction in tool wear was 26.6, 28.5 and 21.9% for the DCT+2, in DCT+1T and DCT inserts as compared to the UT insert. Interestingly, at speed of 150 m/min, the tool wear in the tempered inserts was approximately 90 µm, whereas for the DCT and UT inserts, it was 106 and 125 µm respectively. Although the tempered inserts outperformed the untempered inserts, there was no considerable difference between the tool wear for the DCT+1 and DCT+2T inserts at higher cutting speeds. The tool wear at 150 m/min was reduced by 23.2, 24.8 and 12.8% for the DCT+2, in DCT+1 and DCT inserts respectively in comparison with the UT insert. The rise in temperature of tool-workpiece interface is observed to be the reason for the increased tool wear at high speeds. This associates with the empirical formula (Equation 1) stating that cutting temperature is directly affected by feed and cutting speed (Kaynak, 2014; Zhang *et al.*, 2018)**.**

$$T = Cv^{0.2}f^{0.125} \tag{1}$$

where, T is cutting temperature, v is cutting speed, f is feed and C is a proportionality constant.

According to the given equation, cutting temperature is purely dependent on cutting speed and feed. The higher the values, the higher the temperature in machining. As the thermal conductivity of nickel based alloys is very low, within a short span, the majority of heat congregates over the nose of the tool. Moreover, the tool wear progresses as the extreme temperature initiates dissolution of the carbide particles, causing thermal fracture at the nose (Lu *et al.*, 2016; Kuppuswamy *et al.*, 2017).

Remarkably, the tool wear in the tempered inserts was lower than the untempered inserts at all the cutting speeds. The probable cause could be higher adhesion of coating to the substrate during the tempering, which prevents peeling and abrasion during machining. Conversely, as the coating depletes, the contact stresses increase in the insert enormously mounting residual stresses at the tool tip (Oliveira *et al.*, 2017). This can cause hard nitride grains to diffuse from the coating of the insert during turning of the nickel alloys. This diffused the nitride fragments at the rake face, causing severe abrasion, which resulted in higher tool wear in the untempered inserts. The existence of diffused particles on the chips formed during machining was observed in Figure 12. In addition, the thermal distribution in the inserts degrades because of uneven coating peeling, which results in the thermal fracture, promoting tool wear in the untempered inserts.

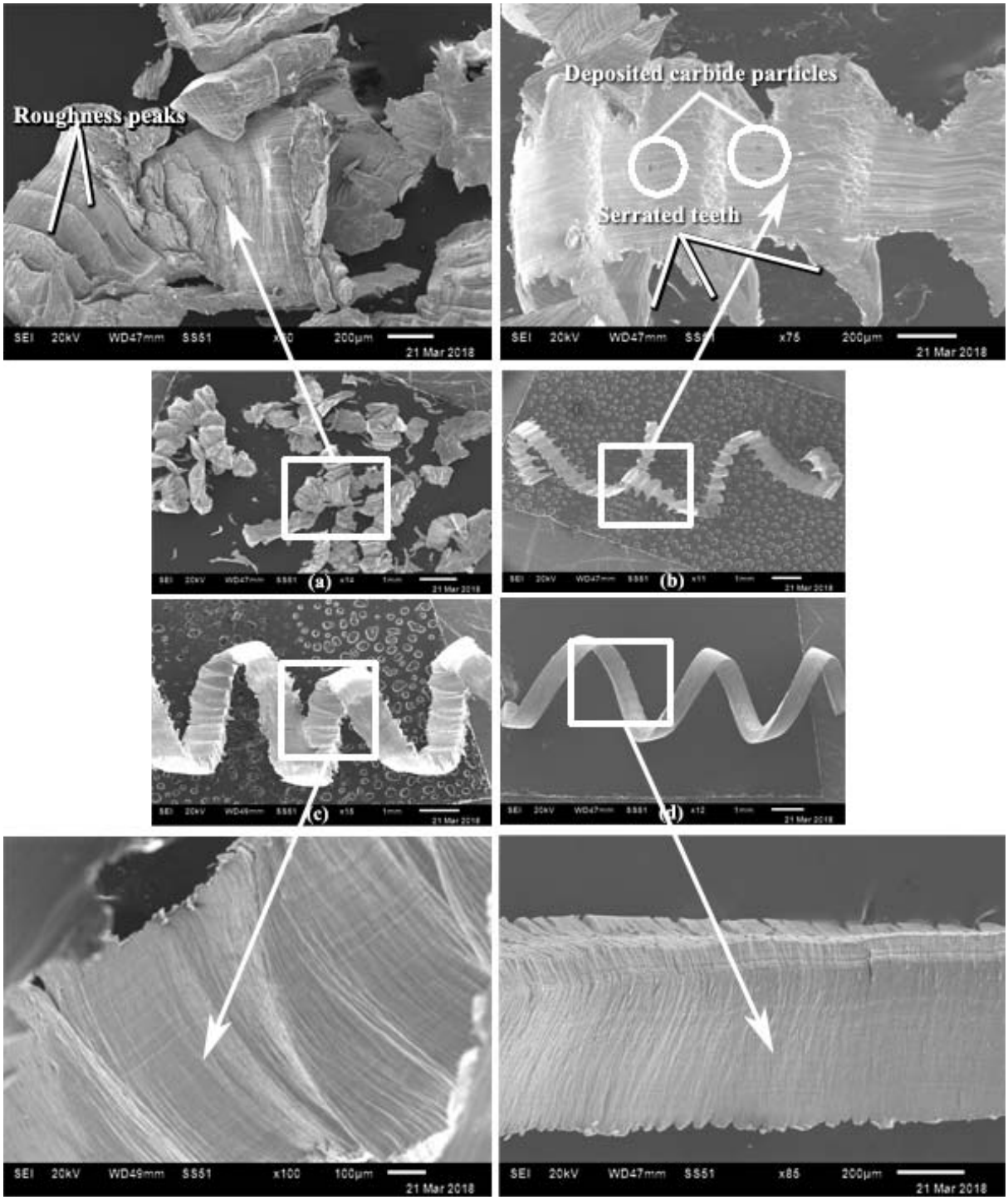

Figure 12: Traces of micrograins on chips produced during machining for the (a) UT, (b) DCT, (c) DCT+1T and (d) DCT+2T inserts.

3.6 Tool Flank Wear

SEM analysis was used to evaluate the flank wear of all the inserts. Figure 13 shows the SEM micrographs of all the inserts at 110 m/min cutting velocity and feed rate of 0.10 mm/rev. From the figure, it is evident that the flank wear of tempered inserts was lower as compared to the untempered inserts. From Figure 13(a), it is very clear that a built-up-edge (BUE) was initiated on the UT insert. On the contrary, there was no BUE observed for the treated and tempered inserts for the same condition. The improved wear resistance and thermal conductivity in tempered inserts restrained the BUE formation. Besides that, the tempering also precluded notch wear, which was observable in the DCT and UT inserts during the turning of Inconel 718. This is because of the enhanced thermal conductivity in the tempered inserts. In general, Inconel 718 has very low thermal conductivity of 11.2 W/mK (Pusavec *et al*., 2014). As the coating on the UT insert diminished, the insert lost the protection to heat, thereby resulting in premature tool failure, causing notch formation while machining. The strain rate in the tempered inserts was low because of the relieved residual stresses during the tempering process, resulting in reduced cutting edge chipping. If the induced stress in the inserts exceeds its ultimate strength, chipping initiates through frittering and evolves into notch wear (Chetan *et al.,* 2017).

The substantial performance of the tempered inserts as compared to the untempered inserts was very obvious, as shown in Figure 14. There was steady and uniform flank wear on the tempered inserts as compared to the untempered ones. This tendency can be attributed to improved cobalt-tungsten (CO-W) densification during the tempering. This enhanced the binding property of the firmly compacted WC matrix against the abrasive Inconel 718 chips. Conversely, the same strain hardening phenomenon caused the untempered inserts to chip off the nose edge. This could be because of the increased stress at the shear zone at elevated feed rates, which in turn induces high thermal fatigue. In addition, the greater tool-chip contact length in the untempered inserts could be the source for higher thermo-mechanical stresses. Due to the greater chemical affinity of nickel in Inconel 718 alloy, the UT insert was subjected to high adhesion and BUE formation, as shown in Figures 13(a) and 14(a). As the feed increased, the material removal rate (MRR) increased. This resulted in high heat generation at the tool tip. While turning the Inconel 718 with carbide inserts, the temperature may shoot up to more than 1,000 °C (Kaynak, 2014; Oliveira *et al.*, 2017). The higher MRR and excessive temperature together yielded edge fracture and BUE generation in the UT insert (Figure 14a) (Firouzdor *et al.*, 2011; He *et al.*, 2014; Kaynak, 2014).

From Figures 14(c) and 14(d), the plastic deformation and edge fracture at the tip of the tempered inserts were observed to be low when compared to the untempered inserts. This is the result of the tempering process, which freed the cutting inserts from residual stresses, which were formed during the sintering process. These stresses play a vital role in fracture failure of carbide inserts under severe cutting conditions.

Besides that, the enhancement in the cobalt binder phase during the tempering might have protected the tempered inserts from excessive tool wear. Furthermore, the reduced coefficient of friction in the tempered inserts might have provided better resistance towards the high friction between the chip and rake face.

From the Figure 15, it can be seen that the coefficient of friction in the DCT, DCT+1T and DCT+2T inserts was reduced by 16.0, 33.8 and 52.9% respectively in comparison to the UT insert. Due to the high friction between the tool-workpiece interface, early coating peeling might have occurred in the untempered inserts. This may have resulted in uneven thermal conductivity of the inserts, which caused the inserts to face thermal impact under severe cutting conditions. The thermal impact initiated the chipping and edge fractures in the inserts, which was found to be low for the tempered inserts as compared to the untempered inserts. The cracks initiated at the rake side and propagated to the flank face, resulting in excessive flank wear of the UT and DCT inserts.

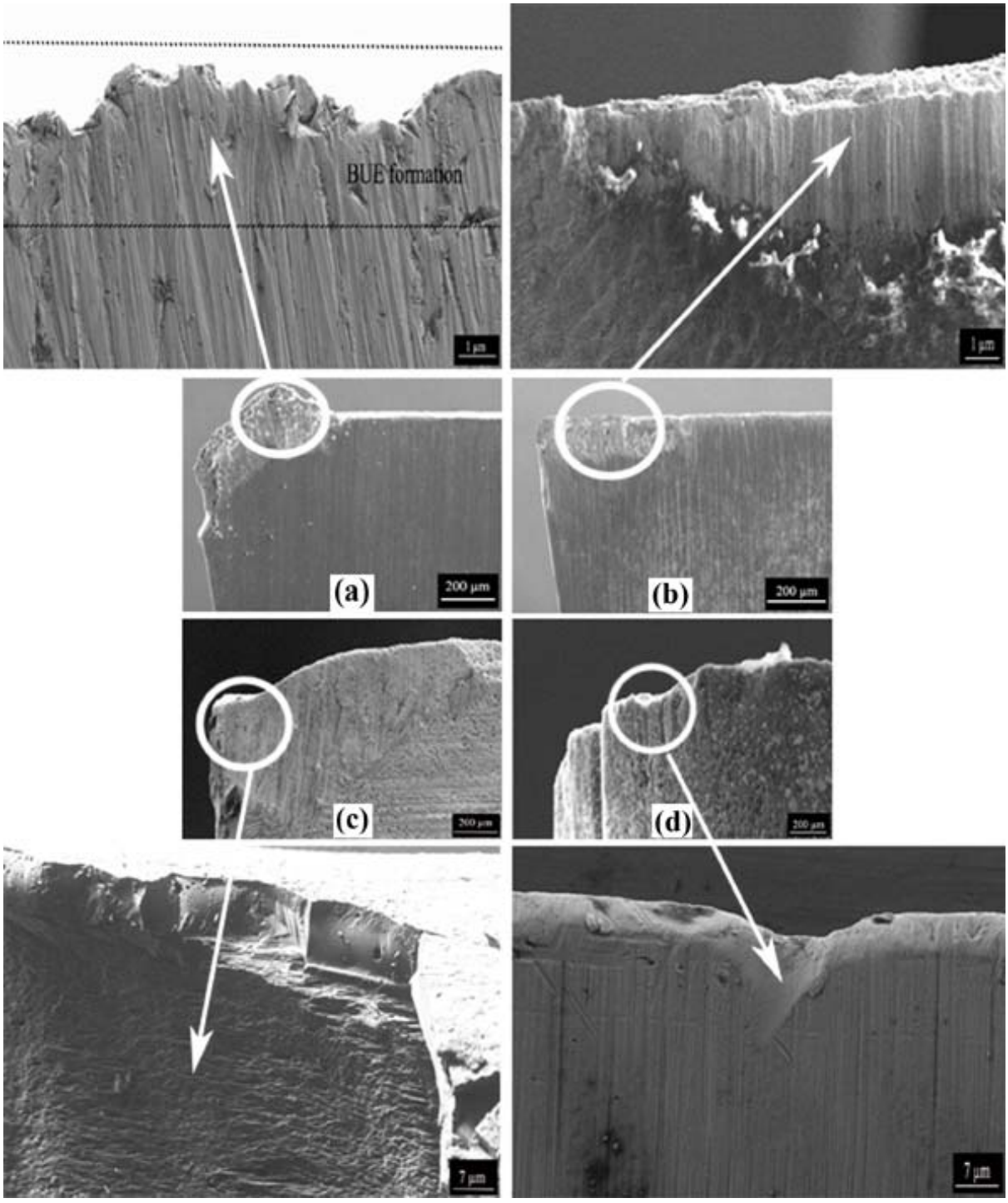

Figure 13: Flank wear at 110 m/min and 0.10 mm/rev for the (a) UT, (b) DCT, (c) DCT+1T and (d) DCT+2T inserts.

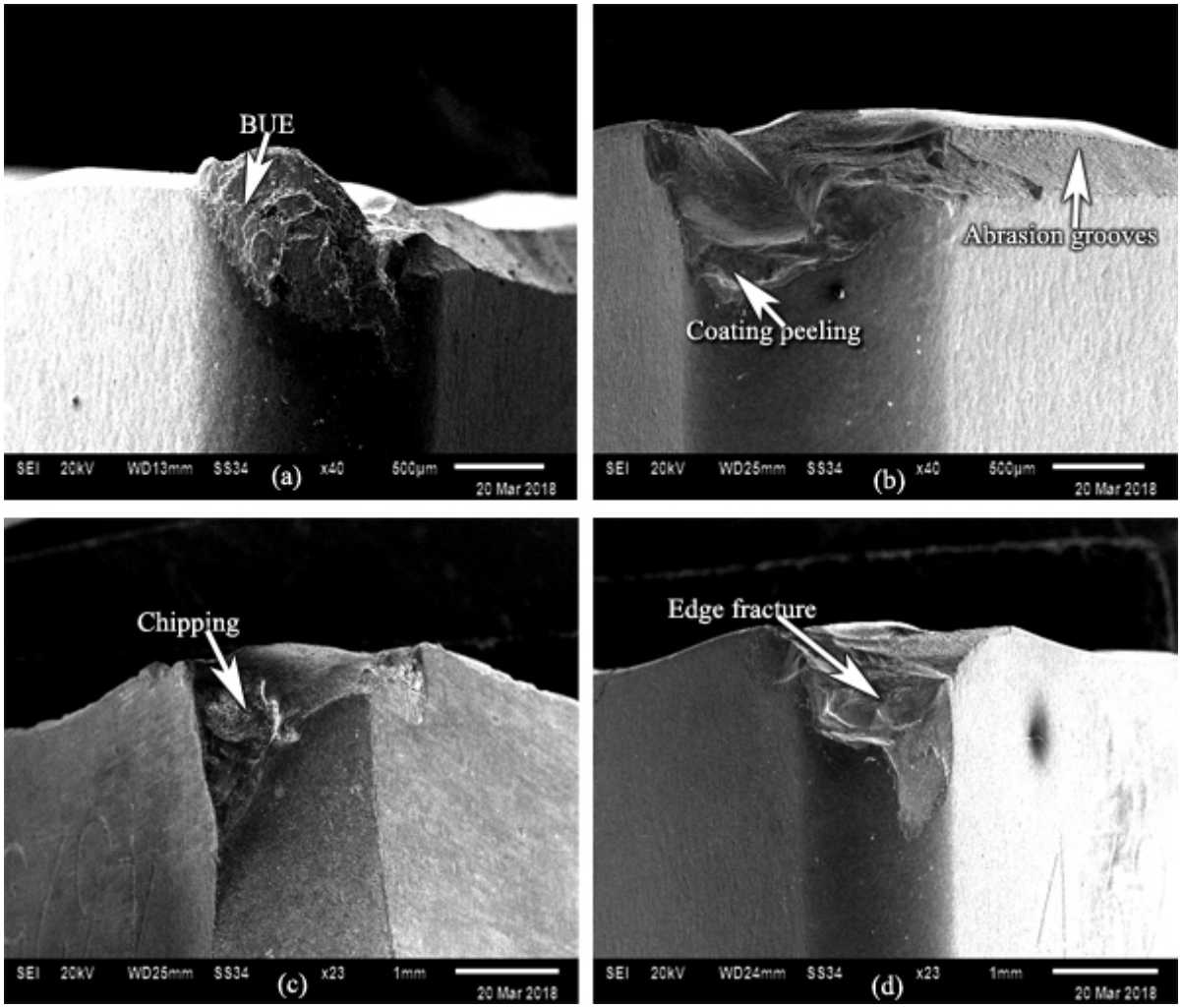

Figure 14: Flank wear of the (a) UT, (b) DCT, (c) DCT+1T and (d) DCT+2T inserts at 110 m/min speed and 0.15 mm/rev feed rate.

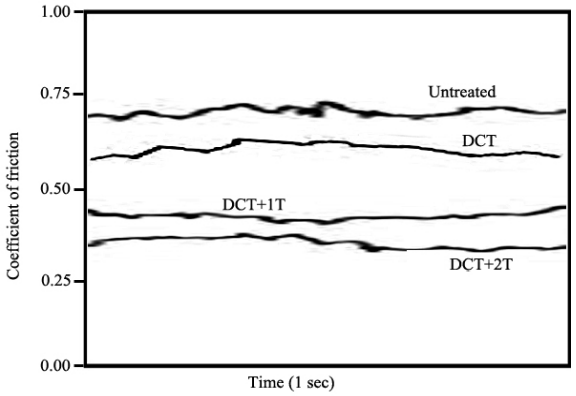

Figure 15: Contact friction of all the inserts.

4. CONCLUSION

DCT as well as DCT followed with single and double tempering (DCT+1T and DCT+2T) were performed on multilayer coated ($TiCN/Al_2O_3/TiN$) carbide inserts, and their performance was compared to the UT insert during the dry turning of Inconel 718. The following are the conclusions drawn from the study:

- The cryogenic process followed by the tempering process enhanced grain refinement and formed η-carbide phase in the inserts, which helped in improving the hardness.
- The tempering process prevented the coating peeling off the carbide inserts. Excessive coating breach was observed to be reduced in the tempered inserts during the scratch test.
- The tempered inserts (DCT+2T and DCT+1T) outperformed the untempered inserts (DCT and UT) in the wear test. Moreover, the flank wear during machining was significantly low in the tempered inserts as compared to the untempered inserts at every speed.
- During machining at high cutting speed, the cutting forces was reduced by 30.1% using the DCT+2T insert and 25.8% using the DCT+1T insert in comparison with the UT insert. Hence, the tempered inserts can effectively reduce the power consumption.
- In the TCCL examination, the tempered inserts outperformed the untempered by substantially reducing the wear track. The tempering process enhanced the scratch resistance of the inserts, resulting in reduced wear track.
- The enriched cobalt binder phase in the tempered inserts improved adhesion between the coating and the substrate, which restrained the notch wear progression. However, as the Inconel 718 possesses less thermal conductivity (11.2 W/mK), severe thermo-mechanical stresses could not curtail the tempered inserts in facing chipping and edge fracture during machining.
- The coefficient of friction was reduced by 52.9% for the DCT+2T insert and 33.8% for the DCT+1T insert, which improved the cutting performance of the tempered inserts. This in return reduced the edge fracture of the tempered inserts during machining.

REFERENCES

Aouici, H., Elbah, M., Yallese, M.A., Fnides, B., Meddour, I. & Benlahmidi, S. (2016). Performance comparison of wiper and conventional ceramic inserts in hard turning of AISI 4140 steel: analysis of machining forces and flank wear. *Int. J. Adv. Manuf. Tech.,* **87**:2221-44.

Arunachalam, R. & Mannan, M.A. (2000). Machinability of nickel-based high temperature alloys. *Mach. Sci. Technol.,* **4**: 127–168.

Cantero, J.L., Díaz-Álvarez, J., Miguélez, M.H. & Marín, N.C. (2013). Analysis of tool wear patterns in finishing turning of Inconel 718. *Wear,* **297**: 885–894.

Chetan, Ghosh, S. & Rao, P.V. (2017). Performance evaluation of deep cryogenic processed carbide inserts during dry turning of Nimonic 90 aerospace grade alloy. *Tribol. Int.,* **115**: 397–408.

Çiçek, A., Kara, K., Kivak, T. & Ekici, E. (2013). Evaluation of machinability of hardened and cryo-treated AISI H13 hot work tool steel with ceramic inserts. *Int. J. Refract Metals Hard Mater.,* **41**: 461-469.

D'addona, D.M. & Raykar, S.J., (2016). Analysis of surface roughness in hard turning using wiper insert geometry. *Procedia CIRP*., **41**:841-846.

Deshpande, Y.V., Andhare, A.B. & Padole, P.M. (2018). Experimental results on the performance of cryogenic treatment of tool and minimum quantity lubrication for machinability improvement in the turning of Inconel 718. *J. Braz. Soc. Mech. Sci. & Eng.,* **40:** 6.

de Paula Oliveira, G., Cindra Fonseca, M. & Araujo, A.C. (2017). Analysis of residual stress and cutting force in end milling of Inconel 718 using conventional flood cooling and minimum quantity lubrication. *Int. J. Adv. Manuf. Tech.,* **92**: 3265–3272.

Dhananchezian, M. & Pradeep Kumar, M. (2011). Wear behaviour of PVD coated and cryogenically treated tools for Ti-6Al-4V turning. *Int. J. Mater Forming,* **51**: 34–40.

Firouzdor, V., Nejati, E. & Khomamizadeh, F. (2011). Effect of deep cryogenic treatment on wear resistance and tool life of M2 HSS drill. *J. Mater. Process. Tech.,* **206**: 467–472.

Huang, J., Zhu, Y., Liao, X., Beyerlein, I., Bourke, M. & Mitchell, T. (2003). Microstructure of cryogenic treated M2 tool steel. *Mater. Sci. Eng.: A,* **339**: 241–244.

Kaynak, Y. (2014). Evaluation of machining performance in cryogenic machining of Inconel 718 and comparison with dry and MQL machining. *Int. J. Adv. Manuf. Tech.,* **72**: 919–933.

Kuppuswamy, R., Zunega, J. & Naidoo, S. (2017). Flank wear assessment on discrete machining

process behavior for Inconel 718. *Int. J. Adv. Manuf. Tech.,* **93**: 2097–2109.
Kursuncu, B., Caliskan, H., Guven, S.Y. & Panjan, P. (2018). Improvement of cutting performance of carbide cutting tools in milling of the Inconel 718 superalloy using multilayer nanocomposite hard coating and cryogenic heat treatment. *Int. J. Adv. Manuf. Tech.,* **1:**1–13.
Molinari, A., Pellizzari, M., Gialanella, S., Straffelini, G. & Stiasny, K.H. (2001). Effect of cutting conditions on wear performance of cryogenically treated tungsten carbide inserts in dry turning of stainless steel. *Tribol. Int.,* **118**: 350-355.
Nirmal Kalsi, S., Rakesh Sehgal & Vishal Sharma, S. (2010). Cryogenic Treatment of Tool Materials: A Review. *Mater. Manuf. Process*., **25**: 1077–1100.
Özbek, N.A., Çiçek, A., Gülesin, M. & Özbek, O. (2014). Investigation of the effects of cryogenic treatment applied at different holding times to cemented carbide inserts on tool wear. *Int. J. Mach. Tool. Manu.,* **86**:34-43.
Podgornik, B., Paulin, I., Zajec, B., Jacobson, S. & Leskovšek, V. (2016). Deep cryogenic treatment of tool steels. *J. Mater. Process. Tech.,* **229**: 398–406.
Pradeep, A.V., Lingaraju, D. & Ramakrishna, S. (2019a). Modelling and statistical analysis of surface roughness by Taguchi and RSM techniques in hard turning of AISI 52100 steel with multilayer coated carbide insert. *Int. J. Machining & Machinability of Materials.,* **21**: 300-320.
Pradeep, A.V., Lingaraju, D. & Ramakrishna, S. (2019b). Effect of MQL on roughness, white layer and microhardness in hard turning of AISI 52100. Emerging Materials Research., **8**: 29-43.
Pradeep, A.V., Lingaraju, D. & Ramakrishna, S. (2019c). Application of response surface methodology in evaluating the performance of conventional, wiper, cryogenically treated and coated (TiN, TiAlN and TiCN) carbide inserts in turning of AISI 52100 steel. Int. J. Agile Systems & Management., **11**: 340-363.
Pusavec, F., Deshpande, A., Yang, S., M'Saoubi, R., Kopac, J., Dillon Jr, O.W. & Jawahir, I.S., (2014). Sustainable machining of high temperature Nickel alloy–Inconel 718: part 1–predictive performance models. *J. Clean. Prod.,* **81**:255-269.
Senthilkumar, D., Rajendran, I., Pellizzari, M. & Siiriainen, J. (2011). Influence of shallow and deep cryogenic treatment on the residual state of stress of 4140 steel. *J Mater. Process. Tech.,* **211**: 396–401.
Sharman, A.R.C., Hughes, J.I. & Ridgway, K. (2004). Workpiece Surface Integrity and Tool Life Issues When Turning Inconel 718^{TM} Nickel Based Superalloy. *Mach. Sci. Technol.,* **8**: 399–414.
Thakur, A. & Gangopadhyay, S. (2016). State-of-the-art in surface integrity in machining of nickel-based super alloys. *Int. J. Mach. Tool. Manu.,* **100**: 25–54.
Thakur, D.G., Ramamoorthy, B. & Vijayaraghavan, L. (2009). Study on the machinability characteristics of superalloy Inconel 718 during high speed turning. *Mater. Design.,* **30**: 1718–1725.
Thakur, D.G., Ramamoorthy, B. & Vijayaraghavan, L. (2015). Effect of posttreatments on the performance of tungsten carbide (K20) tool while machining (turning) of Inconel 718. *Int. J. Adv. Manuf. Tech.,* **76**: 587–596.
Vadivel, K. and Rudramoorthy, R. (2009). Performance analysis of cryogenically treated coated carbide inserts. *Int. J. Adv. Manuf. Tech.,* **42**: 222–232.
Yong, J. & Ding, C. (2011). Effect of cryogenic treatment on WC–Co cemented carbides. *Mater. Sci. Eng.: A,* **528**: 1735–1739.
Zhang, B., Njora, M.J. & Sato, Y. (2015). An investigation of cobalt phase structure in WC–Co cemented carbides before and after deep cryogenic treatment. *Int. J. Refract. Metals Hard Mater.,* **51**: 201–206.
Zhang, B., Njora, M.J. & Sato, Y. (2018). High-speed turning of Inconel 718 by using TiAlN- and (Al, Ti) N-coated carbide tools. *Int. J. Adv. Manuf. Tech.,* **96**: 2141–2147.
Zhu, D., Zhang, X. & Ding, H. (2013). Tool wear characteristics in machining of nickel-based superalloys. *Int. J. Mach. Tool. Manu.,* **64**: 60–77.

SURFACE POTENTIAL AND TEMPERATURE EFFECT STUDIES OF HOMO- AND COPOLYSILOXANES THROUGH LANGMUIR BLODGETT TECHNIQUE

Faridah Lisa Supian*, Darvina Lim Choo Kheng, Mohd Syahriman Mohd Azmi & Mazlina Mat Darus

Department of Physics, Faculty of Science and Mathematics, Sultan Idris University of Education (UPSI), Malaysia

*Email: faridah.lisa@fsmt.upsi.edu.my

ABSTRACT

Hydrophilic backbone chains with substituted hydrophobic organic groups give rise to amphiphilic polysiloxane. This property is of great interest as it can form a Langmuir monolayer, an orderly arranged layer that can be utilised in any potential nanoscale application. Hence, a study was conducted on the surface pressure, surface potential and effective dipole moment of various homopolysiloxane and copolysiloxane Langmuir films to clarify some of their monolayer properties. A NIMA Langmuir 611D trough accompanied with a NIMA surface potential (S-POT) probe was employed in this work. The space filling model, generally known as the Corey, Pauling and Koltun (CPK) precision molecular model, was used to construct the siloxanes unit of each set of polysiloxanes to estimate the siloxane unit size. From the surface pressure isotherm, it was observed that copolysiloxanes are more condensed than homopolysiloxanes. By comparing the results extrapolated from the graph with CPK modelling, the structure was further explored. The correlation of surface potential (ΔV) and effective dipole moment (μ) at room temperature were investigated, and from the results and Helmholtz equation, it seemed to be dependent on each other. A study on the effects of temperature on maximum effective dipole moment (μ_{max}) of each polysiloxane was also carried out. It was found that as the temperature increases, the μ_{max} decreases. These results can be utilised for the potential application studies of polysiloxanes in the future.

Keywords: *Polysiloxane; Langmuir-Blodgett; surface pressure; surface potential; effective dipole moment.*

1. INTRODUCTION

Polysiloxanes are polymers that consist of silicon and oxygen atoms alternately arranged in a chain with certain organic groups bonded to the Si atoms. These compounds have shown potential in countless applications, such as in the fields of coating (Tang & Liu, 2010), medicine (Grigoryan & Kaganova, 2010) and optics (Fleger & Neyer, 2006; Hu *et al*., 2015a, b) due to their various unique properties. In fact, polysiloxanes are considered as one of the 'early birds' in Langmuir monolayer research (Fox *et al*., 1947; Willis, 1971) for their surface-active properties. Langmuir- Blodgett (LB) is a powerful method for an air-water interface, which leads to producing monolayers that are suitable for many characterisations. Our group has been working extensively on the LB technique with other materials, such as a Calixarenes and Schiff based Ligand for ion sensor applications (Supian *et al*., 2010, 2017; Alang Ahmad *et al.,* 2017).

The uniqueness of its chemical structures leads to the special abilities of nanomaterials in terms of flexibility, resistance to climate and oxidation. Hence, polysiloxanes have been broadly used in the biomedical, aerospace and automobile industries (Meng *et al.,* 2012). The main challenge of these nanomaterials is to improve the mechanical properties due to the weak intermolecular force in the chains. Nevertheless, elastomers, gels, lubricants, foams and adhesives are being produced from these materials (Hill, 2005). These materials have also being used as solvent detectors for chloroform, isopropyl alcohol and dichloromethane in another work (Supian, 2017).

Thus, this work is aimed at clarifying some of the surface properties of polysiloxane Langmuir film in terms of the air-water interface, surface pressure, surface potential and effective dipole moment at room temperature and under control with slowly raising low temperatures. A NIMA Langmuir 611D trough connected with NIMA Surface Potential (S-POT) probe was utilised throughout this study.

2. EXPERIMENTAL

2.1 Materials

In this work, six polysiloxanes of different functional groups at the end of their side chain were used, as shown in Figure 1. We have identified and elucidated them to homo- and co- based on their basic structure. In comparison, copolysiloxanes have additional functional chains that exhibit longer and wider structures.

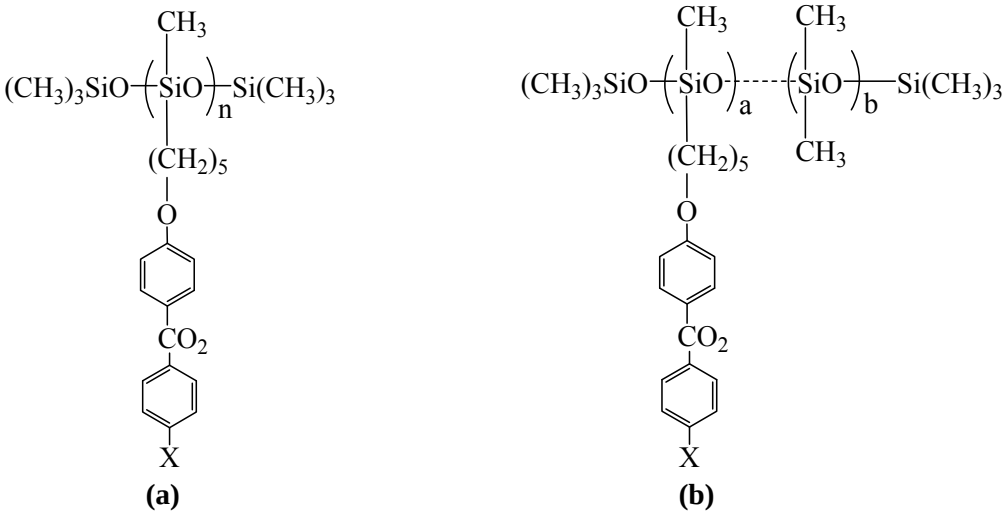

Figure 1: Structures of (a) homopolysiloxanes and (b) copolysiloxanes.

The properties of six types of homopolysiloxanes and copolysiloxanes were established by dividing them into three sets, as shown in Table 1. They were labelled as DL 1, DL 2, DL 3 for homopolysiloxanes, and DL 4, DL 5 and DL 6 for copolysiloxanes. Each set was paired with homo- and co-, while X is the same group. Set A consists of CN, Set B; OCH_3 and Set C; OC_6H_{13} respectively.

Table 1: Properties of the six types of homopolysiloxanes and copolysiloxanes used in this study.

Set	Homopolysiloxanes	X	Copolysiloxanes	X	Ratio of a: b
A	DL 1	CN	DL 4	CN	50: 50
B	DL 2	OCH_3	DL 5	OCH_3	50: 50
C	DL 3	OC_6H_{13}	DL 6	OC_6H_{13}	50: 50

The polysiloxanes were obtained courtesy of Dr. David Lacey's research group from the Department of Chemistry, University of Hull. The chloroform purchased from Sigma Aldrich was used as the solvent to prepare a 0.2 mg/ml solution from each polysiloxane without further purification. Siloxane units for each set was modelled using the Corey, Pauling and Koltun (CPK) precision molecular model as illustrated by Figure 2 for estimation of size and comparison purpose with the surface pressure (Π-A) isotherm data. The CPK model shown in the figure reveals the comparison of the X group, where it can be seen clearly that Set C exhibits a longer chain as compared to Sets A and B.

(a) (b) (c)

Figure 2: CPK models of siloxanes unit for (a) Set A, (b) Set B and (c) Set C.

2.2 Surface Properties Study of Polysiloxanes Langmuir Film

The Langmuir-Blodgett (LB) technique was utilised to study the surface properties of polysiloxanes monolayer on the air-water interface. The polysiloxanes solution was dispersed as small droplets evenly on a NIMA Langmuir 611D trough using a microsyringe. Pure water from Elga Purelab water system with >15 MΩcm was employed as the subphase. Chromatography paper acted as the surface pressure sensor.

A NIMA surface potential (S-POT) probe with a precision of ±2 mV was attached to the existing NIMA interface unit software. A metal plate acting as the counter electrode was immersed under the water subphase and joined to the probe. A small uniform distance was ensured between the vibrating sensor plate on the probe and monolayer.

Subsequently, 5 min was allowed for solvent evaporation before the Π-A isotherm and surface potential (ΔV) of the polysiloxanes monolayer were obtained simultaneously. The compression speed of the movable barrier is 12 mm/min. Identical procedures were repeated for the other polysiloxanes solutions at room temperature. Next, the surface potential procedures were repeated under controlled temperature from 7 to 19 °C in order to analyse the effects of temperature towards the effective dipole moment (μ) of polysiloxane monolayer. The trough was placed inside a metal box containing ice cubes to increase the temperature slowly, while the ΔV values were recorded. The μ_{max} values were then calculated.

3. RESULTS AND DISCUSSION

3.1 Surface Pressure (Π-A) Isotherm

Polysiloxane Langmuir monolayers were studied through Π-A isotherm graphs (Figure 3), which demonstrated the surface pressure against mean molecular area at the air-water interface. The decrement of the mean molecular area accompanied by the increment of surface pressure, as illustrated in all the isotherm graphs, was due to intermolecular forces between the molecules.

As shown Figure 3, the isotherms for copolysiloxanes were more condensed than their respective homopolysiloxanes, similar to the results obtained in Richardson *et al*. (1994). However, there is an exception for homopolysiloxane, DL 1, in which it is more condensed than copolysiloxanes, DL 4. Homopolysiloxanes, DL 1 and DL 2 reached their collapse point much faster than their respective copolysiloxanes, DL 4 and DL 5. DL 1 met its collapse point at 6.33 mN/m, as compared to DL 4,

which collapsed at around 16.20 mN/m, and formed three-dimensional structures. In addition, DL 2 reached its collapse point around 20 mN/m, while DL 5 achieved the collapse point at around 24 mN/m. In contrast, DL 3 achieved higher solid phase and only started to collapse at 28.60 mN/m as compared to DL 6, which began to collapse at around 22 mN/m.

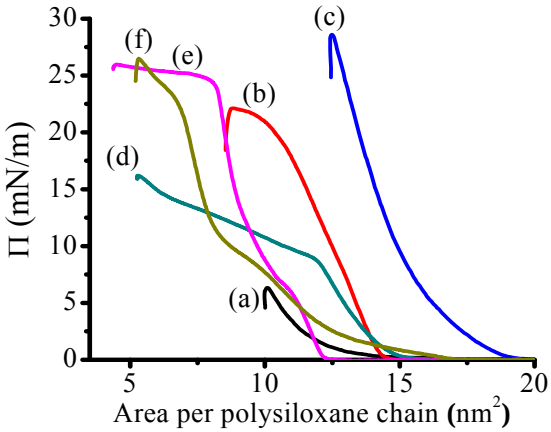

Figure 3: *Π*-A isotherm graphs of homopolysiloxanes (a) DL 1, (b) DL2 and (c) DL 3 as well as copolysiloxanes (d) DL 4, (e) DL 5 and (f) DL 6.

All the polysiloxanes showed a clear phase transition from gaseous state to liquid phase, followed by solid phase before they collapsed as demonstrated by the "kink" in each isotherm curve after passing through the steepest linear part. By extrapolating the steepest linear part of the isotherm curve to 0 mN/m, the limiting area per polysiloxane chain molecule can be obtained. Then, the area of the siloxane unit can be calculated by dividing the limiting area per molecule with each respective number of unit siloxane (Majid *et al*., 1994). Subsequently, as an area of a circle is assumed to be occupied by the siloxane unit, the diameter of the siloxane unit was determined. All the data was tabulated in Table 2. The estimated monomer size from the CPK modelling is slightly different from the isotherm data because the shape of the monomer in the chain is slightly different as compared to the standalone unit due to the Si-O-Si and O-Si-O bonding. In Grigoras (1992), great flexibility occurs in the Si-O-Si angle in the chain ranging from 140 to 180°, with the presence of 0.3 kcal/mol barrier for linearisation altering the optimum occupied area. Meanwhile, the O-Si-O angle also has rigid bone angle values from 102 to 112° that affects the occupied area. When the siloxanes units bind to one another, the area occupied will be varied due to the rotation of the angles as the chain attempts to achieve an equilibrium position.

Table 2: *Π*-A Isotherm data of the polysiloxanes.

Set	A		B		C	
	DL 1	DL 4	DL 2	DL 5	DL 3	DL 6
Degree of Polymerisation	51	27	45	23	53	22
No. of Unit Siloxane	51	54	45	46	53	44
Limiting Area per Molecule (nm^2)	11.83	14.12	14.33	9.84	15.68	9.05
Area Occupied Per Siloxane Unit (nm^2)	0.23	0.26	0.32	0.21	0.30	0.21
Modelled area per siloxane unit from CPK modeling	~0.60	~0.60	~0.60	~0.60	~0.50	~0.50
Estimated siloxane unit size, d (nm)	0.54	0.58	0.64	0.52	0.62	0.52

3.2 Surface Potential (ΔV) and Effective Dipole Moment (μ) at Room Temperature

The ΔV of the polysiloxanes Langmuir monolayers (Figure 4) were determined through capacitance changes in the air gap between the monolayer and vibrating plate due to air vibration (Somasundaran, 2006).

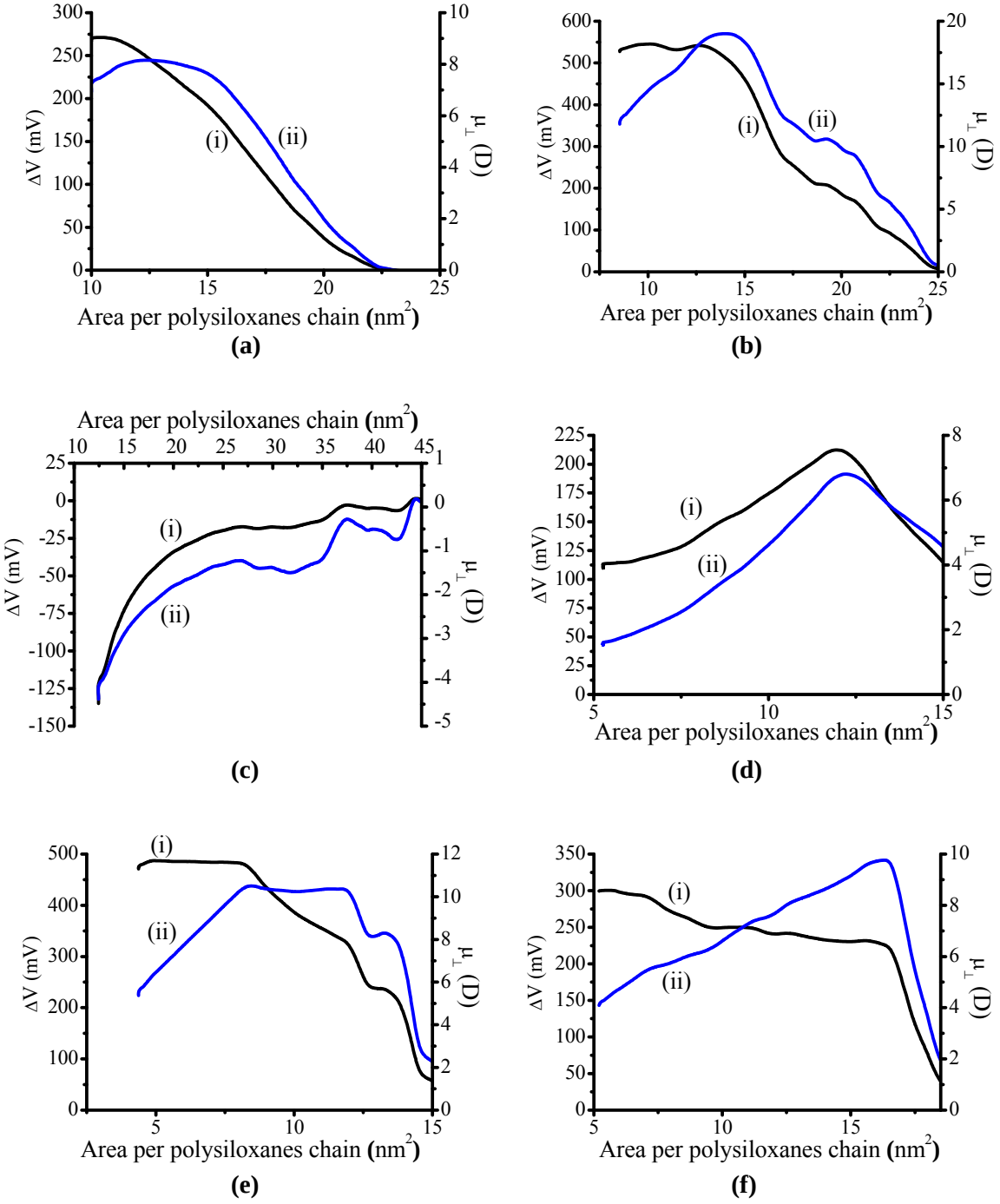

Figure 4: (i) ΔV and (ii) μ graphs for (a) DL 1, (b) DL 2, (c) DL 3, (d) DL 4, (e) DL 5 and (f) DL 6.

The surface potential graphs in Figure 4(a) illustrate that all of the polysiloxanes have positive surface potential, as the area per polysiloxane chain decreased except for DL 3, which demonstrated a negative surface potential. From the ΔV values, the $\mu_{\perp}$ value was calculated using the Helmholtz equation:

$$\mu_{\perp} = \varepsilon_0 \varepsilon A \Delta V \quad (1)$$

where $\mu_{\perp}$ is the effective dipole moment, ε_0 is the vacuum permittivity (8.854×10^{-12} $C^2N^{-1}m^{-2}$), A is the area per molecule and ε is the relative permittivity for the materials between the electrodes, which in this case is taken as 1 since the thickness of air between monolayer and vibrating plate is assumed to be large as compared to the thickness of the monolayer (Korchowiec *et al*., 2007).

3.3 Effective Dipole Moment ($\mu_{\perp}$) Dependence on Temperature

The effects on $\mu_{\perp max}$ due to temperature on the polysiloxanes were investigated. From Table 3 and Figure 5, it can be observed that $\mu_{\perp max}$ decreased as the temperature rose for all the polysiloxanes. This might due to the more ordered orientation of the polysiloxanes at lower temperatures as compared to higher temperatures (Kalachev, 1990).

Table 3: $\mu_{\perp}$ dependence on temperature for the polysiloxanes.

Set	A		B		C	
	DL 1	DL 4	DL 2	DL 5	DL 3	DL 6
7 °C	28.21	52.576	70.56	42.5	-4.55	15.08
9 °C	27.3	51.46	68.04	42.2	-6.37	14.82
13 °C	23.66	51.336	65.52	42	-8.19	14.04
16 °C	19.565	51.088	63	41.8	-8.645	13.26
19 °C	16.835	50.22	61.32	41.5	-10.01	13

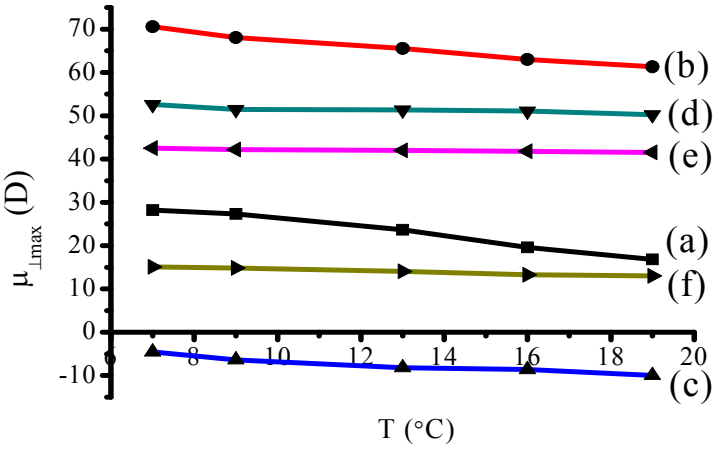

Figure 5: $\mu_{\perp}$ dependence on temperature (T) for (a) DL 1, (b) DL 2, (c) DL 3, (d) DL 4, (e) DL 5 and (f) DL 6.

4. CONCLUSION

Polysiloxane, an amphiphilic polymer that has been widely applied, was investigated in this work, focusing on determining the behaviour of the air-water interface. The Langmuir-Blodgett technique was employed to study the characteristics of several types of polysiloxanes, particularly for the

aspects of isotherm, surface potential and effective dipole moment. It was obvious that copolysiloxanes were more condensed than homopolysiloxanes as result of the being an isotherm. CPK modelling, on the other hand, aided us with more information on the flexibility of the structures and binding angle. Surface potential (ΔV) at room temperature was investigated, illustrating that all the polysiloxanes have positive surface potential as the area per polysiloxane chain decreased except for DL 3, which demonstrated a negative surface potential. In addition, the effect of temperature on the effective dipole moment was also explored, whereby as the temperature increased, the effective dipole moment decreased. The results indicate that polysiloxanes nanomaterials possess good properties on the air-water interface and have promising potential in future applications.

ACKNOWLEDGMENT

The authors are grateful for the contribution of polysiloxane materials by Dr. David Lacey's group, Department of Chemistry, University of Hull for this research. The authors also wish to thank Sultan Idris University of Education (UPSI) and the Government of Malaysia for the scholarship awarded to conduct this study.

REFERENCES

Fleger, M. & Neyer, A. (2006). PDMS microfluidic chip with integrated waveguides for optical detection. *Microelectron. Eng.*, **83**: 1291-1293.

Fox, H., Taylor, P. & Zisman, W. (1947). Polyorganosiloxanes surface active properties. *Ind. Eng. Chem.*, **39**: 1401-1409.

Supian, F.L., Richardson, T.H., Deasy, M., Kelleher, F., Ward, J.P. & McKee, V. (2010). Interaction between Langmuir and Langmuir-Blodgett films of two calix[4]arenes with aqueous copper and lithium ions. *Langmuir*, **26(13)**: 10906-10912.

Ruslan, N.I., Lim, D.C.K., Alang Ahmad, S.A., Abdul Aziz, S.F.N., Supian, F.L., Yusof, N.A. (2017). Ultrasensitive electrochemical detection of metal ions using dicarboethoxycalixarene-based sensor. *J. Electroanal. Chem.*, **799**: 497-504.

Supian, F.L., Juahir, Y. & Morris, B.M. (2017). A Langmuir study of novel schiff base ligand for ion sensor application. *J. Fundam. Appl. Sci*., **9(6S)**: 115-123.

Meng, Y., Wei, Z., Lu, Y.L & Zhang, L.Q. (2012). Structure, morphology and mechanical properties of polysiloxanes elastomer composites prepared by in situ polymerization of zinc dimethacrylate. *eXPRESS Polym. Lett.*, **6(11)**: 882- 894.

Hill, R.G. (2005). *Biomedical Polymers, Biomaterials, Artificial Organs and Tissue Engineering*. Woodhead Publishing, Cambridge.

Supian, F.L., Yahaya, R. & Lim, D.C.K. (2017). Copolysiloxane solvent detector using Langmuir-Blodgett surface potential method. *Int. J. Nanoelectron. Mater.*, **10**: 39- 46.

Grigoras, S. (1992). Polydimethylsiloxane: conformational analysis and configurational properties. *In* Bicerano, J. (Ed.), *Computational Modeling of Polymers*. Marcel Dekker Inc., New York, pp. 161-190.

Grigoryan, G.V. & Kaganova, E.V. (2010). Polymer materials of medical purpose and materials for dentistry. *Polym. Sci. Series D*, **3**: 255-257.

Hu, J., Zhou, Y. & Sheng, X. (2015a). Optical diffusers with enhanced properties based on novel polysiloxane@CeO_2@PMMA fillers. *J. Mater. Chem.*, **3**: 2223-2230.

Hu, J., Zhou, Y. & Sheng, X. (2015b). Hydrothermal synthesis of ZnO@polysiloxane microspheres and their application in preparing optical diffusers. *RSC Advances*, **5**: 17064-17069.

Kalachev, A.A., Sauer, T., Vogel, V., Plate, N.A. & Wegner, G. (1990). Influence of subphase conditions on the properties of Langmuir-Blodgett films from substituted phthalocyaninato-polysiloxanes. *Thin Solid Films*, **188**: 341-353.

Korchowiec, B., Salem, A.B., Corvis, Y., Regnouf de Vains, J.B., Korchowiec, J. & Rogalska, E. (2007). Calixarenes in membrane environment: a monolayer study on the miscibility of three p-

tert-butylcalix[4]arene β-lactum derivatives with 1,2-dimyristoyl-sn-glycero-3-phosphoethanolamine. *J. Phys. Chem*., **111**: 13231-13242.

Majid, W.H.A., Richardson, T., Holder, S. & Lacey, D. (1994). Cyclic polysiloxanes in polar LB assemblies: synthesis, evaluation and pyroelectric behavior. *Thin Solid Films*, **243**: 378-383.

Richardson, T., Majid, W.H.A., Cochrane, E.C.A., Holder, S. & Lacey, D. (1994). Langmuir-Blodgett films of linear polysiloxanes incorporating aromatic side-chains: structure-property relationships. *Thin Solid Films*, **242**: 61-66.

Somasundaran, P. (2006). *Encyclopedia of Surface and Colloid Science*. CRC Press, Florida.

Tang, C. & Liu, W. (2010). Synthesis of novel photosensitive polysiloxanes and their effects on properties of UV-cured epoxy methacrylate coatings. *J. Coat. Technol. Res.*, **7**: 651-658.

Willis, R.F. (1971). Surface pressure and surface potential measurements of polydimethylsiloxane substituted undercanoic acids on aqueous surfaces. *J. Colloid Interface Sci.*, **35**: 1-15.

STUDY OF THERMAL CONDUCTIVITY AND HEAT TRANSFER COEFFICIENT OF MWCNT-OH / DEIONISED WATER-ETHYLENE GLYCOL BASED NANOFLUIDS

Amirah Abdullah[1], Imran Syakir Mohamad[1,2], Ahmad Yusairi Bani Hashim[3], Siti Hajar Sheikh Md Fadzullah[1,2] & Syazwani Zainal Abidin[1]

[1]Fakulti Kejuruteraan Mekanikal
[2]Centre for Advanced Research on Energy
[3]Fakulti Kejuruteraan Pembuatan
Universiti Teknikal Malaysia Melaka (UTeM), Malaysia

*Email: amirahabdullah2911@gmail.com

ABSTRACT

Carbon nanotube (CNT) is a nanoparticle that has better thermal properties of thermal conductivity and heat transfer coefficient. This paper intends to study the thermal conductivity and heat transfer coefficient on hydroxyl multiwalled carbon nanotube (MWCNT-OH) / deionised water-ethylene glycol based nanofluids. The two-step method is used in preparation of nanofluids via homogenisation and sonication on MWCNT-OH nanoparticles (0.1 to 1.0 wt%), polyvinylpyrrolidone (PVP) surfactant (10 % from wt% of nanoparticles) and base fluid (50:50; deionised water (DI): ethylene glycol (EG)). The nanofluids were tested at three various temperatures (6, 25 and 40 °C). The thermal conductivity enhancement was found to be from 0.3024 to 6.536 %, whereby 1.0 wt% at 6 °C had the highest enhancement. The heat transfer coefficient had 2.961 to 26.49 % enhancement, with the superior heat transfer coefficient given high value of Nusselt number. Thermal conductivity and heat transfer coefficient depend on temperature and nanoparticles concentration. The thermal properties were increased when temperature and nanoparticles increased. Moreover, the increment of thermal conductivity performance was affected by the nanoparticles' characteristics, particle size, particle interface, PVP surfactant, dispersion method and particle activity in nanofluids. Meanwhile, factors such as functionalised group (-OH) in MWCNT surface caused the heat transfer coefficient to be higher than the standard base fluid. Additionally, the interaction and as well as collision among particles also have effect in enhancing the heat transfer coefficient. Thus, based on this study, it is shown that thermal conductivity and heat transfer coefficient are improved with the inclusion of MWCNT-OH nanoparticles in base fluids.

Keywords: *Nanofluids; hydroxyl multiwalled carbon nanotube (MWCNT-OH) nanoparticles; polyvinylpyrrolidone (PVP); thermal conductivity; heat transfer coefficient.*

1. INTRODUCTION

In 1995, Stephen U.S. Choi was the first researcher that studied about nanofluids at the Argonne Laboratory, USA (Sayantan & Somjit, 2013). Nanofluid is defined as the dispersion of a new engineering material in nanometre-sized particles in base fluids (Abdolbaqi *et al*., 2015). The nanoparticles are found through carbon nanotube (CNT) investigation. There are several types of CNT, such as single-walled carbon nanotube (SWCNT) and multiwalled carbon nanotube (MWCNT). Nowadays, researchers are interested in CNT investigation due to its high thermal physical properties. The thermal conductivity of CNT nanoparticles is about 1,800 to 2,000 W/m.K (Marquis & Chibante, 2005). Due to it, CNT nanoparticles have been used as nanofluids in car radiators as a coolant because the thermal conductivity and heat transfer of nanofluids are higher than pure fluid (e.g., ethylene glycol, deionised water or oil). The nanofluids allow the radiator to have high thermal properties performance and improve cooling systems in cars (Rahul & Basavaraj, 2013). In addition, according

to Chung *et al*. (2011) and Wu *et al*. (2014), other fields such as electrical, biological and pharmaceutical processes, as well as thermal engineering also use nanofluids in their applications.

The problem of lower thermal physical properties of base fluids, such as deionised water and ethylene glycol, can be overcome by using CNT nanoparticles in the base fluids. Kanagaraj *et al*. (2006) found that MWCNT-ethylene glycol based nanofluids at concentration of 0.5 wt% had 23 % thermal conductivity enhancement. Whilst Kumaresan *et al*. (2012) mentioned that MWCNT based nanofluids in the mixture of deionised water (DI) and ethylene glycol (EG) at ratio 70:30; DI: EG had 19.73 % thermal conductivity increment and 160 % heat transfer coefficient enhancement at 0.45 vol% MWCNT. Mehdi & Masoud (2016) found that 1.0 vol% of MWCNT-COOH based nanofluids at ratio 60:40; DI: EG has 34.7 % thermal conductivity enhancement at temperature of 50 °C. Moreover, Ahmed *et al*. (2017) also stated that MWCNT / graphene nanoplatelets (GNPs) hybrid nanofluid had 43.4 % enhancement of heat transfer coefficient in the mixture of MWCNT and GNPs at concentration of 0.25 wt% of MWCNT and 0.035 wt% of GNP (Ahmed *et al*., 2017).

Nanofluid dispersion and stability of nanofluids is a critical factor in the improvement of thermophysical properties of nanofluids. However, several studies have documented that the dispersion of ultrafine nanoparticles in base fluids is a significant problem in getting stable nanofluids due to the hydrophobic character of nanoparticles that make them arduous to disperse in the base fluids (Yu *et al*., 2012; Amirah *et al*., 2016). Therefore, mechanical techniques (e.g., homogenisation and ultrasonication process) and chemical techniques (e.g., surfactant) are used to solve this problem. The previous research mentioned that using polyvinylpyrrolidone (PVP) surfactant in MWCNT based nanofluids stabilised the nanofluids for more than one month (Fadhillahanafi *et al.*, 2013). Meanwhile, Abdul *et al*. (2015) mentioned that the stability of 0.24 vol% of pristine MWCNT-water based nanofluids is more than 10 days because of high pressure from the homogenisation process. Moreover, stable nanofluids (20:80; EG: DI) has positive outcome for thermal conductivity, which has 0.812 to 17.0 % enhancement, and increases the heat transfer coefficient (Amirah *et al*., 2018).

The low boiling point and high freezing point of deionised water is another problem of base fluids, which causes limitations in thermal properties performance. Due to this, deionised water has disadvantages to be used in cooling and heating systems in some countries that have winter seasons, as deionised water can freeze at 0 °C. Hence, antifreeze solutions or fluid such as methanol and ethylene glycol, which has a low freezing point, can overcome this problem by mixing these fluids. The mixture of deionised water and ethylene glycol as a base fluid in MWCNT nanofluids research is still rarely investigated by the researchers. In addition, MWCNT nanoparticles, which have hydroxyl (-OH) functional group, are also seldom used in nanofluids investigation.

Thus, in this work, the addition of hydroxyl multiwalled carbon nanotube (MWCNT-OH) in base fluid at ratio of 50:50; DI: EG with PVP surfactant has been synthesised using a two-step method to become a nanofluid. The objective of this work is to investigate two thermophysical properties, which are thermal conductivity and heat transfer coefficient, of MWCNT-OH / deionised water-ethylene glycol based nanofluids. It is believed that the addition of MWCNT-OH nanoparticles can enhance and improve the thermal properties of base fluids.

2. METHODOLOGY

2.1 Material Selection

The MWCNT-OH nanoparticles were bought from Nanostructures & Amorphous Material, Inc. The specifications of the MWCNT-OH are presented in Table 1. The PVP used as dispersing agent or surfactant were purchased from Sigma Aldrich Co. It has 1,000 average mol. wt and 1.6 g/cm^3 density. Whilst, ethylene glycol and deionised water were used as base fluid, with the specifications presented in Tables 2 and 3.

Table 1: MWCNT-OH specifications.

Parameter	Specification
Outer diameter	10-30 nm
Inner diameter	5-10 nm
Length	10-30 μm
Density	2.10 g/cm^3
Surface area	40-300 cm^3/g
Melting point	3652-3697 °C

Table 2: QRëC ethylene glycol specification.

Parameter	Specification
Chemical Name	Ethylene Glycol
Other Name	Acetic acid ethyl ester; Acetic ether
Chemical Formula	$C_2H_6O_2$
Molecular Mass	62
Form	Liquid
Colour	Transparent colourless
Purity	Minimum 99.0 %
Melting point	-13 °C
Boiling point	198 °C
Density	1.11 g/cm^3

Table 3: Deionised water specification.

Parameter	Specification
Chemical Name	DI
Resistivity	18 megoohm
Chemical Formula	H_2O
Density	1.00 g/cm^3

2.2 Synthesis of Nanofluids

A two-step preparation process was used in the synthesis of nanofluids, whereby the formulation of all materials was done first before undergoing the next process. Equation 1 is used in the calculation of nanofluid volume. The MWCNT-OH nanoparticles were used from concentration of 0.1 to 1.0 wt%, while the concentration of PVP was 10 % from the MWCNT-OH concentration. Whilst the ratio of base fluid was 50:50; DI: EG. All the materials were mixed via the dispersion process with homogenisation at 10,000 rpm using a Wise Tis HG-15D homogeniser and ultrasonication at 40 kHz using of Branson DTH Ultrasonic Cleaner, and placed in 40 ml bottle. The nanofluid samples were controlled at room temperature and monitored for 100 h to monitor the dispersion and stability of the MWCNT-OH nanofluids. The stable nanofluid samples without any sedimentation formed underwent thermal performance tests, consisting of thermal conductivity and heat transfer coefficient tests. The tests used a TC-KD2 Pro thermal analyser and Pico data logger.

$$Volume = \frac{Weight\ percentage}{Density} \quad (1)$$

3. RESULTS AND DISCUSSION

3.1 Thermal Conductivity Test

The nanofluid samples were tested using a TC-KD2 Pro thermal analyser from Decagon Device, Inc., which uses a KS-1 sensor for measuring the thermal conductivity. The nanofluids were tested at 6, 25 and 40 °C temperature. Meanwhile the temperature of the nanofluids was controlled using a PROTECH 630D refrigerated water bath circulator. First, the nanofluid sample was inserted in a refrigerated water bath until the required temperature was reached. Next, the KS-1 sensor was inserted inside the nanofluids beaker and placed in a perpendicular position to reduce error during the thermal conductivity measurement. Three readings were taken with 15 min gap from each reading as to avoid errors in the measurement.

Figure 1 presents the thermal conductivity of the base fluid (50:50; DI: EG) compared with the American Society of Heating, Refrigerating and Air Conditioning (ASHRAE) thermal conductivity of aqueous solution (50:50; DI: EG) standard, to ensure that the thermal conductivity of that base fluid is matched with the ASHRAE standard. It shows that the thermal conductivity of the base fluid at 6, 25 and 40 °C increases linearly with the increase of temperature. Even though base fluid's thermal conductivity is lower than the ASHRAE standard, it still has the same pattern of results with the ASHRAE thermal conductivity, whereby thermal conductivity increases with temperature. Hence, the thermal conductivity of the base fluid is valid to use as a standard measurement in calculating the performance of MWCNT-OH based nanofluids' thermal conductivity.

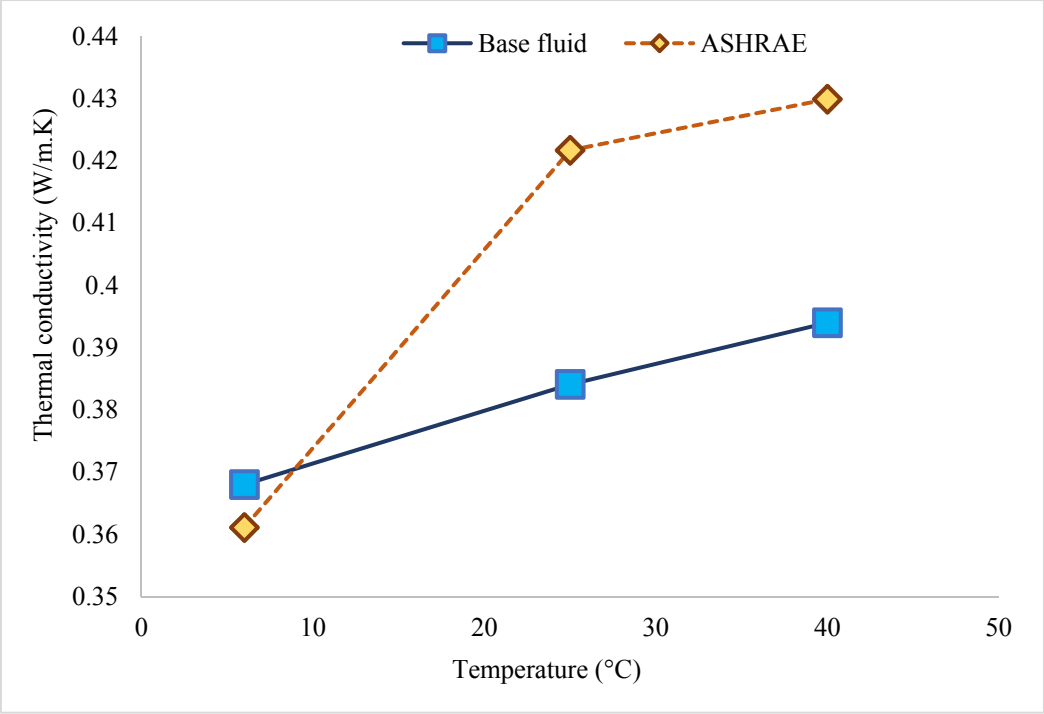

Figure 1: Comparison of the thermal conductivity of the base fluid with the ASHRAE standard.

Figure 2 presents the thermal conductivity of MWCNT-OH based nanofluids in mixture of deionised water and ethylene glycol at ratio 50:50. The straight line at each temperature is the standard thermal conductivity value of the base fluid. These lines are used to determine the MWCNT-OH based nanofluids' thermal conductivity pattern, i.e., either higher or lower than standard base fluid. The standard thermal conductivity values of the base fluid at each temperature are 0.3611, 0.4217 and 0.4299 W/m.K.

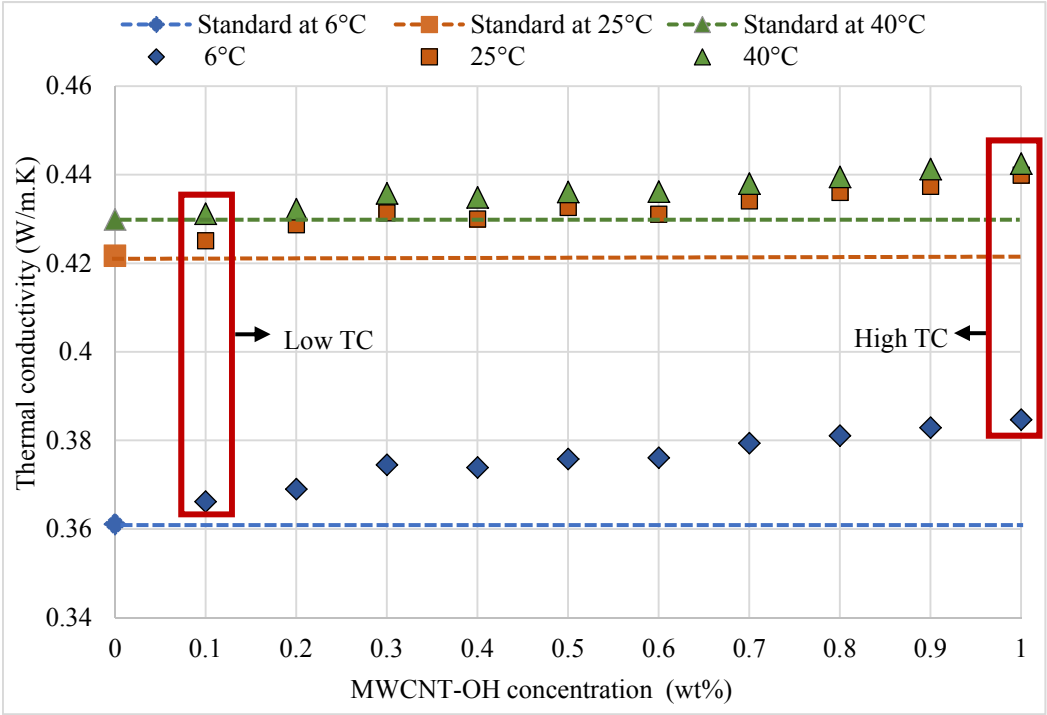

Figure 2: Thermal conductivity of the MWCNT-OH based nanofluids.

The thermal conductivity of MWCNT-OH based nanofluids is higher than the standard base fluid for each concentration and temperature. Based on Figure 2, 0.1 wt% of MWCNT-OH concentration has the lowest thermal conductivity values, which are 0.3662, 0.4251 and 0.4312 W/m.K at 6, 25 and 40 °C. Whilst the highest thermal conductivity occurs at 1.0 wt%. Interestingly, for 0.4 wt%, for each temperature, there is a slight decrement in thermal conductivity values. However, it is still higher than the standard base fluid. The temperature at 40 °C has the highest thermal conductivity, followed by 25 and 6 °C. Hence, the results show that thermal conductivity is influenced by nanoparticle concentration and temperature. Indhuja *et al*. (2013) and Syarifah Norfatin *et al*. (2015) also reported that the increment of nanofluids thermal conductivity is related to high concentration and temperature.

3.1.1 Thermal Conductivity Enhancement

Table 4 presents the percentage of enhancement of thermal conductivity of MWCNT-OH based nanofluids. The percentage enhancement is calculated using the following equation:

$$\%\ Enhancement\ of\ thermal\ conductivity = \left[\frac{T.C\ of\ N.F - T.C\ of\ B.F}{T.C\ of\ B.F}\right] \times 100\% \qquad (2)$$

where:

T.C = Thermal conductivity
N.F = Nanofluid
B.F = Base fluid

Table 4: Thermal conductivity enhancement of MWCNT-OH based nanofluids on 50:50; deionised water: ethylene glycol.

Concentration (wt%)	Thermal conductivity percentage enhancement (%) at different temperature		
	6 °C	25 °C	40 °C
0.1	1.412	0.8063	0.3024
0.2	2.188	1.660	0.535
0.3	3.711	2.300	1.372
0.4	3.545	1.968	1.163
0.5	4.071	2.585	1.442
0.6	4.154	2.229	1.465
0.7	5.068	2.940	1.884
0.8	5.539	3.391	2.233
0.9	6.037	3.723	2.652
1.0	6.536	4.316	2.931

From the results, 0.4 wt% concentration shows slight decrement of thermal conductivity enhancement due to degradation of thermal conductivity value. However, it is still in the positive enhancement trend. The lowest enhancement of thermal conductivity occurs for 0.1 wt% concentration, while the highest is at 1.0 wt%. In addition, temperature of 6 °C has the highest enhancement of thermal conductivity, followed by 25 and 40 °C. The range of thermal conductivity enhancements for MWCNT-OH based nanofluids is from 0.3024 to 6.536 %.

There are several factors that influence the thermal conductivity values, which are nanoparticle characteristics, size of particles and particle interface. The nature of MWCNT-OH nanoparticle characteristics, which has high thermal conductivity value, contributed to the enhancement of thermal conductivity when added into base fluids. It is due to MWCNT-OH being included in the CNT group, which have high thermal conductivity of more than 3,000 W/m.K (Sadik & Anchasa, 2009). In addition, the MWCNT-OH particle size has inner diameter from 5 to 10 nm, while the outer diameter is from 10 to 30 nm and it is tends to have high aspect ratio and surface area (40-300 cm^3/g). This results in increment of thermal conductivity. Such results are supported by studies of Imran Syakir *et al*. (2012), where it is mentioned that high surface area of nanoparticles offers better thermal properties in nanofluids. Meanwhile, particle interface also plays a role in thermal conductivity enhancement because of liquid layering on the solid interface. Ravi & Mabusabu (2013) mentioned that the mixture of nanoparticle and fluid have formed solid-like liquid layers as a thermal bridge and have a tendency to increase thermal conductivity. Mohamed *et al*. (2011) also stated that the atomic arrangement of liquid and solid interface is more effective than bulk liquid.

Moreover, the quantity of PVP surfactant used and the dispersion method also helps in increasing the thermal conductivity. The literature mentioned that small concentration of surfactant used gives a high thermal conductivity rather than a high concentration of surfactant, which causes the decrement of thermal performance (Chen & Xie, 2010; Zhou *et al*., 2012). On the other hand, the dispersion method, which includes homogenisation and sonication processes, is one of the methods to homogenise the MWCNT-OH based nanofluids and provide better thermal properties performance. They tend to break down the bond among nanoparticles in base fluids due to sound waves and electrostatic charge from homogeniser and ultrasonicator, resulting in stable nanofluids. Hence, it can avoid the agglomeration form and increase the thermal properties performance, for both thermal conductivity and heat transfer coefficient (Amirah *et al*., 2016). Imran Syakir *et al*. (2013) found that the addition of nanoparticles increased thermal conductivity because of increment of particle activity and movement in base fluids.

3.2 Heat Transfer Coefficient

For the heat transfer coefficient test, only the three best samples of the MWCNT-OH based nanofluids were selected based on thermal conductivity performance, which were 0.8, 0.9, and 1.0 wt%. Figure 3 shows the schematic diagram of the test. The nanofluids were circulated in the copper pipe, copper coil and fan with the help of a pump at 8 ℓ/min. The objective of using copper pipe and copper coil is to decrease the heat loss to the environment during the experiment. A TC-08 Pico data logger is used to measure the temperature, and the data would be saved automatically in its software. The condition of the nanofluids was assumed as laminar flow, and the Reynolds number was less than 2,300. Table 5 shows the data of some of the variables in this test.

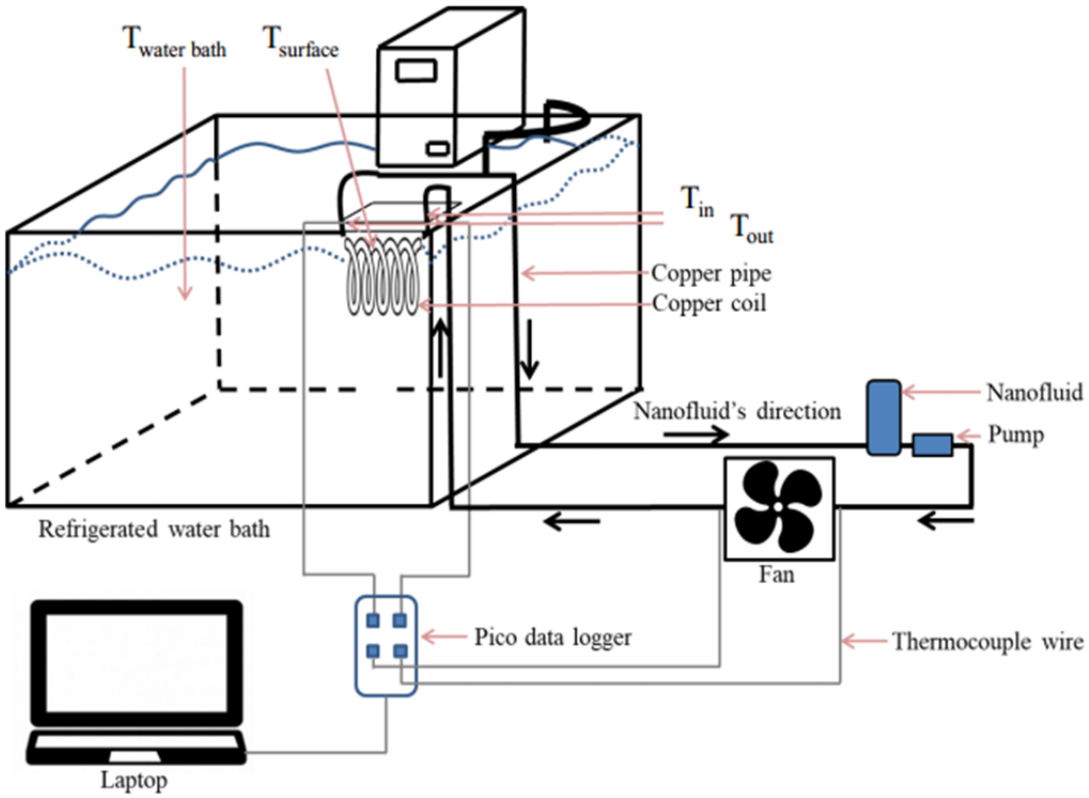

Figure 3: Schematic diagram of the heat transfer coefficient test.

Table 5: Heat transfer coefficient data variables.

Variables	Values
Mass of water	6 kg
Specific heat of water, C_p	4187 J/kg.K
Length of copper coil	2.063 m
Inner diameter of coil	0.0048 m
Outer diameter of coil	0.0064 m
Thickness	0.0016 m
Area of copper coil, A	0.03111 m^2

The following equation was used in calculating the heat transfer coefficient of MWCNT-OH based nanofluids:

$$h = \frac{mC_p\Delta T_1}{A\Delta T_2} \quad (3)$$

where:

ΔT_1 = Temperature difference between water bath and surface ($T_{wb} - T_s$)
ΔT_2 = Logarithmic mean temperature

Figure 4 shows the heat transfer coefficient of MWCNT-OH for 0.8, 0.9 and 1.0 wt% at three different temperatures. Whist 0 wt% shows the heat transfer coefficient value for standard base fluid, which are 121.43, 134.36 and 142.19 kW/m^2.K.

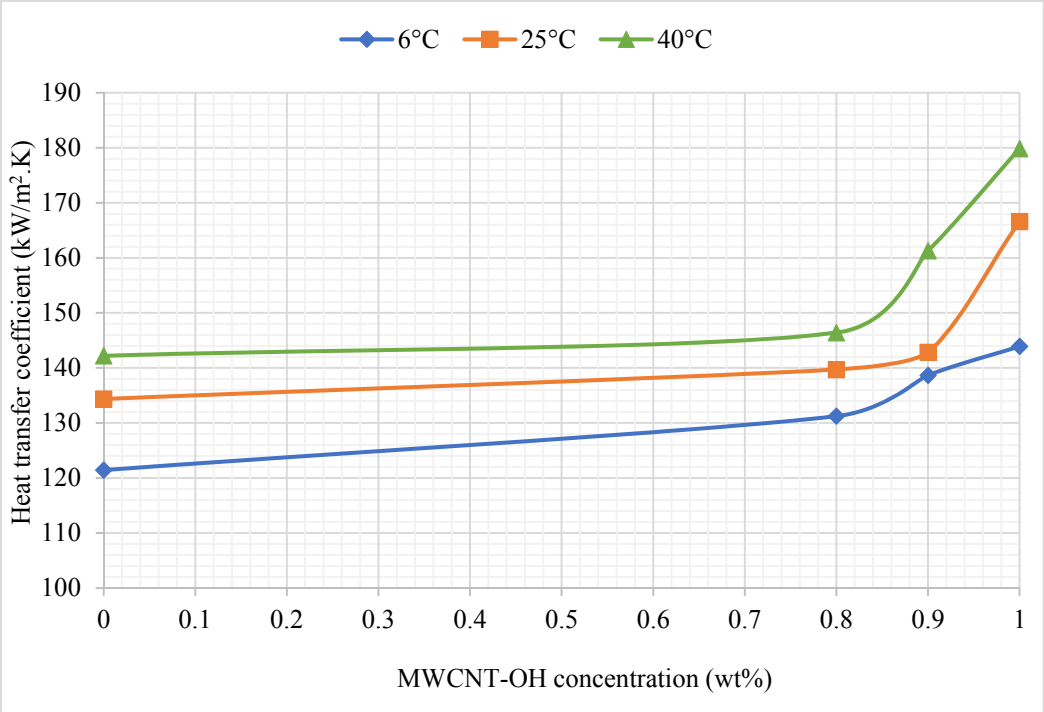

Figure 4: Heat transfer coefficient of MWCNT-OH based nanofluids.

The inclusion of MWCNT-OH nanoparticles in base fluid has shown a positive outcome in which each concentration has a high heat transfer coefficient rather than the standard base fluid heat transfer coefficient. For 1.0 wt% concentration, it has the highest heat transfer coefficient among the other concentrations, which are 143.90, 166.61 and 179.85 kW/m^2.K for temperatures of 6, 25 and 40 °C. Meanwhile, the lowest heat transfer coefficient occurred for 0.8 wt% concentration for each temperature. The trend of the graph is linear increase with temperature and concentration increment. This result is supported by Syazwani *et al*. (2016), where the heat transfer coefficient for carbon nanofiber (CNF) based nanofluids increases when the concentration of nanoparticles is increased.

Table 6 shows the percentage of enhancement of heat transfer coefficient for MWCNT-OH based nanofluids. It is found that the highest enhancement of heat transfer coefficient test occurred at 1.0 wt% MWCNT-OH concentration. Temperature of 40 °C had the highest enhancement of 26.49 %, followed by 25 °C (24 %) and 6 °C (18.51 %). The lowest enhancement occurred at 40 °C for 0.8 wt% concentration, while the second-lowest enhancement was at 25 °C for the same concentration. Meanwhile, 0.9 wt% concentration at 25 °C had third lowest of heat transfer coefficient enhancement of 6.311 %. To conclude, the enhancement of heat transfer coefficient test was from 2.961 to 26.49 %.

Table 6: Percentage of enhancement of the heat transfer coefficient for the MWCNT-OH based nanofluids.

Concentration (wt%)	% Enhancement of heat transfer coefficient (kW/m^2.K) at three different temperatures (°C)		
	6	25	40
0.8	8.070	3.982	2.961
0.9	14.20	6.311	13.42
1.0	18.51	24.00	26.49

However, this experiment had 40 °C as maximum temperature. This is because of the temperature limitation on the apparatus used and surfactant. High temperatures above than 40 °C can damage the surfactant and decrease the thermal performances of MWCNT-OH based nanofluids. It is not practical to increase the temperature and MWCNT-OH concentration when the result is negative and needs more pumping power to flow the nanofluids through the pipe. As mentioned earlier, the pump power is only 8 ℓ/min. In this experiment, the functionalised (-OH) group in the MWCNT surface can transfer more energy to nanofluids through the increment temperature and come out with high heat transfer coefficient (Sedigheh *et al*., 2015). Whilst the high dispersion and distribution of MWCNT-OH nanoparticles in base fluids cause interactions and collisions among particles to occur and enhance the heat transfer coefficient (Xuan & Li, 2003; Ravi & Mabusabu, 2013). It is due to energy transport that occurs among solid particles and fluid particles during the collision. Additionally, thermal conductivity has a strong link with heat transfer coefficient, with excellent thermal conductivity giving a better heat transfer coefficient (Imran Syakir *et al*., 2012). Thus, it is demonstrated from this study that 0.8, 0.9 and 1.0 wt% have high thermal conductivity values and produce high heat transfer coefficient performance. Hence, the good enhancement on thermal properties of MWCNT-OH based nanofluids can replace the lower thermal properties of base fluids and be used in their applications, such as computer central processing unit (CPU) cooling and air conditioning.

In the heat transfer coefficient, the Nusselt number can be used to measure the performance of heat transfer, whereby high value of Nusselt number indicates effective heat transfer coefficient. Equation 4 is used in calculating the Nusselt number. Meanwhile, Table 7 shows the Nusselt numbers for 0.8, 0.9 and 1.0 wt% of MWCNT-OH based nanofluids for temperatures of 6, 25 and 40 °C.

$$Nusselt\ number, Nu = \frac{h\,D}{k} \tag{4}$$

where:

h = Heat transfer coefficient of nanofluid
D = Diameter of copper pipe
k = Thermal conductivity of nanofluid

Table 7: Nusselt numbers for the MWCNT-OH based nanofluids.

Concentration (wt%)	Nusselt number at three different temperatures (°C)		
	6	25	40
Standard	1614.13	1529.35	1587.61
0.8	1652.86	1538.09	1598.91
0.9	1738.35	1567.52	1754.1
1.0	1795.60	1817.98	1950.92

The table shows that all the Nusselt numbers for the MWCNT-OH based nanofluids for each concentration are higher than the standard base fluid. In addition, 1.0 wt% at 40 °C has the highest Nusselt number, which is 1950.92, followed by 25 and 6 °C at the same concentration. Typically, the Nusselt number for water is 3.66. Interestingly, the Nusselt number for the MWCNT-OH based nanofluids is high compared to water and standard base fluid. Hence, it proves that the nanofluids have effective heat transfer coefficient.

The heat transfer coefficient value is related to the Nusselt number, where a high heat transfer coefficient gives a better Nusselt number (Amirah *et al*., 2018). The diameter of the coil has a relation in enhancing the heat transfer coefficient and Nusselt number, which can be seen in Equations 3 and 4, where both equations need diameter in their calculations. Thus, the smaller diameter of the coil (0.0048 m) has the power to enhance the heat transfer coefficient and Nusselt number due to high surface area. It is the same concept with the small size of nanoparticles, which have high surface area and a tendency to increase the thermal properties performance.

4. CONCLUSION

MWCNT-OH based nanofluids were studied on their thermal properties, which are thermal conductivity and heat transfer coefficient. As a result, the seeding of MWCNT-OH nanoparticles in base fluids improved the thermal conductivity and heat transfer coefficient performances. This study revealed that thermal properties depend on temperature and nanoparticle concentration, with high temperature and concentration giving high enhancement of thermal conductivity and heat transfer coefficient values.

Thermal conductivity has the highest increment for concentration of 1.0 wt% at each temperature (6, 25 and 40 °C). Moreover, the temperature of 6 °C had the highest enhancement by as much as 6.536 % as compared to the other temperatures. Even though 0.1 wt% of MWCNT-OH concentration had the lowest thermal conductivity performance, it is still higher than standard base fluid. The factors that contributed to thermal conductivity increment include the high thermal conductivity of MWCNT-OH nanoparticles, small particle size with high aspect ratio and surface area, as well as particle interface among solid particles and fluid particles. In addition, a small quantity of PVP surfactant and dispersion method, which can avoid agglomeration form, also influenced the thermal conductivity performance. Whilst particle activity and movement in fluids by insertion of nanoparticles also caused the thermal conductivity to increase.

For the heat transfer coefficient test, the addition of nanoparticles gave heat transfer coefficient enhancement of 2.961 to 26.49 %. The factors of the functionalised group (-OH) attached on nanoparticles surface, collision among particles, and relation of thermal conductivity and heat transfer coefficient affected the heat transfer coefficient, which increases the heat transfer property. In addition, high value of heat transfer coefficient resulted in Nusselt number that was higher than the standard base fluid. Furthermore, the small diameter of the coil, which has high surface area also caused the heat transfer coefficient to increase.

To conclude, the inclusion of MWCNT-OH nanoparticles in base fluids have proved to increase of thermal conductivity and heat transfer coefficient performance.

ACKNOWLEDGEMENT

The authors acknowledge University Teknikal Malaysia Melaka (UTeM) and Ministry Higher Education (MoHE) for providing the necessary funding and supporting this research under FRGS/ 2010/FKM /SG-03/1 -F0076 and FRGS/2/2013/SG02/UTeM/02/1 research grant. In addition, the first author would like to extend her gratitude to UTeM for the financial support provided through the Research University Zamalah Scholarship.

REFERENCES

Abdolbaqi, M.K., Nor Azwadi, C.S., Rizalman, M., Azmi, W.H. & Gholamhassan, N. (2015). Nanofluids heat transfer enhancement through straight channel under turbulent flow. *Int. J. Auto Mech. Eng*., **11**: 2294-2305.

Abdul, O.C.G., Antônio Remi, K.H. & Enio, P.B.F. (2015). Experimental evaluation of CNT nanofluids in single-phase flow. *Int. J. Heat Mass Transf.*, **86**: 277–287.

Ahmed, A.H., Mohd Zulkfly, A., Nadiahnor, M.Y., Al-Nimr, M.A., Muataz, A.A. & Mohammad, M. (2017). Experimental on forced convective heat transfer enhancement using MWCNTs/ GNPs hybrid nanofluid and mini-tube. *Int. J. Heat Mass Transf*., **115**: 1121-1131.

Amirah, A., Imran Syakir, M., Ahmad Yusairi, B.H., Norli, A., Poh Ban, W., Mohamed Hafiz, M.I. & Syazwani, Z.A. (2016). Thermal conductivity and viscosity of deionised water and ethylene glycol-based nanofluids. *J. Mech. Sci.*, **10**: 2249-2261.

Amirah, A., Imran Syakir, M., Nor Azmmi, M. & Syazwani, Z.A. (2018). Thermal properties characteristics of MWCNT-OH based nanofluids in mixture of ethylene glycol and deionised water. *J. Mech. Eng.*, **15**: 53-71.

Chen, L. & Xie, H. (2010). Surfactant-free nanofluids containing double and single-walled carbon nanotubes functionalized by a wet-mechanochemical reaction. *Thermo. Act*., **497**: 67-71.

Chung, J.N., Chen, T. & Maroo, S.C. (2011). A review of recent progress on nano/micro scale nuclate boiling fundamentals. *Front. Heat Mass Transf.*, **2**: 1-15.

Fadillahanafi, N.M., Leong, K.Y. & Risby, M.S. (2013). Stability and thermal conductivity characteristics of carbon nanotubes based nanofluids. *Int. J. Auto Mech. Eng.,* **8**: 1376-1384.

Imran Syakir, M., Chitrambalam, S.T. & Hamid, S.B.A. (2012). Investigation on the thermo-physical properties of nanofluids-based carbon nanofibers under modified testing conditions. *Int. J. Nanoelectro. Mater.,* **5**: 25-30.

Imran Syakir, M., Chitrambalam, S.T. & Hamid, S.B.A., Chin, W.M., Yau, K.H. & Idral, F. (2013). A comparison study on the heat transfer behaviour of aqueous suspensions of rod-shaped carbon nanotubes with commercial carbon nanotubes. *Adv. Mater. Res*., **667**: 35-42.

Indhuja, A., Kuppusamy, S.S., Sivasubramaniam, M. & Kalpoondi, S.R. (2013). Viscosity and thermal conductivity of dispersions of gum arabic capped MWCNT in water, influence of MWCNT concentration and temperature. *J. Taiwan Inst. Chem. Eng*., **44**: 474-479.

Kanagaraj, S., Varanda, F.R., Oliveira, M.S.A. & Simões, J.A.O. (2006). Theoretical model development for nanofluids thermal effectiveness. *Defect Diff. Forum*., **258-260**: 164-171.

Kumaresan, V., Velraj, R. & Das, S.K. (2012). Convective heat transfer characteristics of secondary refrigerant based CNT nanofluids in a tubular heat exchanger. *Int. J. Ref*., **35**: 2287-2296.

Marquis, F.D.S. & Chibante, F. (2005). Improving the heat transfer of nanofluids and nanolubricants with carbon nanotubes. *J. Miner. Metal. Mater. Soc*., **57**: 32-43.

Mehdi, S. & Masoud, A. (2016). Thermal conductivity enhancement of COOH-functionalized MWCNTs/ethylene glycol-water nanofluid for application in heating and cooling systems. *Appl. Therm. Eng*., **105**: 716-723.

Mohammed, H.A., Bhaskaran, G., Shuaib, N.H. & Saidur, R. (2011). Heat transfer and fluid flow characteristics in microchannels heat exchanger using nanofluids: a review. *Renew. Sustain. Energy. Rev.*, **15**: 1502-1512.

Rahul, B. & Basavaraj, S.K. (2013). A review on applications and challenges of nanofluids as coolant in automobile radiator. *Int. J. Sci. Res. Pub.,* **3**: 1-10.

Ravi, V. & Mabusabu. (2013). A study on heat transfer characteristics of ethylene glycol based nanofluids and carbon nanotube mixture in nucleate pool boiling. *Int. J. Mech. Eng. Res. Appl*., **1:** 28-33.

Sadik, K. & Anchasa, P. (2009). Review of convective heat transfer enhancement with nanofluids. *Int. J. Heat Mass Transf.*, **52**: 3187-3196.

Sayantan, M. & Somjit, P. (2013). Preparation and stability of nanofluids-a review. *IOSR- J. Mech Civil Eng*., **9**: 63-69.

Sedigheh, A., Seyed Mojtaba, Z., Seyed Hossein, N.B., Abbas, Y. & Mehri-Saddat, E.K. (2015) Thermal conductivity of water based nanofluids containing decorated multiwalled carbon nanotubes with different amount of TiO_2 nanoparticles. *Iran. J. Chem. Eng.*, **12**: 30-40.

Syarifah Norfatin, S.I., Nor Salihah, Z., Imran Syakir, M., Norli, A. & Mohd Haizal, M.H. (2015). Comparison of thermal conductivity for HHT-24 CNF based nanofluid using deionised water and ethylene glycol. *J. Tek.,* **77**: 85-89.

Wu, Z., Feng, Z., Bengt, S. & Lars, W. (2014). A comparative study on thermal conductivity and rheology properties of alumina and multi-walled carbon nanotube nanofluids. *Front. Heat Mass Transf*., **5**: 1-10.

Xuan, Y. & Li, Q. (2003). Investigation on convective heat transfer and flow features of nanofluids. *J. Heat Transf*., **125**: 151-155.

Yu, W. & Xie, H. (2012). A review on nanofluids: preparation, stability mechanisms, and applications. *J. Nanomater.,* **2012**: 1-17.

Zhou, M.Z., Xia, G.D., Chai, L.J.L. & Zhou, L.J. (2012). Analysis of factors influencing thermal conductivity and viscosity in different kinds of surfactant solutions. *Exp. Therm. Fluid Sci.,* **36**: 22-29.

THERMAL AND MELT FLOW BEHAVIOUR OF KENAF FIBRE REINFORCED ACRYLONITRILE BUTADIENE STYRENE COMPOSITES FOR FUSED FILAMENT FABRICATION

Syaza Najwa Mohd Farhan Han[1,3], Mastura Mohammad Taha[2,3*] & Muhd Ridzuan Mansor[1,3]

[1]Fakulti Kejuruteraan Mekanikal
[2] Fakulti Teknologi Kejuruteraan Mekanikal dan Pembuatan
[3] Centre for Advanced Research on Energy
Universiti Teknikal Malaysia Melaka (UTeM), Malaysia

*Email: mastura.taha@utem.edu.my

ABSTRACT

The thermal and melt flow behaviour of polymer and fibre materials are vital in producing filaments for fused filament fabrication (FFF), especially for custom-made composites materials. The degradation temperature and melting temperature of commercialised acrylonitrile butadiene styrene (ABS) filament, neat ABS polymer and different loadings of kenaf fibre (KF) reinforced ABS composites were investigated using thermogravimetric analysis (TGA) and differential scanning calorimetry (DSC) respectively. Melt flow index (MFI) was then investigated in view of the viscosity of the materials using a melt flow indexer at 230 °C and 5 kg weight loading. The kenaf fibre reinforced ABS composites were prepared using an internal mixer at 180 °C and crushed to the form of granules. It was found that the addition of kenaf fibre lowered the decomposition temperature and increased the melting temperature of composites as compared to the neat ABS polymer (0% KF – ABS). Meanwhile, the neat ABS polymer had higher value of MFI as compared to the commercialised ABS filament. The value of MFI increased as the kenaf fibre loading increases. Thus, the neat ABS polymer and kenaf fibre reinforced polymer composites are suitable as feedstock filament material for FFF since the low viscosity of commercialised ABS filament is able to be printed from open-source 3D printers.

Keywords: *Fused filament fabrication (FFF); natural fibre composites; melt flow behaviour; thermal properties; kenaf fibre.*

1. INTRODUCTION

Fused filament fabrication (FFF) is the one of the most significant techniques for additive manufacturing (AM) and recently, has been widely used in aerospace (Kumar & Nair, 2017), automotive (Page, 2018), medical (Wang *et al*., 2017) and defence (Rathee *et al*., 2017) industries. The applications of AM in defence support services are to provide platforms with the ability to sustain their systems, recover their ability after damage and reduce costs in the supply chain (Busachi *et al*., 2015). In addition, AM manufactures military personnel equipment, such as body armours kit and special tools for mission requirements (Busachi *et al*., 2016). AM has also contributed to defence support services for the Royal Navy's platforms (Busachi *et al*., 2017). FFF is commonly used in producing conceptual models, prototypes and engineering components (Mohan *et al*., 2017). A three-dimensional object can be produced by successive layer upon layer of materials, where a filament is melted inside a liquefier at a temperature above its melting point and pushed at the nozzle die by solid upstream filament (Carneiro *et al*., 2015). The schematic set up of FFF is shown in Figure 1. It is used for its simple fabrication process (Maasod & Song, 2004), ability to fabricate geometrically complex shapes (MacDonald & Wicker, 2016), less expensive machining (Wong & Hernandez, 2012) and cost-effectiveness (Mohan *et al*., 2017), especially for defence industries in producing weapons (Busachi *et al*., 2016). Besides that, FFF produces less waste material (Grujovic *et al*., 2017).

Thermoplastics are commercial material filaments, such as acrylonitrile butadiene styrene (ABS), polylactic acid (PLA) and polycarbonate (PC), used in FFF for producing three-dimensional printed parts. McMains (2005) stated that thermoplastic filament is used for FFF as it is safer to maintain and less expensive. Wang *et al*. (2017) indicated that custom-made composite material filaments are possible to be used as feedstock material for FFF. However, custom-made composite material is limited to the suitability of melt viscosity since the molten viscosity should be high enough to provide structural support and low enough to enable extrusion (Wang *et al*., 2017).

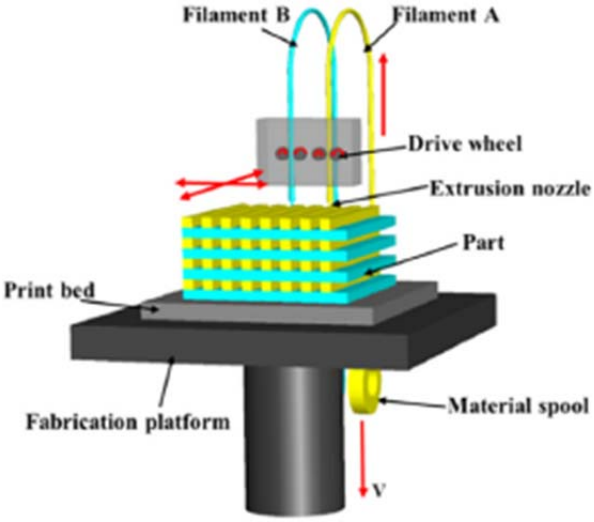

Figure 1: Schematic of FFF setup (Wang *et al*., 2017).

Nowadays, natural fibre reinforced composite (NFRC) materials have been well developed in industries. NFRC is a composite material consisting of polymer matrix with natural fibres. NFRC is widely used in numerous applications due to its lightweight properties, low cost, less damage to processing equipment, biodegradability and good relative mechanical properties (Mohammed *et al*., 2015). Currently, natural fibres have been widely used to replace synthetic or man-made fibres in engineering applications. The advantages of natural fibres, such as low cost, abundantly available, environmentally friendly, low density and higher strength performance, are the reasons that they have been chosen over synthetic fibres (Ahmad *et al*., 2015). There are numerous types of natural fibres used as reinforcement for thermoplastics, such as flax, hemp, jute, coir, kenaf and wood. However, the drawback of natural fibres, such as short lifetime, albeit with minimum environmental damage upon degradation (Mohammed *et al*., 2015), and restricted processing temperature, limit their performance and usage (Gallo *et al*., 2013). Recently, experimentation and investigation of NFRC filaments for FFF technology have been growing along with concerns and awareness on environmental friendly materials. However, the melt flow behaviour of NFRC materials is one of the main issues for FFF. Ramanath *et al*. (2008) stated that melt flow behaviour apparently affects the quality of printed specimens, which depends on pressure, temperature and physical properties, including melting temperature and rheology behaviour.

Up to now, several studies have been conducted on the melt flow behaviour of polymers and NFRC. Singh *et al*. (2016) studied the melt flow behaviour of ABS extrusion grade (ABS-EG) and ABS P400. ABS-EG was selected as an alternative material for FFF filaments, as it is commercially available. The ASTM-D-1238-95 standard was applied for 10 min at 230 °C barrel temperature and 3.8 kg load. The results obtained indicate that the melt flow index (MFI) of ABS-EG and ABS P400 were almost similar, which were 2.381 and 2.398 gm/10 min respectively. Then, both the ABS-EG and ABS P400 filaments were tested using a scanning electron microscope (SEM). The results from the SEM showed that fabricated filaments of ABS-EG contain a lot of air pockets as compared to ABS P400, where there is no presence of air pockets. The study concluded that the fabricated filaments are affected by process parameters of extrusion, including screw speed and barrel

temperature. Islam *et al*. (2013a, b) investigated the MFI of kenaf fibre reinforced recycled polypropylene (RPP) using a MFI tester (Dynisco Instrument) at 230 °C with standard weight of 2.16 kg. Three experiments were conducted, which were RPP; 10%, 20%, 30%, 40% and 50% of raw kenaf fibre RPP (RKPC); and raw kenaf fibre with maleic anhydride grafted polypropylene (MAPP) reinforced RPP (MRKPC). The results of the MFI obtained for RPP; 10%, 20%, 30%, 40, 50% of RKPCP; and MRKPC were 5.58, 2.54, 1.78, 0.46, 0.40, 0.22 and 0.33 g/10 min respectively. The reduction of flow properties for RKPCP was due to the presence of kenaf fibre, whereas MRKPC had the lowest flow due to the presence of MAPP. They also found that the molecular weight of composites and viscosity had an indirect relationship. The results indicated that the higher the percentage of fibre in composites, the more viscous was their melts. Similarly, Mohammad & Arsad (2013) reported that as the loading of kenaf fibre in composites increased, the viscosity increased because the molecular weight of composites increased.

The disadvantages of natural fibre, such as low thermal stability, limit the usage of NFRC for FFF. Torrado *et al*. (2015) investigated the effect of jute fibre reinforced ABS composites on FFF and found that the high temperature of the extrusion process can cause decomposition of jute fibre. Montalvo *et al*. (2018) studied on wood plastic composites (WPC) and found that the decomposition of WPC is between 300 and 500 °C. Therefore, it is vital to study the thermal stability of NFRC before the NFRC filament is produced and extruded on FFF.

The aim of this study is to investigate the thermal degradation temperature, melting temperature, glass transition temperature and melt flow behaviour of commercialised ABS filaments, neat ABS, as well as different loadings of kenaf fibre reinforced ABS composites using thermogravimetric analysis (TGA), differential scanning calorimetry (DSC) and melt flow indexing.

2. MATERIALS AND METHODOLOGY

2.1 Materials

Kenaf (*Hibiscus Cannabinus*) flour core fibres were supplied by ZHF Industries Sdn. Bhd, while ABS pellets (100% pure) were supplied by Macrocom (M) Sdn. Bhd. Commercialised ABS filaments was obtained from a 3D printer supplier.

2.2 Preparation of the Blends

A sieve shaker was used to obtain an average length of 150 μm for the kenaf fibre flour. The ABS pellets and kenaf fibre were dried in an oven at 80 °C for 24 h before being mixed in an internal mixture. The blends were made by mixing ABS with different percentages of kenaf fibre (KF), which were 0, 2.5 and 5 wt.%, which identified as 0% KF – ABS (neat ABS), 2.5% KF – ABS and 5% KF – ABS respectively. A HAAKE Rheomix OS internal mixer was used to mix 2.5% KF – ABS and 5% KF – ABS. The mixture was mixed at 180 °C and 50 rpm for 12 min for each mixing, with a maximum of 50 g allowed for each mixing. First, the ABS pellets were fed into the internal mixer for 5 min and then, the kenaf powder was added into the mixer. Then, a crusher machine was used to crush the composite materials into the form of granules, while the ABS commercialised filaments were cut into 3 mm length.

2.3 Thermal Gravimetric Analysis (TGA)

The instrument used for the TGA test was a Mettler Toledo TGA. The temperature used for the samples is 25 to 550 °C with heating rate of 10 °C/min and the atmosphere used was nitrogen gas. The granules with 2.5% KF – ABS and 5% KF – ABS were weighed to be between 5 – 15 mg and placed in the chamber. The TGA test was conducted to measure the change in mass of the sample as a

function of increasing temperature and the final residue yield on set from degradation of temperature was recorded.

2.4 Differential Scanning Calorimetry (DCS)

The instrument used for the DSC test was a DSC 4000 system. The samples were weighed to be around 5 to 10 mg with 10 °C/ min heating rate. Measurements of melting temperature (T_m) and glass transition temperature (T_g) were recorded as a function of temperature in the range of 30 – 250 °C, and calculated by analysing the different peaks obtained from the graphs.

2.5 Melt Flow Index (MFI)

The MFI was determined using a melt flow indexer (Ray Ran- 6MPCA advanced melt flow system). The melt flow properties of the polymer and composites were measured at temperature of 230 °C with weight loading weight of 5 kg. All the samples were measured for weight of 12 g. Then, 300 s of pre-heating was conducted when samples were fed into instrument's chamber.

3. RESULTS AND DISCUSSION

3.1 Thermogravimetric Analysis (TGA)

The TGA analysis of the commercialised ABS filament, 0% KF – ABS, 2.5% KF – ABS and 5% KF – ABS are presented in Figure 2. Table 1 summarises the TGA results of decomposition temperature and final weight after decomposition. The commercialised ABS filament decomposition temperature was slightly higher as compared to 0% KF – ABS by 1.26%. On the other hand, 0% KF – ABS had higher decomposition temperature as compared to 2.5% KF – ABS and 5% KF – ABS. Figure 5 shows that the increase of fibres decreased the thermal stability as compared to the 0% KF – ABS.

It is found that the thermal stability of kenaf fibre was the lowest with 314.53 °C for decomposition temperature. The overall weight loss of kenaf fibre could be divided into three different phases. For the first phase, weight loss of approximately 6% from initial weight occurred at below 100 °C. The second weight loss of 12.5% occurred at around 260 °C, where this was the initial stage of thermal degradation. The final phase is referred to as major thermal degradation, which occurred with maximum weight loss at 325 °C. The weight loss occurred due to the vaporisation from fibre and decomposition of cellulose (Fauzi *et al*., 2016). As the content of kenaf fibre was increased, the decomposition temperature of the composites decreased since kenaf fibre has low thermal stability as compare to ABS polymer. Both formulations of kenaf fibre reinforced ABS composites also degraded in three phases. For 2.5% KF – ABS, in the first degradation phase, the moisture evaporation started at 250 °C and ended at 348 °C. The second decomposition phase occurred in the range between 370 and 460 °C, while the third phase was between 465 and 490 °C. For 5% KF – ABS, the first decomposition phase occurred between 240 and 340 °C, the second phase was between 350 and 450°C, while the third phase was between 450 and 480 °C. The decomposition steps for kenaf fibre reinforced ABS composites was a very rapid and complicated process.

These results are supported by Azwa & Yousif (2013), where the addition of natural fibre in composites cause the thermal stability to reduce due to less stable fibres. Similarly, Tawakkal *et al*. (2014) studied the effect of kenaf fibre loading reinforced PLA composites on thermal properties and concluded that decreasing trend of degradation temperature for TGA curves of kenaf / PLA composites were found with increasing kenaf content. El-Shekeil *et al*. (2014) investigated the influence of fibre content on thermal properties of kenaf fibre reinforced poly (vinyl chloride) / thermoplastic polyurethane poly-blend composites and found that composites with lower fibre content

had a higher thermal stability as compared to higher fibre contents. The increasing percentage of fibre lowers the thermal stability due weakening of hydrogen bonding and decrease of mobility of cellulose chains in cellulose (Aji *et al.*, 2011).

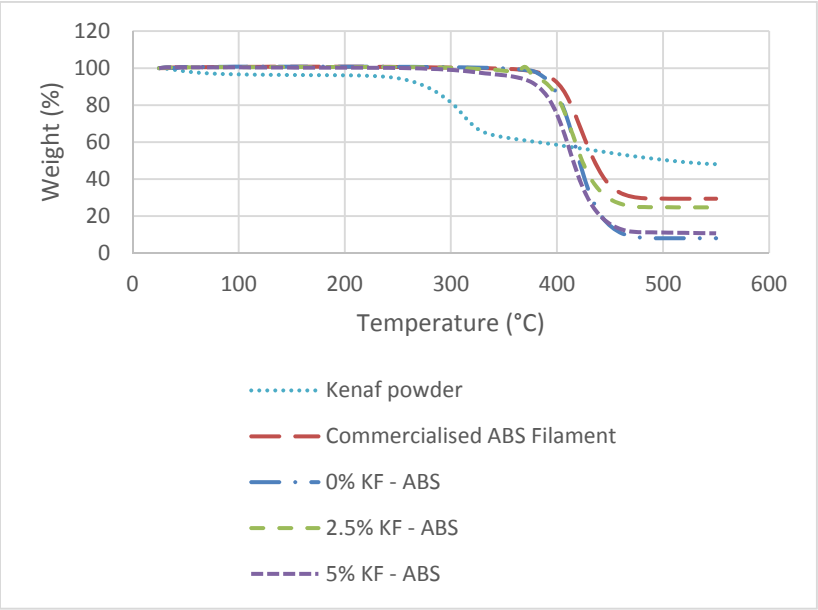

Figure 2: TGA curves.

Table 1: Results of the TGA test.

Materials	Decomposition temperature (°C)	Final weight after decomposition (%)
Kenaf powder	314.53	8.36
Commercialised ABS filament	425.16	4.60
0% KF – ABS	419.83	2.65
2.5% KF – ABS	417.94	3.34
5% KF – ABS	410.39	3.46

3.2 Differential Scanning Calorimetry

Table 2 shows the melting temperature (T_m) and glass transition temperature (T_g) for the commercialised ABS filament, 0% KF – ABS, 2.5% KF – ABS and 5% KF – ABS. The results show that the addition of kenaf fibre increased the Tm of the composites as compared to the 0% KF – ABS., while the Tm of the commercialised ABS was lower than the 0% KF – ABS. The T_g of the 0% KF – ABS increased as the content of kenaf fibre increased, with the commercialised ABS filament giving the highest Tg.

Table 2: Results of the DSC test.

Materials	Melting temperature, T_m (°C)	Glass transition temperature, T_g (°C)
Commercialised ABS filament	213.67	108.46
0% KF – ABS	220.17	100.28
2.5% KF – ABS	222.50	102.43
5% KF – ABS	221.83	107.62

3.3 Melt Flow Behaviour

MFI indicates how fast a material flows in the molten state and is inversely proportional to viscosity. The MFI of commercialised ABS filament and different loadings of kenaf fibre reinforced polymer composites are shown in Figure 3. The commercialised ABS filament had the lowest MFI value, whereas the 0% KF – ABS had the highest value of MFI. The addition of 2.5% KF - ABS decreased the value of MFI, whereas the MFI for 5% KF – ABS increased. The MFI values of the composites increased as the filler loading increased. This is because the presence of kenaf fibre hindered the flowability of the ABS matrix. Lim *et al*. (2015) found that the presence of irregular shapes of natural filler provides an obstruction to the polymer melts of composites. Thus, it leads to lower MFI values for composites as compared to neat polymers. Meanwhile, another study found that the MFI values of composites are much higher than neat polymers due to the orientation of fibre along the flow lines with high aspect ratio (Tayfun *et al*., 2016).

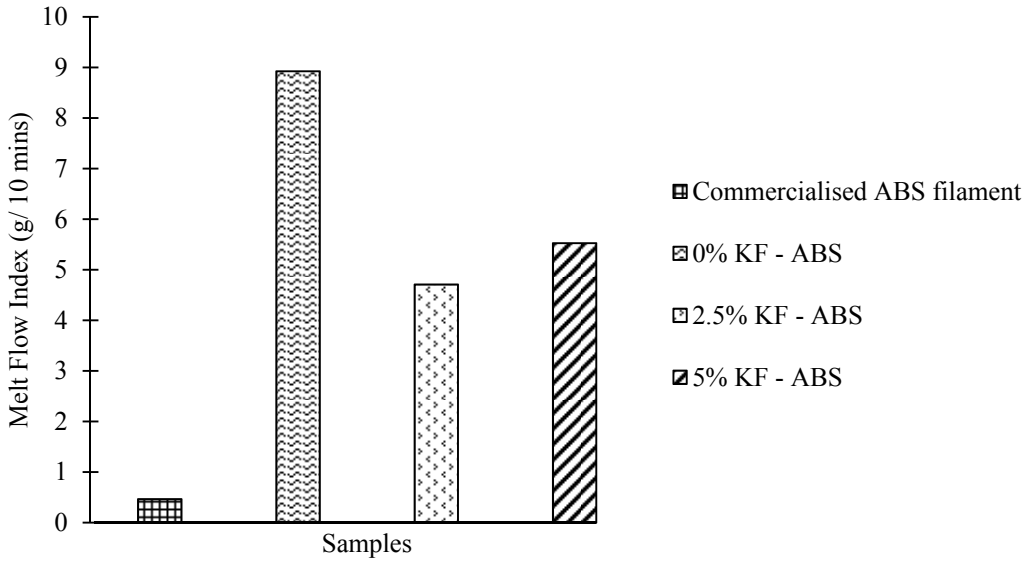

Figure 3: MFI of the ABS polymer and composites.

A higher MFI value indicates an easier flow of material through the dies, which is a low viscosity fluid, while a low MFI indicates as high viscosity fluid (Sa'ude *et al*., 2016). The commercialised ABS filament had the lowest value of MFI as compared to other samples, indicating high viscosity of its fluid. However, the commercialised ABS filament can be printed well via a 3D printer with no clogging at the nozzle. These results contradict with Khaliq *et al*. (2017), where they obtained lower viscosity for commercialised ABS filament. They stated that different ABS filaments will give different viscosities, either low or high, due to material composition. Thus, it indicates that neat ABS polymer and kenaf fibre reinforced polymer composites are suitable as feedstock filament since their low viscosities allow them to be able to be printed using open source 3D printers. In addition, a lower viscosity material is the best for the printing process in 3D printers, but the process parameters of 3D printer can be optimised to obtain the good printing quality by adjusting the speed of extrusion. This condition can enhance the effective heating process, which corresponds to lower viscosity (Khaliq *et al*., 2017).

Han *et al*. (2012) concluded that the strength of kenaf composites is enhanced because of the lower viscosity of polymer matrix, which allows for better wetting of fibres and enhanced strength of composites. The mechanism for enhancement of the strength of composites is closely related to fibre-polymer surface adhesion without considering the chemical treatment. Tayfun *et al*. (2016) investigated the surface modification of fibre by alkaline and silane treatments, and found that the MFI of rice straw and thermoplastic polyurethane (RS-TPU) composites were much higher as compared to neat TPU polymer. Meanwhile, Kim (2015) found that the adhesion between natural fibre and polymer matrix is hindered by lignin and volatile extractives, which leads to poor adhesion of composites between fibre and matrix. This study suggested an addition of coupling agent to increase the contact of surface area between natural fibre and polymer matrix. Based on the observation from SEM, they found that addition of maleic anhydride grafted polypropylene copolymer (MA-g-PP) into kenaf filled PP composites increased the interfacial adhesion as compared to kenaf filled PP composites without MA-g-PP. However, the addition of MA-g-PP into composites decreased the value of MFI as compared to composites without MA-g-PP, which had higher value of MFI. Similarly, Noranizan & Ahmad (2012) reported that treated kenaf fibre with alkaline treatment and compatibiliser improved the interaction of kenaf and high-density polyethylene (HDPE) composites as compared to untreated kenaf fibre. In this investigation, the viscosity of treated kenaf fibre and compatibiliser with HDPE composites was higher as compared to untreated kenaf fibre with increase of fibre loading. Wang *et al*. (2018) concluded that materials that have lower MFI have higher average molar mass. As the filler loading of fibre increases, the viscosity of the composite will increase. Thus, high average molar mass can affect the melt viscosity of the material.

4. CONCLUSION

In conclusion, the thermal and melt flow properties of kenaf fibre reinforced ABS composites were studied and compared with 0% KF – ABS polymer and commercialised ABS filament for FFF applications. The addition of kenaf fibre lowered the decomposition temperature of composites, whereas it increased the melting and glass transition temperatures of the composites. The MFI value of 0% KF – ABS was higher as compared to the commercialised ABS filament. The high viscosity of the commercialised ABS filament is due to the high molecular weight, leading to low value of MFI. The addition of kenaf fibre with ABS polymer reduced the MFI value, but the value of MFI increased with higher loading of kenaf fibre. The mechanism of rheology behaviour reflects the change in molecular weight and the interaction among components. Thus, the viscosity of the composites was affected by the amount of kenaf fibre.

ACKNOWLEDGEMENT

The authors would like to acknowledge the Faculty of Mechanical Engineering, and Faculty of Mechanical and Manufacturing Engineering Technology of Universiti Teknikal Malaysia Melaka (UTeM) and the financial supports provided through grant no PJP/2018/FTK(4A)/S01594.

REFERENCES

Ahmad, F., Choi, H.S. & Park, M.K. (2015). A review: Natural fibre composites selection in view of mechanical, light weight, and economic properties. *Macromolecular Mater. Eng.*, **300**: 10-24.

Aji, I.S., Zainudin, E.S., Khalina, A., Sapuan, S.M. & Khairul, M.D. (2011). Thermal property determination of hybridized kenaf/PALF reinforced HDPE composite by thermogravimetric analysis. *J. Therm. Anal. Calorim.*, **109**: 893-900.

Azwa, Z.N. & Yousif, B.F. (2013). Thermal degradation study of kenaf fibre/epoxy composites using thermo gravimetric analysis. In *Proc. 3rd Malaysian Postgrad. Conf. (MPC 2013)*, pp. 256-264.

Busachi, A., Erkoyuncu, J., Colegrove, P., Drake, R., Watts, C. & Martina, F. (2016). Defining next-generation additive manufacturing applications for the ministry of defence (MoD). *Procedia CIRP*, **55**: 302-307.

Busachi, A., Erkoyuncu, J., Colegrove, P., Drake, R., Watts, C. & Wilding, S. (2018). Additive manufacturing applications in Defence Support Services: current practices and framework for implementation. *Int. J. Syst. Assurance Eng. Man.*, **9**: 657-674.

Busachi, A., Erkoyuncu, J., Colegrove, P., Martina, F. & Ding, J. (2015). Designing a WAAM based manufacturing system for defence applications. *Procedia CIRP*, **37**: 48-53.

Carneiro, O.S., Silva, A.F. & Gomes, R. (2015). Fused deposition modelling with polypropylene. *Mater. Design*, **83**: 768-776.

El-Shekeil, Y.A., Sapuan, S.M., Jawaid, M. & Al-Shuja'a, O.M. (2014). Influence of fibre content on mechanical, morphological and thermal properties of kenaf fibres reinforced poly (vinyl chloride)/thermoplastic polyurethane poly-blend composites. *Mater. Design*, **58**: 130-135.

Fauzi, F.A., Ghazalli, Z., Siregar J.P. & Tezara, C. (2016). Investigation of thermal behaviour for natural fibres reinforced epoxy using thermogravimetric and differential scanning calorimetric analysis. *In MATEC Web Conf.*, **78**: 01042.

Gallo, E., Schartel, B., Acierno, D., Cimino, F. & Russo, P. (2013). Tailoring the flame retardant and mechanical performances of natural fibre-reinforced biopolymer by multi-component laminate. *Compos. Part B Eng.*, **44**: 112-119.

Grujovic, N., Zivic, F., Zivkovic, M., Sljivic, M., Radovanovic, A., Bukvic, L., Mladenovic, M. & Sindjelic, A. (2017). Custom design of furniture elements by fused filament fabrication. *Proc. Inst. Mech. Eng., Part C J. Mech. Eng. Sci.*, **231**: 88-95.

Han, S.O., Karevan, M., Sim, I.N., Bhuiyan, M.A., Jang, Y.H., Ghaffar, J. & Kalaitzidou, K. (2012). Understanding the reinforcing mechanisms in kenaf fibre/PLA and kenaf fibre/pp composites: A comparative study. *Int. J. Polym. Sci*.

Islam, M.R., Beg, M.D. & Gupta, A. (2013a). Characterization of laccase-treated kenaf fibre reinforced recycled polypropylene composites. *BioResour.*, **8**: 3753-3770.

Islam, M.R., Beg, M.D.H., Gupta, A. & Mina, M.F. (2013b). Optimal Performances of Ultrasound Treated Kenaf Fibre Reinforced Recycled Polypropylene Composites as Demonstrated by Response Surface Method. *J. Appl. Polym. Sci.*, **128**: 2847-2856.

Khaliq, M.H., Gomes, R., Fernandes, C., Nóbrega, J., Carneiro, O.S. & Ferrás, L.L. (2017). On the use of high viscosity polymers in the fused filament fabrication process. *Rapid Prototyping J.*, **23**: 727-735.

Kim, K.J. (2015). Modification of nano-kenaf surface with maleic anhydride grafted polypropylene upon improved mechanical properties of polypropylene composite. *Compos. Interfaces*, **22**: 433-445.

Kumar, L.J. & Nair, C.K. (2017). Current trends of additive manufacturing in the aerospace industry. *In* Wimpenny, D., Pandey, P. & Kumar, L. (Eds), *Adv. in 3D printing & additive manufacturing tech.*, Springer, Singapore, pp. 39-54.

Lim, B.Y., Poh, C.S., Voon, C.H. & Salmah, H. (2015). Rheological and thermal study of chitosan filled thermoplastic elastomer composites. *Appl. Mech. Mater.*, **754**: 34-38.

MacDonald, E. & Wicker, R. (2016). Multiprocess 3D printing for increasing component functionality. *Sci.,* **353:** aaf2093 .

Masood, S.H. & Song, W.Q. (2004). Development of new metal/polymer materials for rapid tooling using fused deposition modelling. *Mater. Design*, **25**: 587-594.

McMains, S. (2005). Layered manufacturing technologies. *Commun. ACM*, **48**: 50-56.

Mohammad, N.N.B. & Arsad, A. (2013). Mechanical, thermal and morphological study of kenaf fibre reinforced rPET/ ABS composites. *Malaysian Polym. J.*, **8**: 8-13.

Mohammed, L., Ansari, M.N., Pua, G., Jawaid, M. & Islam, M.S. (2015). A review on natural fibre reinforced polymer composite and its applications. *Int. J. Polym. Sci.,* **Vol. 2015**: 243947.

Mohan, N., Senthil, P., Vinodh, S. & Jayanth, N. (2017). A review on composite materials and process parameters optimization for the fused deposition modelling process. *Virt. Phy. Prototyping*, **12**: 47-59.

Montalvo, J.I. & Hidalgo, M.A. (2018). 3D printing with natural reinforced filaments. *Solid Freeform Fab. (SFF) Symp.*, pp. 922-934.

Noranizan, I.A. & Ahmad, I. (2012). Effect of fibre loading and compatibilizer on rheological, mechanical and morphological behaviors. *Open J. Polym. Chem.*, **2**: 31-41.

Page, T. (2018). A Survey of the use of additive fabrication in component replacement and customised automotive modifications. *Int. J. of Manuf., Mater. Mech. Eng.*, **8**: 23-34.

Ramanath, H.S., Chua, C.K., Leong, K.F. & Shah, K.D. (2008). Melt flow behaviour of poly- ε-caprolactone in fused deposition modelling. *J. Mater. S. Mater. Med.*, **19**: 2541-2550.

Rathee, S., Srivastava, M., Maheshwari, S. & Siddiquee, A.N. (2017). Effect of varying spatial orientations on build time requirements for FDM process: A case study. *Defence Tech.*, **13**: 92-100.

Sa'ude, N., Ibrahim, M. & Ibrahim, M.H.I. (2016). Melt flow rate (MFR) of abs-copper composite filament by fused deposition modeling (FDM). *ARPN J. Eng. App. Sci.*, **11**: 6562-6567.

Singh, R., Singh, S. & Mankotia, K. (2016). Development of ABS based wire as feedstock filament of FDM for industrial applications. *Rapid Prototyping J.*, **22**: 300-310.

Tawakkal, I.S., Cran, M.J. & Bigger, S.W. (2014). Effect of kenaf fibre loading and thymol concentration on the mechanical and thermal properties of PLA/kenaf/thymol composites. *Ind. Crops Prod.*, **61**: 74-83.

Tayfun, U., Dogan, M. & Bayramli, E. (2016). Effect of surface modification of rice straw on mechanical and flow properties of TPU-based green composites. *Polym. Compos.*, **37**: 1596-1602.

Tayfun, U., Dogan, M. & Bayramli, E. (2016). Influence of surface modifications of flax fibre on mechanical and flow properties of thermoplastic polyurethane based eco-composites. *J. Nat. Fibres*, **13**: 309-320.

Torrado, A.R., Shemelya, C.M., English, J.D., Lin, Y., Wicker, R.B. & Roberson, D.A. (2015). Characterizing the effect of additives to ABS on the mechanical property anisotropy of specimens fabricated by material extrusion 3D printing. *Additive Manuf.*, **6**: 16-29.

Wang, S., Capoen, L., D'hooge, D.R. & Cardon, L. (2018). Can the melt flow index be used to predict the success of fused deposition modelling of commercial poly (lactic acid) filaments into 3D printed materials?. *Plastics, Rubber Compos.*, **47**: 9-16.

Wang, X., Jiang, M., Zhou, Z., Gou, J. & Hui, D. (2017). 3D printing of polymer matrix composites: A review and prospective. *Compos. Part B Eng.*, **110**: 442-458.

Wong, K.V. & Hernandez, A. (2012). A review of additive manufacturing. *ISRN Mech. Eng.*, **1012**: 208760.

EFFECT OF SIX DIFFERENT TORSO SUB-SYSTEM ARMOURED VESTS ON PHYSIOLOGICAL AND COGNITIVE PARAMETERS

Ananthan Subramaniam[1], Brinnell Caszo[2], Zubaidah Hasain[3], Victor Feizal Knight[3] & Justin Gnanou[2*]

[1]Centre for Tropicalisation, National Defence University of Malaysia (UPNM), Malaysia
[2]School of Medicine, International Medical University, Malaysia
[3]Faculty of Medicine and Defence Health, National Defence University of Malaysia, Malaysia

[*]Email: justin@upnm.edu.my

ABSTRACT

This study documents an assessment of six soldier torso sub-system armoured vests on physiological and cognitive measures. The six systems were similar in weight (9.0 ± 1.1 kg) but differed in the material composition, ease of use and comfort. Six male army physical training instructors of similar age (32.7 ± 2.2 years) were recruited for the study. The subjects were assigned the armoured vests based on a lot system and in a cross-over study design during the experimental study period. On each of the experimental days, baseline physiological measures such as body weight, blood pressure, pulse rate, peripheral capillary oxygen saturation (SPO_2), aural body temperature, urine osmolality and cognition status were carried out. Subjects were subsequently required to complete a military obstacle course and a jungle trek, and the physiological measures were repeated at the end of the physical exertion. Overall analysis of the data did not show any statistically significant difference between the six vests. However, looking at the data qualitatively, this study provides fundamental data on the use of protective body armour in a tropical jungle working environment. Interesting trends were observed which seemed to indicate there was some effect which could be attributed to the individual characteristics of the vests. The findings of this study also suggest that physiological and physical demands are added on by the protective body armour in a tropical jungle working environment.

Keywords: *Armoured vests; protective body armour; tropical; anthropometry; obstacle course; cognition.*

1. INTRODUCTION

Military protective body armour is an essential part of a soldier system that is worn to protect soldiers from injury during active duty. Though the main function of protective body armour is for protection, it should not compromise and impair soldier performance. Soldier performance involves two main areas namely physiological fitness (maximal oxygen capacity, heart rate maintenance and heat tolerance) and physical performance (strength, speed and balance). Different armoured vests have been tested on military personnel for its effect on physiological fitness. DeMaio *et al.* (2009) showed that using a Kevlar vest, the maximum oxygen uptake (VO_2 max) decreased when compared to control during a maximal uphill walking. Ricciardi *et al.* (2008) also showed that a body armour of approximately 10 kg caused a significant increase in heart rate after a thirty-minute treadmill walking at slow and moderate paces. A similar result on heart rate with a tactile vest of 7.5 kg was shown by Cheuvront *et al*. (2008). Studies on heat tolerance or thermal stress have shown that different armoured vest configurations did not show any significant differences in rectal or core body temperature after physical exertion (Payne *et al*., 1988; Cadarette *et al*., 2001).

Numerous studies have also been done to determine the effect of armoured vests on physical performance (Potter *et al*., 2015). In a study by Pandorf *et al*. (2003) on female soldiers, a body armour of approximately 14 kg with additional equipment loads (27 and 41 kg) caused a significant decrease in time in completing a 3.2 km run and an obstacle course. Hasselquist *et al*. (2008) showed that an armoured vest of 8.7 kg caused a poorer performance in a 10 min run, walk and repetitive box lift and carry. Similar results were obtained by Ricciardi *et al*. (2008) on stair step test, pull ups and hang time with an armoured vest of 10 kg. A point to note is that these above studies were carried out in a controlled laboratory or in a temperate environment. Very few studies have been done to verify the effect of different environmental conditions on armoured vests' effect on physical and physiological performance. Montain *et al*. (1994) compared the effect of full personal protective clothing between tropical (35°C and 50% humidity) and desert (43°C and 20% humidity) environments. However, this study did not show any difference in physiological tolerance between the two climatic conditions.

Tolerance to heat while wearing an armoured vest is an important factor to be considered in military operations and training (Hunt *et al*., 2016). In the United Kingdom, approximately 80 military personnel are treated for heat stress symptoms in a year even with an ambient temperature of 20°C mainly due to the thermal insulation of the armoured vest (Crockford, 1999). Thermal stress could add on to the effect of the armoured vest on the physical and physiological performance indices. This becomes even more important when non-acclimatized military personnel have to be deployed to active duty in a tropical environment (Buller *et al*., 2015; Stewart *et al*., 2016). Hence, development of a framework for human factor assessment for functional performance in a tropical environment is important. This can help in designing and developing armoured vests which are well suited for a tropical environment. The objective of this study is to compare six different armoured vests based on physical, physiological and cognitive parameters in a tropical jungle environment.

2. METHODOLOGY

2.1 Subject Selection and Characterisation

Six subjects from a local military unit were recruited for the study. They were selected based on a similar age, role, service and fitness level. The subjects were briefed about the study protocol and informed consent was obtained. The study protocol was reviewed by the University Research Committee and the study was conducted in accordance with the Declaration of Helsinki and the guidelines of Resolution on 198/96 of the National Health Council (World Medical Association, 2001). Body stature and basic anthropometry measures were also taken followed by a complete body composition analysis using a bio-impedance analyser. The lung function of the subjects was also measured using a spirometer.

2.2 Vest Selection

A total of six different vests were selected. The vests were chosen so that they each approximately weigh the same and comprise of personal webbing, patrol pack, armoured plate inserts and each subject were given a standardised ration of water to carry on them.

2.3 Experimental Design

A cross-over study design was utilised to compare the six different types of vests. Subjects were required to complete the study protocol from day 1 through day 6 of the study. The subject-vest combination for each of the days is as shown in Table 1. Each subject was also assigned numbers 1 to 6 and they would wear a different vest labelled with alphabets A to F (Figure 1) on each of the study days.

Table 1: Cross over design for subject-vest combination.

Subject	Day 1 Vest	Day 2 Vest	Day 3 Vest	Day 4 Vest	Day 5 Vest	Day 6 Vest
1	A	F	E	D	C	B
2	B	A	F	E	D	C
3	C	B	A	F	E	D
4	D	C	B	A	F	E
5	E	D	C	B	A	F
6	F	E	D	C	B	A

Figure 1: Subject-Vest combination on Day 1.

2.4 Study Protocol

A 6 km jungle trek at a military camp was selected as the tropical jungle field laboratory. On the day of the experiment, the environmental temperature and humidity levels were measured. At the start of the protocol, baseline physiological measurements such as body weight, blood pressure, pulse rate, peripheral capillary oxygen saturation (SPO2), body temperature and urine osmolality were measured. A baseline cognition test was also administered.

2.5 Performance Test

In order to quantitate the impact of armoured vest on military personnel performing their duties in a tropical environment, simulated military tasks such as completing an obstacle course were carried out and these tasks were timed. The obstacle course comprised of standard military obstacles which included a 3-foot hurdle jump, uneven wall, monkey bars, wall climb-down, 6-foot wall climb, rope swing, tunnel crawl, swinging bridge, belly roll, staggered steps, log run and a leopard crawl in sequence. At the end of the performance test, body temperature, body weight and urine osmolality measurements were made. After a 30-minute rest period, a 5 km jungle trek was carried out. During the trek the subjects were allowed to drink water and the water intake was recorded. At the end of the jungle trek which took approximately 1 hour 15 minutes to complete, the physiological measurements (blood pressure, pulse rate, body weight, SPO2, body temperature and urine osmolality) were measured. The cognition test was also repeated at the end of the trek.

2.6 Statistical Analysis

The data was expressed as mean ± standard deviation. In order to compare the six different armoured vests, repeated measures analysis of variance (ANOVA) was carried out on the physiological and cognitive markers measured at baseline, at the end of the obstacle course and at the end of the jungle trek using SPSS 17.0. A p value of < 0.05 was considered as statistically significant.

3. RESULTS AND DISCUSSION

3.1 Anthropometric Measures of the Participants

Anthropometric measurements provide the necessary details to compare different body sizes amongst a specific population. In the military, such measurements are vital for the design and evaluation of soldier systems to ensure good fit and ergonomic considerations are met (Edwards *et al*., 2014). Basic anthropometric measurements of the six participants in this study were collected. The average measures of each item are listed in Table 2.

Table 2: Anthropometry measures.

	Average (cm)	SD (cm)
Upper neck	38.4	1.7
Lower neck	38.7	1.8
Chin	5.7	0.5
Neck rear	8.8	1.4
Neck front	8.2	0.6
Shoulder	46.8	1.8
Arm size	13.1	2.3
Arm length	53.9	0.8
Chest	37.5	2.5
Iliac line	44.4	3.2
Iliac line to heel	90.0	4.9
Lower waist	47.2	1.9
Hip size	49.7	1.3
Thigh circumference	22.0	1.5
Calf circumference	16.2	1.0

3.2 Physiological Characterisation of the Participants

The baseline physiological characteristics as shown in Table 3 indicated that the subjects had normal blood pressure and pulse rate. These data also describe the body composition analysis of each of the six subjects. The subjects had an average body weight of 69.3 ± 5.6 kg and a height of 166.6 ± 5.3 cm. The average BMI was 25 ± 0.7 kg/m^{2}which is at the upper limit of normal as used by the Malaysian military (MAF HQ, 2011). This could be due to their higher muscle mass (49.3 ± 4.9 kg) rather than due to body fat mass considering that the subjects were all military physical training instructors. Their average percentage body fat was 23.7 ±1.7 which is within the normal limit for their age. Lung function tests revealed that the subjects had forced vital capacity (FVC) which is the volume of air that can forcibly be blown out after full inspiration and forced expiratory volume in 1 second (FEV1) which is the volume of air that can forcibly be blown out in first 1 second after full inspiration, at more than 85% of the predicted values.

Table 3: Baseline physiological measures.

Physiology	Average	SD
Age (years)	33	2
Height (cm)	166.0	5.0
Weight (kg)	69.0	5.0
Systolic BP (mm/Hg)	122	12
Diastolic BP (mm/Hg)	76	6
Resting Pulse Rate (per min)	68	4
Muscle Mass (kg)	49.3	5.0
Fat Free Mass (kg)	52.8	5.0
Body Fat Mass (kg)	16.4	0.8
Skeletal Muscle Mass (kg)	29.0	3.1
Body Mass Index	24.9	0.7
Percentage Body Fat (%)	23.7	1.7
Lung Function	**Average**	**% Predicted**
Forced Vital Capacity (FVC in L)	3.85 ± 0.5	86.96 ± 5.7
Forced Expiratory volume in 1 second (FEV1 in L)	3.20 ± 0.36	85.40 ± 4.0

3.3 Vest Characteristics

Table 4 shows the weight of each of the six vests. The average vest weight was 9.0 ± 1.1 kg.

Table 4: Weight of the six different armoured body vest.

	Vest Weight (Kg)	Change in Vest Weight after obstacle course (Kg)	Change in Vest Weight after jungle trek (Kg)	Change in Vest Weight after immersion in water (Kg)
Vest A	10.9	0.7 ± 0.90	1.18 ± 0.89	0.8
Vest B	8.6	0.87 ± 1.19	1.22 ± 1.31	2.9
Vest C	8.7	0.90 ± 1.04	1.08 ± 1.39	0.5
Vest D	9.1	0.88 ± 1.22	1.48 ± 1.25	1.6
Vest E	7.6	1.05 ± 1.34	1.30 ± 1.60	1.9
Vest F	8.8	0.7 ± 1.42	1.10 ± 1.09	2.4

Besides this initial weight, measurements were also taken after the obstacle course and jungle trek. The vests were later immersed in water during a simulated river crossing to determine the individual differences of the vests in absorbing water. Our data shows that Vest C absorbed the least water (0.5 kg) while Vest B absorbed the most water (2.9kg) after the simulated river crossing. Figures 2 (a) and (b) further illustrate the above findings. This variance could be due to the difference in the fabric and method of fabrication of the vests and this characteristic could play an important role in determining the functionality of the vests especially when exposed to wet environments.

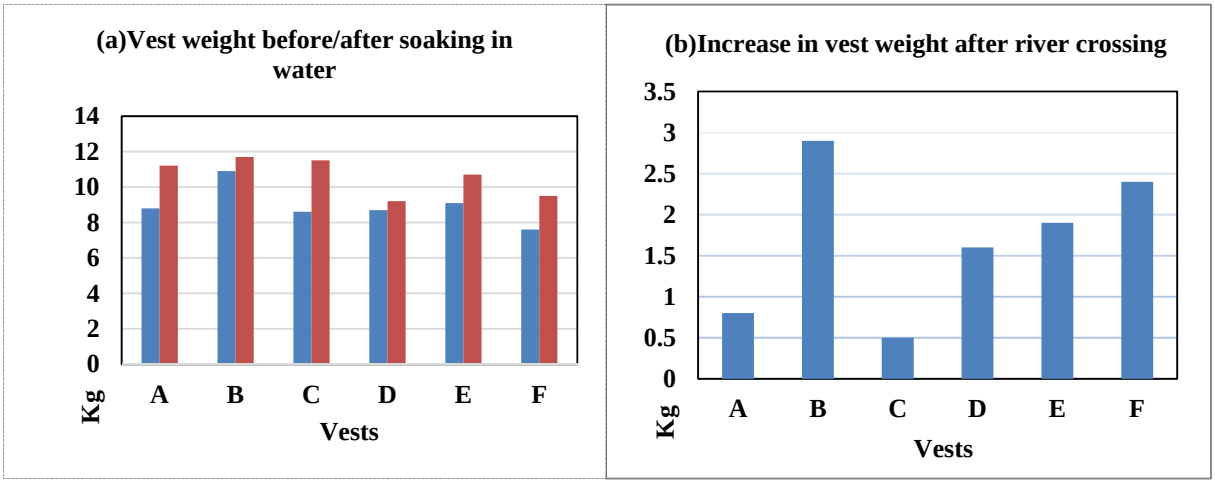

Figure 2: Vest characteristics: (a) Weight before and after soaking in water. (b) Increase in vest weight after soaking in water.

3.4 Environmental Characteristics

Data from the Malaysian Meteorological Department was used to illustrate the environmental conditions under which the study was conducted. The data obtained showed that the average temperature was 24 – 32^{o}C (minimum – maximum) with the relative average humidity of 80% over the period of the study (klim@met.gov.my, email communication, October, 24, 2017).

3.5 Effect on Weight of Vests After Obstacle Course and Jungle Trek

Changes in the weight of the vests after the obstacle course and jungle trek would give an indication of the added burden of the vests on the subjects (Hasselquist *et al*., 2008). Different vests would have different sweat/fluid absorption, sweat/fluid retention characteristics depending on the materials used, method of fabrication and methods of drainage used. A vest that retains less sweat/fluid or can shed excess sweat/fluid would add a smaller burden to the subject during use. Due to the tropical environment in which these vests were assessed which included high humidity from the environment (RH of more than 60) it is assumed that the tropical conditions would be a strain on the ability of the subjects to perform tasks while using these vests. The physical exertion of the subjects and their associated sweating could increase the weight of the vests from the absorption of sweat by the material of the vests and possibly by the reduced evaporation of sweat from the vest while in use. Data from our study (Figure 3) shows that all six vests had comparable increases in weight after the obstacle course and the jungle trek. There was no statistically significant difference between the weights of the vests using repeated measures ANOVA; $p >$ 0.5. However, looking at the data qualitatively, we observe that vest F and A had the smallest increases in weight after the obstacle course, while vest C has the least increase in weight after the jungle trek.

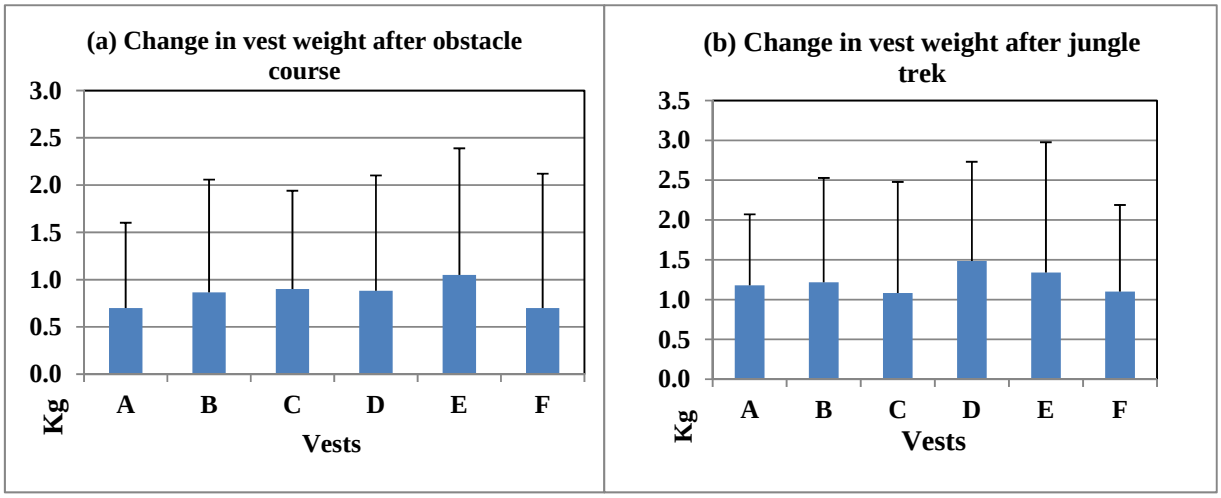

Figure 3: Change in vest weight after (a) obstacle course, and (b) jungle trek.

3.6 Effect of Vests on Body Temperature After Obstacle Course and Jungle Trek

Increase in core body temperature or hyperthermia is an important factor that affects performance after strenuous physical activity (Cheuvront *et al.*, 2008). Thus an armoured vest that helps to keep the body cool or does not retain or trap body heat would be best suited for a tropical environment like in Malaysia. Muscular activity in hot and humid environments are known to increase the heat strain suffered by military personnel using body armour (Santee *et al.*, 2015). The data from our study shows that both after the obstacle course and jungle trek, vest C caused the greatest increase in body temperature (more than 1^{o}C) while vest E and vest A caused the least increase in body temperature. However, statistically, there was no significant difference between the vests. Figure 4 shows the change in body temperature after the obstacle course and jungle trek respectively.

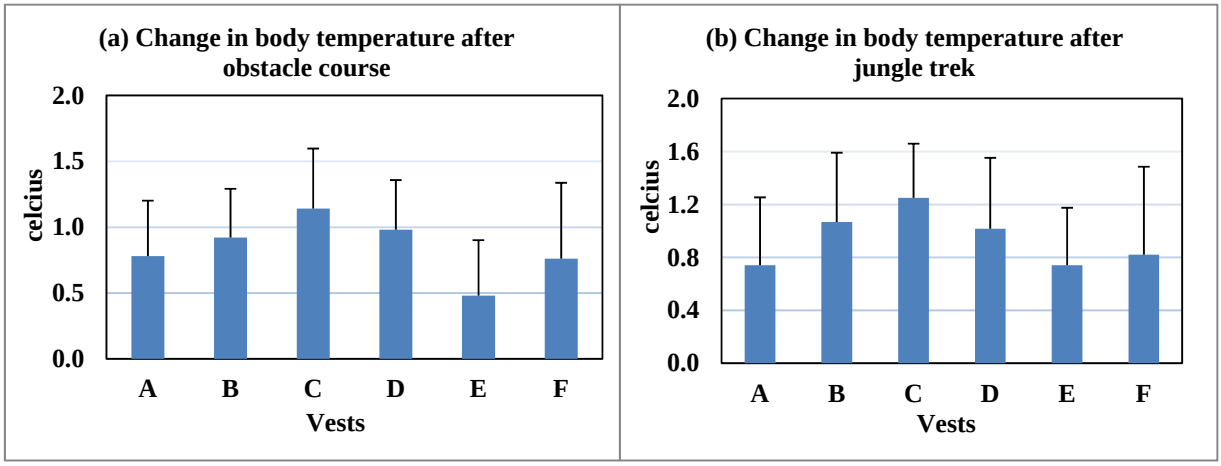

Figure 4: Change in body temperature after (a) obstacle course, and (b) jungle trek.

For these measures the aural temperature was measured to indicate the core body temperature. Measuring the core body temperature is currently done by using a temperature sensor capsule that is swallowed by

the subject and is monitored by telemetry using a data capture device worn by the subject. Due to the absence of devices to directly measure the core temperature in this study, the aural temperature was used instead. However, it has been reported in the literature that the use of ingested temperature measuring capsules to measure core body temperature have resulted in incomplete data capture especially in aggressive and robust physical manoeuvres as the data capture unit on the subject has been noted to get displaced or was unable to maintain consistent data recovery throughout the physical activities performed.

3.7 Effect of Vests on Urinary Osmolality After Obstacle Course and Jungle Trek

Urine osmolality is the measure of the solute concentration in the urine. It is one of the markers of dehydration, with 300 to 900 mosm/kg considered as the normal range for urine osmolality. Values below 300 mosm/kg indicate dilute urine while values above 900 mosm/kg indicate highly concentrated urine (Convertino *et al*., 1996). Results from our study showed that at the end of the obstacle course, subjects with vests A, B and D showed a decline in urine osmolality when compared to the baseline (Figure 5). With vests C and F, the subjects were able to maintain good hydration. However, no statistically significant difference was observed. At the end of the jungle trek, all the subjects, regardless of the type of vest worn, showed a decline in urine osmolality when compared to the baseline. Subjects using vest F had the greatest decline, while those using vest C had the least. Similarly, with the jungle trek, there was no statistically significant difference between the vests worn, with respect to urine osmolality changes. An important point to note is that none of the subjects suffered from dehydration and ad libitum access to drinking water was provided.

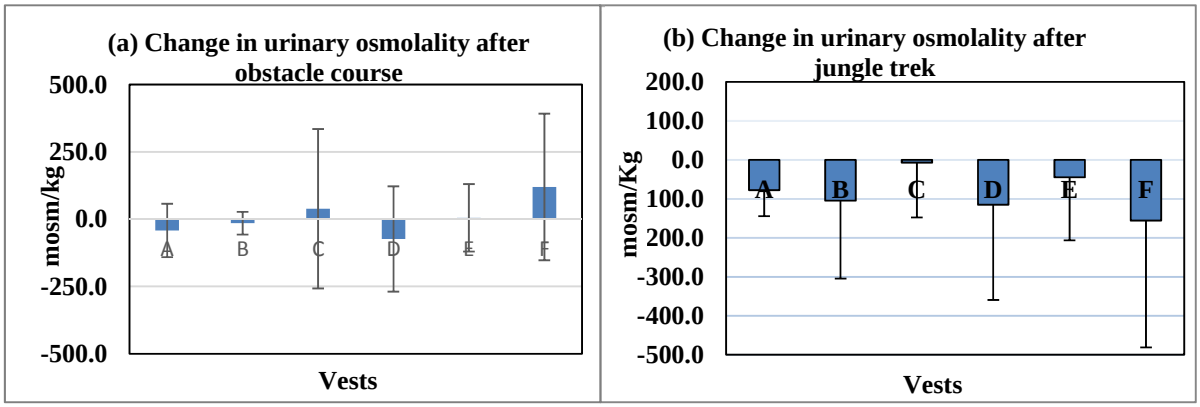

Figure 5: Change in urine osmolality after (a) obstacle course and (b) jungle trek.

3.8 Effect of Vests on Blood Pressure After Jungle Trek

Blood pressure usually rises during exercise due to an increased cardiac output (Barret *et al*., 2010) caused by that exercise, but it is also associated with falling peripheral vascular resistance. In this study, blood pressure was recorded after the jungle trek had been completed and showed a lower blood pressure among the subjects. This is caused primarily by the decrease in total peripheral resistance caused by the vasodilation of resistance arteries within the exercising muscles, and because of a peripheral pooling of blood (Barret *et al*., 2010). The data from our studies is consistent with this phenomenon and there was an overall decline in both systolic and diastolic blood pressure after the jungle trek. Recordings for Vest F for systolic blood pressure and vest B for diastolic blood pressure were exceptions but are minor. The same differences were comparable across all the 6 vests used by the subjects (Figure 6).

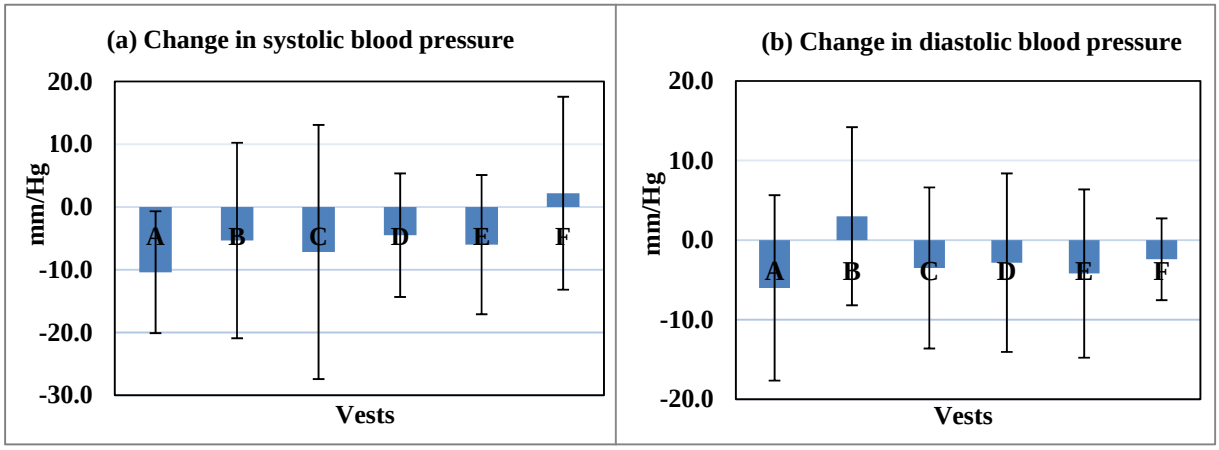

Figure 6: Changes after jungle trek: (a) Systolic blood pressure. (b) Diastolic blood pressure.

The measurement of blood pressure involved the use of a sphygmomanometer cuff to the upper arm of the subject. This was at times less optimal because of the sleeve of the uniform jacket used by the subject and the added material could add to the magnitude of error in sphygmomanometer reading. The use of a wrist type sphygmomanometer would have eliminated this factor.

3.9 Effect of Vests on Pulse Rate and SpO_2 After Jungle Trek

Data from the pulse rate and SpO_2 shows that at the end of the jungle trek, the subjects had an increase in pulse rate ranging from a minimum of 18 beats/min (vest A) to a maximum of 29 beats/min (Vests B and F). Pulse rate which is an indicator of the heart rate is indicative of the intensity of physical activity, generally the higher the heart rate, the greater the intensity of physical activity (Barret *et al*., 2010). In our study, since the intensity of the jungle trek was kept constant, differences in heart rate may reflect the burden of the armoured vest worn by the subjects as they completed the jungle trek. Looking at the data, vest A seems to be the vest with the least increase in heart rate when compared to all other vests, however this difference was not found to be statistically significant (Figure 7).

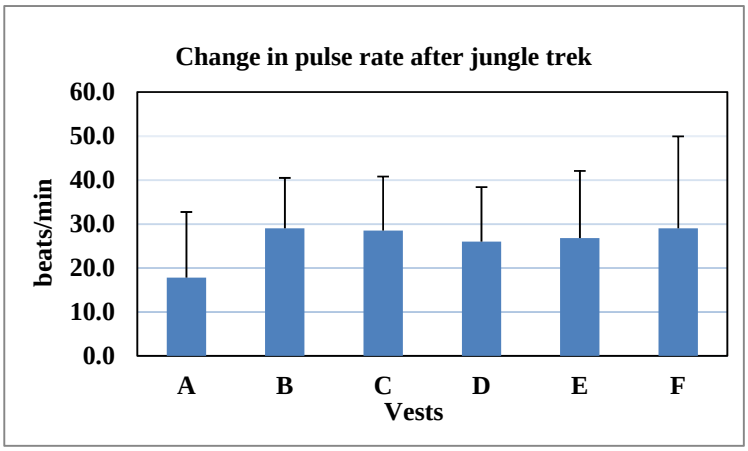

Figure 7: Change in pulse rate after jungle trek.

SpO_2 is a measure of the percent saturation of haemoglobin of the blood. At rest, $SpO_2$is about 99 to 100% and after exercise, due to increased demand of oxygen by the skeletal muscles and changes in oxygen affinity to haemoglobin, one would expect a decrease in SpO_2 (Vanderlei *et al*., 2013). In our data, we also see a decrease in SpO_2 at the end of the jungle trek by about 0.5 to 1%. Though there is no statistically significant difference ($p>0.05$) between the vests, Vest C and Vest A seem to have the least decrease in SpO_2 when compared to other vests (Figure 8).

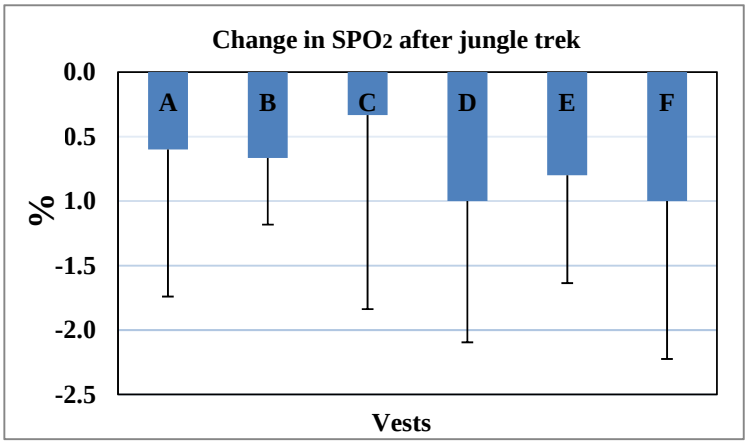

Figure 8: Change in SPO_2 rate after jungle trek.

3.10 Effect of Vests on Cognition and Rated Perceived Exertion After Jungle Trek

Physical activity is shown to affect cognition (Ferris *et al*., 2007). We carried out a MINICOG test before and after the jungle trek in order to compare the effect of the six vests on cognition after the jungle trek. In our study, cognitive function remained comparable with the resting state values, for all the vests. There was a slight increase in cognition for vests D and E, though this finding was not statistically significant (Figure 9a). Rated perceived exertion scale or RPE scale is used as a measure of perceived exercise intensity by the subjects. The subjects rate the physical exertion from a scale of 0 (very mild) to 10 (very intense). In our study, RPE values varied between 3 to 4 (moderate) scores for all the vest types. This is a subjective measure that was self-reported by the subjects. It was interesting that the subjects did not rate the exertion higher despite the fact that they do not use any body armour in the course of their daily duties as physical training instructors and are unfamiliar with body armour as a part of their daily routine (Figure 9b).

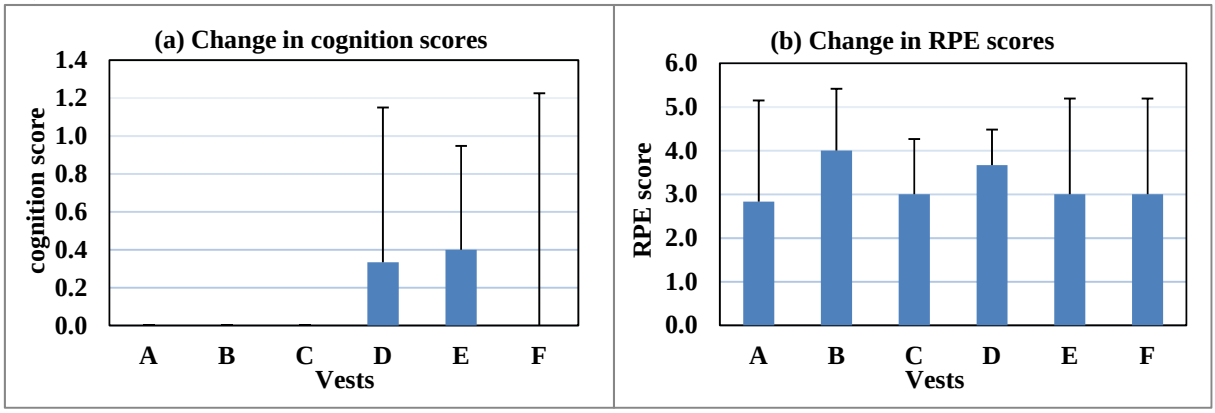

Figure 9: Changes after jungle trek: (a) Cognition scores. (b) RPE scores.

4. CONCLUSION

Analysis of changes in physiological parameters and cognition after the obstacle course and jungle trek revealed many qualitative differences between the six different types of vests in a jungle tropical environment. Some important observation from this study are: Vest C appeared to absorb the least water after soaking, showed the least gain in vest weight after use, greatest increase in body temperature and whose wearer (subject) demonstrated the least change in urine osmolality after the jungle trek. Another interesting observation was regarding vest A; where subjects showed the smallest increase in pulse rate however they had the greatest decrease in blood pressure at the end of the jungle trek. Our data also showed no change in cognition status as assessed by the MINICOG instrument after the jungle trek irrespective of the vest worn. From these above observations, we inferred that vest C appeared to be the vest with least physiological demand compared to other vests after a jungle trek in a tropical environment.

One area of improvement in our study would have been the use of plasma osmolality instead of urine osmolality. Plasma osmolality is a more sensitive measure of dehydration at a cellular level as compared to urine values which are values after water reuptake at the level of the kidneys. Another area of improvement would have been the use of a more controlled regime of rehydration which would show a difference in the ability of the subjects to endure heat stress and water loss. This may provide additional information as regards the effect of increased work effort caused by the use of the armoured vests in a tropical environment. Thus, further studies are required to develop a standardised framework for assessing the effect of protective body armour on physical and physiological performance indices in a tropical jungle working environment.

REFERENCES

Barret, K.E., Marman, S.M., Boitano, S. & Brooks, H.L. (2010). *Ganong's Review of Medical Physiology*, *23rd Ed*. McGraw-Hill, USA.

Buller, M.J., Welles, A.P., Stevens, M, Leger J., Gribok, A., Jenkins, O.C., Friedl, K.E. & Rumpler, W. (2015). Automated guidance from physiological sensing to reduce thermal-work strain levels on a novel task. *Body Sensor Netw. Conf. 2015*. Cambridge, USA.

Cadarette, B.S., Blanchard, L., Staab, J.E., Kolka, M.A. & Sawka, M.N. (2001). Heat stress when wearing body armour. *Technical Report T-01/9*. Natick, MA, Thermal and Mountain Medicine Division, United States Army Research Institute of Environmental Medicine (USARIEM).

Cheuvront, S.N., Goodman, D.A., Kenefick, R.W., Montain, S.J. & Sawka, M.N. (2008). Impact of a protective vest and spacer garment on exercise heat-strain. *Eur. J. App. Physiol.*, **102**: 577-583.

Convertino, V.A., Armstrong, L.E., Coyle, E.F., Mack, G.W., Sawka, M.N., Senay, L.C. Jr. & Sherman W.M. (1996). American College of Sports Medicine position stand: Exercise and fluid replacement. *Med. Sci. Sports Exerc*., **28**: i-vii.

Crockford, G.W. (1999). Protective clothing and heat stress: Introduction. *Ann Occup Hyg*., **43**: 287-288.

DeMaio, M., Onate, J., Swain, D., Morrison, S., Ringleb, S. & Naiak, D. (2009). *Physical Performance Decrements in Military Personnel Wearing Personal Protective Equipment (PPE)*. RTO-MP-HFM-181, NATO Military Operations (Science, Technology and Ethics), Brussels.

Edwards, M., Furnell, A., Coleman, J. & Davis, S. (2014). *A Preliminary Anthropometry Standard for Australian Army Equipment Evaluation*. Department of Defence, Australia.

Ferris, L.T., Williams, J.S. & Shen, C.L. (2007). The effect of acute exercise on serum brain-derived neurotrophic factor levels and cognitive function. *Med. Sci. Sports Exerc*., **39**: 728-734.

Hasselquist, L., Bensel, C.K., Corner, B., Gregorczyk, K.N. & Schiffman, J.M. (2008). *Understanding the Physiological, Biomechanical and Performance Effects of Body Armour Use*. Natick, Natick Soldier Research, Development and Engineering Centre, Storming Media.

Hunt, A.P., Billing, D.C., Patterson, M.J. & Caldwell, J.N. (2016). Heat strain during military training activities: The dilemma of balancing force protection and operational capability *Temperature (Austin)*, **3**: 307-317.

MAF HQ (2011), *Armed Forces Medical Classification System* (AFMeCS). Health Services Division, Malaysia.

Montain, S.J., Sawka, M.N., Cadarette, B.S., Quigley, M.D. & Mckay, J.M. (1994). Physiological tolerance to uncompensable heat stress: Effects of exercise intensity, protective clothing and climate. *J. App. Physiol*., **77**: 216-222.

Pandorf, C.E., Nindl, B.C., Montain, S.J., Castellani, J.W., Frykman, P.N., Leone, C.D. & Harman E.A. (2003). Reliability assessment of two military relevant occupational physical performance tests. *Can. J. App. Physiol*., **28**: 27-37.

Payne, W., Portier, B., Fairweather, I. Zhi, S. & Snow, R. (1988). Physiological and psychological responses to wearing fully encapsulated protective clothing during simulated work in various thermal environments. *Workplace Australia*., **2**: 68.

Potter, A.W., Gonzalez, J.A., Karis, A.J. & Xu, X. (2015). Biophysical assessment and predicted thermophysiologic effects of body armour. *PLoS ONE*., **10**: e0132698.

Ricciardi, R., Deuster, P. & Talbot, L. (2008). Metabolic demands of body armour on physical performance in simulated conditions. *Mil. Med*., **173**: 817-824.

Santee, W.R., Xiaojiang, X., Yokota, M., Buller, M.J., Karis, A.J., Mullen, S.P. Gonzalez, J.A., Blanchard, L.A., Welles, A.P., Cadarette, B.S., Tharion, W.J., Potter, A.W. & Hoyt, R.W. (2015). *Core Temperature and Surface Heat Flux During Exercise in Heat While Wearing Body Armour*. USARIEM Technical Report T16-1. Biophysics and Biomedical Modelling Division, U.S. Army Research Institute of Environmental Medicine, USA.

Stewart, R.P., Gregory, S.A., Michael, J.T., David, D., Terry, E.G., Brian, J.S., et al. (2016). Towards best practice in physical and physiological employment standards. *Appl Physiol Nutr Metab*., **41**: S47-S62.

Vanderlei, F.M., Moreno, I.L., Vanderlei, L.C., Pastre, C.M., de Abreu, L.C. & Ferreira, C. (2013). Effects of different protocols of hydration on cardiorespiratory parameters during exercise and recovery. *Int. Arch. Med*., **6**: 1-10.

World Medical Association. (2001). World Medical Association Declaration of Helsinki: Ethical principles for medical research involving human subjects. *Bull. World Health Organ.*, **79**: 373-374.

BIOAEROSOL STUDY FOR TWO LABORATORIES IN STRIDE

Ahmad Razi Mohamed Yunus[*1], Noorliza Hamdan[1], Mohd Badrolnizam Jamhari[1], Asmariah Jusoh[1] & Nur Faeza Mustafa[2]

[1]Biosurveillance and Biological Defence Branch
[2]Analysis and Textile Technology Branch
Protection & Biophysical Technology Division, Science & Technology Research Institute for Defence (STRIDE), Malaysia

[*]Email: razi.yunus@stride.gov.my

ABSTRACT

Airborne microbes might pose an environmental hazard when present in high concentration in indoor environments, resulting in potential health problems. In Malaysia, there is only limited information currently available on individual exposure to bioaerosols. The aim of this study was to assess the level of bacterial and fungal contaminations in two air-conditioned laboratories in STRIDE's Main Complex, Kajang, Selangor. The study was conducted in three sampling locations (two laboratories and one outdoor). Each measurement was conducted in three time intervals (morning, noon and evening). Each air sample was collected for 2 min at sampling flow rate of 28.3 L/min. The samples were assessed in the laboratory for enumeration of viable bacteria and fungi. Agar plates for bacteria were incubated at 35^{o}C for 24-48 h. The outdoor environment showed bacteria count of 120 CFU/m^{3}, which is still acceptable based on the limit set by the World Health Organization (WHO) (500 CFU/m^{3}). However, it showed very high fungal count of 2,537 CFU/m^{3}, which exceeded the limit set by the American Conference of Governmental Industrial Hygienists (ACGIH) (1,000 CFU/m3). The average concentration of the bacterial and fungal aerosols on the two studied laboratories did not exceed the limits. The analysis of microbial contamination showed that the concentration of bacterial and fungal aerosols were higher outdoors than indoors. The results obtained in this study indicated that the two laboratories' exposure to airborne bacteria and fungi is generally low and safe for laboratory workers.

Keywords: *Bioaerosols; health effects; ventilation; indoor air; outdoor environment.*

1. INTRODUCTION

Most people spend most of their working time in office environments. Exposure to airborne microbes in indoor working environments has become a subject of concern due to it potentially affecting the health condition of indoor occupants (Hwang & Yoon, 2016). Biological particles suspended in the air can be present in viable (culturable and non-culturable) as well as nonviable forms. Their aerodynamic sizes determine the depth of penetration and subsequent deposition in the human respiratory system, which in turn determines the possible health effects (Golofit-Szymczak & Gorny, 2010). Such inhalation exposure can initiate numerous immunopathogenic reactions, including allergies, infections, toxic reactions (Mbakwem-Aniebo *et al*., 2016) and other unspecified symptoms, such as sick building syndrome (Bohlan & Subratty, 2002). Sick building syndrome, which is a condition where occupants within the building suffer serious health problems due to the amount of time spent within this environment, has been attributed to poor building design, lack of maintenance of buildings as well as the activities within such environments (Douglas & Robinson, 2018).

Aerosols are liquid or solid particles suspended in a gaseous medium with size ranges from 0.001 to 100 µm (Geogakapolus *et al*., 2009). Bioaerosols consists of aerosols containing microorganism (bacteria, fungi and virus) or organic compounds derived from microorganisms (endotoxins, metabolites, toxin and other microbial fragments) (Heikkienen *et al*., 2005). Due to their light weight, airborne particles are readily transported, transferred and displaced from one environment to another (Hagreaves *et al*., 2003). Airborne microbes might pose environmental hazards when present in high concentration in indoor environments, resulting in health problems (Stetzenbach *et al*., 2004).

Bioaerosols contribute to about 5 to 34% of indoor air pollution (Srikanth *et al*., 2008). The sources of bioaerosols in indoor air include furnishing and building materials, microbiological contamination within the walls, as well as ceiling and floor activities. In non-industrial indoor environments, one of the most important sources of airborne bacteria is the presence of humans (Stetzenbach, 1997; Feysa *et al*., 2019), especially within their shoes and clothes. Particular activities, such as talking, sneezing, coughing, walking, washing and toilet flushing, can generate airborne biological particulate matter (Cox & Wathess, 1995). Sources of indoor bioaerosols are often located outdoors and particles are transferred to the inside through openings of the building envelope, such as windows and doors. However, one of the most important factors affecting indoor air quality is how the building is heated, ventilated and air conditioned (Seppaenen & Fisk, 2002), as well as its occupancy (Barlett *et al*., 2004).

An air conditioning system is practically the only technical solution used to both improve air quality and provide employees with proper working conditions. The atmospheric air, which is delivered into the building through the air conditioning system, should be free from most common pollutants and ensure ideal temperature and moisture. Unfortunately, bad maintenance of air conditioning systems or their low efficiency can often lead to unintentional contamination of office or laboratory spaces (Golofit-Szymczak & Gorny, 2010). The quality of air in offices or laboratory buildings depends on numerous physical, chemical and biological factors. Regarding microbial pollutants, among their typical indoor sources are people, plants, animals, soil, water and human-made materials. In this type of work environment, biological contaminants can cause adverse health effects when transported in the air as bioaerosols (Skowron & Golofit-Szymczak, 2004). Although the air is not conducive to the growth and survival of microorganisms, it is the most important medium for carrying and spreading of biological contaminants (Dutkiewicz *et al*., 1988).

A laboratory can usually be referred to as a space, room or building equipped for scientific research and also to carry out any testing of chemicals, biological and physical materials. A clean and optimum indoor environment of the laboratory is crucial to ensure the well-being of the occupants and also to maintain all the expensive instruments, materials and samples in good condition (Yau *et al*., 2012). The microbial compositions from indoor environment in various types of biological laboratories are less well understood (Hazrin *et al*., 2015; Xi *et al*., 2018). Lab workers, especially personnel handling microbiological work, would be more exposed to bioaerosols than those in other occupations (Hwang & Yoon, 2016). Most laboratory workers feel they are safer when standard safety practices are applied, but evidence based research is lacking to confirm that supposition (Hwang & Yoon, 2016). Xi *et al*. (2018) identified both the environmental and human factors as important factors in shaping the diversity and dynamics of these possible microbial contaminations in biological laboratories. The most common microbes in the indoor environment are bacteria and fungi. The spores produced by fungi can mix into the air, while some fungi can also produce toxic substances, such as mycotoxins or volatile organic compounds. Most airborne bacteria exhibit optimum growth in mesophilic condition (20 to 35 $^{\circ}$C) (Feysa *et al*., 2019).

The aim of this study was to assess the level of bacterial and fungal contaminations in two air-conditioned laboratories in STRIDE's Main Complex, Kajang, Selangor. This information is needed

to find out the baseline data of microbial concentration in these premises. There is not a lot information regarding the level of bacterial and fungal contamination in office premises, especially in laboratory working areas in Malaysia.

2. METHODOLOGY

2.1 Study Location

The study was conducted in three sampling locations (two laboratories and one outdoor) in April 2019. Laboratories chosen for this study were Laboratories A and B, which are in the same building and at the same floor. Laboratory A started operations in 2018, while Laboratory B has been operating since 2013. Laboratory A was selected to be studied as this facility is used to carry out microbiological tests and analyses. Meanwhile, Laboratory B is used to test and analyse textile samples received from other laboratories in STRIDE. Both laboratories use split air conditioning systems, which were in operation during the study. Each measurement was conducted in three time intervals (morning, noon and evening). The air samples were taken in the centre of each sampling sites locations or at the height of about 1.5 m above the ground for the outdoor samples, to simulate respiration in the human breathing zone.

2.2 Air Sampling Equipment and Procedure

At each site, a series of air samples in triplicate were collected on Tryptic Soy Agar (TSA) agar (bacteria) and Malt Extract Agar (MEA) (fungi) plates using a BioStage® single stage viable cascade impactor attached to a SKC Quick Take 30 sample pump. Each air sample was collected for 2 min at a sampling flow rate of 28.3 L/min (NIOSH, 1998). The sampling pump with representative sampler in line was calibrated before each use using rotameter and the impaction aperture cleaned with sterile alcohol wipes between sampling events to minimise cross contamination between locations. The samples were transported promptly to the laboratory for analysis.

2.3 Bioaerosols Observed and Enumerations

The samples were assessed in the laboratory for enumeration of viable bacteria and fungi. The agar plates for bacteria were incubated at 35 $^{\circ}$C for 24-48 h. Meanwhile, the agar plates for fungi were incubated at 25 $^{\circ}$C, with the growth observed between 3 to 5 days after sampling. Enumeration of the colony growth was measured using an automatic colony counter. The results were expressed as colony forming unit (CFU) per cubic metre of air (m^3) based on the following equation:

$$\text{CFU } (m^3) = \frac{\text{Numberof Colonies\# x 1,000}}{\text{Sampling time(min)x Flow rate (L/min)}} \quad (1)$$

adjusted for multiple –jet impaction using the positive hole correction table (Macher, 1989)

The maximum acceptable value for total bacteria count used in this study is not more than 500 CFU/m^3 (WHO, 1990), while the maximum acceptable value for fungi is not more than 1,000 CFU/m^3 (ACGIH, 2009).

2.4 Statistical Analysis

The data was analysed using Statistical Packages for Social Sciences (SPSS version 22.0). The normal distribution of data was analysed using the Kolmogorov- Smirnov test. For the non-parametric tests, the Kruskal-Wallis test was used since the data was not normally distributed for the comparison of the bioaerosol data of the three different locations (Laboratories A and B, and outdoors) and three time intervals (morning, noon and evening). A *p*-value of less than 0.05 was considered significant.

3. RESULT & DISCUSSION

The average concentration (median) of the bioaerosols in the three sampling sites is presented in Table 1. Laboratory B had both total bacteria and fungal counts that were higher than Laboratory A. However, statistical analysis with the Kruskal-Wallis test of the bacteria and fungal counts did not show statistically significant differences between both laboratories ($p > 0.05$). The outdoor environment had bacteria count of 120 CFU/m^3, which is still an acceptable value based on WHO (1990). However, it had very high fungal count (2,537 CFU/m^3), which exceeded the limit of 1,000 CFU/m^3 set by ACGIH (2009). The Kruskal-Wallis test showed statistically significant differences between Laboratory A and the outdoor environment ($p < 0.05$), and between Laboratory B and the outdoor environment ($p < 0.05$) for both bacteria and fungal counts.

Table 1: Comparison of bacteria and fungi concentration in the three different sampling sites.

Workplaces	Total Bacteria Count (CFU/m^3)		Total Fungi Count (CFU/m^3)	
	Median	Standard	Median	Standard
Laboratory A (*N*=45)	35	500 (WHO, 1990)	71	1,000 (ACGIH, 2009)
Laboratory B (*N*=18)	64		131	
Outdoor (*N*=36)	120		2,537	

N - Number of samples

The low levels of microbial contamination in the studied laboratories suggested that, in most cases, efficient and regularly maintained air conditioning systems ensure proper hygienic conditions of office workplace. The study by Stanley *et al*. (2019) found that buildings with air conditioning systems had lower bacterial contamination as compared to buildings with natural ventilations. The analysis of microbial contamination showed that the concentration of bacterial and fungal aerosols were higher outdoors than indoors. This is a good indicator that this building is protected from the higher bacterial and fungal contaminations from the outdoor environment.

The results were further examined for the three different time intervals. Figure 1 highlights the bacteria concentration for the time intervals. Overall, the results showed lower average bacteria concentration indoors (Laboratories A and B) than outdoors for the time intervals. Significantly higher bacterial concentration was recorded for outdoors (166 CFU/m3) in the morning time interval. Comparatively, the indoor samples (Laboratories A and B) had very low concentration of less than 70 CFU/m3 for all three time intervals. Using the Kruskal-Wallis test, there were no significant difference between Laboratories A and B, and outdoors for all time intervals ($p = 0.659$). We assumed that the distribution of bacteria concentration was quite similar throughout the day. This is due to low bacteria concentration recorded indoors and outdoors due to the weather condition during this study,

and regular cleaning and housekeeping in the two laboratories and outside the building. The bacteria colony growth in the petri dishes showed lower number of colony growth for outdoors (Figure 2a) as compared to indoors (Figure 2b).

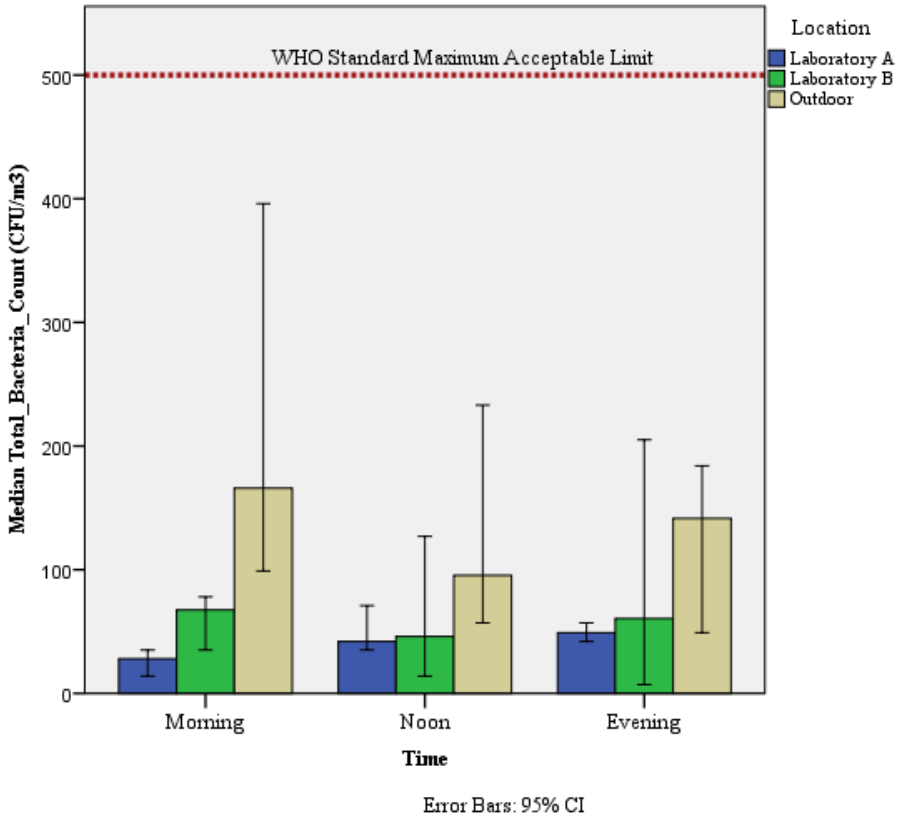

Figure 1: Comparison of bacteria detection between the three different interval times.

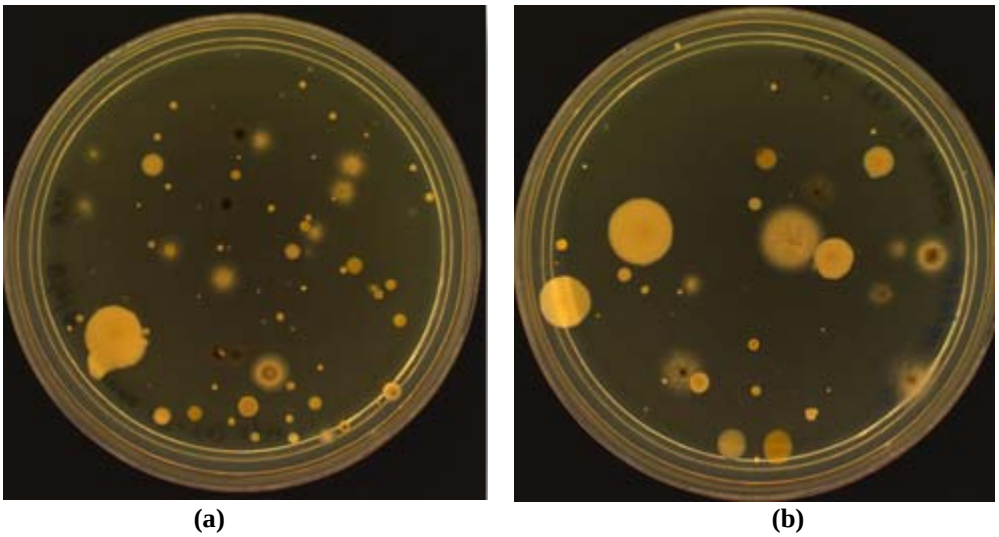

(a) **(b)**

Figure 2: Examples of bacteria growth in TSB Media: (a) Outdoors (b) Indoors (Laboratory B).

Figure 3 highlights the fungal concentration for the three different time intervals. Overall, the results showed very low fungal concentration for indoors (Laboratories A and B) (less than 200 CFU/m^3) for the morning and noon samples. Slightly high fungal concentration in Laboratory B (371 CFU/m^3) for the evening samples was recorded. However, significantly high fungal concentration was recorded for

outdoors for all three time intervals, exceeding the limit of 1,000 CFU/m^3. Using the Kruskal-Wallis test, there were no significant difference between Laboratories A and B, and outdoors for all three time intervals (p = 0.599) for fungal concentration. We assumed that the very high distribution of fungal concentration outside the building is due to the presence of plants and trees, including flower trees, grass and decorative trees (Feysa *et al*., 2019). The higher fungal contamination for outdoors could also be due to paint on the walls and ceilings of the building peeling off. The fungal colony growth in petri dishes showed very high fungal concentration for outdoors (Figure 4a) and very low fungal concentration for indoors (Figure 4b - Laboratory A and Figure 4c - Laboratory B). This study showed that this building is free from fungal contamination due to high fungal concentration outdoors rather than indoors. The indicator that a building has a problem with fungal contamination is when fungal concentration is higher indoors as compared to outdoors. We assumed that the air conditioning systems in this building managed to control the temperature and humidity indoors so that the level of relative humidity is low. Low moisture is able to control fungal growth indoors (Dedesko & Siegel, 2015).

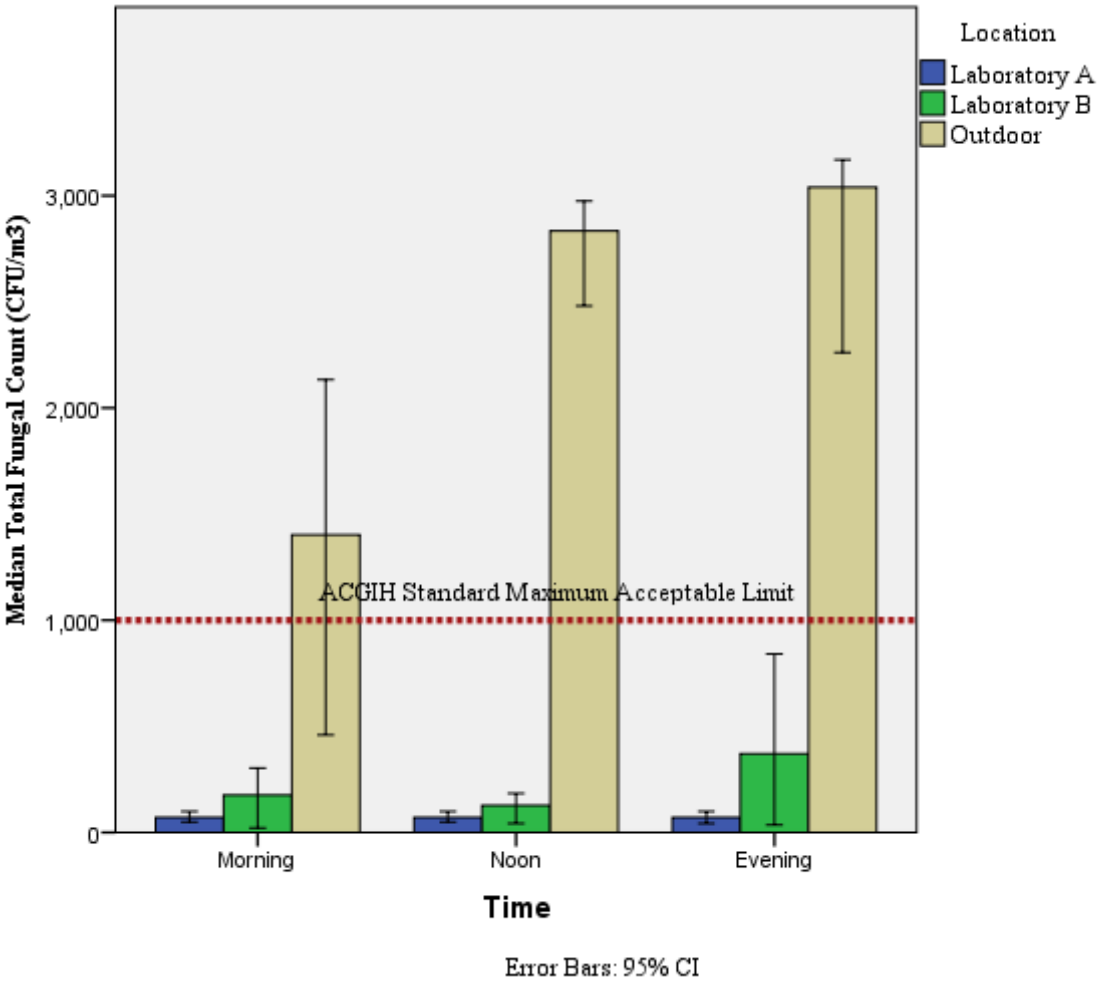

Figure 3: Comparison of fungi concentration for the three different time intervals.

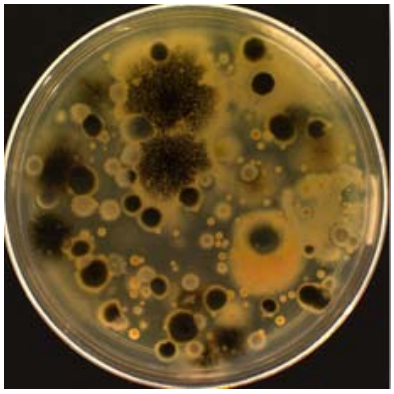

(a)

(b)

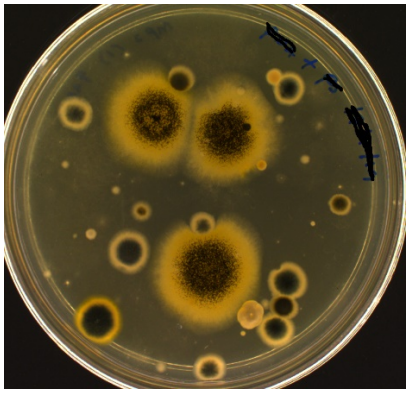

(c)

Figure 4: Examples of fungal growth in MEA Media: (a) Outdoors as well as indoors (b) Laboratory A and (c) Laboratory B.

4. CONCLUSION

The results obtained in this study indicated that the two laboratories' exposure to airborne bacteria and fungi is generally low and safe for laboratory workers. This study showed that the average concentration of bacterial and fungal aerosols in indoors environment did not exceed 500 CFU/m^3 for bacteria and 1,000 CFU/m^3 for fungi. The recorded low contamination levels of viable bacteria and fungi suggested that efficient and regularly maintained air conditioning systems ensure proper hygienic quality of office buildings (Golofit-Szymczak & Gorny, 2010). It is therefore important to provide appropriate indoor work conditions in order to ensure high productivity and to avoid health concerns of the workers in the laboratories.

REFERENCES

ACGIH (American Conference of Governmental Industrial Hygienists) (2009). Threshold limit values (TLVs) for chemical substances and physical agents and biological exposures indices (BEIs). American Conference of Governmental Industrial Hygienists (ACGIH), Ohio.

Barlett, K.H., Kennedy, S.M., Brauer, M., Van, N.C. & Dill, B. (2004). Evaluation and determinants of airborne bacterial concentrations in school classrooms. *J. Occup. Environ. Hyg.*, **1**:639-47.

Bohlan, R. & Subratty, A.H. (2002). Indoor biological contaminants and symptoms of sick building syndrome in office buildings in Mauritius. *Int. J. Environ. Health Res.*, **12**: 93-8.

Cox, C.S. &Wathess, C.M. (1995). *Bioaerosol Handbook*. Lewis Publishers, New York.

Dedesko, S. & Siegel, J. A. (2015). Moisture parameters and fungal communities associated with gypsum drywall in buildings. *Microbiome*, **3**: 71.

Douglas, S.I & Robinson, V.K. (2018). Fungal pollution of indoor air of some health facilities in Rivers State. *Int. J. Tropical Dis. Health*, **32**:1-7.

Dutkiewicz, J., Jblonski L. & Olenchocck S.A. (1988). Occupational biohazards: a review. *Am. J. Industrial Med.*, **14**: 605-623.

Feysa, B., Elanur, A., Suleyman, S. & Yasar, N. (2019). The determination of microorganisms in indoor and outdoor atmosphere in the Y.T.U Davutpasa Campus. *Sigma J. Eng. Nat. Sci.*, **37**: 563-571.

Geogakapolus, D.G, Despress, V. & Froehlich-Nowoisky, J. (2009). Microbiology and atmospheric processes: biological, physical and chemical characterization of aerosol particles. *Biogeosci.*, **6**: 721-37.

Golofit-Szymczak, M. & Gorny, R.L. (2010). Bacterial and fungal aerosols in air-conditioned office building in Warsaw, Poland. *Int. J. Occup. Saf. Ergon.*, **16**: 465-476.

Hagreaves, M., Parapppukkaran, S, Morawska, L., Hitchins, J. Congrong, H., & Gilbert, D. (2003). A pilot investigation into association between indoor airborne fungal and no biological particle concentrations in residential houses in Brisbane. *Sci. Total Environ.*, **312**: 89-101.

Hazrin, A.H., Anis Syazana, A.A., Noor, F.H.N., Norhidayahm A. & Mohd, S.M.A. (2015). Indoor microbial contamination and its relation to physical indoor air quality (IAQ) characteristics at different laboratory conditions. *J. Tek.*, **77**:39-44.

Heikkienen, M.SA., Hjelmroos-Koski, M.K., Haggblom, M.M. &Macher, J.M. (2005). Biaoeroslos. *In* Ruzer, L.S. & Harley, N.H. (Eds.), *Aerosol Handbook*. CRC Press, Boca Raton, pp. 291-342.

Hwang, S.H. & Yoon, C.S. (2016). Main environmental factors affecting concentrations of culturable airborne bacteria in indoor laboratories over a period of one year. *Appl. Ecol. Environ.Res.*, **15**: 321-333.

Macher, J. (1989). Positive-hole correction of multiple-jet impactors for collecting viable microorganisms. *Am. Ind. Hyg. Assoc. J.*, **50**:561-568.

Mbakwem-Aniebo, C., Stanley, H.O. & Onwukwe, C.D. (2016). Assessment of indoor air quality of majors' biological laboratories in Ofrima Complex, University of Port-Harcourt, Nigeria. *J. Pet. Environ. Biotechnol.*,**7**: 1000285.

NIOSH (National Institute of Occupational Safety and Health) (1998). Method 0800: Biaerosol sampling (indoor air). *In NIOSH Manual of Analytical Methods* (NMAM), 4th Ed. National Institute of Occupational Safety and Health (NIOSH), Ohio.

Seppaenen, O. & Fisk, W.J. (2002). Association of ventilation system type with SBS symptoms in office workers. *Indoor Air*, **12**:98-112.

Skowron, J. & Golofit-Szymczak, M. (2004). Microbiological air pollution in the working environment-sources, types and monitoring. *Bromat. Chem. Toksykol.*, **37**: 91-98.

Srikanth, P., Sudharsanam, S. & Steinberg, R. (2008). Bioaerosols in indoor environment: Composition, health effects and analysis. *Indian J. Med. Microbiol.*, **26**: 302-312.

Stanley, H.O., Onwuna, B. & Ugboma, C.J. (2019). Microbial assessment of indoor air quality of ventilation systems. Asian J. Adv. Res. Rep. **3**: 1-7.

Stetzenbach, L.D (1997). Introduction to aerobiology. *In* Yates, M.V., Nakatsu, C.H., Miller, R.V. & Pillai, S.D. (Eds.) *Manual of Environmental Microbiology*. ASM Press Washington DC, pp. 619-628.

Stetzenbach, L.D., Buttner, M.P. & Cruz, P. (2004). Detection and enumeration of airborne contaminants. *Curr. Biotechnol.*, **15**:170-174.

WHO (World Health Organization) (1990). *Indoor Air Quality: Biological Contaminants*. World Health Organization (WHO), Geneva.

Xi, L., Xue, Z., Wenji, W. & Kang, N. (2018). Microbial contamination screening and interpretation for biological laboratory environments. *bioRxiv*: doi: https://doi.org/10.1101/439570

Yau, Y.H., Chew B.T. & Saifullah A.Z.A. (2012). Studies on the indoor air quality of pharmaceutical laboratories in Malaysia. *Int. J. Sustain. Built Environ.*, **1**:110-124.

RELATIONSHIP ANALYSIS OF FORMAL AND EXPERIENTIAL LEARNING IN MILITARY SURVIVAL SKILLS USING TEXT MINING

Zuraini Zainol[1*], Puteri N.E. Nohuddin[2], Nur Diyana Kamarudin[3], Angela S.H. Lee[4] & Sharyar Wani[5]

[1]Department of Computer Science, Faculty of Science and Defence Technology, National Defence University of Malaysia (UPNM), Malaysia

[2]Institute of Visual Informatics, Universiti Kebangsaan Malaysia (UKM), Malaysia

[3]Cyber Security Centre, National Defence University of Malaysia (UPNM), Malaysia

[4]Department of Computing and Information System, Sunway University (SU), Malaysia

[5]Department of Computer Science, International Islamic University Malaysia (UIAM), Malaysia

[*]Email: zuraini@upnm.edu.my

ABSTRACT

Tacit knowledge tends to be an invaluable knowledge repository in lifelong learning. Critical domains such as military learning cannot solely rely on traditional manuals and methods due to the unforeseen and uncertain scenarios brought about by advances in modern warfare methods and technology. There is essential knowledge hidden in experiential learning that is very difficult to formalise but critical to be incorporated and taught. The current work aims to extract the relationships between lesson learnt from experiences and current basic military survival skills training among a group of officer cadets using the framework of document and keyword relationship analysis (FDKRA). Finally, the relationships are presented using various visualisation techniques, including word cloud, network graph and bubble graph. The research reveals the existence of important knowledge, not contained otherwise in formal documentation, and thus, highlighting the need to examine and generate a tacit knowledge corpus especially in critical domains.

Keywords: *Tacit knowledge; text mining; experiential learning; military survival skills; keyword relationship analysis.*

1. INTRODUCTION

The nature of warfare has evolved over the past decades, not only with the dramatic advances in warfare technology but primarily because of the uncertain scenarios it brings along. The traditional nature of training was focused on specialised training mechanisms and guide books that covered most of the probable scenarios and their off-shoots of combat deployment. Modern education, in general, stresses on lifelong learning, which has particularly and largely affected military training given the critical nature and dynamic changes in this field. Over the years, military deployments have incorporated far greater techniques and responses, often not contained in traditional manuals. This is referred as tacit knowledge, which is knowledge that exists as skills and experiences over time, and that is difficult to transfer in a codified manner. Tacit knowledge has not been given much importance, owing to the fact that it varies from person to person, situation to situation, etc. However, tacit knowledge has come to be regarded as an unmatched knowledge repository that contains vital and critical knowledge for many areas in military training especially the gamut of survival skills owing to the uncertainty in modern warfare. Numerous researches strongly suggest the aforementioned conclusions (Nohuddin & Zainol, 2014; Yusof *et al.*, 2016, 2018; Zainol *et al.*, 2017a; Alkhred *et al.*, 2018). The nature of tacit knowledge makes it difficult to formalise it. However, due to its unprecedented importance, it is a valuable asset in the modern-day warfare. The research in this

area can effectively reveal and bridge the gap between formal and field knowledge for cadets in learning institutions.

Therefore, this paper aims to study the relationships between lesson learnt from experiences of military respondents (officer cadets) and selected important keywords in basic military survival skills at the National Defence University of Malaysia (UPNM). A combination technique of text mining and network analysis is developed to discover interesting patterns and relationships derived from the undertaken military trainings. In this study, network analysis is an abstract model that contains a set of nodes and edges (linkages) that are connected together in the form of a graph. The nodes represent selected keywords and linkages between keywords that are established according to term frequency-inverse document frequency (TF-IDF) weightage for each keywords. This information was obtained using online survey questionnaires relating to military survival and situation awareness tasks. Finally, the paper presents the relationships using document and keyword matrix (DKM), network graph and bubble graph.

The remainder of the paper is organised as follows: Section 2 discusses related works concerning military survival skills, text mining, document analysis and keyword extraction using TF-IDF. Section 3 presents the framework for relationship analysis, while Section 4 focuses on the experimental setup and its results. Finally, the conclusion is discussed in Section 5.

2. BACKGROUND AND RELATED WORKS

This section presents some background information that is related to the topics on military survival skills, text mining, document analysis and keyword extraction using TF-IDF.

2.1 Military Survival Skills

The entrance of new educational technology that involves lifelong learning has changed the nature of contemporary higher military education. Future cadets are believed to be more profiled than specialised in their military training (Terziev & Nichev, 2017). In other words, the future cadets' military training will be focused on explicit tasks to improve the quality and competitiveness of the military education in general, increasing personal cadets' satisfaction in the process of training, and improving the organisation and content of the military professional training. The motivation of military survival skills is to teach soldiers or cadets the skills necessary for captivity survival under conditions of high fidelity and realism (Vartanian *et al.*, 2018). In this regard, according to Myrseth *et al.* (2018), future cadets should have a strong ability to learn how to survive in difficult situations or emergency deployment, and bear with uncertainty in various conditions to mitigate the effects of stressors, such as sleep deprivation, exhaustion, starvation, dehydration, and physical distress on physiological and psychological performance.

For many years, the literature focused more on military psychology and its impact on stress reactions and impaired performance (Taylor *et al.*, 2011; Lauria *et al.*, 2017; Crane *et al.*, 2018; Lo Bue *et al.*, 2018) and less on military tacit knowledge representation for military survival skills (Hedlund *et al.*, 2003; Zainol *et al.*, 2017b, 2018a). Tomczak *et al.* (2017) claimed that numerous endurance strength military trainings together with sleep deprivation can improve performance, and thus, it should be introduced during military survival training. To assess their physical and psychological abilities during survival training, a measure of perceived specific military skills comprises of three subscales that can be used under operational and combat circumstances. The three subscales are individual coping capacity (ICC), cooperation in difficult situations (CDS) and motivation to achievements (Myrseth *et al.*, 2018). Similar survival attributes, such as coping skills, defence mechanisms and self-motivational or self-efficacy, were discussed in Pope *et al.* (1999).

2.2 Text Mining

Text mining or text analysis refers to the numerous techniques to extract informative patterns or useful information from huge amount of textual data (Sohrabi *et al.*, 2018). The text concept of text mining is different from data mining, where it focuses only on extracting useful knowledge representation from unstructured or semi-structured text, as compared to databases in data mining (Nagarkar & Kumbhar, 2015). Several attempts have been made by the researchers to process unstructured data (Figure 1), which covers most of the big data processes, such as information technology, text analysis, pattern recognition, statistics, data visualisation, database technology, machine learning and data mining technology (Shuai *et al.*, 2018). Various text mining techniques have been implemented to discover useful knowledge of text, although it still needs human intervention to interpret the output of text mining (Hakim *et al.*, 2018).

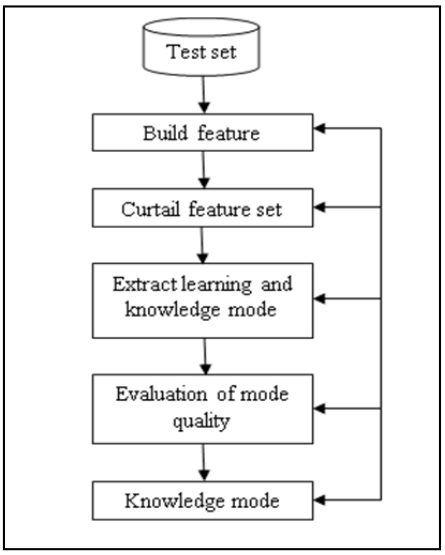

Figure 1: General process of text mining (Shuai *et al.*, 2018).

In general, several scholars from diverging fields have employed text mining to extract useful information via social media (Abbasi *et al.*, 2018; Adamopoulos *et al.*, 2018; Bollegala *et al.*, 2018). In Valle-Cruz *et al.* (2017), a radial word cloud is generated based on data collected to classify topics in Twitter. These radial words are partitioned into three categories consisting of core words (with the highest frequency), middle words (with important frequency) and border words (less significant frequency with bad or nasty words). Other researchers have implemented text mining for their research development, including biomedical literature mining (Bhasuran *et al.*, 2018; Rasid *et al.*, 2018; Sun *et al.*, 2018; Xing *et al.*, 2018); defence and security (Li *et al.*, 2016; Sohrabi *et al.*, 2018; Zainol *et al.*, 2018b); automated surveillance systems (Baek & Hong, 2017; Kwon *et al.*, 2017); political communications (Mhamdi *et al.*, 2018; Redek and Godnov, 2018); and relationship analysis of keywords and chapters of the Quran and Hadith (Nohuddin *et al.*, 2013; Nohuddin *et al.*, 2015; Zainol *et al.*, 2016). Several others have used semantic networks, human communication principles, logic, linguistics, etc., to extract and represent important information within the text (Wani *et al.*, 2018, 2019; Zainol *et al.*, 2018c). Some other studies have applied text mining that focused on frequent patterns to generate association rules (Kulkarni & Kulkarni, 2016; Zainol *et al.*, 2018e).

In the military operations context, Marzukhi *et al.* (2018) proposed a framework of "Knowledge-Based System" to assist the Malaysian United Nations Military Observers (UNMO) in conducting the United Nations (UN) peacekeeping operations at the countries of deployment. By using data mining techniques (e.g., clustering or association rule mining), beneficial knowledge, including hidden patterns from various sources related to the peacekeeping mission that is required by UNMO, can be integrated into the rugged tablet or any pervasive equipment to assist in peacekeeping operations. Research of text mining in social media has gained increasing attention of current researchers, covering various social media platforms, such as Facebook and Twitter. To analyse the sentiment in

social media posts, Gil *et al.* (2018) performed a tweet analysis of feelings and opinions from Twitter related to the Colombian post conflict, which has become a widely debated topic in the world. A total of 250 tweets of Colombians and 250 tweets of foreigners were collected. Word cloud and Excel tool "TEXT2DATA" were implemented, with the latter being a prominent tool for text and keyword classification that offers text analytics SaaS services such as in-depth analysis, social media data, cloud computing and features such as sentiment analysis application programming interface (API), Twitter sentiment engine, and user classification models. Using comparative analysis, they have observed that the tweets of foreigners have more positive feelings as compared to the Colombian tweets.

In addition, scholars in China have adopted text mining for medical records and literature to determine the commonalities between rheumatoid arthritis (RA) and diabetes mellitus (DM) to understand the mechanisms of Chinese medicine (CM) and provide intervention in diagnosis (Zhao *et al.*, 2018). They applied semi-structured data from PubMed articles with the terms *rheumatoid arthritis* and *diabetes mellitus*. The dataset was downloaded in the form of an XML file. One dataset containing 104,481 items for RA, and another dataset containing 260,008 items for DM were obtained, and a similar process of text mining was implemented. The calculation of the network of patterns associated with Chinese herbal medicine (CHM) is performed using a different approach, which is based on the association of the patterns with CHM. The calculation was based on the principle of co-occurrence of CM pattern and CHM within the same article. The commonalities existing between networks of CM patterns, herb formula, and biological networks of diseases RA and DM were measured, and statistical analysis between attributes were calculated using the SAS 9.1.3 statistical package.

2.3 Document Analysis

Text mining has been successfully used by many researchers to examine huge amounts of text data in the business, health-care and education sectors. According to Abdous & He (2011), text mining has the ability to transform raw data into valuable information that can be actionable. Their research used text mining to study questions that students uploaded online, and identified student learning trends and technology-related problems. Besides that, a research conducted by Yassine & Hajj (2010) used text mining to determine the emotions of the texts in social media. Their research used text clustering, text classification, data pre-processing and data mining to determine whether there are emotions in the texts.

Text mining consists of two phases, which are text refining and knowledge distillation. In the text refining phase, text documents are transformed into either document-based intermediate form or concept-based intermediate form. A document-based intermediate form can also be converted into a concept-based intermediate form by extracting the related information. This is represented in Figure 2, Stage 2. The knowledge distillation phase consists of a process whereby patterns and facts from the intermediate form is understood in Stage 2 (representations). Document-based intermediate form falls under clustering, categorisation and visualisation in Stage 3 (analysis) (Lee *et al.*, 2018).

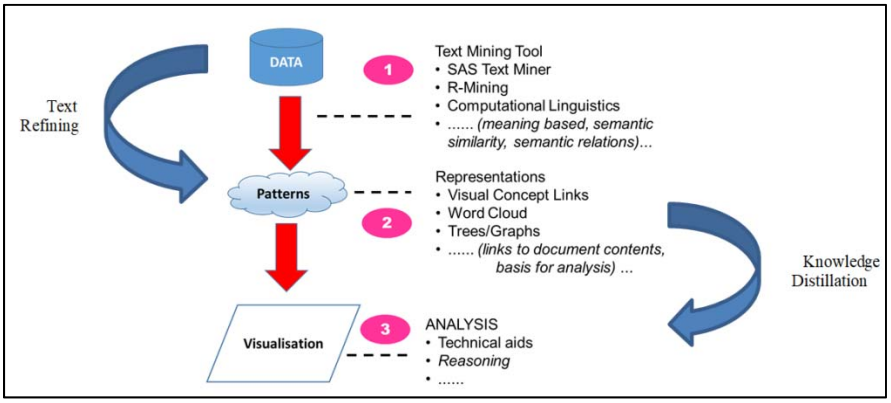

Figure 2: Text mining phases (Adopted from Lee *et al.*, 2018).

2.4 Keyword Extraction Using Term Frequency-Inverse Document Frequency (TF-IDF)

The term information extraction was known and has grown since the 1980s. One of the most important aspects of text mining is information extraction, which extracts and identifies important information hidden in the texts. The information identified relates to some entities, events or relationships between the entities. The information extracted will then be transferred and kept in a database for queries and mining to discover the hidden knowledge (Umajancy & Thanamani, 2013). According Sarawagi (2008), information extraction relates to identifying entities relationship and also the characteristics that describe the entities. Information extraction differs from information retrieval, whereby the aim of information extraction is to identify particular features from the unstructured text contained in a document instead of the whole document.

Corpus is a collection of documents, where these documents consist of a set of tokens. A token is a string of characters, whereas a term is a sequence of tokens. Natural language processing is employed to try to figure out what term is indicated by the token. Therefore, various weighing strategies are introduced to count the terms. The basic strategy for quantifying each term involves obtaining the corpus of terms and performing simple data cleaning such as stemming, text parsing and text filtering. Next is to represent each document and each term into a matrix form in a vector space to perform topic clustering. In order to measure which term has the highest weight, term frequency (TF) will be needed to count how frequently the word appears in the document. There are times where a word occurring in a document is unimportant, even though the frequency count is high. Therefore, simple data cleaning process needs to be conducted such as removing the stop words and stemming. A list of stop words may be generated from here (Zipf, 1949; Hong *et al*., 2013).

Another strategy is to look at the term's inverse document frequency (IDF), whereby it uses the entropy weight formulas. The formulas decrease the weight of commonly used words that appear in the document and increase the weight of words that have less frequency. In other words, if a term appears in every document, then IDF weighs it as 1. In order to know whether the word is important or not, each term frequency will be taken into consideration. The general formula used for IDF (Hong *et al.*, 2013) is as follows:

$$(TF\text{-}IDF)_{i,j} = TF_{i,j} \times IDF_{i} \quad (1)$$

Besides the above strategy, another well-known formula would be Zipf's Law (Zipf, 1949). The Zipf formula is to rank words in decreasing frequency from a very large text document and plot a log graph (Figure 3). Zipf's Law allows the identification of important terms used in the documents (Chakraborty *et al*., 2013).

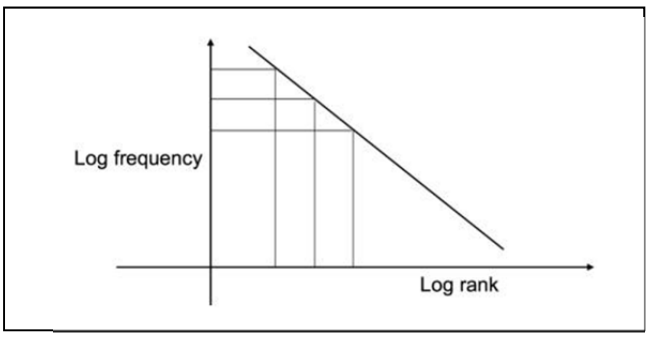

Figure 3: IDF with Zipf's Law (Adopted from Robertson, 2004).

3. FRAMEWORK OF DOCUMENT AND KEYWORD RELATIONSHIP ANALYSIS

The proposed framework is an enhanced version adopted from Nohuddin & Zainol (2014) and Zainol *et al.* (2018d). The optimised framework is used to generate term relationships' from the survey documents, answered by military respondents. Figure 4 illustrates the framework of document and keyword relationship analysis (FDKRA). It consists of four phases: (i) An online platform for survey collection from respondents; (ii) Processing and conversion of the survey content into military tacit knowledge base; (iii) Document and keyword analysis module; and (iv) Visualisation features to present experiment findings. Document and Keyword Analysis is the main analysis engine for extraction and ranking of documents and keywords / term relationships from the military tacit knowledge base. Finally, the discovered document and keyword relationships are presented using three visualisation types; word cloud, network graph and bubble graph. The data repository is called as Military Tacit Knowledge Base. It embraces the term "knowledge base" to characterise its knowledge repositories to serve as a repository of manuals, procedures, policies, best practices, reusable designs and code, etc. A knowledge base is a special kind of database that offers resources for the computerised collection, organisation and retrieval of knowledge in a specific field (Ritchey *et al.*, 2011).

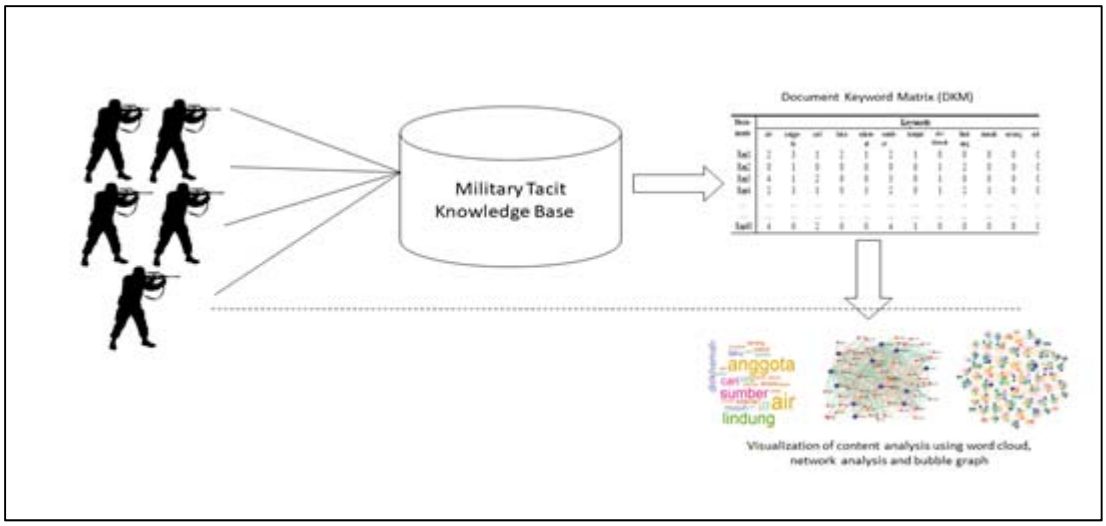

Figure 4: Framework of document and keyword relationship analysis (FDKRA).

The tacit knowledge was collected using an online survey, among officer cadets at UPNM. This method offers higher response speed as compared to other survey methods (Sue & Ritter, 2011), such as interview, face-to-face interview, mail, etc. The questions in the online survey are based on the basic military survival skills. Table 1 presents a sample of the questions used in the online survey. The respondents consist of both male and female officer cadets from UPNM, who are in their third or fourth year of studies. The diverse sampling is achieved by including officer cadets from different undergraduate courses in three different military services, i.e., Malaysian Army, Royal Malaysian Navy and Royal Malaysia Air Force. The survey dataset underwent text pre-processing to ensure correct format for different terms and keywords before text analysis.

The next element in the FDKRA describes the representation of the document, which refers to respondent and keyword findings and analysis. Based on the keyword pattern found in the documents, the related patterns within a group are discovered. The relationship of the keywords should represent the content of respondents' answers in the survey. As mentioned earlier in Section 3, this paper is a part of the second component of FDKRA, focussing on grouping of selected keywords and visualising them as important keywords from lessons learnt through experiences and skills among officer cadets.

Table 1: Sample of the online surveys questions adopted from Zainol *et al.* (2018d)

	Questions
1.	*Anda sebagai Pegawai Muda dan anda ditugaskan untuk mengetuai sebuah operasi di hutan Grik untuk mengesan saki baki komunis. Pada pendapat anda apakah perkara yang paling utama perlu dilakukan selepas menduduki pangkalan?* You as a young officer and you are assigned to head an operation in the Grik forest to detect the remnants of communism. In your opinion what is the most important thing to do after occupying the base?
2.	*Sila nyatakan kenapa anda beranggapan begitu?* Please indicate why you think so?
3.	*Sekiranya anda mendapati sumber air yang pasukan anda minum tercemar kerana telah diracuni pihak musuh. Apakah tindakan anda?* In case you have found a source of drinking water that is contaminated because your team has poisoned the enemy. What is your action?

3.1 Document and Keyword Module

This module is developed based on the concept of TF-IDF, counting and ranking the words in the given content, followed by selecting words that occur more than the threshold. This module generates a DKM, which is a *m* x *n* matrix that represents documents (surveys) versus terms (frequent keywords). DKM tracks the term frequency for each term in all the surveys. Thus, DKM can become a very large sparse matrix, depending on the number of surveys and number of terms in each survey. DKM representation is a method to represent the documents as numeric structures. Representing text as a numerical structure is a common starting point for text mining and analytics, such as search and ranking, creating taxonomies, categorisation, document similarity and text-based machine learning.

3.2 Keyword Relationship Visualization Module

The module consists of three different types of visualisations: (i) Word Cloud, a graphical representation of keyword frequency. Keywords are usually single words, with the importance of each keyword is differentiated with font size or colour; (ii) Network Graph illustrates relationships between survey documents and keywords. Keywords are displayed as round nodes and lines are used to represent the relationships between them; and (iii) Bubble Graph exhibits each document and its keywords. Each document is presented in a bubble and keywords associated with the documents are represented in sub-bubbles, following the DKM. Sub-bubbles are differentiated with colours and sizes.

4. RESULTS AND DISCUSSION

This section presents the experimental results using FDKRA. In this experiment, a set of 60 respondents from the online surveys is applied as the input. Each respondent corresponds to a single document. The online surveys are prepared as plain text documents. Text pre-processing is an important step in most text mining techniques and applications. It prepares the input data for consequent analysis. Low quality of text data affects the accuracy of text mining results. Most text-based documents are often very noisy containing typos, errors and multiple acronyms for the same word. The text is pre-processed to remove stop words, numbers, symbols, punctuation marks, etc., in order to achieve a reliable result. This can improve both the quality of data and accuracy, and effectiveness of text mining. There are two main steps in pre-processing: stop words removal and stemming. At first, all text documents (Figure 5) are converted into lowercase for standardisation. This is to ensure that multiple form of keywords such as "*pegawai*", "*Pegawai*", "*pegaWai*" and

"*PEGAWAI*" are treated similarly in the experiment. It is followed by removal of numbers, whitespace, punctuation marks and symbols from the plain text documents. The stop word removal and stemming steps are conducted manually as the automatic tools for Bahasa Malaysia are not readily available.

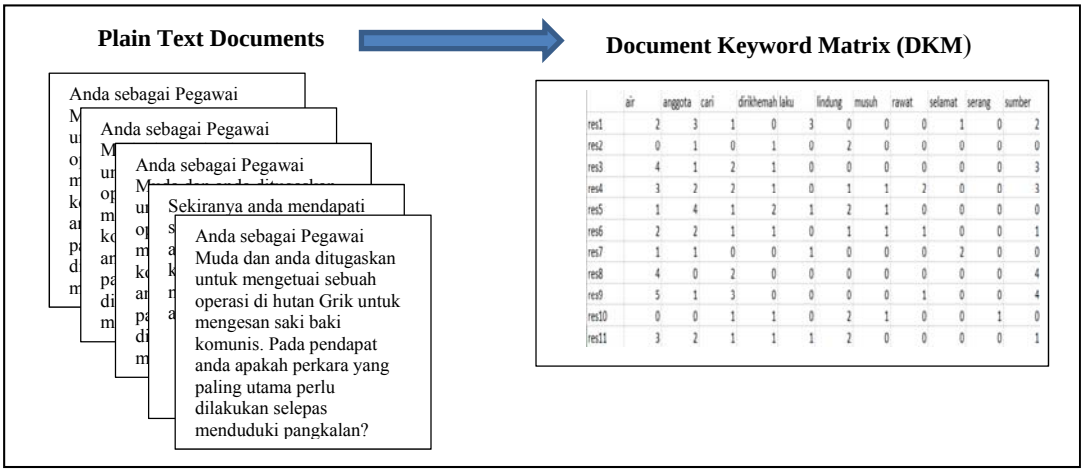

Figure 5: DKM processing

Most of text mining tasks require data to be represented in the form of a matrix or vector – document term matrix (DTM) or term document matrix (TDM). As illustrated in Figure 5, the Document Keyword Matrix (DKM) consists of 305 terms extracted from 60 documents with 94% sparsity. Sparsity refers to the threshold of relative document frequency for a term. The table below shows that 94% of the row entries in DKM contains zero entries. In other words, most keywords on DKM do not appear in most of text documents. For example, the keywords "*awal*", "*asing*", "*asas*", and "*aliran*" are marked as zero in most text documents. Therefore, these less frequent keywords need to be removed.

Table 2 shows the results of removing sparse in DKM, with 12 keywords extracted from 60 documents with 75% sparsity. In other words, a 60 x 12 matrix is created representing 12 unique keywords and 60 text documents. The new DKM becomes an input for the word cloud and network analysis graph for keywords and respondents. Figure 6 shows the visualisation of most frequently used keywords within the text documents, in the form of a word cloud. The size of keywords corresponds to the frequency of the terms. The larger font size corresponds to a higher frequency value. Based on our observation, the terms "*air*" (93), "*anggota*" (75), "*lindung*" (64), "*sumber*" (61), "*cari*" (46), "*laku*" (31), "*dirikhemah*" (40), "*musuh*" (30), "*tempat*" (26), "*serang*" (22), "*selamat*" (24) and "*sebut*" (24) have the highest frequencies in the dataset.

Table 2: Partial DKM (TF) after removing sparse terms.

Documents	Keywords											
	air	*anggo-ta*	*cari*	*laku*	*selam-at*	*sum-ber*	*temp-at*	*diri-khemah*	*lind-ung*	*musuh*	*sera-ng*	*sebut*
Res1	2	3	1	2	1	2	1	0	0	0	0	0
Res2	0	1	0	0	0	0	0	1	2	0	0	0
Res3	4	1	2	0	0	3	0	1	0	0	0	0
Res4	2	3	1	0	3	2	0	1	2	1	0	1
…	…	…	…	…	…	…	…	…	…	…	…	…
…	…	…	…	…	…	…	….	…	…	…	…	…
Res60	4	0	2	0	0	4	1	0	0	0	0	0

Figure 6: Word cloud of the DKM.

After the text documents are pre-processed, the DKM is transformed into a TF-IDF representation, which highlights important terms in the survey. The term-weighting statistics is applied for identifying important keywords in a collection of text documents. Each keyword is assigned a weight, which represents its importance in the text document (Table 3). The infrequent keywords with less weight are discarded. Thus, the list of terms in a text document can be arranged according to its importance. In this experiment, a subset of the most important terms is selected as keywords. The DKM also becomes an input for the network analysis map and bubble graph.

Table 3: Partial DKM (TF-IDF).

Documents	***Keywords***											
	air	***ang-gota***	***cari***	***laku***	***sela-mat***	***sum-ber***	***tempat***	***diri-khem-ah***	***lind-ung***	***mus-uh***	***sera-ng***	***sebut***
Res1	0.026	0.041	0.020	0.066	0.043	0.045	0.039	0	0	0	0	0
Res2	0	0.049	0	0	0	0	0	0.063	0.127	0	0	0
Res3	0.089	0.024	0.071	0	0	0.118	0	0.030	0	0	0	0
Res4	0.066	0.041	0.099	0.026	0	0.058	0.067	0.015	0.014	0.029	0	0.067
…	…	…	…	…	…	…	…	…	…	…	…	…
…	…	…	…	…	…	…	…	…	…	…	…	…
Res60	0.098	0	0.078	0	0	0.173	0.075	0	0	0	0	0

Although the DKM consists of the summary of respondents and their related keywords, it lacks visual representation of data, particularly mapping the relationship between keyword and respondents. Therefore, the DKM is transformed into a network analysis map to illustrate the connection of keywords and respondents linked to one another. Figure 7 illustrates the network analysis visualisation of the 60 respondents with all the keywords. The blue nodes represent the 12 keywords such as "*lindung*", "*sumber*", "*air*", "*anggota*", "*musuh*", "*dirikhemah*", "*tempat*", "*sebut*", "*selamat*" "*serang*", "*musuh*" and "*cari*". On the other hand, the red nodes represent the 60 respondents of the survey. The green and red lines represent the linkages between respondents and keywords. The thickness of colours for each connection is represented by the value of the occurrence of keywords in related documents, as per the DKM. For example, it can be clearly seen that the keyword "*air*" is linked to Respondents 5, 6, 12, 14, 26, 36, 45 47, 49, etc. These linkages denote that the keyword "*air*" is often mentioned by respondents in the survey. This relates to the survey on finding a water source after occupying the base during the mission.

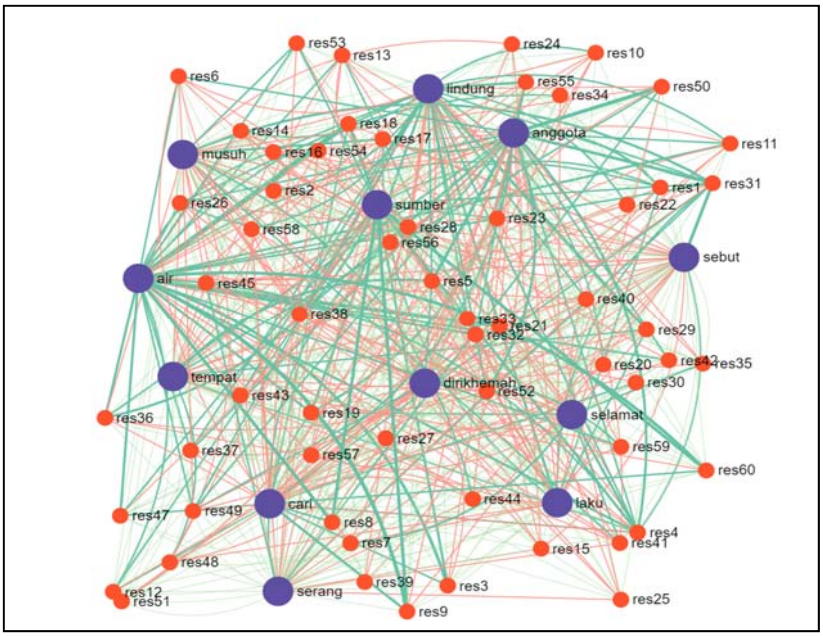

Figure 7: DKM network analysis map for selected important keywords.

Figure 8 visualises a bubble graph that illustrates 60 respondents with its important keywords developed from the DKM. This diagram is developed using Java Script. Each respondent is represented in a bubble together with its related keywords as sub-bubbles. The size of bubbles is dependent on the weight of a respondent and associated keywords. The legend on the left hand side contains 12 different coloured boxes indicating the type of keywords. The details of sub-bubbles can be further visualised by clicking on the selected bubble.

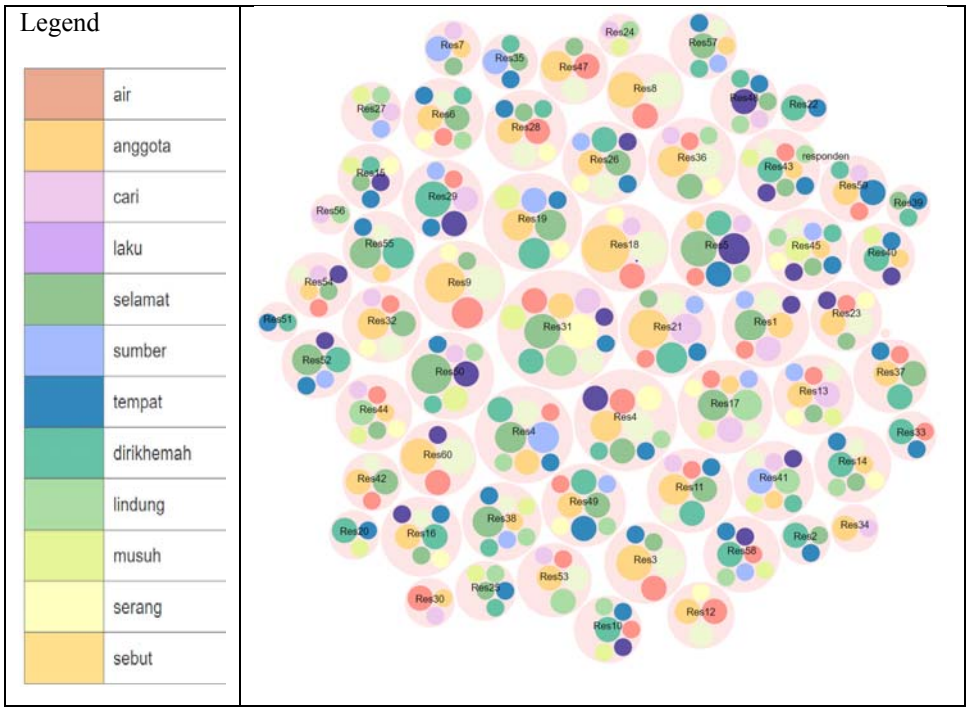

Figure 8: Bubble graph for 60 respondents and 12 keywords.

For example, the bubble graph for Respondent 18 can be further visualised in Figure 9. Basically, it consists of five small sub-bubbles that relate to important keywords such as "*serang*", "*anggota*", "*cari*", "*musuh*" and "*air*", which indicate that "*anggota akan mencari dan menyerang musuh, serta mencari sumber air*". In other words, the troops will search and attack the enemies, as well as look for water source.

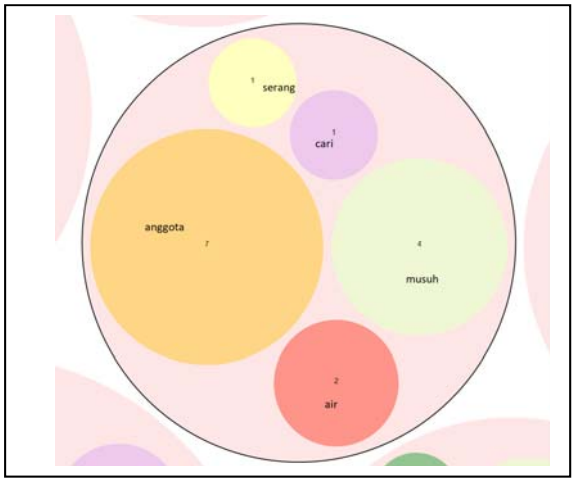

Figure 9: Bubble graph for Respondent 18.

5. CONCLUSION

In this paper, the FDKRA framework was used to enable the collection and processing of the content of military tacit knowledge using four main phases: (i) The first phase provides an online platform for survey collection from respondents; (ii) The second phase processes the survey content into military tacit knowledge base; (iii) The third phase consists of the document and keyword analysis module and (iv) The fourth phase provides visualisation features to present experimental findings. The results presented demonstrate specific findings from experiential-based learning and decisions that may not be explicitly taught as formal skills. It also highlights the need to examine the experiential corpora for the generation of a tacit knowledge corpora pertaining to different aspects of army training, in particular, and other critical domains, in general. The current study focused on the cadets undergoing training inside a specific institution. However, the broader aim was to understand the existence of tacit knowledge and revealing some critical information hidden in it, as compared to classical handbooks. Formal methods and dynamic tacit knowledge can together enhance the skills of the cadets, and prepare them to be better equipped to tackle modern day situations. This also applies to other critical domain such as healthcare, etc. This research investigated the best techniques for capturing military tacit knowledge amongst officer cadets. Future work will focus on knowledge collection and the process of extraction of keywords, based on semantic text patterns.

ACKNOWLEDGMENT

The authors wish to thank the National Defence University of Malaysia (UPNM) and Cyber Security Centre (PKS) for supporting this research. We also acknowledge the participation and cooperation received from officer cadets from Akademi Latihan Ketenteraan (ALK).

REFERENCES

Abbasi, A., Zhou, Y., Deng, S. & Zhang, P. (2018). Text analytics to support sense-making in social media: A language-action perspective. *MIS Quart.,* **42:** 427-464.

Abdous, M.H. & He, W. (2011). Using text mining to uncover students' technology□related problems in live video streaming. *Brit. J. Edu. Tech.,* **42**: 40-49.

Adamopoulos, P., Ghose, A. & Todri, V. (2018). The impact of user personality traits on word of mouth: text-mining social media platforms. *Inform. Syst. Res*., **29**: 612-640.

Alkhred, F., Nohuddin, P.N.E., & Zainol, Z. (2018). Sharing explicit knowledge: designing a peacekeeping operation databank. *Adv. Sci. Lett.,* **24**: 956-960.

Baek, S.-C. & Hong, W.-H. (2017). Exploring convergence research trends of spatial information based on UAV using text mining technique. *Spat. Inf. Res.,* **25**: 315-322.

Bhasuran, B., Subramanian, D. & Natarajan, J. (2018). Text mining and network analysis to find functional associations of genes in high altitude diseases. *Comput. Biol Chem.,* **75**: 101-110.

Bollegala, D., Maskell, S., Sloane, R., Hajne, J., & Pirmohamed, M. (2018). Causality patterns for detecting adverse drug reactions from social media: text mining approach. *JMIR Public Health Surveill.,* **4:** e51.

Chakraborty, G., Pagolu, M. & Garla, S. (2013). *Text-Mining and Analysis: Practical Methods, Examples, and Case Studies Using SAS*. SAS Institute Inc., Cary, North Carolina, USA.

Crane, M. F., Boga, D., Karin, E., Gucciardi, D. F., Rapport, F., Callen, J. & Sinclair, L. (2018). Strengthening resilience in military officer cadets: A group-randomized controlled trial of coping and emotion regulatory self-reflection training. *J. of Consult. Clin. Psychol*., **87**: 125.

Gil, V., Montoya, L. & Puerta, I. (2018). Sentiment analysis on post conflict in Colombia: A text mining approach. *Asian J. Appl. Sci.,* **6**: 53-59.

Hakim, L., Kusumasari, T.F. & Lubis, M. (2018). Text mining of UU-ITE implementation in Indonesia. *J. Phys.: Conf. Ser*. **1007**: 012038.

Hedlund, J., Forsythe, G.B., Horvath, J.A., Williams, W.M., Snook, S. & Sternberg, R.J. (2003). Identifying and assessing tacit knowledge: understanding the practical intelligence of military leaders. *Leadership Quart.,* **14**: 117-140.

Hong, T.-P., Lin, C.-W., Yang, K.-T., & Wang, S.-L. (2013). Using TF-IDF to hide sensitive itemsets. *Appl. Intel.,* **38**: 502-510.

Kulkarni, M., & Kulkarni, S. (2016). Knowledge discovery in text mining using association rule extraction. *Int. J. Comput. Appl.,* **143**: 30-35.

Kwon, H., Kim, J. & Park, Y. (2017). Applying LSA text mining technique in envisioning social impacts of emerging technologies: the case of drone technology. *Technovation,* **60**: 15-28.

Lauria, M. J., Gallo, I. A., Rush, S., Brooks, J., Spiegel, R. & Weingart, S. D. (2017). Psychological skills to improve emergency care providers' performance under stress. *Ann. Emerg. Med.,* **70**: 884-890.

Lee, A. S. H., Yusoff, Z., Zainol, Z., & Pillai, V. (2018). Know your hotels well! -- an online review analysis using text analytics. *Int. J. Eng. & Tech.,* **7**: 341-347.

Lo Bue, S., Kintaert, S., Taverniers, J., Mylle, J., Delahaij, R. & Euwema, M. (2018). Hardiness differentiates military trainees on behavioural persistence and physical performance. *Int. J. Sport Exercise Psy.,* **16**: 354-364.

Marzukhi, S., Mohammad Daud, N. H., Zainol, Z. & Zakaria, O. (2018). Framework of knowledge-based system for United Nations peacekeeping operations using data mining technique. *Proc. 4th Int. Conf. on Inf. Retrieval Knowl. Man. (CAMP),* pp 1-6.

Mhamdi, C., Al-Emran, M. & Salloum, S. A. (2018). Text mining and analytics: a case study from news channels posts on Facebook. *In* Shaalan, K., Hassanien, A.E. & Tolba, F. (Ed.) *Intelligent Natural Language Processing: Trends and Appl.*, Springer. pp. 399-415.

Myrseth, H., Hystad, S. W., Säfvenbom, R. & Olsen, O. K. (2018). Perception of specific military skills–the impact of perfectionism and self-efficacy. *J. Milit. Studies*, In press

Nagarkar, S.P. & Kumbhar, R. (2015). Text mining: An analysis of research published under the subject category 'information science library science' in web of science database during 1999-2013. *Libr. Rev.,* **64**: 248-262.

Nohuddin, P.N.E., Chua, S., & Ahmad, S. R. (2013). Keyword and chapter relationship analysis in the Tafseer of Al-Quran. *Proc. Taibah University Int. Conf. Adv. Info. Tech. Holy Quran Sci.*, pp. 264-269.

Nohuddin, P.N.E., & Zainol, Z. (2014). Context-based keyword pattern cluster analysis technique on tacit knowledge of military centre of expertise (COE): A preliminary study. *Proc. Int. Conf. Comp. Sci. Tech. (ICCST)*, Kota Kinabalu, Malaysia, pp. 1-5.

Nohuddin, P.N.E., Zainol, Z., Chao, F.C., James, M.T., & Nordin, A. (2015). Keyword based clustering technique for collections of Hadith chapters. *Int. J. Islamic Appl. Comp. Sci. Tech. (IJASAT),* **4**: 11-18.

Pope, R.P., Herbert, R., Kirwan, J.D., & Graham, B.J. (1999). Predicting attrition in basic military training. *Mil. Med.,* **164**: 710-714.

Rasid, N., Nohuddin, P.N.E., Zainol, Z., Hamzah, I., Alias, H. & Nordin, A. I. (2018). Experience mining through ethnography study among pediatric cancer patients in Malaysia. *Adv. Sci. Lett.,* **24**: 1562-1566.

Redek, T. & Godnov, U. (2018). Twitter as a political tool in EU countries during the economic crisis: A comparative text-mining analysis. *Drus. Istraz.,* **27**: 691-711.

Richey, R. C., Klein, J. D., & Tracey, M. W. (2011). *The Instructional Design Knowledge Base: Theory, Research, and Practice*. Routledge, New York, USA.

Robertson, S. (2004). Understanding inverse document frequency: on theoretical arguments for IDF. *J. Doc.,* **60**: 503-520.

Sarawagi, S. (2008). Information extraction. *Found. Trends Datab.,* **1:** 261-377.

Shuai, Y., Song, T., Wang, J. & Zhan, W. (2018). Hybrid reliability parameter selection method based on text mining, frequent pattern growth algorithm and fuzzy bayesian network. *J. Shanghai Jiaotong Uni. (Sci.),* **23**: 423-428.

Sohrabi, B., Vanani, I.R., & Shineh, M. B. (2018). Topic modeling and classification of cyberspace papers using text mining. *J. Cyberspace Studies,* **2**: 103-125.

Sue, V.M. & Ritter, L.A. (2011). *Conducting Online Surveys*. Sage Publications, Newbury Park, California.

Sun, W., Cai, Z., Li, Y., Liu, F., Fang, S. & Wang, G. (2018). Data processing and text mining technologies on electronic medical records: a review. *J. Healthcare Eng.,* **Vol. 2018:** 4302425.

Taylor, M.K., Stanfill, K.E., Padilla, G.A., Markham, A.E., Ward, M.D., Koehler, M.M., Anglero, A., & Adams, B.D. (2011). Effect of psychological skills training during military survival school: a randomized, controlled field study. *Mil. Med.,* **176**: 1362-1368.

Terziev, V. & Nichev, N. (2017). Analysis of the environment for military educational system functioning and its impact on the preparation of cadets for military professional activities in the Republic of Bulgaria. *Int. E-J. Advances Edu.*, **3**: 371-374.

Tomczak, A., Dabrowski, J. & Mikulski, T. (2017). Psychomotor performance of Polish Air Force cadets after 36 hours of survival training. *Ann. Agr. Env. Med,* **24**: 387-391.

Umajancy, S. & Thanamani, A. S. (2013). An analysis on text mining text retrieval and text extraction. *Int. J. Adv. Res. Comp. Comm. Eng.,* **2**: 3125-3129.

Valle-Cruz, D., Vega-Hernández, J. E. & Sandoval-Almazán, R. (2017). Justice of the marquesa: A twitter trend analysis using text mining and word clouds. *Proc. 18th Int. Conf. Digital Government Res.*, pp. 592-593.

Vartanian, O., Fraser, B., Saunders, D., Ralph, C.S., Lieberman, H.R., Morgan III, C.A. & Cheung, B. (2018). Changes in mood, fatigue, sleep, cognitive performance and stress hormones among instructors conducting stressful military captivity survival training. *Physiol. Behav.,* **194**: 137-143.

Wani, S., Sembok, T.M.T. & Mir, M.S. (2019). Context aware knowledge bases for efficient contextual retrieval: design and methodologies. *Comput. Sci. Tech.,* Springer. pp. 569-579.

Wani, S., Sembok, T.M.T. & Wahiddin, M.R. (2018). Constructing a knowledge base for Al-Qur'an utilizing principles of human communication. *Proc. 4th Int. Conf. Infor. Retrieval Knowledge Manage. (CAMP)*, pp. 1-5.

Xing, Y., Wu, C., Yang, X., Wang, W., Zhu, E. & Yin, J. (2018). ParaBTM: a parallel processing framework for biomedical text mining on supercomputers. *Molecules,* **23**: 1028.

Yassine, M., & Hajj, H. (2010). A framework for emotion mining from text in online social networks. *Proc. IEEE Int. Conf. Data Mining Workshops*, pp. 1136-1142.

Yusof, W. S. E. Y. W., Zakaria, O., & Zainol, Z. (2016). Establishing of knowledge based framework for situational awareness using Nonaka's and Endsley's models. *Int. Conf. Infor. Commun. Tech. (ICICTM),* pp. 47-50.

Yusof, W.S.E.Y.W., Zakaria, O. & Zainol, Z. (2018). Establishment of user requirements handbook based on the situational awareness knowledge for Malaysian military observers. *Int. J. Eng. Tech.,* **7**: 35-38.

Zainol, Z., Azahari, A.M., Marzukhi, S., Sudin, M.N., Nohuddin, P.N.E. & Zakaria, O. (2018a). Development of web portal for sharing and capturing knowledge: a study in military tacit knowledge for officer cadets at Universiti Pertahanan Nasional Malaysia (UPNM). *J. Fund. Appl. Sci.,* **10**: 2402-2416.

Zainol, Z., Azahari, A. M., Wani, S., Marzukhi, S., Nohuddin, P.N.E. & Zakaria, O. (2018b). Visualizing military explicit knowledge using document clustering techniques. *Int. J. Acad. Res. Bus. Soc. Sci.,* **8**: 1127-1143.

Zainol, Z., Jaymes, M. T. H. & Nohuddin, P. N. E. (2018c). VisualUrText: A text analytics tool for unstructured textual data. *J. Phys.: Conf. Ser.,* **1018**: 012011.

Zainol, Z., Marzukhi, S., Nohuddin, P.N.E., Noormaanshah, W.M.U. & Zakaria, O. (2017a). Document clustering in military explicit knowledge: a study on peacekeeping documents. *Proc. 5th Int. Visual Inf. Conf. (IVIC),* Bangi, Malaysia, pp. 175-184.

Zainol, Z., Nohuddin, P. N. E., Jaymes, M. T. H., & Marzukhi, S. (2016). Discovering "interesting" keyword patterns in hadith chapter documents. *Int. Conf. Inf. Commun. Tech. (ICICTM),* Kuala Lumpur, Malaysia, pp. 104-108.

Zainol, Z., Nohuddin, P.N.E., Mohd, T.A.T. & Zakaria, O. (2017b). Text analytics of unstructured textual data: a study on military peacekeeping document using R text mining package. *Int. Conf. Comput. Inf. (ICOCI 17),* pp. 1-7.

Zainol, Z., Nohuddin, P. N. E., Noormanshah, W. M. U., & Hijazi, M. H. A. (2018d). Visualization of context-based keyword pattern cluster analysis on tacit knowledge among officer cadets at Universiti Pertahanan Nasional Malaysia (UPNM). *Adv. Sci. Lett.,* **24**: 1550-1554.

Zainol, Z., Wani, S., Nohuddin, P. N. E., Noormanshah, W. M. U., & Marzukhi, S. (2018e). Association analysis of cyberbullying on social media using apriori algorithm. *Int. J. Eng. Tech.,* **7**: 72-75.

Zhao, N., Zheng, G., Li, J., Zhao, H.y., Lu, C., Jiang, M., Zhang, C., Guo, H.-t., & Lu, A.-p. (2018). Text mining of rheumatoid arthritis and diabetes mellitus to understand the mechanisms of Chinese medicine in different diseases with same treatment. *Chin J. Integr. Med.*, **24**: 777-784.

Zipf, G. (1949). *Human Behaviour and the Principle of Least-Effort*. Addison-Wesley, Cambridge, Massachusetts.

IONOSPHERIC EARTHQUAKE PRECURSOR USING GLOBAL POSITIONING SYSTEM (GPS) DATA

Ho Yih Hwa* & Yew Poh Leng

Centre for Telecommunication Research & Innovation, Fakulti Kejuruteraan Elektronik & Kejuruteraan Komputer, Universiti Teknikal Malaysia Melaka (UTeM), Malaysia

*Email: yihhwa@utem.edu.my

ABSTRACT

The ionosphere is the region in the Earth's atmosphere that is ionised by the sun's radiation. A radio wave traveling through it will experience a delay that varies with the frequency of the signal. The radio signals from Global Positioning System (GPS) on L1 (1,575.42MHz) and L2 (1,227.6MHz) will experience different delays when passing through the ionosphere. The total electron content (TEC) can be obtained from the difference of ionospheric delay between the L1 and L2 signals. In this paper, Japan's nationwide dual frequency GPS network data was used to investigate the ionospheric TEC as an earthquake precursor. The TEC with 15 s interval was computed from L1 and L2 measurements. Ionospheric TEC anomalies were investigated for three selected earthquake events with Mw > 6.0. The results show deviation in TEC as early as two weeks prior to all three seismic events. It is suggested continuous observations of TEC variations and peculiar anomalies using GPS receivers can be considered as one of the important parameters for earthquake precursor detection.

Keywords: *Global Positioning System (GPS); Ionosphere; total electron content (TEC) anomaly; earthquake precursor.*

1. INTRODUCTION

Earth is formed by many pieces like a puzzle that is not flat, slowly moving around and bumping to each other. The pieces that are moving around are known as tectonic plates, with the edges of the plates called as plate boundaries, which are made up by many of faults. An earthquake is formed when the faults collide with each other and break due to increased pressure. The earth will send out transient signals, sometimes strong, more often subtle and fleeting prior to large earthquakes (Pulinets, 2007). The deformation on the crust from the source of the earthquake activates the electronic charged carriers known as positive holes giving rise to peroxy defects in the crystals and minerals of crustal rocks (Freund *et al*., 2009; Freund, 2011; Grantet *et al*., 2015). These positive holes leave the electrons and move to the surface leading to the ionisation of the lower atmosphere and further move through the troposphere up to the lower ionosphere where they join with the electrons. Depending upon the process of ionisation, the electrons may either decrease or increase. These signals with a wide range of frequencies will induce a variety of atmospheric and ionospheric perturbations. Furthermore, active geochemical processes, such as emanation of several types of gaseous components during the earthquake preparation period, induce ion cluster formation in the near ground layer of the atmosphere in earthquake preparation zone. As a result, this layer becomes rich in ions, leading to the generation of an anomalously strong vertical electric field. The electric field leads to the occurrence of ionospheric plasma (negative or positive) in the ionosphere (Pulinets *et al.,* 2004; Klimenko *et al.*, 2011). More recently, De Santis *et al*. (2017), Akhoondzadeh *et al.* (2018), Marchetti & Akhoondzadeh (2018), Akhoondzadeh *et al*. (2019) and Marchetti *et al.* (2019) performed deep analyses of particular important case studies, where some original techniques were applied in order to discriminate between solar effects and potential lithospheric effects preceding strong earthquakes.

The ionosphere is a part of the Earth's atmosphere that contains a lot of free negatively charged electrons before bonding with positively charged ions (Ho *et al*., 2017). The free electrons inside the plasma are formed by sun activities and the thermosphere. The counteract heating in the thermosphere leads to energy release and forms the free electrons. In addition, the sun activities, such as ultraviolet radiations, may affect the volume of free electrons (Aon *et al*., 2017). The density of the free electrons, also known as total electron content (TEC), which is a measure of the number of free negatively electrons in a cross sectional area. One TEC unit is 10^{16} electrons/m^2.

Ionospheric TEC modelling is one of the possible methods to be used as an earthquake precursor, where ionospheric anomalies are observed prior to seismic event. Sunardi *et al.* (2016) studied a Japanese 9.0 Mw earthquake in March 2011 and pointed out that the TEC fluctuations were higher than the normal condition observed using GPS. In addition, they found that ionospheric TEC modelling can be used as an earthquake early warning system for higher magnitude earthquakes. However, ionospheric TEC modelling for earthquakes early warning system still needs to be further isolated from solar and geomagnetic field activities, with was confirmed by other earthquake events (Dogan *et al*., 2011; Katamzi, 2011; Heki *et al.,* 2013).

In the present study, Japanese nationwide GPS data were used to measure the TEC variation in the ionosphere that might have been induced by earthquakes. Three earthquake events were chosen, which are the Tohoku earthquake (2011), Kumamoto earthquake (2016) and Hokkaido earthquake (2018). Slant TEC (STEC) was computed using both phase and code values for L1 and L2 GPS frequencies in order to eliminate the effect of tropospheric water vapour and clock errors. Based on the assumption of thin-shell ionosphere at a fixed height of 450 km, STEC is converted into equivalent vertical TEC (VTEC). The results were analysed with other inducing factors (geomagnetic storm and solar flare) affecting TEC in order to constraint the causative factor.

2. GPS DATA PROCESSING

Dual frequency GPS data were obtained from the Geospatial Information Authority of Japan. The ionospheric TEC anomalies were investigated for a period of two weeks before the three earthquake events in Japan. Figure 1 and Table 1 show the epicentres of the earthquake events.

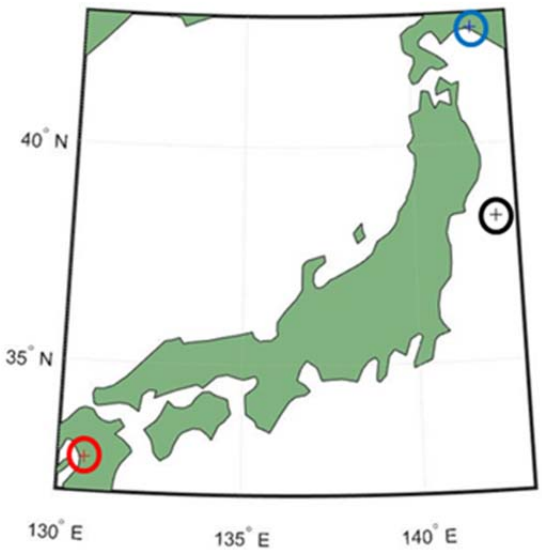

Figure 1: Epicentres of earthquake events in Japan, with the blue marker for the Hokkaido earthquake, the black marker as the Tohoku earthquake, and the red marker as the Kumamoto earthquake.

Table 1: Coordinates of the three earthquake events.

Date	Time	Region	Place	Epicentre
11/3/2011	05:46	Central	Tohoku	38.510°N, 142.792°E
15/4/2016	16:25	South	Kumamoto	32.791°N, 130.754°E
5/9/2018	18:08	North	Hokkaido	42.671°N, 141.933°E

The GPS data was used to calculate the STEC using the following equation (Ma *et al*. 2003):

$$STEC = \frac{2(f_1 f_2)^2}{K\left(f_1{}^2 - f_2{}^2\right)}(P_2 - P_1) \quad (1)$$

where:

f_1 - GPS L1 signal frequency = 1,575.42 MHz
f_2 - GPS L2 signal frequency = 1,227.60 MHz
K - constant value = 40.3
P_1 - code of pseudoranges
P_2 - code of pseudoranges

In order to determine the VTEC, the elevation angle from each satellite was needed as in the following equation (Abdullah *et al*., 2009):

$$VTEC = \left(\frac{STEC - |bR + bS|}{S(E)}\right) \quad (2)$$

where:

bR - receiver bias
bS - satellite bias

$$S(E) = \frac{1}{\cos x'} \quad (3)$$

with the cos *x'* formula being:

$$\cos x' = \sqrt{1 + \left(\frac{R_x \cos x}{R_{x+} h_m}\right)^2} \quad (4)$$

where:

R_x - the mean of radius of earth
h_m - height of ionospheric layer = 350 km
x - elevation angle of the satellite
x' - $(90^0 - x)$

In order to investigate the TEC anomalies, the median of the TEC value, X and the standard deviation of the TEC value, σ for 14 running days were computed and further used to determine the upper boundary (UB) and lower boundary (LB) of the TEC signal using the following equations (Sharma *et al*., 2017):

$$UB = X + 1.34 * \sigma \quad (5)$$

$$LB = X - 1.34 * \sigma \quad (6)$$

The TEC values, and upper and lower boundaries were plotted for further analysis. Any TEC values crossing these limits are considered anomaly. Hence, a mathematical model was constructed that gives the anomalous behaviour of ionospheric TEC, where VTEC must lie between the upper and lower boundary limit in normal ionospheric condition. Geomagnetic field and solar flux data and from Canada.ca were obtained to isolate the anomalous fluctuation signals that were not affected by solar flux and geomagnetic field.

3. RESULTS AND DISCUSSION

In this study, ionospheric TEC was used to investigate the time evolution of ionosphere anomalies that is expected for earthquakes with magnitude larger than 6.0 Mw.

3.1 Tohoku Earthquake (11 March 2011)

The main shock magnitude of the Tohoku earthquake was 9.1 Mw, with the details shown in Table 2. The GPS data used for the study was from 25 February to 10 March 2011. The epicentre and the nearby GPS receiver stations are shown in the Figure 2.

Table 2: Details of the Tohoku earthquake.

Earthquake	Date	UTC time	Coordinate of earthquake	Magnitude of earthquake
Foreshock	9/3/2011	02:45	38.424°N, 142.836°E	7.2
Main shock	11/3/2011	05:46	38.510°N, 142.792°E	9.1
After shock	11/3/2011	06:26	38.510°N, 142.792°E	7.1

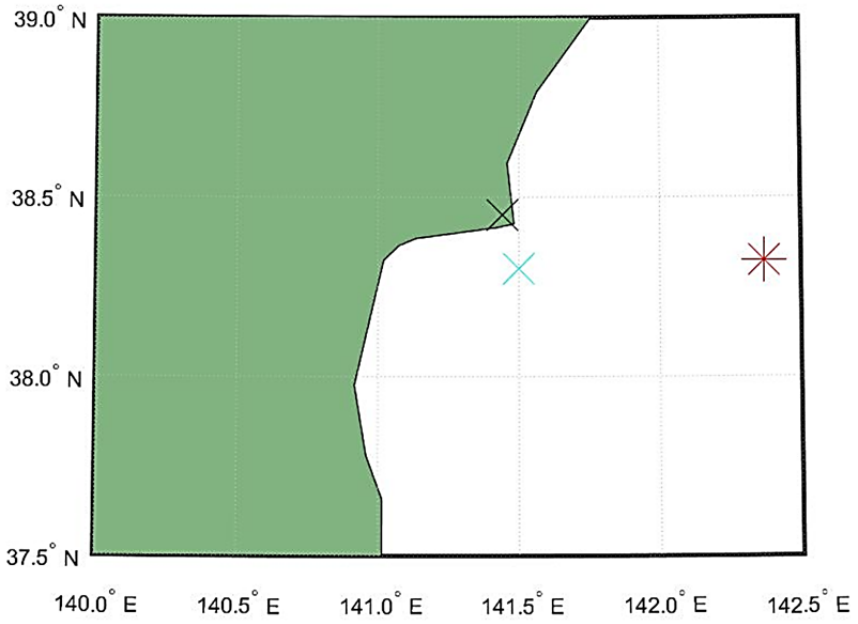

Figure 2: Coordinates of the epicentre of the earthquake (red marker) and nearby GPS receiver stations (blue and black markers).

Table 3 shows the geomagnetic field, *Kp* for two weeks before the earthquake occurred, where majority values are found to be low during the period. The *Kp* index on 1 and 10 March 2011 shows that geomagnetic activities may have induced ionospheric fluctuations. Therefore, any TEC anomalies on these two days were not identified as earthquake precursor.

Table 3: Geomagnetic field for two weeks before the earthquake.

Date	Time (UTC)							
	0-3	3-6	6-9	9-12	12-15	15-18	18-21	21-24
	Geomagnetic field, *Kp*							
2/25/11	0	0	0	0	1	0	1	0
2/26/11	0	1	0	1	1	1	1	0
2/27/11	0	0	0	0	1	1	0	0
2/28/11	0	0	1	1	1	0	0	1
3/1/11	2	2	3	3	4	4	4	3
3/2/11	3	3	2	2	3	3	2	3
3/3/11	3	2	3	2	3	2	2	3
3/4/11	2	2	2	2	2	1	2	2
3/5/11	1	2	0	1	2	1	1	1
3/6/11	0	1	0	0	2	1	2	2
3/7/11	2	2	1	1	2	1	3	2
3/8/11	3	1	1	0	1	1	1	0
3/9/11	1	0	1	0	1	1	1	1
3/10/11	2	2	4	3	2	2	3	4

The daily solar flux is shown in Figure 3, with higher value found on 8 March 2011. It means that a solar storm had occurred, releasing particles and molecules to the ionosphere which could have increased the TEC values.

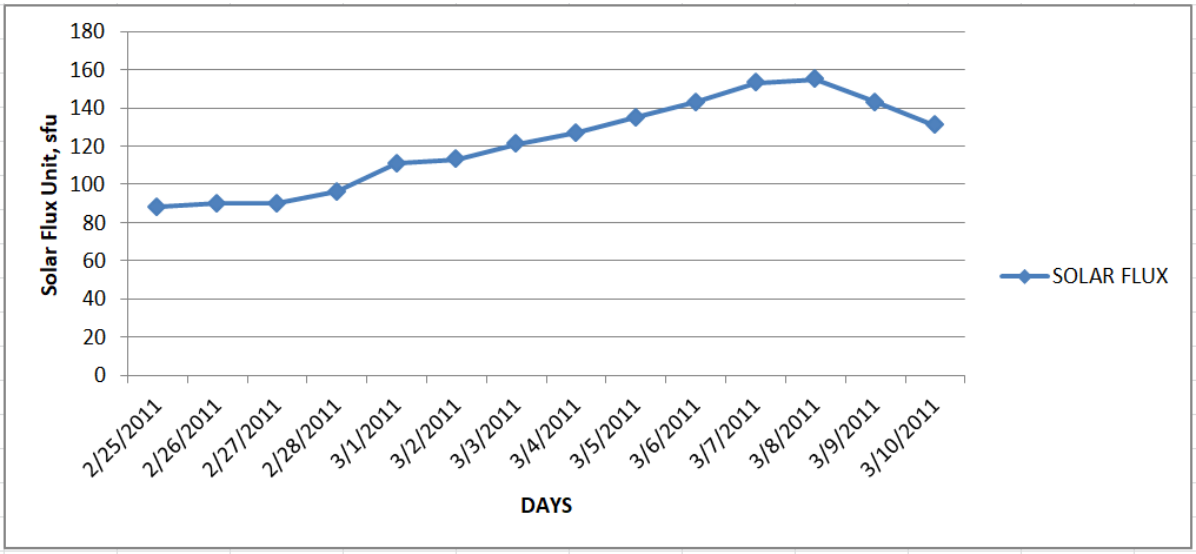

Figure 3: Daily solar flux for two weeks before the earthquake.

The daily TEC values along with the upper and lower boundaries were plotted, as shown in Figure 4. After excluding all of the events possibly triggered by geomagnetic and solar activities, the TEC anomalies identified as earthquake precursor were found to have occurred on 25 February, and 2 to 9 March 2011.

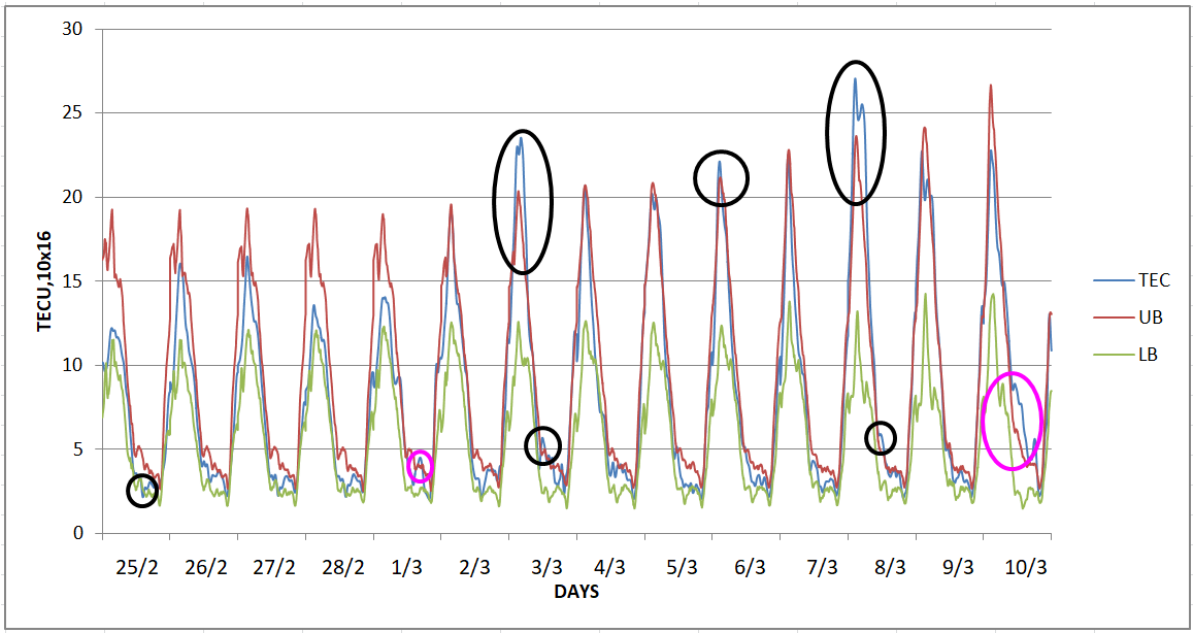

Figure 4: Daily TEC values for the second GPS receiver station, where the blue plot is the TEC data; red plot is the upper boundary; green plot is the lower boundary; purple circles are event possibly triggered by geomagnetic and solar activities; and black circles are TEC anomalies identified as earthquake precursor.

The GPS receiver stations in Tohoku were damaged on the earthquake day. Therefore, there is no available data beyond 10 March 2011. The summary of ionospheric TEC anomaly analysis for the Tohoku earthquake is shown in Table 4. The anomalies on 1 and 10 March 2011 are excluded as earthquake precursor due to active geomagnetic field and solar events.

Table 4: The relationship between geomagnetic field and solar flux on the anomaly days.

Anomaly date	Solar flux	Geomagnetic field	TEC
1/3/2011	111	Active	Lower than lower boundary
2/3/2011	113	Quiet	Higher than upper boundary
3/3/2011	121	Quiet	Higher than upper boundary
4/3/2011	127	Quiet	Higher than upper boundary
5/3/2011	135	Quiet	Higher than upper boundary
6/3/2011	143	Quiet	Higher than upper boundary
7/3/2011	153	Quiet	Higher than upper boundary
8/3/2011	155	Quiet	Higher than upper boundary
9/3/2011	143	Quiet	Higher than upper boundary
10/3/2011	131	Active	Higher than upper boundary

3.2 Kumamoto Earthquake (16 April 2016)

The main shock magnitude of the Kumamoto earthquake was 7.0 Mw, with the details shown in Table 5. The GPS data used for the study was from 1 to 22 April 2016. The epicentre and nearby GPS receiver stations are shown in Figure 5.

Table 5: Details of the Kumamoto earthquake.

Earthquake	Date	UTC time	Coordinate of earthquake	Magnitude of earthquake
Foreshock	14/4/2016	12:26	32.753°N, 130.762°E	6.1
Main shock	15/4/2016	16:25	32.791°N, 130.754°E	7.0

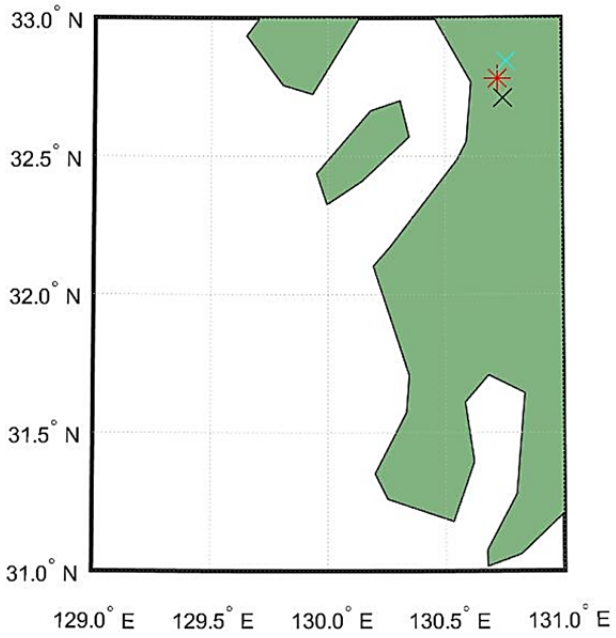

Figure 5: Coordinates of the epicentre of the earthquake (red marker) and nearby GPS receiver stations (blue and black markers).

Table 6 shows the geomagnetic field for two weeks before and one week after the earthquake occurred. The majority values of *Kp* index are low during the period. The *Kp* index on 7 to 9 and 12 April 2016 shows that geomagnetic activities started to become active, while the *Kp* index on 2 to 3 April and 13 to 14 April 2016 shows that geomagnetic storms had occurred. *Kp* index that is 5 or higher is categorised as geomagnetic storm and the fluctuations on these four days were not identified as earthquake precursor. A geomagnetic storm also occurred on 17 April 2016, but it was after the earthquake occurred.

The daily solar flux is shown in Figure 6, with higher values found for 9 to 15 April 2016. It means that a solar storm had occurred, releasing particles and molecules to the ionosphere for around two to three days on these days, which could have increased the TEC values.

The daily TEC values along with the upper and lower boundaries were plotted, as shown in Figures 7 and 8. Figure 7 shows the daily TEC values for two weeks before the earthquake, while Figure 8 shows the daily TEC values for one week after the earthquake. After excluding all of the events possibly triggered by geomagnetic and solar activities, the TEC anomalies identified as earthquake precursor were found to have occurred on 3 to 12 April 2016 (Figure 7). From the Figure 8, ionospheric TEC anomalies still occurred after the earthquake indicating the recovery phase of earthquake ionosphere.

The summary of ionospheric TEC anomaly analysis is shown in Table 7. The anomalies on 3-4 and 13-15 April 2016 are excluded as earthquake precursor due to active geomagnetic field and solar events.

Table 6: Geomagnetic field for two weeks before and one week after the earthquake.

Date	Hours							
	0-3	3-6	6-9	9-12	12-15	15-18	18-21	21-24
	Geomagnetic field, *Kp*							
4/1/2016	0	0	0	0	0	1	1	1
4/2/2016	2	0	0	0	2	4	3	5
4/3/2016	5	3	3	3	1	1	1	3
4/4/2016	2	2	2	1	2	1	1	0
4/5/2016	1	1	1	0	2	1	2	2
4/6/2016	2	1	1	2	1	1	1	1
4/7/2016	1	0	0	1	1	1	3	4
4/8/2016	4	2	2	0	0	0	1	1
4/9/2016	0	0	0	0	1	1	1	0
4/10/2016	0	1	4	2	0	0	1	2
4/11/2016	0	0	0	1	1	2	1	1
4/12/2016	2	1	2	2	3	3	3	4
4/13/2016	6	5	6	4	4	4	2	2
4/14/2016	3	2	3	6	6	3	2	3
4/15/2016	4	2	0	0	1	1	1	1
4/16/2016	0	0	3	3	2	2	3	3
4/17/2016	3	6	4	3	3	2	3	2
4/18/2016	2	1	1	1	0	0	1	1
4/19/2016	0	0	1	0	1	0	0	0
4/20/2016	0	1	2	3	0	0	0	0
4/21/2016	0	1	0	0	1	2	1	2
4/22/2016	2	1	2	2	2	2	3	3

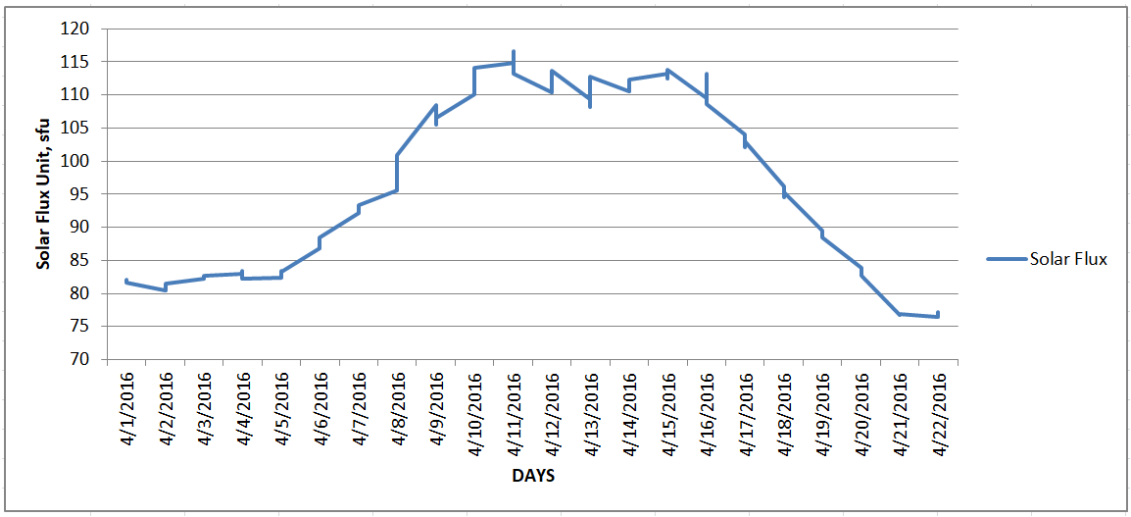

Figure 6: Daily solar flux for two weeks before and one week after the earthquake.

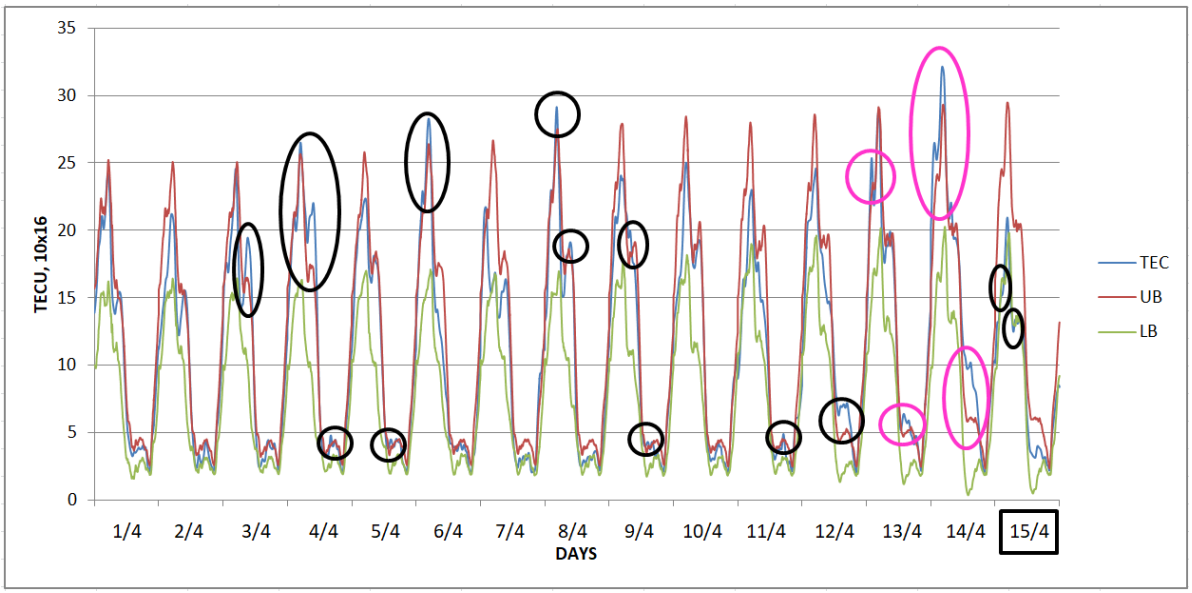

Figure 7: Daily TEC values for two weeks before the earthquake for the first GPS receiver, where the blue plot is the TEC data; red plot is the upper boundary; green plot is the lower boundary; purple circles are event possibly triggered by geomagnetic and solar activities; and black circles are TEC identified as earthquake precursor.

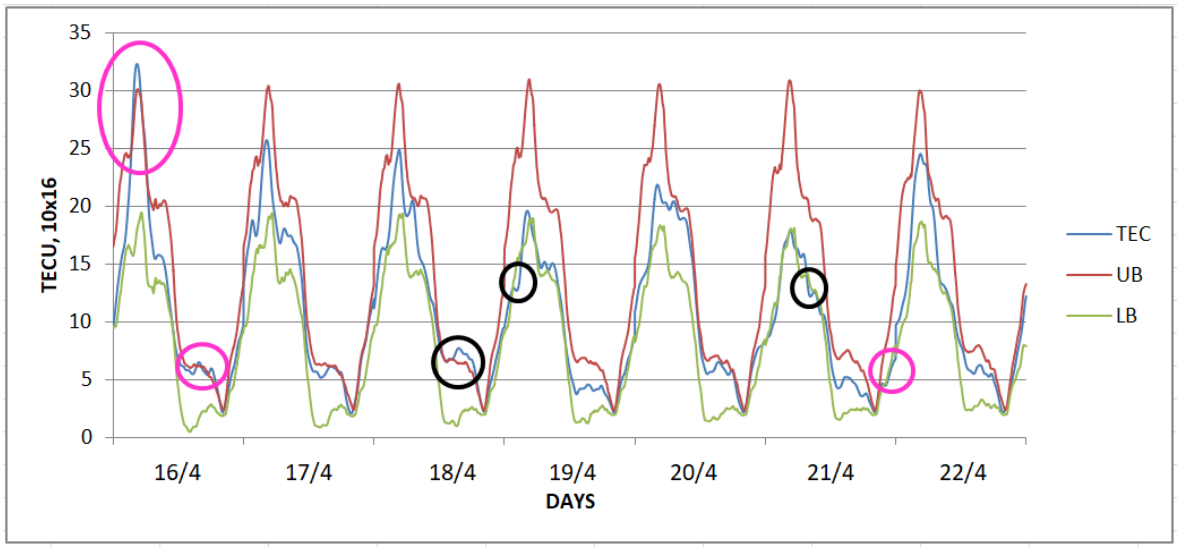

Figure 8: Daily TEC values for one week after the earthquake for the first GPS receiver, where the blue plot is the TEC data; red plot is the upper boundary; green plot is the lower boundary; purple circles are event possibly triggered by geomagnetic and solar activities; and black circles are TEC anomalies during the earthquake recovery phase.

Table 7: The relationship between geomagnetic field and solar flux on the anomaly days.

Anomaly date	Solar flux	Geomagnetic field	TEC
3/4/2016	82	Active	Higher than upper boundary
4/4/2016	83	Active	Higher than upper boundary
5/4/2016	83	Quiet	Higher than upper boundary
6/4/2016	87	Quiet	Higher than upper boundary
8/4/2016	98	Quiet	Higher than upper boundary
9/4/2016	107	Quiet	Higher than upper boundary
11/4/2016	115	Quiet	Higher than upper boundary
12/4/2016	112	Quiet	Higher than upper boundary
13/4/2016	110	Active	Higher than upper boundary
14/4/2016	143	Active	Higher than upper boundary
15/4/2016	131	Active	Lower than lower boundary
16/4/2016	110	Quiet	Higher than upper boundary
18/4/2016	95	Quiet	Higher than upper boundary
19/4/2016	89	Quiet	Lower than lower boundary
21/4/2016	77	Quiet	Lower than lower boundary
22/4/2016	77	Quiet	Lower than lower boundary

3.3 Hokkaido Earthquake (6 September 2018)

The main shock magnitude of the Hokkaido earthquake was 6.6 Mw, with the details shown in Table 8. The data used for the study was from 22 August to 12 September 2018. The epicentre and nearby GNSS receiver stations are shown in the Figure 9.

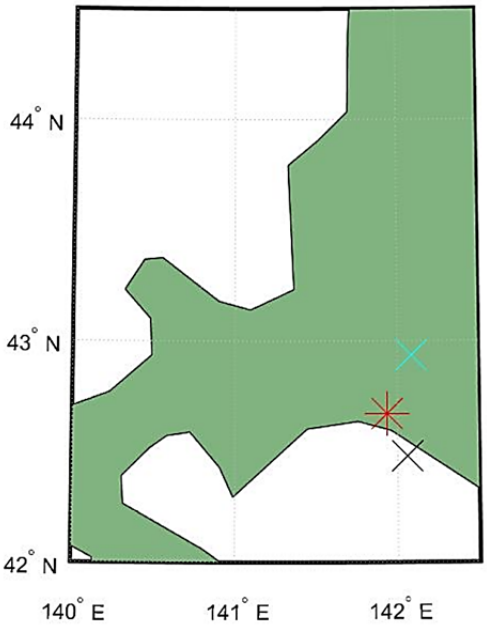

Figure 9: Coordinates of the epicentre of the earthquake (red marker) and nearby GPS receiver stations (blue and black markers).

Table 8: Details of the Hokkaido earthquake.

Earthquake	Date	UTC time	Coordinate of earthquake	Magnitude of earthquake
Main shock	5/9/2018	18:08	42.671°N, 141.533°E	6.6

Table 8 shows the geomagnetic field for two weeks before and one week after the earthquake occurred. The majority of *Kp* index are low during the period. The *Kp* index on 28 August, and 4 and 10 September 2018 shows that geomagnetic activities started to become active, while the *Kp* index on 26 and 27 August 2019 had values higher than 5, indicating that geomagnetic storms had occurred. Therefore, the fluctuations on these two days were not identified as earthquake precursor. A geomagnetic storm also occurred on 11 September 2019, after the earthquake occurred.

The daily solar flux is shown in Figure 10, with higher values found on 24 August and 11 September 2018. This indicates that solar storms occurred, releasing particles and molecules to the ionosphere around these days, which could have increased the TEC values.

Table 9: Geomagnetic field for two weeks before and one week after the earthquake.

Date	Hours							
	0-3	3-6	6-9	9-12	12-15	15-18	18-21	21-24
	Geomagnetic field, *Kp*							
8/22/2018	1	3	2	0	1	1	0	2
8/23/2018	1	1	1	0	1	1	1	1
8/24/2018	0	1	2	2	2	1	0	1
8/25/2018	1	1	1	1	2	2	3	3
8/26/2018	6	7	8	6	6	5	3	3
8/27/2018	1	3	5	5	4	4	4	2
8/28/2018	2	3	3	4	3	1	1	0
8/29/2018	1	2	2	1	1	2	2	1
8/30/2018	1	1	1	0	0	1	0	1
8/31/2018	1	0	0	0	1	2	2	1
9/1/2018	1	0	0	0	1	1	1	1
9/2/2018	1	2	2	0	1	1	1	1
9/3/2018	2	2	0	0	1	1	0	0
9/4/2018	1	3	4	1	1	2	1	2
9/5/2018	3	2	1	3	2	1	1	1
9/6/2018	2	1	2	0	1	1	1	1
9/7/2018	2	1	0	1	1	1	0	1
9/8/2018	0	0	2	0	1	1	1	2
9/9/2018	0	0	1	0	1	1	1	2
9/10/2018	0	0	2	1	3	3	3	4
9/11/2018	3	5	7	7	5	2	2	2
9/12/2018	2	1	0	1	2	1	2	2

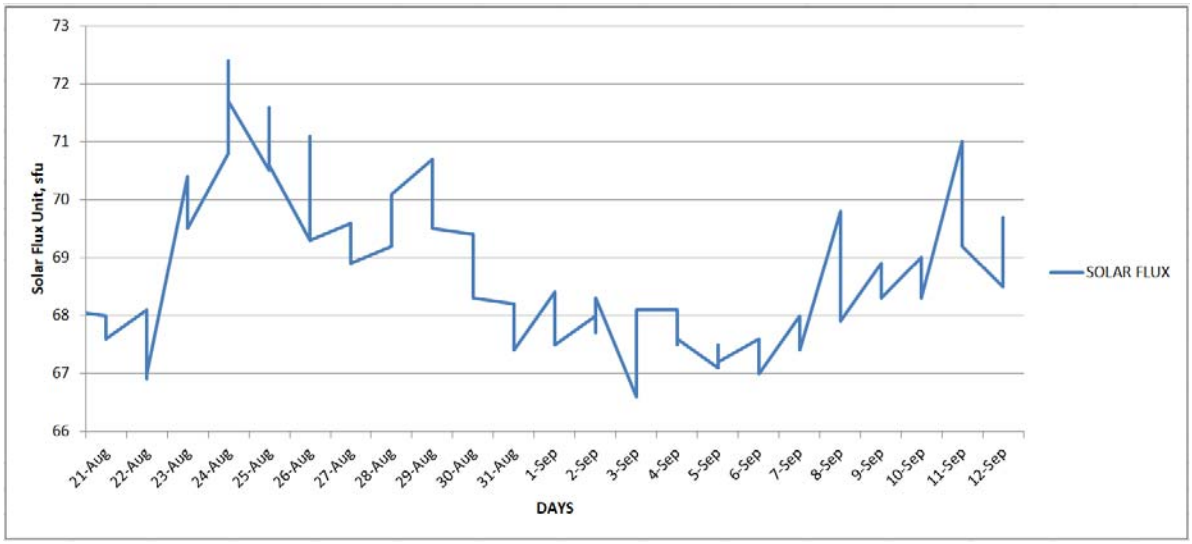

Figure 10: Daily solar flux for two weeks before and one week after the earthquake.

The daily TEC values along with the upper and lower boundaries were plotted as shown in Figures 11 and 12. The Figure 11 shows the daily TEC values for two weeks before the earthquake while Figure 12 shows daily TEC values one week after the earthquake. After excluding all of the events possibly triggered by geomagnetic and solar activities, the TEC anomalies identified as earthquake precursor were found to have occurred on 22, 23 and 28 August, and 4 and 5 September 2018 (Figure 11). From the Figure 12, ionospheric TEC anomalies still occurred after the earthquake indicating the recovery phase of earthquake ionosphere.

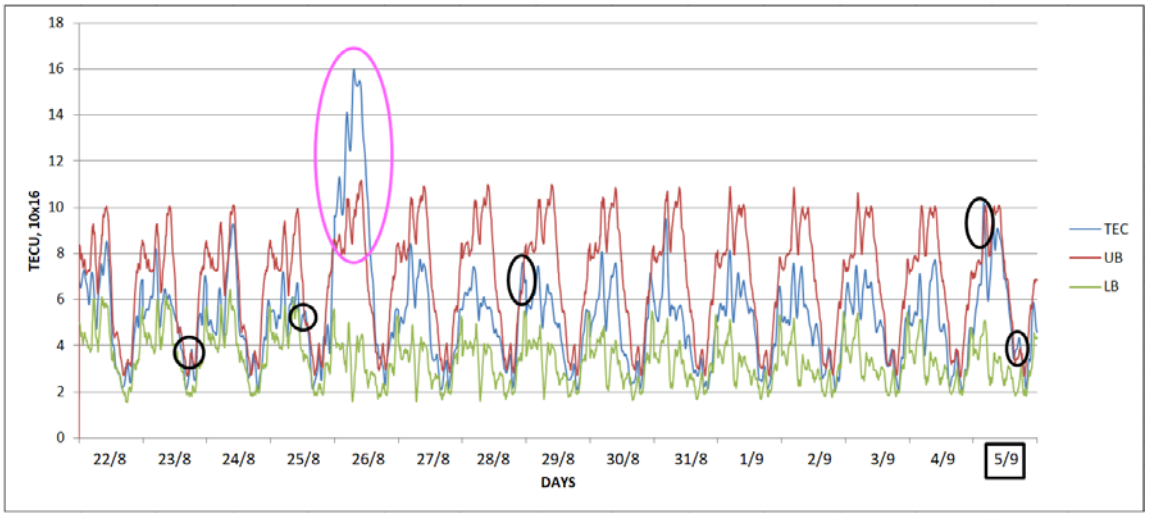

Figure 11: Daily TEC values two weeks before the earthquake for second GNSS receiver, where the blue plot is the TEC data; red plot is the upper boundary; green plot is the lower boundary; purple circles are event possibly triggered by geomagnetic and solar activities; and black circles are TEC identified as earthquake precursor.

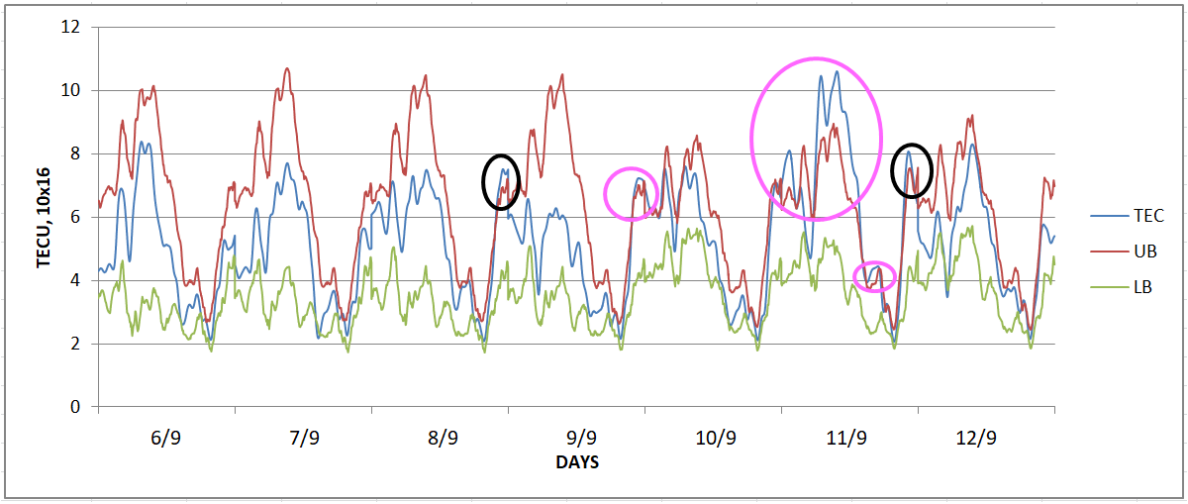

Figure 12: Daily TEC values one week after the earthquake for first GNSS receiver, where the blue plot is the TEC data; red plot is the upper boundary; green plot is the lower boundary; purple circles are event possibly triggered by geomagnetic and solar activities; and black circles are TEC anomalies during the earthquake recovery phase.

The summary of ionospheric TEC anomaly analysis is shown in Table 10. The anomalies on 26 August and 10-11 September 2018 are excluded as earthquake precursor due to active geomagnetic field and solar events.

Table 10: The relationship between geomagnetic field and solar flux on the anomaly days.

Anomaly date	Solar flux	Geomagnetic field	TEC
22/8/2018	67	Quiet	Lower than lower boundary
23/8/2018	70	Quiet	Lower than lower boundary
26/8/2018	70	Active	Higher than upper boundary
28/8/2018	70	Quiet	Higher than upper boundary
4/9/2018	68	Quiet	Lower than lower boundary
5/9/2018	67	Quiet	Higher than upper boundary
9/9/2018	69	Quiet	Higher than upper boundary
10/9/2018	69	Active	Higher than upper boundary
11/9/2018	70	Active	Higher than upper boundary
12/9/2018	69	Quiet	Higher than upper boundary

4. CONCLUSION

By using ionospheric TEC modelling, it was validated that ionospheric anomalies that occur prior to earthquake activities can be used as a precursor indicator. In this study, three earthquake events with Mw more than 6.0 in Japan was investigated, with the ionospheric TEC anomalies related to the earthquake precursor being successfully identified. It is suggested that continuous observation of TEC variations and peculiar anomalies using GPS receivers can be considered as one of the important parameters for earthquake precursor detection.

ACKNOWLEDGEMENT

This study was supported by the Ministry of Education Malaysia under research grant FRGS/2018/FKEKK-CETRI/F00358. The authors would like to acknowledge the GPS data provided by the Geospatial Information Authority of Japan.

REFERENCES

Abdullah, M, Zain A.F.M, Ho, Y.H. & Abdullah, S. (2009). TEC and Scintillation Study of Equatorial Ionosphere: A Month Campaign over Sipitang and Parit Raja Stations, Malaysia, *Am. J. Eng.. Appl Sci.*, **2**: 44–49.

Akhoondzadeh, M., De Santis, A., Marchetti, D., Piscini, A. & Cianchini, G. (2018) Multi precursors analysis associated with the powerful Ecuador (MW=7.8) earthquake of 16 April 2016 using Swarm satellites data in conjunction with other multi-platform satellite and ground data., *Adv. Space Res.*, **61**:248–263.

Akhoondzadeh, M., De Santis, A., Marchetti, D., Piscini, A. & Jin, S. (2019) Anomalous seismo-LAI variations potentially associated with the 2017 Mw=7.3 Sarpol-e Zahab (Iran) earthquake from Swarm satellites, GPS TEC and climatological data, *Adv. Space Res.* 2019, **64**: 143–158.

Aon, E. F., Othman, A.R., & Ho, Y.H. (2017). Study of GPS scintillation during solar maximum at malaysia. *Int. J. Inform. Comm. Tech.,* **10**: 299-307.

De Santis, A., Balasis, G., Pavón-Carrasco, F.J., Cianchini, G. & Mandea, M. (2017). Potential earthquake precursory pattern from space: The 2015 Nepal event as seen by magnetic Swarm satellites, *Earth Planet. Sci. Lett.* 2017, **461**:119–126.

Dogan, U., Ergintav, S., Skone, S., Arslan N. & Oz D. (2011). Monitoring of the ionosphere TEC variations during the 17th August 1999 Izmit earthquake using GPS data, *Earth Planet Sp.*, **63**: 1183.

Freund, F. (2011). Pre-earthquake signals: Underlying physical processes., *J. Asian Earth Sci.*, **41**: 383-400.

Freund, F.T., Kulahci, I.G., Cyr, G., *et al.* (2009). Air ionization at rock surfaces and pre-earthquake signals, *J. Atmospheric Sol.-Terr. Phys*., **71**: 1824-1834.

Grant, R.A., Raulin, J.P., Freund, F.T. (2015). Changes in animalactivity prior to major (M=7) earthquake in the Peruvian Andes., *Phys. Chem.Earth,* **85-86**: 69-77.

Heki, K., and Enomoto, Y. (2013). Preseismic ionospheric electron enhancements revisited, J. *Geophys. Res. Space Physics*, **118**: 6618– 6626.

Ho, Y.H. and Aon E.F.M. (2017). Prediction of scintillation and signal quality on GPS L2 band. *Defence S&T Tech. Bull.,* **10**(3): 218-228.

Katamzi, Z.T. (2011). *Statistical Analysis of Ionospheric Total Electron*. Ph.D Thesis, University of Bath, Somerset, UK.

Klimenko, M.V., Klimenko, V.V., Zakharenkova, I.E., Pulinets, S.A., Zhao, B. & Tsidilina, M.N. (2011). Formation mechanism of great positive TEC disturbances prior to Wenchuan earthquake on May 12, 2008, *J. Adv. Space Res*., **48**: 488–499.

Ma, G. & Maruyama, T. (2003). Derivation of TEC and estimation of instrumental biases from GEONET in Japan, *Ann. Geophys*., **21**: 2083-2093.

Marchetti, D. & Akhoondzadeh, M. (2018). Analysis of Swarm satellites data showing seismo-ionospheric anomalies around the time of the strong Mexico (Mw=8.2) earthquake of 08 September 2017., *Adv. Space Res.* 2018, **62**: 614–623.

Marchetti, D., De Santis, A., D'Arcangelo, S., Poggio, F., Jin, S., Piscini, A. & Campuzano, S.A. (2019) Magnetic Field and Electron Density Anomalies from Swarm Satellites Preceding the Major Earthquakes of the 2016–2017 Amatrice-Norcia (Central Italy) Seismic Sequence,. *Pure Appl. Geophs.* 2019, in press.

Pulinets S.A. (2007). Natural radioactivity, earthquakes, and the ionosphere, *Eos Trans. AGU*, **88**:: 217– 218.

Pulinets, S.A. (2004). Ionospheric precursors of earthquakes: recent advances in theory and practical applications, *Terr. Atmos. Oceanic Sci.*, **15**: pp. 413–435.

Pulinets, S.A. & Boyarchuk, K. (2004). *Ionospheric Precursors of Earthquakes*. Springer, Berlin.

Sharma, G., Champati, P.K., Mohant,Y.S. & Kannaujiya, S. (2017). Ionospheric TEC modelling for earthquakes precursors from GNSS data, *Quatern. Int.*, **462**: 65–74.

Sunardi, B., Muslim, B., Sakya, A.E., Rohadi, S., Sulastri, S. & Murjaya, J. (2016). Ionospheric earthquake effects detection based on Total Electron Content (TEC) GPS correlation. *IOP Conf. Ser. Earth Environ. Sci.*, **132**: 012014.

EVALUATION OF THE EFFECTIVENESS OF RECEIVER AUTONOMOUS INTEGRITY MONITORING (RAIM) IN GLOBAL POSITIONING SYSTEM (GPS) RECEIVERS

Dinesh Sathyamorthy*, Zainal Fitry M Amin & Esa Selamat

Science & Technology Research Institute for Defence (STRIDE), Ministry of Defence, Malaysia

*Email: dinesh.sathyamoorthy@stride.gov.my

ABSTRACT

In this study, Global Positioning System (GPS) simulation is used to evaluate the effectiveness of receiver autonomous integrity monitoring (RAIM) in GPS receivers. The study is conducted on two GPS receivers: 1) A receiver that supports RAIM - a GM1-86UB receiver that uses a u-blox 6 GPS chipset; 2) A receiver that does not support RAIM - a Garmin GPSmap 60CSx receiver. For the GPS receiver that does not support RAIM, it is unable to detect the pseudorange error in the GPS signal, resulting in increasing positional error due to increasing error in the coordinates computed by the GPS receiver. For the GPS receiver that supports RAIM, it is able to detect the pseudorange error in the GPS signal and exclude the corresponding satellite from the position solution, resulting in low positional error values. It is able to maintain this performance for number of visible satellites of five and above. However, when only five satellites are visible, after exclusion of the faulty satellite, the position integrity is not assured as the receiver does not have the required redundancy to compute the solution with different measurements and confirm that the solution is indeed correct. When only four satellites are visible, the receiver no longer supports RAIM, and thus the faulty satellite causes increasing positional error.

Keywords: *Global Positioning System (GPS) simulation; receiver autonomous integrity monitoring (RAIM); pseudorange error; positional error; redundancy measurement.*

1. INTRODUCTION

Global Navigation Satellite System (GNSS) position solutions are dependent on the integrity of the signals transmitted from GNSS satellites. This integrity is of particular importance for safety-critical GNSS applications, such as in aviation or marine navigation. However, GNSS does not include any internal information about the integrity of its signals. A GNSS satellite could broadcast incorrect information, such as due to critical satellite clock error, that will cause navigation information to be incorrect, but the GNSS receiver would be unable to determine this using the standard techniques (Ober, 2003; Kaplan & Hegarty, 2006; Yang & Xu, 2016). For example, on 1 January 2004, the clock on GPS satellite SV-23 drifted for approximately 3 h by a pseudorange error rate of 70.6 m/s before the command centre marked it as unhealthy, by which time the pseudorange error had grown from 0 to 285 km (Eastlack, 2004). A similar clock failure occurred for GPS satellite SV-22 on 28 July 2001, where its clock drifted for 90 min, leading to pseudorange error of up to 200 km (Lavraks, 2005). Using Global Positioning System (GPS) simulation, Dinesh *et al.* (2015a) demonstrated that standalone GPS receivers without any form of integrity monitoring are unable to detect such errors.

Receiver autonomous integrity monitoring (RAIM) is a GNSS receiver algorithm that determines the integrity of the position solution. RAIM detects faults in a GNSS signal by comparing redundant GNSS pseudorange measurements of combinations of subsets of four satellites that are visible. A pseudorange that differs significantly from the expected value may indicate a fault of the associated GNSS signal. In order for a GNSS receiver to perform RAIM, a minimum of five GNSS satellites

with satisfactory geometry should be visible. Traditional RAIM uses fault detection (FD) only, while newer GPS receivers incorporate fault detection and exclusion (FDE). FDE requires a minimum of six visible satellites to detect a fault and exclude it from the position solution. Detection and exclusion of position faults allows the GNSS navigation to continue without interruption. RAIM availability is an important issue as due to GNSS satellite geometry. The more satellites in view, the more combinations of subsets of four satellites are available to detect potentially faulty satellites and the better the geometric observability. However, RAIM is not always available, as that the GNSS receiver could sometimes have fewer than five satellites in view (Ober, 2003; Kaplan & Hegarty, 2006; Yang & Xu, 2016).

This study is aimed at evaluating the effect of effectiveness of RAIM in GPS receivers. The study is conducted on two GPS receivers: 1) A receiver that supports RAIM - a GM1-86UB receiver that uses a u-blox 6 GPS chipset (u-blox, 2011); 2) A receiver that does not support RAIM - a Garmin GPSmap 60CSx receiver (Garmin, 2007). Both GPS receivers employ the GPS L1 coarse acquisition (C/A) signal, which is an unencrypted civilian GPS signal widely used by various GPS receivers. The signal has a fundamental frequency of 1,575.42 MHz and a code structure which modulates the signal over a 2 MHz bandwidth (DOD, 2001; Kaplan & Hegarty, 2006; USACE, 2011).

This study is conducted using GPS simulation, which allows for the tests to be held with various repeatable conditions, as defined by the authors. As the tests are conducted in controlled laboratory environments, they are not be inhibited by unintended signal interferences and obstructions (Aloi *et al*., 2007; Kou & Zhang, 2011; Pozzobon *et al*., 2013). In our previous studies, in addition to GPS satellite clock error, GPS simulation was used to evaluate the vulnerabilities of GPS to radio frequency interference (RFI) (Dinesh *et al*., 2012, 2017a), multipath (Dinesh *et al*., 2013, 2014), varying speeds (Dinesh *et al*., 2015b), power consumption (Dinesh *et al*., 2016) and GPS antenna orientation (Dinesh *et al*., 2017b).

2. METHODOLOGY

The apparatus used in the study are an Aeroflex GPSG-1000 GPS simulator (Aeroflex, 2010) and a notebook running GPS Diagnostics v1.05 (CNET, 2004) The study is conducted in STRIDE's mini-anechoic chamber (Kamarulzaman, 2010) to avoid external interference signals and unintended multipath errors. The test setup employed is as shown in Figure 1. Simulated GPS signals are generated using the GPS simulator and transmitted via the coupler. The following assumptions are made for the tests conducted:

i) No ionospheric or troposheric delays
ii) Zero unintended GPS satellite clock or ephemeris error
iii) No obstructions or multipath
iv) No interference signals.

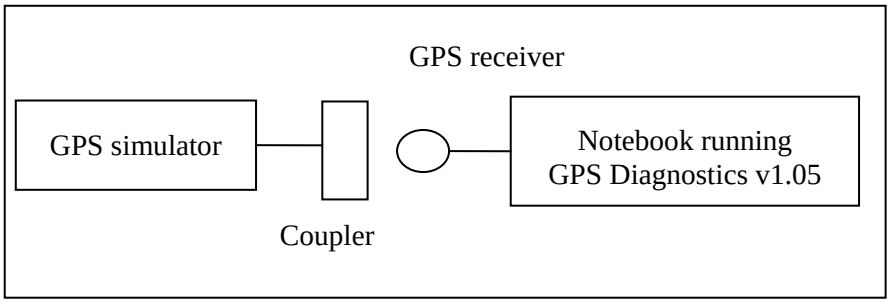

Figure 1: The test setup employed.

The tests are conducted for coordinated universal time (UTC) times of 0000, 0300, 0600 and 0900, with the location set at Kajang, Selangor (N 2° 58', E 101° 48', 0 m). The almanac data for the periods is downloaded from the US Coast Guard's web site (USCG, 2018) and imported into the GPS simulator. The GPS signal power level is set at -130 dBm.

For each UTC time, the GPS satellite with the highest elevation is used to simulate critical failure that causes pseudorange error in the transmitted signal. The pseudorange error is increased incrementally by 100 m from 0 to 1,000 m. In addition, the number of satellites is reduced one by one until only four satellites are visible. For each reading, the coordinates computed by the GPS receiver are recorded for a period of 15 min and the average positional error is computed.

3. RESULTS & DISCUSSION

For the tests conducted, the computed positional errors are shown in Figures 2-3. For the GPS receiver that does not support RAIM (Garmin GPSmap 60CSx, Figure 2), it is unable to detect the pseudorange error in the GPS signal, resulting in increasing positional error due to increasing error in the coordinates computed by the GPS receiver. The readout from GPS Diagnostics does not indicate any error. For example, the dilution of precision (DP) values remain constant with increasing pseudorange error, as this is a function of GPS satellite geometry rather than signal quality. It is observed that the maximum positional error caused by the pseudorange error is in the range of 934.61 to 1212.96 m. The positional errors caused are constrained by the limitation of the pseudorange error function (1 km) provided by the GPS simulator. In comparison, the critical failures suffered by GPS satellites SV-22 in 2001 and SV-23 in 2004 caused pseudorange errors of up to 200 and 285 km respectively (Eastlack, 2004; Lavraks, 2005).

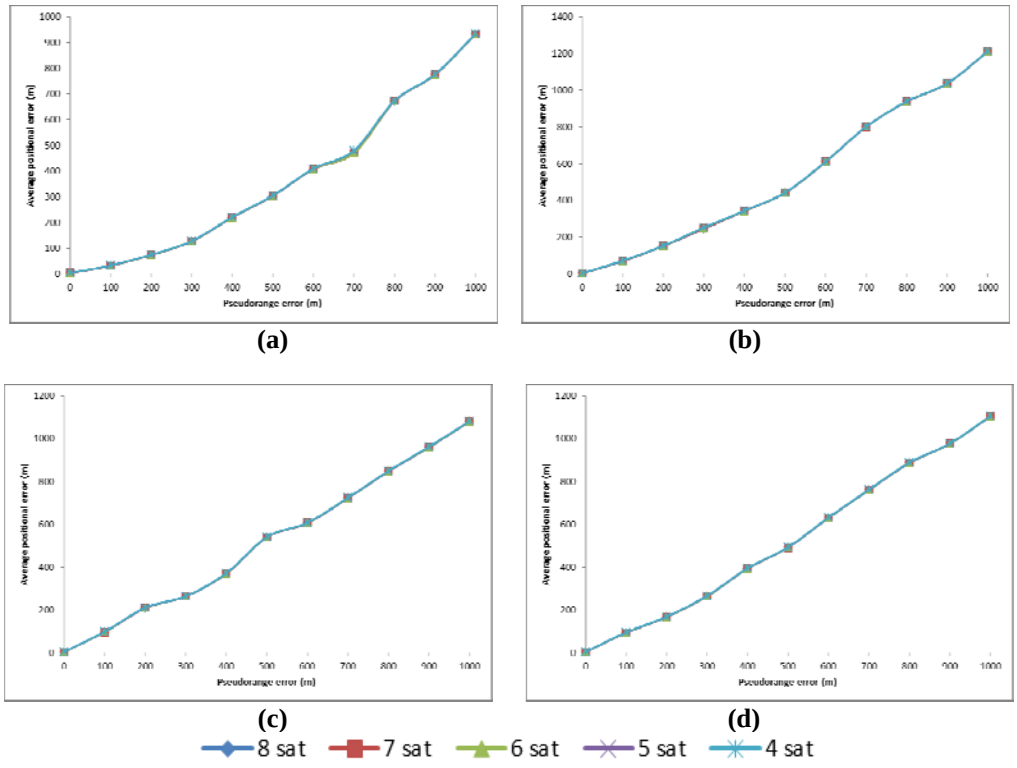

Figure 2: Recorded average positional error values for the GPS receiver that does not support RAIM (Garmin GPSmap 60CSx) for UTC times of: (a) 0000 (b) 0300 (c) 0600 (d) 0900.

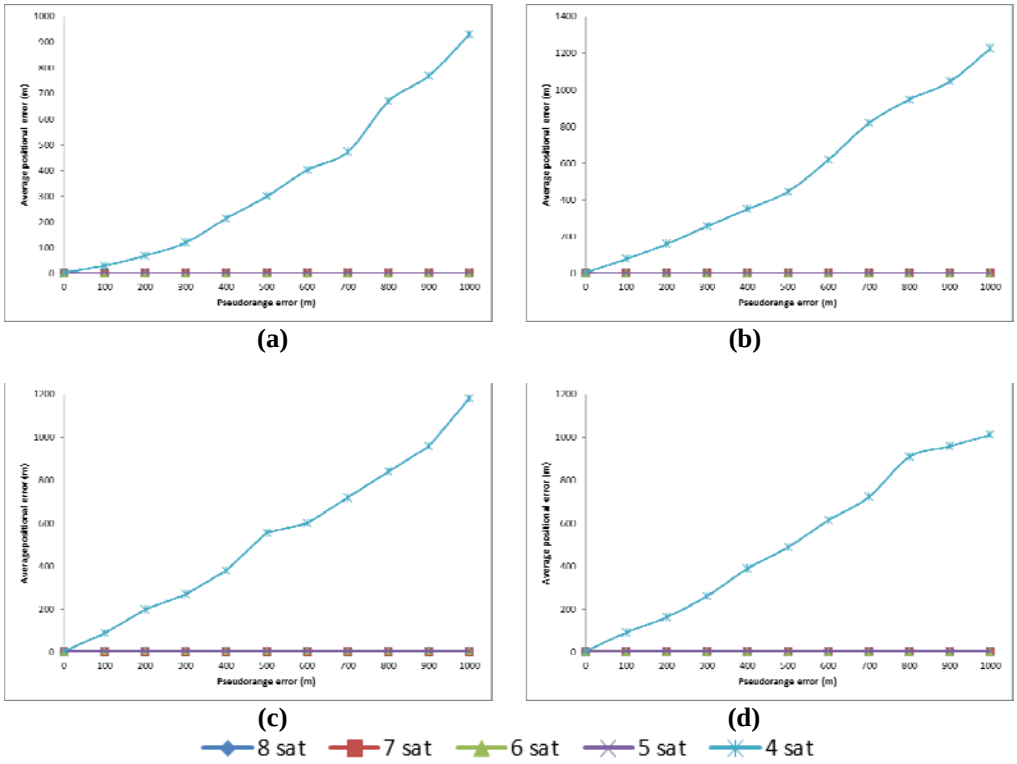

Figure 3: Recorded average positional error values for the GPS receiver that supports RAIM (GM1-86UB) for UTC times of: (a) 0000 (b) 0300 (c) 0600 (d) 0900.

For the GPS receiver that supports RAIM (GM1-86UB, Figure 3), it is able to detect the pseudorange error in the GPS signal and exclude the corresponding satellite from the position solution, resulting in low positional error values (in the range of 3-4 m). It is able to maintain this performance for number of visible satellites of five and above. However, when only five satellites are visible, after exclusion of the faulty satellite, the position integrity is not assured as the receiver does not have the required redundancy to compute the solution with different measurements and confirm that the solution is indeed correct. When only four satellites are visible, the receiver no longer supports RAIM, and thus the faulty satellite causes increasing positional error.

Varying average positional error patterns are observed for the each of the readings. This is due to the GPS satellite constellation being dynamic, causing varying GPS satellite geometry over location and time, resulting in GPS accuracy being location / time dependent (DOD, 2001; Kaplan & Hegarty, 2006; Dinesh *et al*., 2010).

The tests conducted in this study employed GPS signal power level of-130 dBm. Usage of lower GPS signal power levels would result in reduced carrier-to-noise density (C/N_0) levels, which is the ratio of received GPS signal power level to noise density. Lower C/N_0 levels would result in increased data bit error rate when extracting navigation data from GPS signals, and hence, increased carrier and code tracking loop jitter. This, in turn, results in more noisy range measurements and thus, higher rates of increase of positional error values (DOD, 2001; Kaplan & Hegarty, 2006; Petovello, 2009; USACE, 2011).

It should be noted that the tests conducted in this study were for only two GPS receivers. Additional tests using a wider range of GPS receivers are needed to further validate the findings of this study. Furthermore, a limitation faced in this study was that the GPS simulator used only allows the transmission of the GPS L1 C/A signal. The proposed future work is for the procurement of a GNSS simulator that will allow transmission of other GPS signals, in particular L2C and L5, along with signals of other GNSS systems (GLONASS, BeiDou and Galileo).

4. CONCLUSION

In this study, GPS simulation was used to evaluate the effectiveness of RAIM in GPS receivers. For the GPS receiver that does not support RAIM, it was unable to detect the pseudorange error in the GPS signal, resulting in increasing positional error due to increasing error in the coordinates computed by the GPS receiver. For the GPS receiver that supports RAIM, it was able to detect the pseudorange error in the GPS signal and exclude the corresponding satellite from the position solution, resulting in low positional error values. It was able to maintain this performance for number of visible satellites of five and above. However, when only five satellites were visible, after exclusion of the faulty satellite, the position integrity was not assured as the receiver did not have the required redundancy to compute the solution with different measurements and confirm that the solution is indeed correct. When only four satellites were visible, the receiver no longer supported RAIM, and thus the faulty satellite caused increasing positional error. Further studies are required using a wider range of GPS signals, in particular L2C and L5, as well as other GNSS systems, in order to evaluate the effectiveness of RAIM in detecting and mitigating critical signal failures.

REFERENCES

Aeroflex (2010). *Avionics GPSG-1000 GPS / Galileo Portable Positional Simulator*. Aeroflex Inc., Plainview, New York.

Aloi, D.N., Alsliety, M. & Akos, D.M. (2007). A methodology for the evaluation of a GPS receiver performance in telematics applications. *IEEE T. Instrum. Meas.*, **56**: 11-24.

CNET (2004). *GPSDiag 1.0*. Available online at: http://download.cnet.com/GPSDiag/3000-2130_4-4951103.html (Last access date: 31 January 2010).

Dinesh, S., Wan Mustafa, W.H., Mohd Faudzi, M., Kamarulzaman, M., Hasniza, H., Nor Irza Shakhira, B., Siti Robiah, A., Shalini, S., Jamilah, J., Aliah, I., Lim, B.T., Zainal Fitry, M.A., Mohd Rizal, A.K., Azlina, B. & Mohd Hasrol, H.M.Y. (2010). Evaluation of the effect of radio frequency interference (RFI) on Global Positioning System (GPS) accuracy. *Defence S&T Tech. Bull.*, **3**: 100-118.

Dinesh, S, Mohd Faudzi, M. & Zainal Fitry, M.A. (2012). Evaluation of the effect of radio frequency interference (RFI) on Global Positioning System (GPS) accuracy via GPS simulation. *Defence. Sci. J.*, **62**: 338-347.

Dinesh, S., Shalini, S., Zainal Fitry, M.A. & Siti Zainun, A. (2013). Evaluation of the repeatability of Global Positioning System (GPS) performance with respect to GPS satellite orbital passes. *Defence S&T Tech. Bull.*, **6**: 130-140.

Dinesh, S., Shalini, S., Zainal Fitry, M.A., Siti Zainun, A., Siti Robiah, A., Mohd Idris, I. & Mohd Hasrol Hisam, M.Y. (2014). Evaluation of the effect of commonly used materials on multipath propagation of Global Positioning System (GPS) signals via GPS simulation. *Adv. Mil. Tech.*, **9**: 81-95.

Dinesh, S., Shalini, S., Zainal Fitry, M.A., Asmariah, J. & Siti Zainun, A. (2015a). Evaluation of the effect of Global Positioning System (GPS) satellite clock error via GPS simulation. *Defence S&T Tech. Bull.*, **8**: 51-62.

Dinesh, S., Shalini, S., Zainal Fitry, M.A., Asmariah, J. & Siti Zainun, A. (2015b). Evaluation of the accuracy of Global Positioning System (GPS) speed measurement via GPS simulation. *Defence S&T Tech. Bull.*, **8**: 121-128.

Dinesh, S., Shalini, S., Zainal Fitry, M.A., Asmariah, J. & Siti Zainun, A. (2016). Evaluation of trade-off between Global Positioning System (GPS) accuracy and power saving from reduction of number of GPS receiver channels. Appl. Geomatics, **8**: 67-75.

Dinesh, S., Zainal Fitry, M.A. & Shahrudin, A.H. (2017a). Evaluation of Global Positioning System (GPS) adjacent band compatibility via GPS simulation. *Defence S&T Tech. Bull.*, **10**: 229 – 235.

Dinesh, S., Shalini, S., Zainal Fitry, M.A., Mohamad Firdaus, A., Asmariah, J. & Siti Zainun, A. (2017b). Evaluation of the effect of Global Positioning System (GPS) antenna orientation on GPS performance. *Defence S&T Tech. Bull.*, **10**: 33-39.

DOD (Department of Defence) (2001). *Global Positioning System Standard Positioning Service Performance Standard, Command, Control, Communications, and Intelligence*. Department of Defence (DOD), Washington D.C.

Eastlack, H. (2004). *SVN-23/PRN-23 Integrity Failure of 1 January 2004*. Second Space Operations Squadron, US Air Force, Washington, D.C.

Garmin (2007). *GPSmap 60CSx Owner's Manual*. Garmin International Inc., Olathe, Kansas.

Kamarulzaman, M. (2010). *Technical Specification for STRIDE's Mini-Anechoic Chamber*. Science & Technology Research Institute for Defence (STRIDE), Ministry of Defence, Malaysia.

Kaplan, E.D. & Hegarty, C.J. (2006). *Understanding GPS: Principles and Applications*. Artech House, Norwood, Massachusetts.

Kou, Y. & Zhang, H. (2011). Verification testing of a multi-GNSS RF signal simulator. *Inside GNSS*, **6**: 52-61.

Lavraks, J.W. (2005). *An Overview of Civil GPS Monitoring.* Institute of Navigation (ION), Manassas, Virginia.

Ober P.B. (2003). *Integrity Prediction and Monitoring of Navigation Systems*. Integricom Publishers, Leiden, Netherlands.

Petovello, M. (2009). Carrier-to-noise density and AI for INS / GPS integration. *Inside GNSS*, **4:** 20-29.

Pozzobon, O., Sarto, C., Chiara, A.D., Pozzobon, A., Gamba, G., Crisci, M. & Ioannides, R. (2013). Developing a GNSS position and timing authentication testbed: GNSS vulnerability and mitigation techniques. *Inside GNSS*, **8**: 45-53.

u-blox (2011). *u-blox 6 GPS Modules*. u-blox, Thalwil, Switzerland.

USACE (US Army Corps of Engineers) (2011). *Engineer Manual EM 1110-1-1003: NAVSTAR Global Positioning System Surveying.* US Army Corps of Engineers (USACE), Washington D.C.

USCG (US Coast Guard) (2018). *GPS NANUs, Almanacs, & Ops Advisories*. Available online at: http://www.navcen.uscg.gov/?pageName=gpsAlmanacs (Last access date: 18 September 2018).

Yang, Y. & Xu, J. (2016). GNSS receiver autonomous integrity monitoring (RAIM) algorithm based on robust estimation. *Geodesy Geodynamics*, **7**: 117-123

PREDICTION OF AIR BLAST PRESSURE FOR MILITARY AND COMMERCIAL EXPLOSIVE USING ANSYS AUTODYN

Mohammed Alias Yusof[1*], Norazman Mohammad Nor[1], Muhamad Azani Yahya[1], Vikneswaran Munikan[1] & Arifin Ismail[2]

[1]Faculty of Engineering
[2]Faculty of Management Studies
National Defence University of Malaysia (NDUM), Malaysia

[*]Email: alias@upnm.edu.my

ABSTRACT

The ability of engineers to design any structural system is dependent on the prediction of the loading the structure. When designing structures to withstand a high explosive blast, the engineer needs to predict the blast peak overpressure resulting from the detonation of the explosive. This data is required for the preparation of the design of blast resistant structures. The objective of this research is to predict the air blast pressure resulting from military and commercial explosives using simulation. Two types of military explosives, which are Trinitrotoluene (TNT) and Composition 4 (C-4), as well as one type of commercial explosive, which is ammonium nitrate / fuel oil (ANFO), have been used in this research. These explosives were modelled using the ANSYS AUTODYN simulation program and detonated at 1m from the centre of the explosive. The simulation result shows that the detonation of military explosive, namely C-4, produced the highest peak over pressure as compared to TNT and ANFO.

Keywords: *Trinitrotoluene (TNT); Composition 4 (C-4); Ammonium nitrate / fuel oil (ANFO); ANSYS AUTODYN; peak overpressure.*

1. INTRODUCTION

The prediction of air blast pressure due to detonation of either military or commercial explosives has become an important consideration for structural designers in the design of protective structures. Normally the conventional structures are not designed to resist blast loads and as the magnitudes of design loads are significantly lower than those produced by most explosions, conventional structures are susceptible to damage from explosions. There are several methods of prediction of blast peak over pressure, such as empirical methods, semi-empirical methods and also simulation methods. Empirical methods are essentially correlations with experimental data. Semi-empirical methods are based on simplified models of physical phenomena. These methods are dependent on extensive data and case study. Another approach to predict blast loading on structures is using simulation software, such as such as AUTODYN, DYNA3D and LS DYNA (Ngo *et al*., 2007).

Explosives is defined as solid, gases, or liquid substances mixed with one another that are capable of undergoing a rapid chemical reaction that will release a large amount of energy. Explosives are substances containing fuel and oxidiser that when react will release of a large amount of potential energy. The energy from the explosion dissipates as blast wave, gas and heat. The gases produced by the detonation of an explosive consist of carbon dioxide, nitrogen, carbon monoxide and oxides of nitrogen (Meyer *et al*., 2016). Generally, an explosive is used for breaking rocks into smaller size for the

application as gravel that will be used in concrete or asphalt roads. In wars, explosives can also be used for the military operations to defend the country from foreign intrusions by destroying tanks, shells and bombs.

The objective of this research is to predict the air blast pressure resulting from military and commercial explosives using the ANSYS AUTODYN simulation program. This information shall be able to assist engineers in the designing blast resistant structures.

2. LITERATURE REVIEW

2.1 Classification of Explosives

Explosives can be classified into high and low explosives (Davis, 1997). The explosives classification is shown in Figure 1. High explosives have the velocity of detonation ranging from 1,000 – 9,000 m/s. These explosives are normally reliable, easy to manufacture, and have high velocity of detonation, shuttering effects and long shelf life. Normally these materials are widely used in mines, quarrying, shells and bombs. The common types of high explosives are Trinitrotoluene (TNT), Pentaerythritol Tetranitrate (PETN), RDX and HMX. Meanwhile, low explosives have velocity of detonation between 600 – 1,000 m/s. These explosives only deflagrate and burn. Example of low explosives are black powder, propellants and smokeless powder (Mahadevan, 2013).

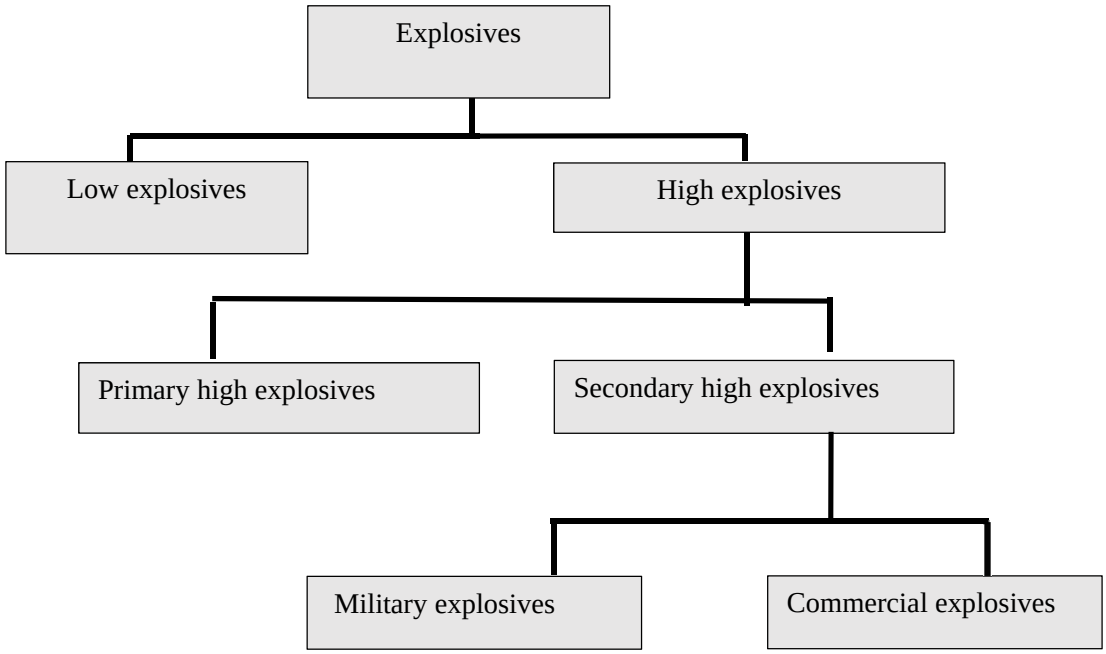

Figure 1: Explosives classification (Akhavan, 2011).

2.2 Military Explosives

Military explosives are commonly used in demolitions, bombs and war heads. These explosives are very stable, insensitive to shock, heat and friction. They have long shelf-life, high density, high detonation velocity and good storage capability, as well as adopt under a wide range of temperature and environment. The most common military explosives are TNT, Composition 4 (C-4), RDX and PETN (Akhavan, 2011).

a) TNT was invented by German chemist Julius Wilbrand in 1863. TNT has a velocity of detonation up to 7,000 m/s. It is widely used in cutting and breaching of structures, as a booster charge, grenades, as filling material for artillery shells and bombs.
b) Composition C-4 is known as plastic explosive (PE-4) by the British Army and C-4 by the US Armed Forces. It has a detonation velocity of 8,092 m/s and it is widely used for cutting steel, timber, breaking concrete structures and also for demolition works.
c) RDX is a crystalline solid white explosive with high chemical stability and velocity of detonation of up to 8,639 m/s. It is widely used in shape charges and for demolition works.
d) PETN is widely used as a base charge in electric detonators and detonation cords. PETN is very sensitive to friction and impact. The velocity of detonation for PETN is 7,975 m/s (Davis, 1997).

2.3 Commercial Explosives

Commercial explosives are made from a mixed composition of ammonium nitrate and fuel. They have lower velocity of detonation than military explosives. Commercial explosives are commonly used in mining, quarrying, civil engineering works and tunnelling works. Examples of commercial explosives are, ammonium nitrate / fuel oil (ANFO) and emulsion explosives (Mahadevan, 2013):

a) Ammonium nitrate is a blasting agent that is very insensitive. It is commonly used as a fertiliser. ANFO is produced as a result of ammonium nitrate – fuel mixture with a ratio of 96% ammonium nitrate and 4 % of fuel oil. It is widely use in boreholes to break rock in quarries or other civil engineering works such as road constructions and tunnelling works.
b) An emulsion explosive consists of ammonium nitrate, water, fuel, waxes, emulsifier and hollow particles, such as glass micro balloons, resin-based product or perlite, as sensitiser. Most of these explosives are used in blasting of rocks, mining and tunnelling works.

2.4 Blast Phenomena

An explosion from the detonation of explosives produces a very high temperature, which is about 3,000 – 4,000 °C, releasing gases such as carbon monoxide and nitrogen oxide, as well as high pressure waves up to 30 GPa (Ngo *et al*., 2007). This pressure wave is also known as a blast wave, which travels at speed of sound, and is illustrated in Figure 2.

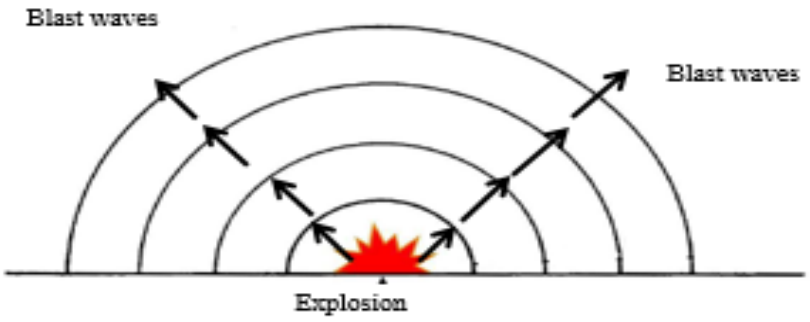

Figure 2: Illustration of blast wave from an explosion (Mohammed Alias *et al.*, 2018).

The blast wave that is produced from the detonation of an explosive can be presented in an idealised profile of the pressure-time history, which is shown in Figure 3.

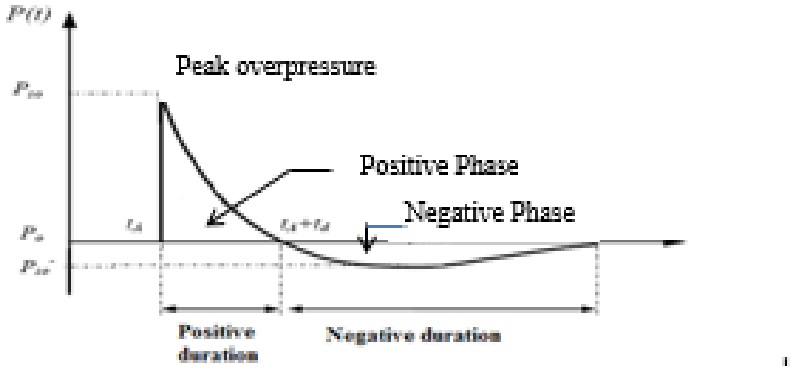

Figure 3: Typical blast wave profile (Ngo *et al.*, 2007).

The explosive detonation in the air will create a blast wave that eventually pushes the surrounding atmosphere. The blast wave or pressure will reach a peak level within a very short duration, which is known as peak overpressure or also sometimes as incident pressure. This phenomenon is also known as the positive phase of the explosion. During this phase, the explosion produces strong heat and fireballs. Due to the impact of high peak pressure, most of the structures or surroundings will be badly damaged. The blast pressure will then decrease rapidly beyond the ambient pressure with a longer duration until it reaches the ambient pressure. This phase is known as the negative phase of the explosion. At this point, suction forces and strong wind will occur and then creates vacuum that sucks fragments and debris surrounding the blast source and eventually pushing it far from the blast source. This explosion then produces flames and gases until it is stable. This blast phenomena event normally happens in a very short duration and sometimes in few milliseconds only (Ngo *et al.*, 2007).

3. METHODOLOGY

The simulations of explosion were carried out using a blast effect computational program, ANSYS AUTODYN (AUTODYN, 2007), to simulate the peak over pressure resulting from detonation of 1 kg of TNT, C-4 and ANFO at a standoff distance of 1 m from the centre of the explosition. The initial set up was done using 2D symmetrical. The air and explosive were modelled using Euler 2D. Air was modelled using the Equation of State (EOS) model, which is as follows:

$$P = (y - 1)\rho e \quad (1)$$

where;

y = Constant value
ρ = Air Density
e = Specific internal energy

The air density used is ρ = 1.225 kg/m^3 and air initial internal energy used is 2.068 x 10^5 kJ/kg, which is obtained from the AUTODYN material library. The Jones–Wilkens–Lee (JWL) equation of state was used to model the rapid expansion of explosives, which is also obtained from the AUTODYN material library. The JWL equation is shown in the following equation:

$$P = A\left(1 - \frac{\omega}{R_1 v}\right)e^{-R_1 v} + B\left(1 - \frac{\omega}{R_2 v}\right)e^{-R_2 v} + \frac{\omega E}{V} \quad (2)$$

where;

E = Internal specific energy
V = Volume of the material at pressure divided by the initial volume of unreacted explosive
A, B, ω, R_1 *and* R_2 = Empirically derived constants.\

A mesh size of 0.1 mm was selected for the modelling. The boundary condition of the Euler sub-grid was set as outflow boundary. The flow chart of the simulation process is shown in Figure 4.

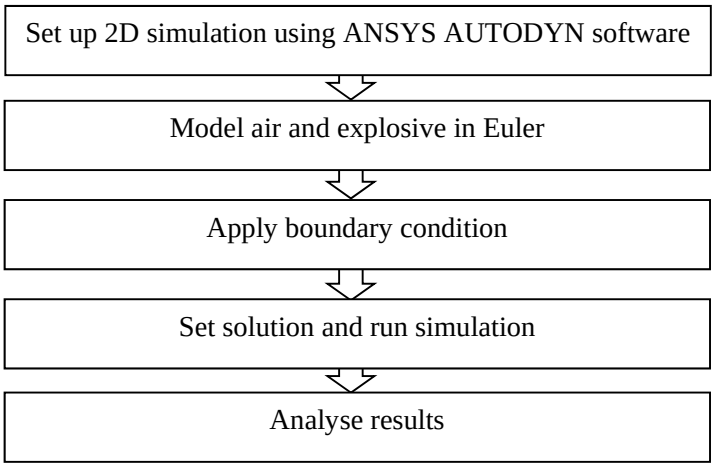

Figure 4: Flow chart of the simulation process.

The air blast pressure from the explosion is recorded using a gauge that is placed at a distance of 1 m from the centre of the explosition to measure the pressure at this location. The location of the gauge as well as the models for TNT, C-4 and ANFO are shown in Figure 5.

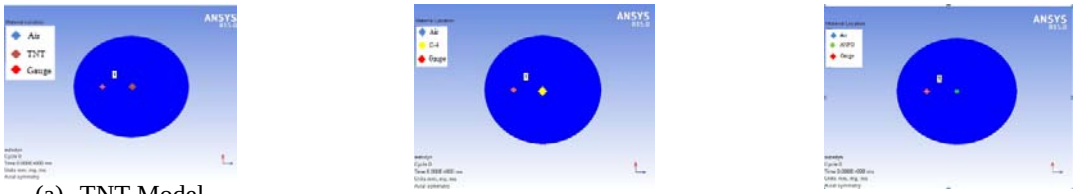

(a) TNT Model (b) C-4 Model (c) ANFO Model

Figure 5: Models of explosives and the gauge location.

4. RESULTS & DISCUSSIONS

4.1 Peak Over Pressure for TNT Explosion

Figure 6 shows the pressure-time history graph for the explosion of 1 kg of TNT, which was recorded until 1.5 ms of blast detonation. From the graph, it shows that the pressure resulting from the detonation increased rapidly at 0.4 ms until its reached maximum peak overpressure of up to 3,000 kPa at 0.5 ms, which is the positive phase of the explosion. Then, the blast pressure decreased rapidly until 1.5 ms and reached ambient pressure. The simulation model for the detonation of TNT is shown in Figure 7.

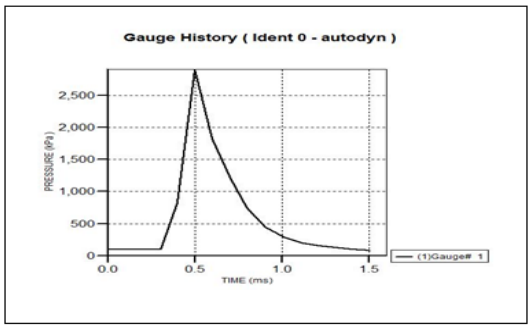

Figure 6: Pressure versus time history for TNT.

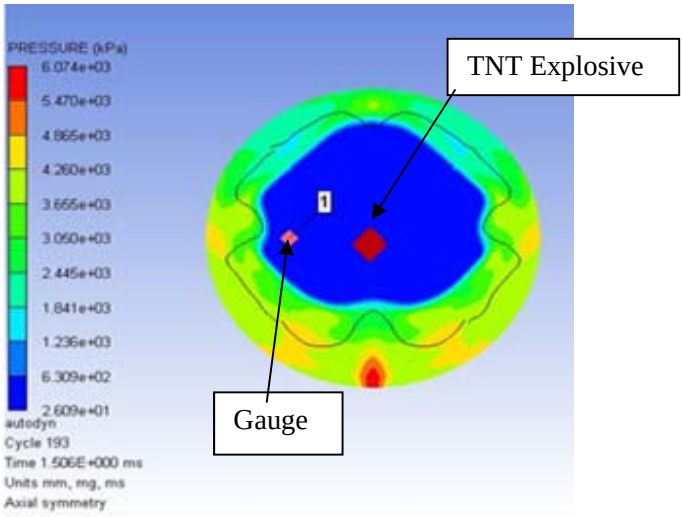

Figure 7: Simulation model for TNT explosive.

4.2 Peak Overpressure for C-4 Explosition

Figure 8 shows the pressure-time history graph for the explosion of 1 kg of C-4, which was recorded until 1.5 ms of blast detonation. The results show that the peak overpressure resulting from the detonation is 3,900 kPa at 0.3 ms. Then, the blast pressure decreased rapidly until 1.5 ms and reached ambient pressure. The simulation model for the detonation of C-4 is shown in Figure 9.

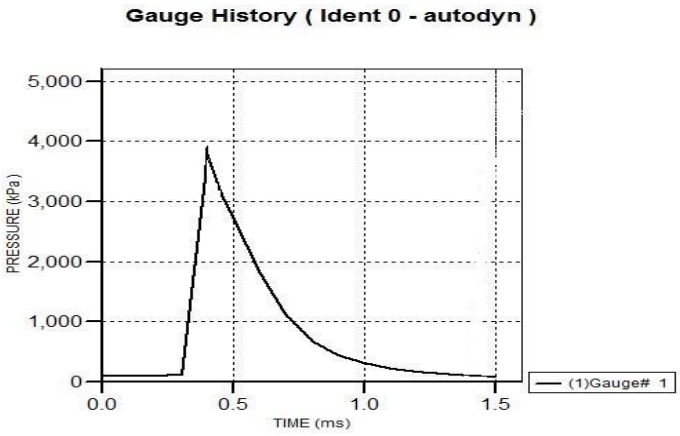

Figure 8: Pressure versus time history for C- 4.

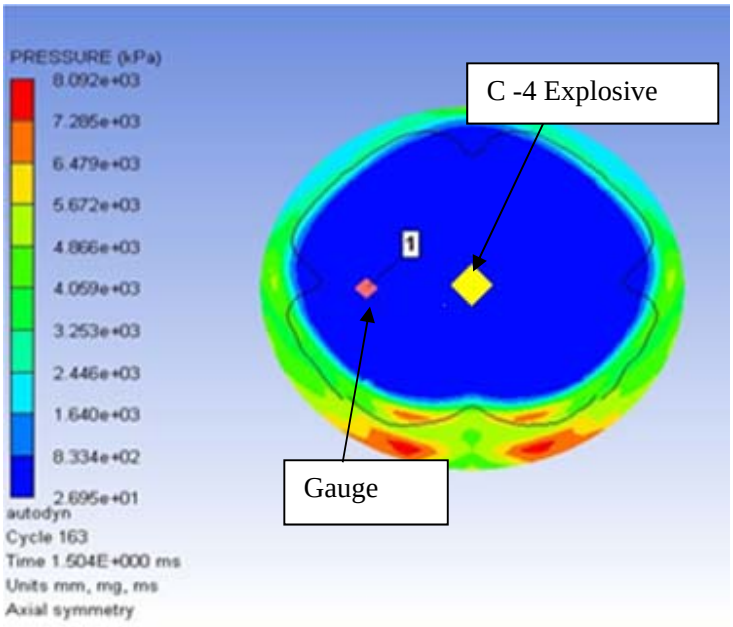

Figure 9: Simulation model for C- 4 explosive.

4.3 Peak Over Pressure for ANFO Explosition

Figure 10 shows the pressure time history graph for the explosion of 1 kg of ANFO, which was recorded until 1.5 ms of blast detonation. From the graph, it was found that the peak overpressure resulting from the detonation is 2,200 kPa at 0.7 ms. After the positive phase of the explosion, then the blast pressure decreased rapidly until 1.5 ms and reached ambient pressure. The simulation model for the detonation of 1 kg of ANFO is shown in Figure 11.

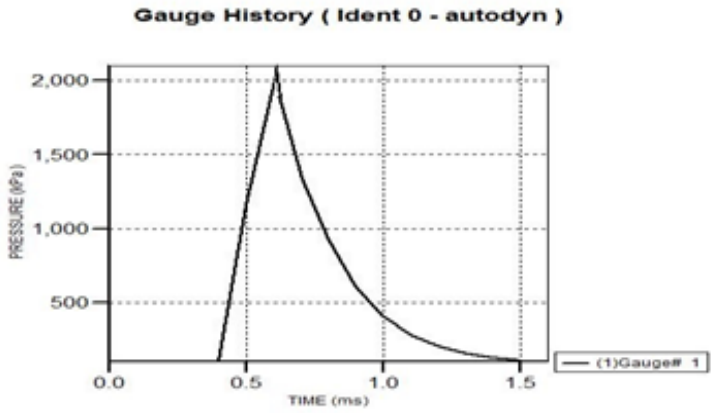

Figure 10: Pressure versus time history for ANFO.

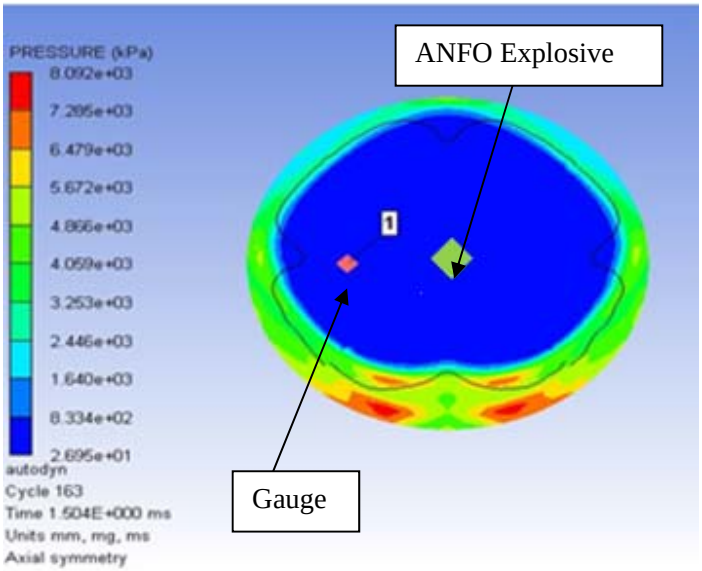

Figure 11: Simulation model for ANFO explosive.

4.4 Summary

The summary of the peak over pressure results obtained from the simulation for TNT, C-4 and ANFO are shown in Table 1. The results show that C-4 produced the highest peak over pressure, followed by TNT and ANFO. Both military explosives, C-4 and TNT, had higher detonation velocities and thus, produced higher peak overpressures than the commercial explosive, ANFO.

Table 1 : Results of peak overpressure for TNT, C-4 and ANFO

No.	Types of explosive	Peak overpressure (kPa)
1	Military explosive (TNT)	3,000
2	Military explosive (C-4)	3,900
3	Commercial explosive (ANFO)	2,200

5. CONCLUSION

From the results obtained, it shows that both military explosives, C-4 and TNT, produced higher peak overpressures than the commercial explosive, ANFO. The C-4 explosive produced the highest blast peak over pressure as compared to the other explosives, thus indicating that this type of explosive is more powerful and has more ability to be used in demolition works. The blast peak overpressure data from this stidy is essential for structural engineers in designing blast resistant structures.

REFERENCES

Akhavan, J. (2011). *The Chemistry of Explosives.* Royal Society of Chemistry, UK.

ANSYS AUTODYN (2007). User Manual, Version 11.0. *Concord*, USA.

Davis, C.W. (1997). *Explosive Effects and Applications.* Springer, USA.

Mahadevan, E.G. (2013). *Ammonium Nitrate Explosives for Civil Engineering Application*. Wiley –VCH, Germany.

Meyer, R., Kohler, J. & Homburg, A. (2016). *Explosive, 7th Ed*. Wiley –VCH, USA.

Mohammed Alias, Y., Norazman Mohamad, N. & Arifin, I. (2018). *Blast Resistant Material.* UPNM Press, Malaysia.

Ngo.T, Mendis, P, Gupta, A & Ramsey, J. (2007). Blast loading and blast effect on structure. *Electr. J. Structural Eng.*, **7**: 76-91.

BALLISTIC RESISTANCE OF MAGNESIUM ALLOY, AZ31B REINFORCED WITH CARBON NANOTUBE AND LEAD UNDER GAS GUN SIMULATION

Mohamad Faizal Abdullah[1*], Shahrum Abdullah[2], Risby Mohd Sohaimi[1] & Mohamad Khairul Faidzi[1]

[1]Department of Mechanical Engineering, Faculty of Engineering, National Defence University of Malaysia (UPNM), Malaysia
[2]Centre for Materials Engineering and Smart Manufacturing, Faculty of Engineering & Built Environment, Universiti Kebangsaan Malaysia (UKM), Malaysia

[*]Email: m.faizal@upnm.edu.my

ABSTRACT

This paper presents the improvement of ballistic resistance of magnesium alloy, AZ31B with reinforcement of carbon nanotubes (CNT) and leads (Pb). Magnesium alloy can support high shock absorbency for 100 times greater than aluminium alloys. However, it is necessary to increase the impact energy absorption properties better. Thus, the nanomaterials can merge together with the structure of magnesium alloy to increase ballistic resistance. Ballistic resistance was determined using simulation of magnesium alloy under gas gun impact. The Cowper-Symonds model was used to improve the simulation impact. From the simulation, the ballistic limit was determined using the Retch-Ipson model. The results of the simulation showed that the ballistic resistance of magnesium alloy increased as much as 40%. In addition, the ballistic limit also increased from 600 to 680 m/s. It shows that a mixture of magnesium alloy and nanomaterial can enhance the ballistic resistance and ballistic limit.

Keywords: *Ballistic limit; magnesium alloy; carbon-nanotube (CNT); lead (Pb); gas gun simulation*.

1. INTRODUCTION

Armoured vehicle technology has been growing along with material technology. Currently, armoured vehicle bodies do not fully use steel for ballistic penetration resistance. Instead, lightweight materials, such as magnesium alloy, have been utilised with steel for armoured vehicle bodies (Mertz *et al*., 2000). The lightweight materials increase the strength-to-weight ratio of the armoured vehicle, hence improving the vehicle manoeuvrability (Rahman *et al*., 2018).

The AZ31B magnesium alloy can generally withstand the effects of an impact because the unique combination of the alloy that provides it with high shear strength of up to 410 MPa, low density of 1.8 g/cm^3, and superior shock absorption that is 100 times greater than that of normal aluminium (Jones *et al*., 2007). Magnesium also has the highest energy absorption capacity among those metals that are used in shielding applications. Therefore, this alloy is an ideal choice for automotive applications and for the sections that are exposed to impacts because of its energy absorption properties and its lightweight. The "AZ" element in AZ31B stands for aluminium and zinc, which are the two main elements of alloy materials. The values of "3" and "1" denote the proportion of aluminium and zinc, and lastly, the "B" in AZ31B shows that the third component is one that is registered with the American Society for Testing and Materials (ASTM) (Feng *et al.*, 2014).

However, magnesium alloy has some issues on ductility due to its weaknesses in the hexagonal close-packed cell (HCP) structure that have weakened the bonds between molecule structures. Therefore, an addition of carbon nanotubes (CNT) into the material structure can lock the HCP structure on dislocation between the structure of the materials (Eslam *et al*., 2012). Besides, lead (Pb) material has been used to enhance the ductility of magnesium alloy (Abdullah *et al*., 2016).

While AZ31B has high energy absorption capability, the addition of nano reinforcement material can improve impact properties. This study aims to investigate the improvement of the ballistic limit for AZ31B reinforced with CNT and Pb through gas gun simulation.

2. BALLISTIC LIMIT THEORY

Ballistic applications have guidelines in determining which materials could withstand ballistics resistance. This model of ballistic limit is always used in determining residual velocities when the bullet either penetrates the material or not. The ballistic limit model is the Retch-Ipson model, which is to predict residual velocities. This model was developed by Recht and Ipson in 1963. The equation of the model is as follows (Múgica *et al*., 2014):

$$v_r = a\left(v_i^P - v_{bl}^P\right)^{1/P} \tag{1}$$

where a and P are empirical constants using experimental data. The original Retch-Ipson model shows $a = m_p/(m_p - m_{pl})$ and P is 2, where m_p and m_{pl} indicate the masses of the bullet and plate. It can only be used if the plastic deformation of bullets is ignored. If there are no significant changes of plate deformation, the equation can be estimated by a as 1 and P will be matched with the data trends. The method of smallest square root is used to obtain equivalent of P and v_{bl} (Zhikharev *et al*., 2014).

3. METHODOLOGY

A specific simulation software package was used to develop a 3D model for the ballistic tests. The 3D model shows the effect of ballistic impact on the AZ31B plate. Finite element analysis (FEA) was used to accommodate the Cowper-Symonds (CS) material model. The CS material model was used because it considers the damage evolution in the fracture and the thermal sorting effect in the material behaviour. This model is commonly used for impact simulation (Hernandez *et al*., 2017). The CS model is represented by the following equation:

$$\sigma_y = \sigma_0\left[1+\left(\frac{\dot{\varepsilon}}{C}\right)^{\frac{1}{p}}\right] \tag{2}$$

where C and p are the Cowper-Symonds coefficients, $\dot{\varepsilon}$ is the strain-rate, σ_y is the dynamic stress or strength and σ_0 is the quasi-static stress or strength. The coefficients obtained for Equation 2 are presented in Table 1, along with the strain rate range of applicability and the mean squared value, R^2 for the tested materials. CS parameters for steel 1006 was obtained from a previous study (Hernandez *et al*., 2017), while the CS parameters for the magnesium alloys AZ31B and AZ31B+Pb+CNT were obtained from experimental work that involved tensile test and split-Hopkinson pressure bar test.

Table 1: Material properties and Cowper-Symonds (CS) model parameters.

Material Properties	Steel 1006	AZ31B	AZ31B +Pb +CNT
Density, ρ (kg/m^3)	7872	1770	1770
Young's Modulus, E (GPa)	206	45	45
Yield strength, σ (MPa)	165	220	220
Strain rate constant, C	80	7124.56	3574.73
Strain rate exponent, q	4	1.56	3.47
Mean squared value, R^2	0.87	0.91	0.89

Figure 1 shows the simulation model set up for gas gun, with the projectile used being a conic nose steel 1006 projectile with diameter of 11 mm. The energy equivalent method was used based on a previous study (Avila *et al*., 2007) to determine the initial velocity required for this projectile, which was was 600 m/s.

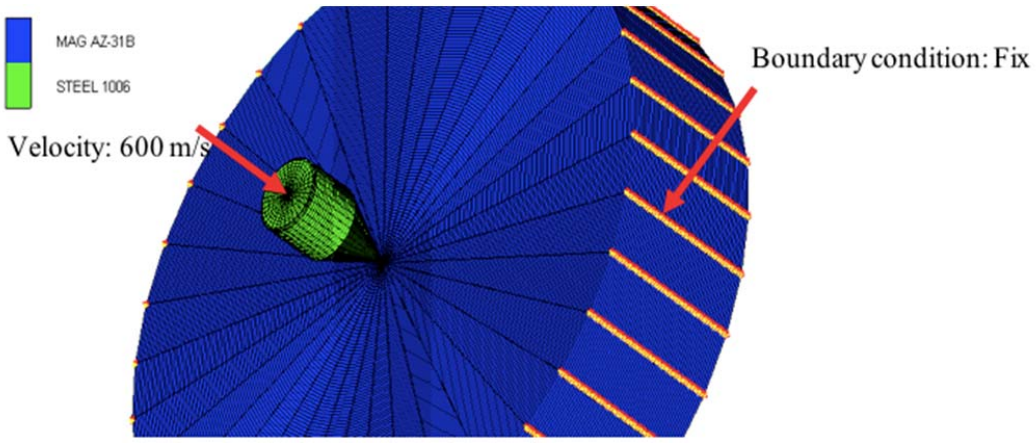

Figure 1: Geometric model and boundary condition used for the gas gun simulation.

4. RESULTS AND DISCUSSION

Figure 2 shows the material deformation patterns of each plate at times between 6 to 115 μs at initial projectile velocity of 600 m/s. Figure 3 shows stress distribution patterns of each plate at times between 6 to 115 μs at initial projectile velocity of 600 m/s. Based on the simulation observation, the concentration of stress for each time was around the tip of the projectile. The projectile retained its shape when penetrating the plate, with its tip being progressively deformed at the same time as the material in the panel was displaced and a hole was formed. The deformation that occurred on the projectile nose during penetration had led to an immense heat generation and the material of the panel was locally melted and lost all mechanical strength, it was similar effect that Lesuer *et al*. (1998) was found.

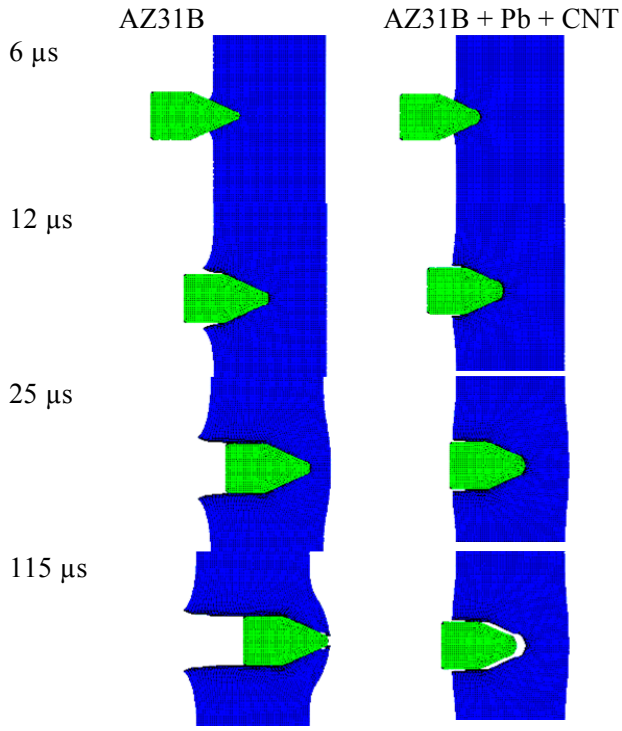

Figure 2: Materials deformation patterns of each plate at times between 6 to 115 µs at initial projectile velocity of 600 m/s

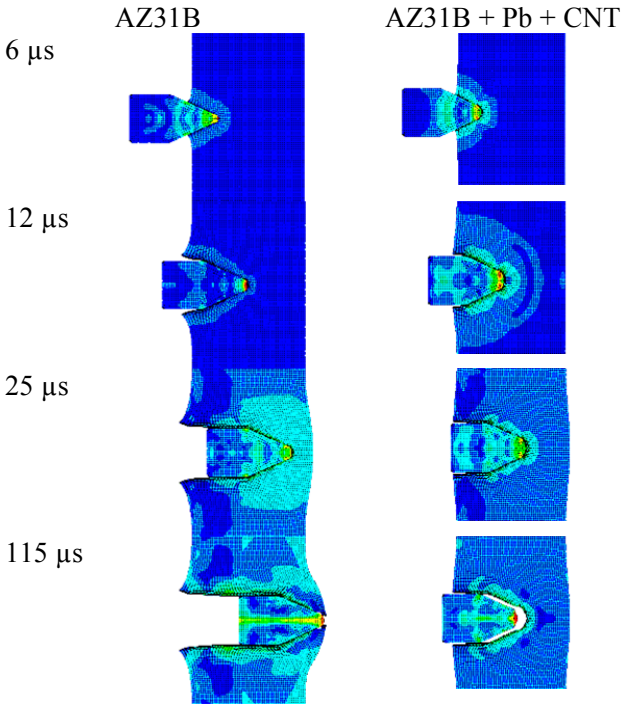

Figure 3: Stress distribution patterns of each plate at times between 6 to 115 µs at initial projectile velocity of 600 m/s.

Figure 4 (a) shows the energy (J) absorbed through magnesium alloys AZ31B and AZ31B+Pb+CNT. It can be seen that the resulting graph of response shows that the energy absorption of the magnesium alloys is uniform at 50 µs for AZ31B+Pb+CNT and at 80 µs for AZ31B. Figure 4 (b) shows that the velocity (m/s) decreased through the plates. From the analysis, the AZ31B plate was totally penetrated but the behaviour of material itself can still support the energy from the projectile to stop it. The AZ31B+Pb+CNT can support the projectile with 15.06 mm penetration. It seems that the reinforcement of CNT and Pb onto AZ31B decreased by about 40 % of the depth penetration as compared to the original material.

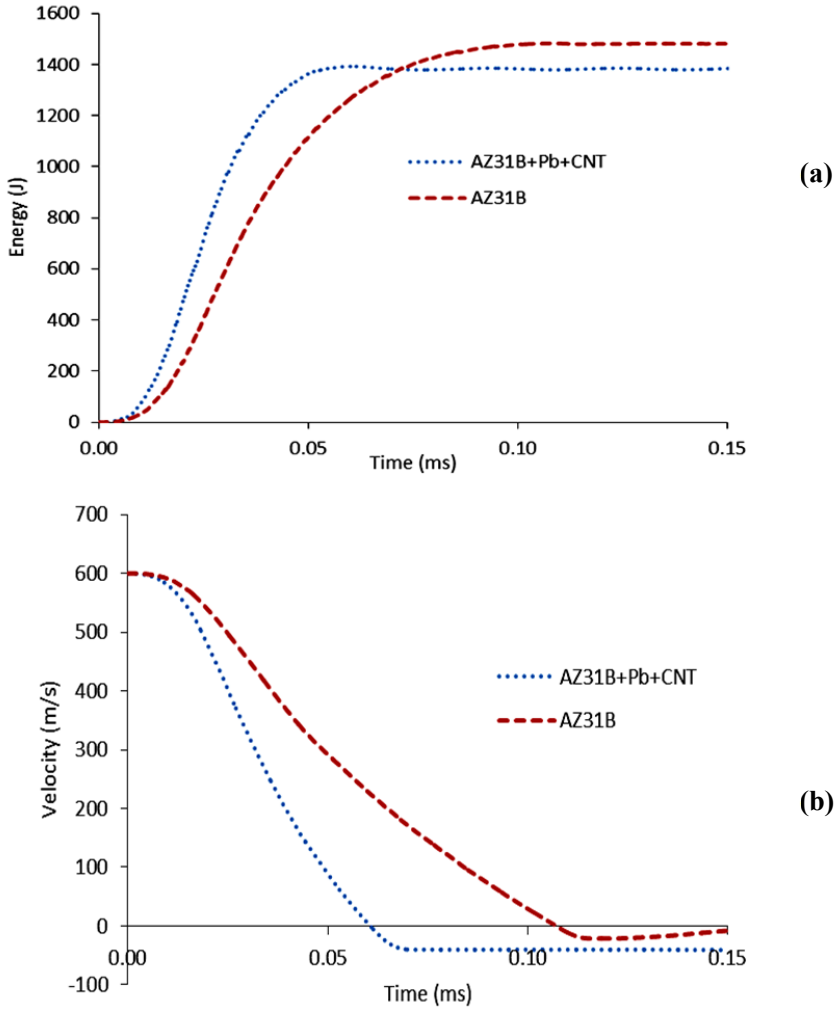

Figure 4: Trends of (a) energy absorption increase and (b) velocity decrease through the plates.

After the stress and energy absorption analysis, the ballistic limit for each material was determined using the Retch-Ipson model. Table 2 shows the parameters of the Retch-Ipson model for AZ31B and AZ31B+Pb+CNT, where a and P are empirical constants from simulation and v_{bl} is the ballistic limit. It was found that the ballistic limit for hybrid magnesium alloy was higher (680 m/s) as compared to the original magnesium alloy. Figure 5 shows the graph of ballistic limit on magnesium alloy using the Retch-Ipson model. The R^2 correlation was shown between 0.9736 to 0.9791, which was close to perfect condition of 1.000. The addition of nanomaterials gave an increase of ballistic limit by much as 13% in relation to the original AZ31B.

Table 2: Parameters of the Retch-Ipson model for the magnesium alloys.

	AZ31B	AZ31B+Pb+CNT
a	1	1
V_{bl} (m/s)	600	680
P	1.6	1.6

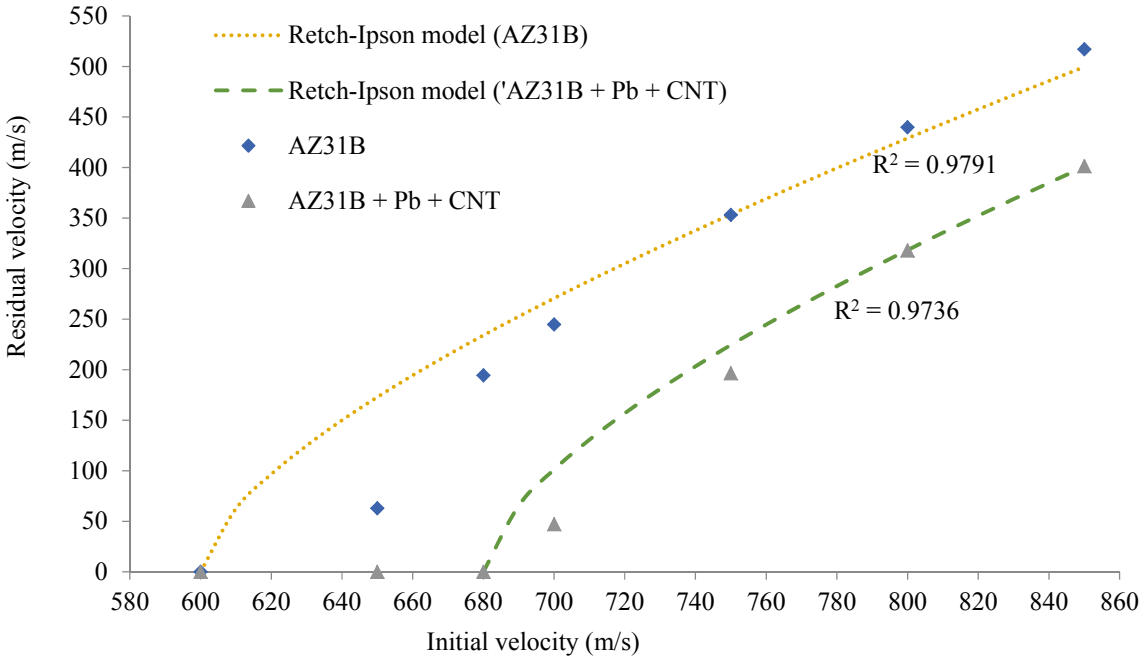

Figure 5: Ballistic limits of the magnesium alloys.

5. CONCLUSION

The fracture behaviour of magnesium alloy with Pb and CNT reinforcement has reduced the depth of penetration up to 40% compared to the original material. The ballistic limit has also increased 13% of the initial velocity. The reinforcement materials such as Pb and CNT have been able to increase the capability of energy absorption of the materials. Energy absorption is an important factor in controlling the depth of penetration as well as extending ballistic limit. Thus, the use of magnesium alloy in ballistic applications is feasible, but several of its properties need to be improved. Furthermore, the addition of an element in the original alloy composition has enhanced the durability characteristics and resulted in a difference in energy absorption.

ACKNOWLEDGEMENT

The authors would like to express their gratitude to Ministry of Higher Education Malaysia via Universiti Kebangsaan Malaysia (UKM) and National Defence University of Malaysia (UPNM) (research funding: LRGS/2013/UPNM-UKM/DS/04) for supporting this research.

REFERENCES

Abdullah, M.F., Abdullah, S., Rahman, N.A., Risby, M.S., Omar, M.Z. & Sajuri, Z. (2016). Improvement of high velocity impact performance of carbon nanotube and lead reinforced magnesium alloy. *Int. J. Automotive Mech. Eng.,* **13**: 3423-3433.

Avila, A.F., Soares, M.I. & Neto, A.S. (2007). A study on nanostructured laminated plates behaviour under low-velocity impact loadings. *Int. J. Impact Eng.* **34**: 28-41.

Eslam, M. S., Michael, P. S. & Mahmoud R. T. (2012). Low-velocity impact of thin woven carbon fabric composites incorporating multi-walled carbon nanotubes. *Int. J. Impact Eng.,* **47**: 39-47.

Feng, F., Huang, S., Meng, Z., Hu, J., Lei, Y., Zhou, M. &Yang, Z. (2014). A constitutive and fracture model for AZ31B magnesium alloy in the tensile state. *Mat. Sci. Eng. A*, **594**: 334-343.

Hernandez, C., Maranon, A., Ashcroft, I.A. & Casas-Rodriguez J.P. (2013). A computational determination of the Cowper–Symonds parameters from a single Taylor test. *Appl. Math. Model.*, **37**: 4698-4708.

Jones, T.L., Richard, D.D. Matthew, S.B. & William, A.G. (2007). Ballistic performance of magnesium alloy AZ31B. *23rd Int. Sym. on Ballistics,* Tarragona, Spain, pp. 989-995.

Lesuer, D.R., Syn, C.K., Sherby, O.D. & Wadsworth J. (1998). Laminated metals composites-fracture and ballistic impact behaviour. *Third Pacific Rim Conf. Adv. Mat. Proc.,* 12-16 July 1998, Honolulu, Hawaii

Mertz, A., Honsel GmbH & Meschede, C.K.G. (2000). Weight and cost saving with magnesium die castings. *Proc.5th Int. Conf. Magnesium Alloys Their Appl.,* Munich, pp. 397-401.

Múgica, J. I., Aretxabaleta, L., Ulacia, I. & Aurrekoetxea, J. (2014). Impact characterization of thermoformable fibre metal laminates of 2024-T3 aluminium and AZ31B-H24 magnesium based on self-reinforced polypropylene. *Composites Part A: App. Sci. Manuf.* **61**: 67-75.

Rahman, N.A, Abdullah, Abdullah, M.F., Omar, M.Z., Sajuri, Z. & Zamri, W.F.H. (2018). Ballistic limit of laminated panels with different joining materials subjected to steel-hardened core projectile. *Int. J. Integrated Eng.,* **10**: 8-14.

Zhikharev, M. V. & Sapozhnikov, S. B. (2017). Two-scale modeling of high-velocity fragment GFRP penetration for assessment of ballistic limit. *Int. J. Impact Eng.***101**: 42-48.

TERRAIN MASKING AND RADAR EXPOSURE MODELLING BASED ON RASTER CELLS FOR PRE-FLIGHT PLANNING FOR LOW FLYING HELICOPTERS

Shahril Ahmad*, Khairol Amali Ahmad, Fakroul Ridzuan Hashim & Wan Mohamed Syafuan

Faculty of Engineering, National Defence University of Malaysia (UPNM), Malaysia

*Email: shahril@upnm.edu.my

ABSTRACT

In some operations, military helicopters are required to hover or fly very low to ground to avoid or minimise radar detection. Hence, during pre-flight planning, helicopters pilots need to identify routes that offer the least exposure to radar detection. Raster cell visibility based on line-of-sight (LoS) provides an effective and efficient approach in determination of degree of terrain masking or radar exposure. In this paper, a software environment was created to establish Terrain Masking and Radar Exposure Index. The environment incorporated local terrain characteristics and generic radars used by ground based air defence (GBAD) units. The analysis and discussion were based on the visibilities of the surface terrain that was represented by the raster cells. This paper concludes that raster cell visibilities can be used pragmatically as a metric of quantifier in determining hovering points or routes for helicopters.

Keywords: *Helicopter; masking; radar; terrain; raster cell visibility.*

1. INTRODUCTION

Previously, radars for most ground based air defence (GBAD) units operate with short integration times and low unambiguous velocity, which most likely will complicate the detection of low flying objects, such as helicopters. With the advent of technology, radars used by GBAD units nowadays are capable of detecting low flying helicopters efficiently and effectively (Davis, 2015).

In some operations, military helicopters are required to fly tactically for critical missions where the main threats are from anti air-craft weapons and supporting sensors, in particular radars (Shenoy, 2015). In order for helicopters to be detected by GBAD radars, a line-of-sight (LoS) must exist between them. If helicopters manage to avoid the LoS, then they are undetected. Hence, it is very important for helicopter pilots to come up with a legitimate flight plan in avoiding or minimising radar detection (Hutchings & Street, 2001).

Presently, with the development of very reliable geographic information systems (GIS) and associated peripherals, spatial information can be utilised to optimise terrain masking techniques (Pelosi, 2012). In this paper, the authors propose a very pragmatic approach of utilising raster data in establishing the degree of terrain masking or radar exposure to form a metric for the purpose of quantifying. Through the use of this quantifier, the degree of terrain masking and radar exposure can be gauged systematically at any particular hovering point or route.

2. THEORETICAL FRAMEWORK

2.1 Conventional Surveillance Radars

Conventional ground surveillance radars illuminate a large portion of space with electromagnetic wave with high average transmission power from kilowatts to megawatts of energy (Hall, 1991). Most of these radars are static and very bulky due to high input power requirement and large antenna (Shenoy, 2015). Atmospheric attenuation for long range surveillance poses a major challenge, whereby low transmission frequencies are generally used to mitigate the issue (Bryant *et al*., 2000). Nonetheless, these radars are capable of detecting targets hundreds of kilometres away, especially when the targets are flying at high altitude (Yongjie, 2011).

2.2 GBAD Surveillance Radars

Modern surveillance radars used by GBAD units are capable of detecting hovering or low flying helicopters. The signal processing of these radars is capable of abstracting the complex echoes of helicopters efficiently and effectively (Shenoy, 2015). Nonetheless, the antennas of these radars are smaller in size due to input power limitation and transportability requirement. Typically, they operate within the upper gigahertz (GHz) region and transmit low average transmission power (Skolnik, 2001). When these parameters are used along with heavy ground clutter and low radar-cross-section of helicopters, the detection range is shortened.

2.3 Refractive Effect

For long range detection, the earth's curvature plays an important role as it can mask radar detection similar to elevated terrain. On the other hand, due to refractive effects, the detection range can be slightly longer since the radar's LoS is longer than the geometric LoS (Anderson & Krolik, 2002). Over-the-horizon (OTH) radars use the refractive nature of high frequency (HF) ionospheric propagation to perform wide-area surveillance of targets at long ranges beyond the horizon of conventional LoS radars. Typically, OTH surveillance radars work in the megahertz (MHz) region (Adrian, 2007).

Most primary radars, especially radars used by GBAD units, operate at higher frequencies. Signals at these frequencies do not follow the curvature of the earth very well. They work best in LoS, where under standard atmospheric conditions, they undergo "standard refraction" or bending following the earth curvature (Doerry, 2013). Thus, in this paper, the "effective earth radius" is taken into consideration during terrain masking modelling.

3. METHODOLOGY

3.1 Digital Elevation Model (DEM)

A digital elevation model (DEM) represents the elevations of the bare ground surface without any objects, such as plants and buildings. For this paper, the DEM was provided by the Department of Survey and Mapping of Malaysia (JUPEM), where the elevation resolution is 20 m. The study was based on the operation area shown in Figure 1. It stretches from 4.1229080 to 4.4865670 °N of latitude and 101.0763480 to 101.3907140 °E of longitude , which covers an area of approximately 2.5 mil. m^2, with elevation ranging from about 0 to 2,000 m above sea level. The areas on the left of the operation area constitute low grounds, while most areas on the right are mountainous.

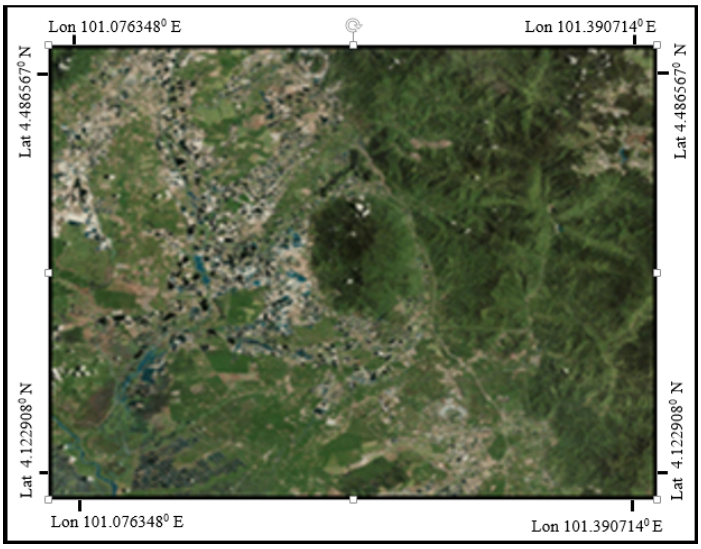

Figure 1: Image of the operation area.

3.2 Terrain Masking

In principle, terrain masking is achieved by hiding behind terrain features (Jiang *et al.*, 2014). For a helicopter, it is achieved by hovering or flying through low elevations, keeping the higher elevations between the helicopter and LoS of a sensor as shown in Figure 2. Hence, terrain masking is an essential technique to be exploited by defence forces operating in countries that are mountainous in nature.

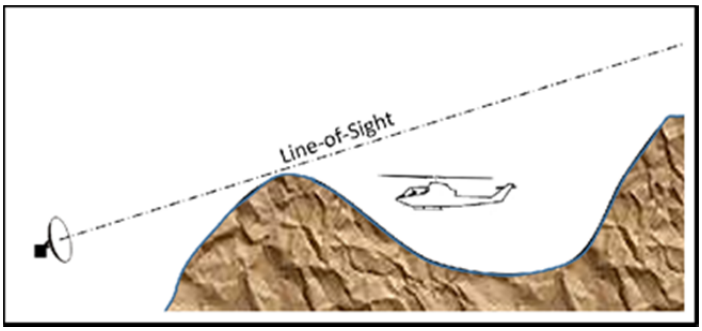

Figure 2: A high elevation feature blocking the LoS.

3.3 Degree of Masking of a Single Point

Assuming that an observer is standing at a certain elevation above ground at point A, as shown in Figure 3, and looking at a certain angle from the ground plane, the LoS shows the visibilities of the surface terrain along the line from point A to D. The surface terrain from points A to B is visible to the observer since there is no obstruction to the LoS. However, the terrain from points B to C and D to E are concealed due to the high elevation features at points B and D. If the surface of the terrain is represented by raster cells, then the visibilities of the cells can be used as an indicator for the degree of masking. Thus, if the observer rotates his view by 360^0 horizontally and -90^0 to $+90^0$ vertically, then the degree of masking of the observer at point A can be represented in 3D .

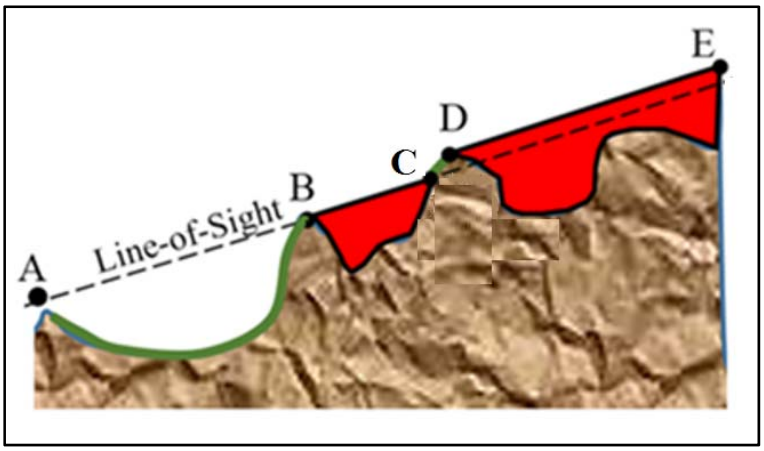

Figure 3: Visibilities of various points from Point A.

3.4 Degree of Masking of a Path

Figure 4 illustrates an observer at point O looking at a helicopter path flying from points A to F. W, X and Z represent high elevation features that are higher than point O, while Y represents a high elevation feature that is only slightly higher than point O. Generally, the helicopter is concealed from the observer from points A to B, C to D and E to F since points W, X and Z are blocking the LoS. The helicopter is visible from points B to C and still visible while flying from points D to E provided that the elevation of point Y is low enough not to block the LoS. Again, if the surface of the terrain along the path is represented by raster cells, then the visibilities of the cells can used as an indicator for the degree of masking for a particular path in 3D.

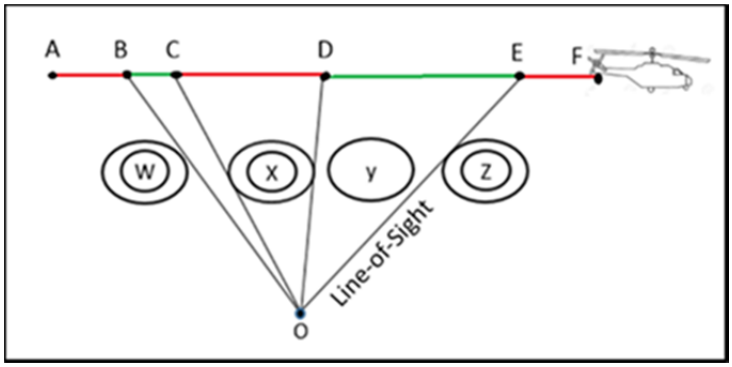

Figure 4: Visibilities along a path.

3.5 Radar Coverage

In some countries, GBAD consists of several types of surveillance radars ranging from short range air defence radars to battle field surveillance radars. In order to achieve a high degree of situational awareness, the information from these radars are interfaced or integrated through systematic data fusion process (Shenoy, 2015). Modern short range surveillance radars are required to detect the presence of moving targets of up to 40 km with 80% probability depending type of targets (Hall, 1991).

The main threat to hovering or low flying helicopters is from battlefield surveillance radars (BSR) that are capable of detecting helicopters for up 15 km by exploiting the high Doppler signals from the fuselage and blades' flash. Even when the Doppler signals from the helicopter's skin line or the fuselage are masked by clutter background, the Doppler signals from the blades are still available at large since they can reach up to 8 kHz (Misiurewicz, 1988). However, the strength of the Doppler

signals is low due to the low radar-cross-section of the blades, which leads to shorter detection range. The aspect angle between a radar and helicopter also does have effect on detection range (Ahmad & Ahmad, 2017). In this study, the search radius of BSR for detecting low flying helicopters is used in determining the correlation between the radar detection coverage and degree of terrain masking.

4. RESULTS AND DISCUSSION

In this paper, a software environment was constructed for the purpose of investigation, where it incorporated a GIS, DEM, as well as generic BSR characteristics and performances.

4.1 DEM

The DEM of this operation area is shown in Figure 5. The DEM is based on WGS84 World Mercator projection. It consists of 19,700,270 raster cells, where the size of each cell is 11 by 11 m. The surface elevations are broken into 10 classes through the equal interval method. The raster cells elevations are represented by colours as shown by the inset of the figure.

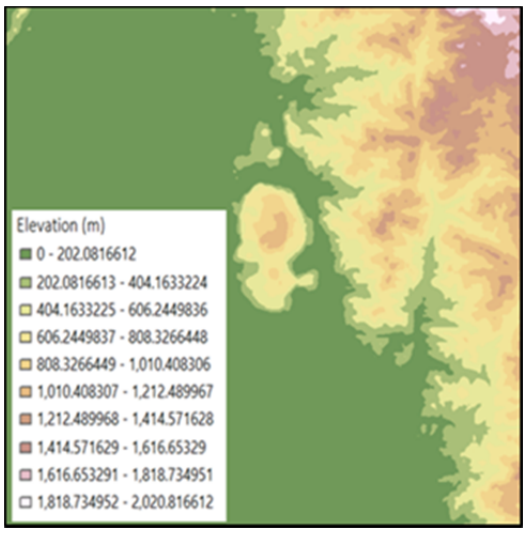

Figure 5: DEM of the operation area.

4.2 Terrain Masking of a Single Point

Figure 6 depicts the visibility of an observer at 150 m above point A (4.3277 ^{0}N, 101.1940 ^{0}E) looking from 0^0 to 360^0 horizontally and $+90^0$ to -90^0 vertically to targets positioned exactly on each raster cell within the operation area. The light green colour represents raster cells or locations that are visible to the observer while the pink colour defines the opposite. In other words, the observer is exposed to targets lying within the light green areas while concealed to those targets in the pink areas. Table 1 shows that 7,876,782 (40%) raster cells are visible, whilst 11,823,488 (60%) cells are concealed to the observer at point A. Thus, the number cells according to their visibility can be used to indicate the degree of terrain masking.

Figure 7 illustrates raster cell visibilities from the same observer at point A looking towards points F and Z. Point F lies within the visible areas while point Z is the opposite. Both straight lines represent the LoS.

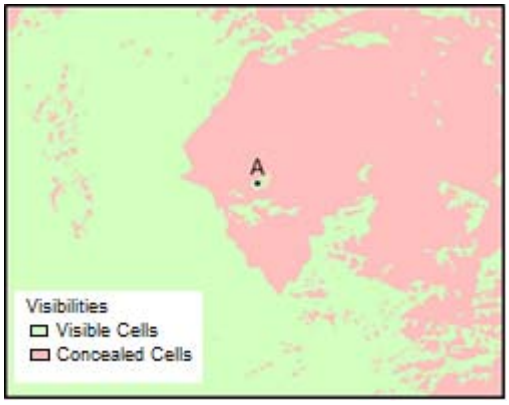

Figure 6: Raster cell visibilities of an observer.

Table 1: Number of cells based on visibilities.

Observer height relative to ground (m)	Visibilities			
	Visible		Concealed	
	No. of Cells	%	No. of Cells	%
150	7,876,782	40	11,823,488	60

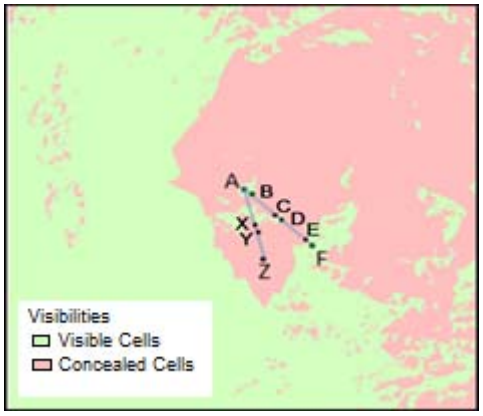

Figure 7: An observer at point A looking towards points F and Z.

Figure 8 shows the surface profile from point A to F. The surface terrain from points A to B, C to D and E to F are visible to the observer. However, the area from points B to C and D to E are masked. Based on this profile, it can be seen that although point F is exposed, there are huge areas that are concealed from the observer due to high feature obstruction to the LOS. Hence, the degree of masking of a particular point is dictated by the height of its surrounding. By exploiting this factor, a high degree of terrain masking can be achieved.

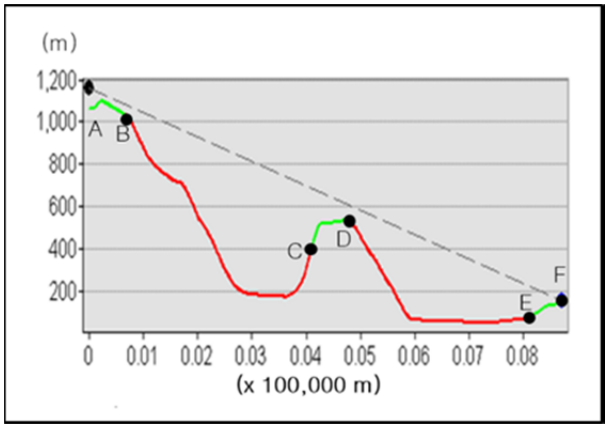

Figure 8: Surface profile looking from points A to F.

Figure 9 illustrates the surface profile from points A to Z. The high feature at point X provides huge concealment starting from points X to Z. However, any target along points X to Z can be made visible if its elevation is raised to a certain height. For example, by raising the elevation of a target above point Y to 100 m makes it possible to be observed. Thus, the elevation of a target or its offset from ground level does contribute to the degree of terrain masking.

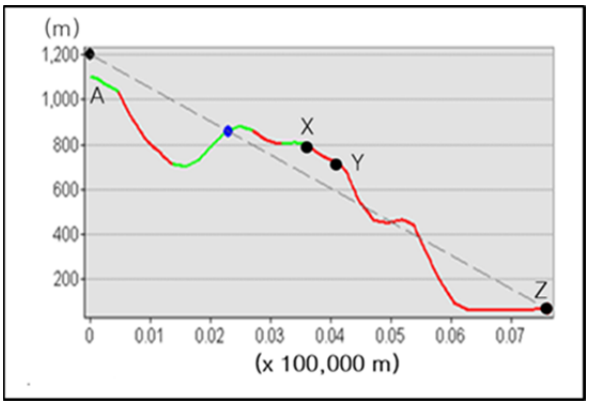

Figure 9: Surface profile looking from A to Z.

Figure 10 depicts visibility as the observer at point A that is elevated by 50 m from the previous height. At this height, more raster cells are visible, especially raster cells at the right side of the figure. Table 2 illustrates the visibilities of raster cells at various elevations of point A. As the height or the offset of the observer at point A is increased, the degree of masking decreases. This deduction can be made pragmatically based on the raster cells visibilities shown in the table.

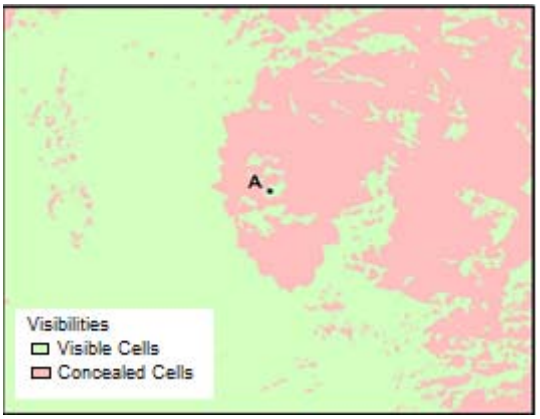

Figure 10: Visibility of observer at point A at 150 m from the ground.

Table 2: Visibilities of point A at various offsets from ground level.

Observer height relative to ground (m)	No. of raster cells			
	Visible		Concealed	
	No. of cells	%	No. of cells	%
50	8,252,181	42	11,448,089	58
100	11,823,488	60	7,876,782	40
150	12,663,160	64	7,037,110	36
200	13,076,284	66	6,623,986	34

4.3 Clipping Consideration

Point O in Figure 11 is placed at the edge of the operation area, where visible and concealed areas are represented by green and pink colours respectively. It is very obvious that the upper area of point O is clipped by the upper border of the operation area. This is a very important aspect to be considered due to the fact that if point O is replaced by a helicopter, then the degree of terrain masking at all angles must be taken into consideration. Thus, the top part of the operation area should be extended accordingly in order to have reliable data for the purpose of comparison.

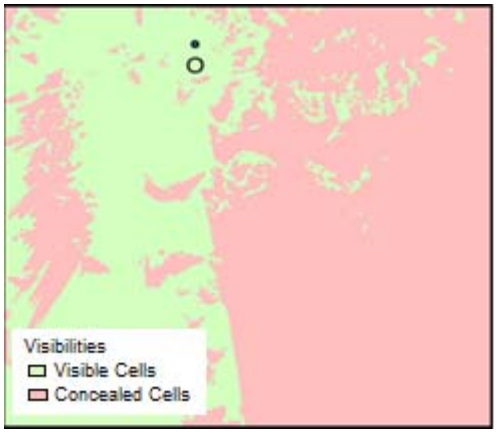

Figure 11: Visibilities clipping at point O.

4.4 Terrain Masking of a Path

Points 1 to 10 in Figure 12 represent a path that is 150 m above ground and about 10 km long. There are 10 points with distance of 1.11 km between each point. The profile of the terrain along the line from points 1 to 10 is shown in Figure 13.

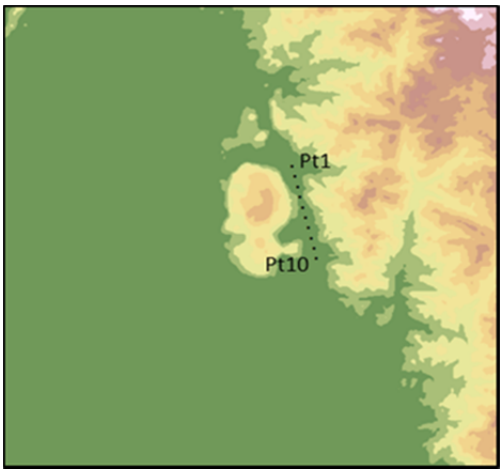

Figure 12: A path that is about 10 km long and 150 m above ground.

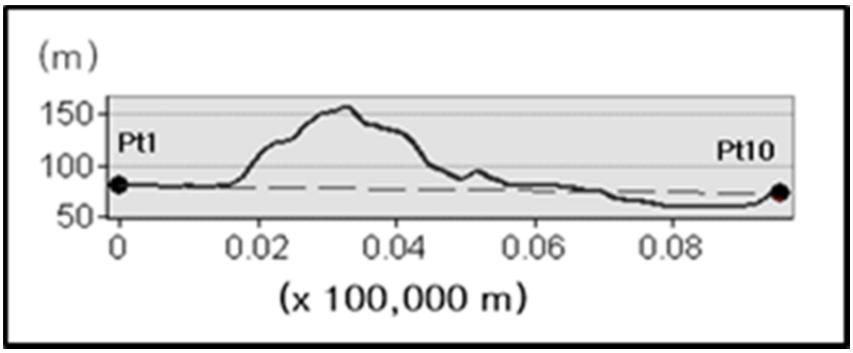

Figure 13: Surface profile along the path in Figure 12.

The visibilities along the path is determined by the combination of the visible raster cells from the 10 points. The light green areas along the path are those surfaces or raster cells that are visible along the path as shown in Figure 14. Table 3 shows the number of raster cells based on the visibilities of each point. Based on Figure 14 and Table 3, the degree of terrain masking of a path can be determined based on the total number of visible cells from the 10 points. Nonetheless, terrain masking at any of the 10 points is still important because it indicates the degree of exposure at each point.

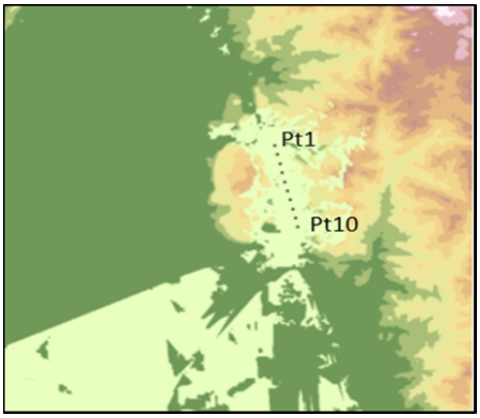

Figure 14: Raster cell visibilities along the path.

Table 3: Raster cells visibilities for each point.

Point	Lat.	Lon.	Visibilities			
			Visible		Concealed	
			No. of cells	%	No. of cells	%
1	101.2280^0	4.3752^0	421,225	2	19,279,045	98
2	101.2293^0	4.3657^0	353,720	2	19,346,550	98
3	101.2318^0	4.3549^0	433,588	2	19,266,682	98
4	101.2344^0	4.3449^0	562,279	3	19,137,991	97
5	101.2368^0	4.3352^0	475,002	2	19,225268	98
6	101.2393^0	4.3254^0	465,689	2	19,234,581	98
7	101.2417^0	4.3157^0	668,695	3	19,031,575	97
8	101.2442^0	4.3059^0	1,035,275	5	18,664,995	95
9	101.2465^0	4.2961^0	2,185,960	11	17,514,310	89
10	101.2490^0	4.2864^0	3,292,937	17	16,407,333	83
Total			9,894,370		187,108,330	
Percentage			5%		95%	
Terrain Masking Index (TMI)			5			

A better way of representing the degree of masking terminology is by naming it as terrain masking index (TMI). In the case of a point, TMI is the ratio between visible raster cells of a point to the total cells within an operation area. For a path, TMI is the ratio between the total number visible raster cells of a particular path to the total number of cells within an operation area. Hence, if there is another path from points 1 to 10, the degree of terrain masking between these two paths can be compared systematically using TMI.

4.5 Correlation Between Terrain Masking and Radar Detection

Figure 15 depicts the visibility of an observer 150 m above point A with the search radius limited to 15 km only, which covers about 30% of the total area. The visibility pattern is similar to Figure 6 except it truncates within a 15 km diameter. The number of visible raster cells represented by light green is only 2,543,235, while the number of concealed cells is 3,100,533. The reason for limiting the search radius to 15 km is to assimilate the capabilities of BSR in detecting low flying helicopters. Thus, if the observer at point A is replaced by a BSR radar, areas detectable or exposed to the radar are represented by the light green colour, while the pink colour represents the opposite. Similarly, if the observer above point A is a hovering helicopter, then a BSR radar that is positioned in any location within the light green areas is able to detect the helicopter.

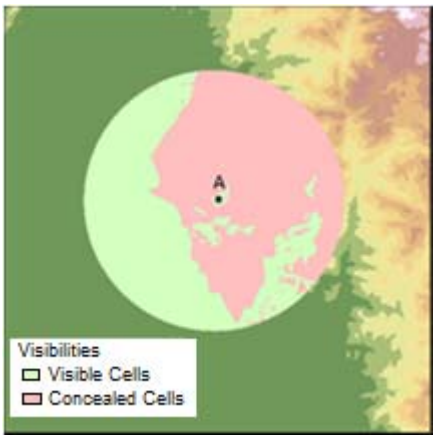

Figure 15: Raster cells visibilities within a 15 km radius.

Figure 16 shows the terrain masking achieved by a helicopter when it is flying using the same route as Figure 12, but the radius is limited to only 15 km. Table 4 shows the visibilities of raster cells as the radius is fixed up to only 15 km. It is very obvious that the processing time is shorter since the total number cell processed is reduced from 197,002,700 cells to only 61,998,920 cells. Although the number of processed cells is reduced, the difference between the two approaches in terms of raster cell visibilities is only 3%. Thus, determining the degree of terrain masking based on certain radius offers some advantages.

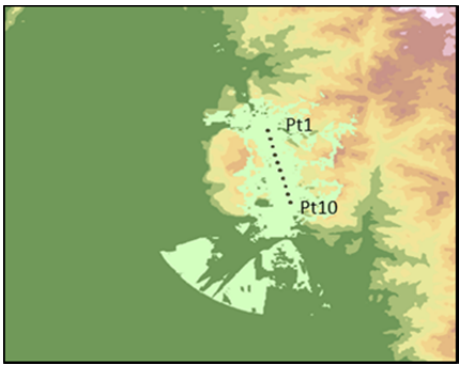

Figure 16: Radar exposure along a path.

Table 4: Raster cells visibilities within 15 km radius.

Pt	Lat.	Lon.	Visibilities			
			Visible		Invisible	
			No. of cells	%	No. of cells	%
1	101.22800	4.37520	415,709	7	5,778,183	93
2	101.22930	4.36570	338,217	5	5,855,675	95
3	101.23180	4.35490	348,303	6	5,845,589	94
4	101.23440	4.34490	467,104	7	5,786,788	93
5	101.23680	4.33520	375,946	6	5,817,946	94
6	101.2393^0	4.32540	395,442	6	5,798,450	94
7	101.2417^0	4.31570	477,781	8	5,716,111	92
8	101.2442^0	4.30590	578,093	9	5,615,799	91
9	101.2465^0	4.29610	717,389	12	5,476,503	88
10	101.2490^0	4.28640	967,864	16	5,226,028	84
Total			5,081,848		56,917,072	
Percentage			8%		92%	
Radar Exposure Index (REI)			8			

A better way of representing the degree of masking limited by certain radius in order to imitate radar coverage is by naming it as radar exposure index (REI). In the case of a point, REI is the ratio between the number of visible raster cells of a point to the total number of raster cells within a particular radius. For a path, REI is the ratio between the number visible raster cells of a particular path to the total raster cells within a particular radius.

As mentioned earlier, if a point or route is located at the edge of an operation area, then the result may not be comprehensive for the reasons stated earlier. To overcome this problem, the length of the search radius can be used as a yard stick for map extension.

4. CONCLUSION

Earth surfaces or terrain profiles that are represented by raster cells can be used pragmatically in determining the degree of terrain masking or radar exposure based on LoS. By applying this unique property, the visibilities of the raster cells relative to a particular point or path can be used as metric for terrain masking or radar exposure quantifier. TMI or REI can be used as a quantifier metric in evaluating hovering points or paths for helicopters during pre-flight planning, which can subsequently enhance helicopter survivability. For future studies, these indices can be combined with other considerations, such as topographic information from digital surface models (DSM), in order for the pilots to come up with more exhaustive pre-flight planning.

ACKNOWLEDGEMENTS

The authors of this paper are grateful to the Department of Survey and Mapping of Malaysia (JUPEM) for providing the valuable DEM data and the National Defence University of Malaysia (UPNM) for the funding of this study.

REFERENCES

Adrian, O. (2007). Future surface radar technology. *2007 IEEE Radar Conf.*, pp. 49-54.

Ahmad, S. & Ahmad, K.A. (2017). Doppler spectrum analysis for active seeker head. *J. Fundamental Appl. Sci.*, 116-130.

Anderson, R.H. & Krolik, J.L. (2002). Track association for over-the-horizon radar with a statistical ionospheric model. *IEEE Trans. Signal Proc.*, **50:** 2632 - 2643

Bryant, T.G., Morse, G.B., Novak, L.M. & Henry, J.C. (2000). Tactical radars for ground surveillance. *Lincoln Lab. J.*, **12**: 341-354.

Davis, M.E. (2015). A history of battlefield surveillance radar. *2015 IEEE Radar Conf*., pp. 1345-1350.

Doerry, A.W. (2013). *Earth Curvature and Atmospheric Refraction Effects on Radar Signal.* Sandia Report, New Mexico.

Hall, P.S. (1991). *Radar.* Brassey's, Shrivenham, UK.

Hutchings, P.J. & Street, N.J. (2001). Future short range ground-based air defence. *RTO SCI Symp.*, pp. 6-1).

Jiang, B., Bishop, A.N., Anderson, B.O., & Drake, S.P. (2014). Path planning for minimizing detection. *19th World Congress Int. Fed. Autom. Control*, pp. 10200-10206.

Misiurewicz, J. (1988). Analysis of radar echo from a helicopter rotor hub. *International Conference on Microwaves & Radar* (pp. 866-870). Krakow: IEEE.

Pelosi, M. (2012). Range-limited UAV trajectoy using terrain masking under radar detection risk. *Appl. Artif. Intell.*, **26**: 743-759.

Shenoy, R. P. (2015). Radar: Development and state-of-art in hardware. *IETE J. Res.*, **24**: 499-506.

Skolnik, M. (2001). *Introduction to Radar Systems.* Mc Graw Hill, New York.

Yongjie, Q. (2011). Detection probability of early warning radar against hypersonic. *Proc. 2011 Int Radar Conf.* , pp. 1733-1736.